A novel regulatory mechanism of the plant TIR immune signaling

Inaugural-Dissertation

zur
Erlangung des Doktorgrades
der Mathematisch-Naturwissenschaftlichen Fakultät

der Universität zu Köln

vorgelegt von

Dongli Yu

aus Shenyang, China

Köln, July 2022

Die vorliegende Arbeit wurde am Max Planck Institut für Pflanzenzüchtungsforschung in Köln Arbeitsgruppe Prof. Dr. Jijie Chai and Prof. Dr. Paul Schulze-Lefert durchgeführt.

The work described in this thesis was conducted under the supervision of Prof. Dr. Jijie Chai and Prof. Dr. Paul Schulze-Lefert at the Max Planck Institute for Plant Breeding Research

Berichterstatter:	Prof. Dr. Jijie Chai Prof. Dr. Elmar Behrmann
Prüfungsvorsitzender:	Prof. Dr. Bart P.H.J. Thomma
Tag der Disputation:	12.September.2022

Contents

Nomenclature

Amino acids

Alanine	Ala, A
Arginine	Arg, R
Asparagine	Asn, N
Aspartate	Asp, D
Cysteine	Cys, C
Glutamate	Glu, E
Glutamine	Gln, Q
Glycine	Gly, G
Histidine	His, H
Isoleucine	Ile, I
Leucine	Leu, L
Lysine	Lys, K
Methionine	Met, M
Phenylalanine	Phe, F
Proline	Pro, P
Serine	Ser, S
Threonine	Thr, T
Tryptophan	Trp, W
Tyrosine	Tyr, Y
Valine	Val, V

Chemicals

Adenosine triphosphate	ATP
Deoxyadenosine triphosphate	dATP
Adenosine diphosphate	ADP
Adenosine monophosphate	AMP
ADP-Ribose	ADPR
Nicotinamide	NAM
Nicotinamide mononucleotide	NMN
Nicotinamide adenine dinucleotide	NAD^+
Cyclic ADPR	cADPR
Cyclic AMP	cAMP
Salicylic acid	SA

Immunology terms

Pathogen-associated molecular patterns	PAMPs
Damage-associated molecular patterns	DAMPs
Pattern recognition receptors	PRRs

Toll-like receptors	TLRs
Receptor-like kinases	RLKs
Receptor-like cytoplasmic kinases	RLCKs
Receptor-like proteins	RLPs
RNase-like protein associated with haustoria	RALPH
Candidate secreted effector proteins	CSEPs
N-acetylglucosamine	NAG
Nucleotide-binding leucine-rich repeat immune receptors	NLRs
Coiled-coil domains	CC domains
Toll/interleukin-1 receptor domains	TIR domains
Nucleotide binding oligomerization domain	NOD
Nucleotide binding domain	NBD
Leucine rich repeat	LRR
NLRs with N terminal CC domains	CNLs
NLRs with N terminal TIR domains	TNLs
Helper NLRs	RNLs
Caspase activation and recruitment domains	CARDs
Pyrin domains	PYDs
Hematopoietic expression, interferon-inducible, and nuclear localization	HIN domain
Lysin motif	LysM
Nucleoside diphosphate-linked moiety X	Nudix
Pattern-triggered immunity	PTI
Effector-triggered immunity	ETI
Regulated cell death	RCD
Plasma membrane	PM

Gene full names

Brassinosteroid insensitive 1-associated receptor kinase 1	BAK1
Flagellin sensing 2	FLS2
Chitin elicitor receptor kinase 1	CERK1
Rice chitin elicitor-binding protein	*Os*CEBiP
AvrPtoB-tomato interacting protein 9	Bti9
Lysin-motif receptor-like kinase 5	LYK5
Lectin S-domain-1 RLK	LORE
Does not respond to nucleotides 1	DORN1
L-type lectin receptor kinase I.5	LECRK-I.5
Extracellular protein 6	ECP6
Chorismate mutase 1	CMU1
Suppressor of necrosis 1	SNE1
Small proteins into the xylem sap 6	Six6

Myeloid differentiation primary response 88	MyD88
HOPZ-activated resistance 1	ZAR1
Resistance related kinase 1	RKS1
Hopz-effector-triggered immunity deficient 1	ZED1
ZED1-related kinase 3	ZRK3
AvrPphB susceptible1-like protein 2	PBL2
Locus orchestrating victorin effects 1	LOV1
Resistance to *Pseudomonas syringae* pv. *maculicola* 1	RPM1
Resistance to *Pseudomonas syringae* protein 2	RPS2
Recognition of *Peronospora parasitica* 1	RPP1
Senescence-associated E3 ubiquitin ligase 1	SAUL1
Chilling sensitive 1	CHS1
Suppressor of chs1-2, 3	SOC3
Enhanced disease susceptibility 1	EDS1
Phytoalexin deficient 4	PAD4
Senescence-associated gene 101	SAG101
N requirement gene 1	NRG1
Activated disease resistance 1	ADR1
Sterile alpha and TIR pattern-containing protein 1	SARM1
Resistance to powdery mildew 8	RPW8
cGAMP synthase	cGAS
Absent in melanoma 2	AIM2
Interferon gamma inducible protein 16	IFI16
RPM1-interacting protein 4	RIN4
Botrytis-induced kinase 1	BIK1
RPM1-induced protein kinases	RIPKs
Signalling effector stimulator of interferon genes	STINGs
Mitogen-activated protein kinases	MAPKs
Mixed lineage kinase domain-like	MLKLs
Cyclic nucleotide-gated channels	CNGCs
Xanthomonas outer protein Q	XopQ
Recognition of XopQ 1	ROQ1
Arabidopsis. thaliana recognized 1	ATR1
Resistance to *Ralstonia solanacearum* 1	RRS1
Resistance to *Pseudomonas syringae 4*	RPS4

Abbreviations

Proteins containing TIR domain, except for full-length TNL	TIR domain proteins, TIRs
2′,3′-cAMP and 2′,3′-cGMP, without special distinction	2′,3′-cAMP/cGMP
2′,3′-cAMP, 2′,3′-cGMP, 2′,3′-cCMP, and 2′,3′-cUMP	2′,3′-cNMPs

Abstract

Plant defense against microbial pathogens is mainly realized by pattern-triggered immunity (PTI) mediated by pattern recognition receptors (PRRs) at the cell surface, and effector-triggered immunity (ETI) mediated by nucleotide-binding leucine-rich repeat (NLR) immune receptors inside cells. Based on their N-terminal domains, plant NLRs can be divided into two categories: CC-NLRs (CNLs) with a coiled-coil (CC) domain and TIR-NLRs (TNLs) with a toll/interleukin 1 receptor (TIR) domain. Specific recognition of pathogen effectors induces oligomerization of NLRs, termed resistosomes, to transduce plant immune signaling. CNLs are able to form pentameric resistosomes upon activation and function as calcium (Ca^{2+})-permeable channels in the plasma membrane. Whether TNLs form resistosomes in response to pathogen infection remained an open question, although the TIR domain in TNLs has NADase activity that is required for TNL-mediated immunity. NADase activity, although essential, is not sufficient for TIR-triggered immune responses in plants, suggesting that other components may be required for TIR-mediated signaling. In my dissertation, I employed multiple approaches including biochemistry and structural biology to address these questions. The thesis contains three parts:

In the first part, I present multiple lines of evidence showing that the *Arabidopsis* TNL RPP1 (for recognition of *Peronospora parasitica* 1) forms a tetrameric resistosome upon recognition of the cognate *Hyaloperonospora arabidopsidis* effector ATR1. Biochemical and structural data are summarized revealing the mechanism underlying the requirement of the RPP1 resistosome formation for NADase activity. The data from this study define the mechanism of direct effector recognition by a TNL, and demonstrate that the assembly of RPP1 resistosomes is required for TIR-encoded NADase activity and RPP1 function.

In the second part, I describe biochemical evidence that TIR domain proteins also exhibit 2′,3′-cAMP/cGMP synthetase activity with RNA and probably DNA (RNA/DNA) as substrates. Then I present functional data supporting the physiological relevance of the synthetase activity in TIR-mediated immune responses. Structural data on a TIR domain protein bound by its dsDNA substrate are described, and the mechanisms of how TIR domain proteins encode both NADase and synthetase activities and how the two activities may act together to mediate TIR signaling are discussed. The data presented in this part reveal a novel enzymatic activity of plant TIR domain proteins and establish a role of 2′,3′-cAMP/cGMP in plant immunity.

In the last section of my thesis, I describe experiments testing whether the RNase-like effector proteins associated with haustoria (RALPH effectors) have RNase activity.

1. General Introduction

Terrestrial plants are sessile organisms under constant threat of invasion by potential pathogens throughout their life cycles. These pathogenic microorganisms, including viruses, bacteria, fungi, and oomycetes, not only hijack nutrients but also perturb physiological processes, arrest growth and inflict tissue damage on their hosts via production of toxins, cell-wall-degrading enzymes, and virulence proteins (Dou and Zhou, 2012). To withstand and combat microbial attack, plants are endowed with sophisticated innate immune systems consisting of a repertoire of cell-surface and intracellular immune receptors (Jones and Dangl, 2006; Kourelis and van der Hoorn, 2018). Cell-surface immune receptors, collectively referred to as pattern recognition receptors (PRRs), form the front line of the immune surveillance. PRRs activate pattern-triggered immunity (PTI) by sensing a variety of immunogenic signals derived from pathogens or the host, known as pathogen-associated molecular patterns (PAMPs) or damage-associated molecular patterns (DAMPs), respectively. To establish successful infections, pathogens deliver effectors into different cellular compartments of the host to dampen PTI. Inside the cell, the presence of these effectors is typically recognized by nucleotide-binding leucine-rich-repeat receptors (NLRs), the major class of intracellular immune receptors. NLRs sense non-self molecules or infection-associated damage signals and elicit a long-lasting and robust defense responses, termed effector-triggered immunity (ETI). ETI is often associated with a hypersensitive response (HR), a form of regulated cell death (RCD), which is thought to restrict the spread of pathogen from attempted infection sites. Mounting evidence indicated that ETI can potentiate PTI, while PTI can also boost the defense output of ETI (Ngou et al., 2021; Tian et al., 2021; Yuan et al., 2021b), suggesting a continuum and synergy between PTI and ETI to achieve appropriate plant immunity (Lu and Tsuda, 2021; Thomma et al., 2011; Yuan et al., 2021c).

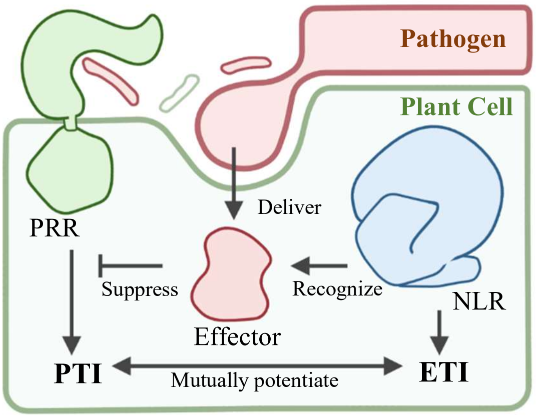

Figure 1. Schematic view of plant innate immunity. Upon sensing PAMPs/DAMPs and effectors (pink), PRRs (green) and NLRs (blue) activate PTI and ETI, respectively.

1.1 Plant immunity activated by cell-surface immune receptors (PTI)

Pathogen infection is generally accompanied by the release of conserved molecules and endogenous danger signals, PAMPs and DAMPs, respectively. PAMPs and DAMPs are recognized by cell surface localized PRRs in both animals and plants (Botos et al., 2011; Couto and Zipfel, 2016). Plant PRRs largely fall into two subfamilies, receptor-like kinases (RLKs) and receptor-like proteins (RLPs), both of which are plasma membrane (PM) localized (Wan et al., 2019b; Zhou and Zhang, 2020). RLKs typically contain an extracellular ligand sensor domain, such as an LRR, LysM or lectin domain (Couto and Zipfel, 2016); a transmembrane region; and an intracellular kinase domain for immune signal transduction (Han et al., 2014; Oh et al., 2011). RLPs have a similar structural organization to RLKs but lack the intracellular kinase domain. Therefore, RLPs inherently require a co-receptor kinase to form bimolecular equivalents of genuine RLKs (Gust and Felix, 2014; Liebrand et al., 2014). Perception of PAMPs/DAMPs results in activation of the intracellular kinase domains in RLK- or RLP-containing signaling complex, leading to cascade of acute immune responses, including phosphorylation of downstream receptor-like cytoplasmic kinases (RLCKs) and mitogen-activated protein kinases (MAPKs), production of nitric oxide (NO), burst of reactive oxygen species (ROS) and increase of cytosolic Ca^{2+} concentrations within minutes (Naveed et al., 2020).

1.1.1 PTI triggered by PAMPs

The conserved 22-amino-acid epitope of bacterial flagellin (flg22) is directly bound by the LRR domain of *Arabidopsis* LRR-PRR FLS2 (for flagellin sensing 2). Upon recognition of flg22, FLS2 recruits another LRR-PRR BAK1 (for brassinosteroid insensitive 1-associated receptor kinase 1) through the C-terminus of the FLS2-bound flg22 and activates PTI responses (Sun et al., 2013; Zipfel et al., 2004).

In addition to flg22, chitin, an N-acetylglucosamine (NAG) polymer that is the major structural carbohydrate of fungal cell walls, also acts as a PAMP and can activate plant PTI (Zhang and Zhou, 2010). Chitin directly interacts with the LysM-RLK *At*CERK1 (for chitin elicitor receptor kinase 1) and *At*LYK5 (for lysin-motif RLK 5) in *Arabidopsis* (Miya et al., 2007), and with the RLK *Os*CERK1 and the RLP *Os*CEBiP (for chitin elicitor-binding protein) in rice (Kaku et al., 2006; Xu et al., 2022). *At*CERK1 has three tightly packed LysMs (LysM1-3) in the extracellular space on the cell surface of the host cells. Binding of $(NAG)_8$ to LysM2 induces homo-dimerization of *At*CERK1, which is required for activation of its kinase activity (Liu et al., 2012). The mechanism of chitin recognition and dimerization is conserved among other plant LysM-PRRs (Cao et al., 2014; Liu et al., 2016; Shimizu et al., 2010; Xu et al., 2022).

Other well characterized PAMPs such as the conserved bacterial epitope, elf18, derived from elongation factor Tu (EF-Tu), or peptidoglycan, or lipopolysaccharide, are recognized by EF-Tu receptor (EFR) (Zipfel et al., 2006), LYM1/LYM3 (Willmann et al., 2011) and lectin S-domain-1 RLK LORE (Ranf et al., 2015), respectively. The recognition of these PAMPs by plant PRRs activates PTI responses and establishes a first line of induced plant immune responses.

1.1.2 PTI triggered by DAMPs

In contrast to PAMPs, DAMPs are host-derived endogenous danger signals released by pathogen-infected cells or wounded tissues (Rubartelli and Lotze, 2007). One of the best characterized DAMP families encompasses plant elicitor peptides (Peps) (Yamaguchi et al., 2006). Peps are processed from their precursors called proPeps through Ca^{2+}-dependent metacaspase cleavage and the mature Peps are released to the extracellular space through an unknown mechanism (Hander et al., 2019). In *Arabidopsis*, the LRR-RLKs Pep1 receptor 1/2 (PEPR1/2) have been identified as the receptors of Peps (Tang et al., 2015; Yamaguchi et al., 2010).

Nucleotide derivatives can also function as DAMPs. ATP, a universal source of energy for biochemical reactions in cells, can be released into the extracellular matrix in response to environmental stimuli and triggers immune responses (Chivasa et al., 2009b; Khakh, 2009). In plants, leakage of ATP can result from physical wounding, insect infestation and microbial pathogen infection (Chivasa et al., 2009a; Chivasa et al., 2009b; Medina-Castellanos et al., 2014). The released ATP molecules are perceived by *Arabidopsis* lectin-RLK DORN1 (for does not respond to nucleotides 1) and LECRK-I.5 (for L-type lectin receptor kinase I.5, also known as P2K2), through their extracellular lectin domains (Choi et al., 2014; Pham et al., 2020). These two lectin-RLKs interact with each other at the PM and cross-phosphorylate upon extracellular ATP treatment. Application of ATP mimics PAMP-induced PTI responses in wild-type (WT) *Arabidopsis* (Reichler et al., 2009; Tanaka et al., 2010), but not in *dorn1* mutant plants (Choi et al., 2014). Moreover, *p2k2 and Dorn1/p2k2* mutant plants showed increased susceptibility to *Pseudomonas. syringae* infection (Pham et al., 2020).

Similar PTI-inducing effects were observed upon exogenous application of another universal cellular small molecule, NAD^{+} (Wang et al., 2017). Supporting a DAMP role for this small molecule, *P. syringae* pv. *tobacco* (*Pst*) DC3000/*avrRpt2* infection caused NAD^{+} leakage into the *Arabidopsis* apoplast at concentrations sufficient to induce PTI responses (Zhang and Mou, 2009). Extracellular NAD^{+} also play critical roles in the regulation of systemic acquired resistance (SAR) (Hou et al., 2019). Although direct application of NAD^+ failed to induce SAR, reducing its concentration by overexpressing the extracellular NADase CD38, significantly compromises SAR induction by local pathogen infection (Zhang and Mou, 2012).

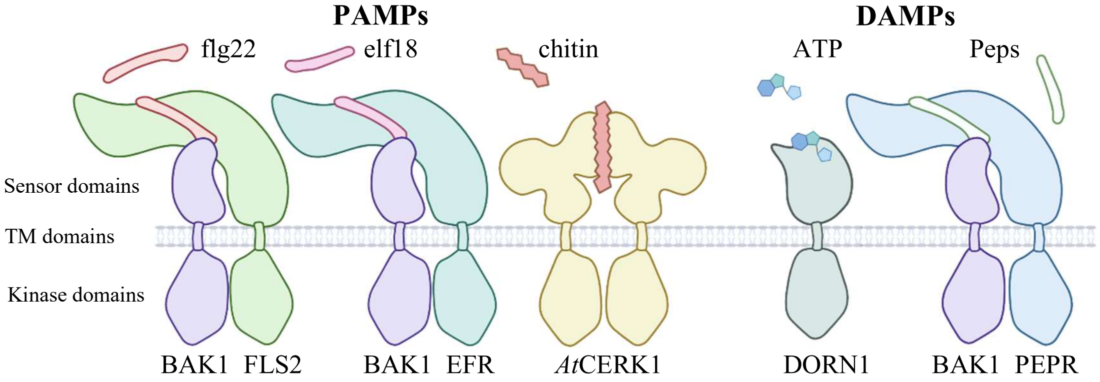

Figure 2. Schematic view of ligand recognition mechanism of different PRRs. Membrane localized PRRs perceive PAMPs and DAMPs to initiate PTI responses. TM: transmembrane.

Another well-studied type of DAMP is the mis-localized DNA (non-nuclear DNA) induced by microbial infection or cellular stresses (Kuthanova et al., 2008; Ryerson and Heath, 1996). In animals, self-DNA fragments can come from dead cells or from damaged mitochondria. These DNA fragments are mainly perceived by the endosome-localized LRR-PRR TLR9 (Dolina et al., 2020; Fitzgerald and Kagan, 2020; Gallucci and Maffei, 2017) or by cyclic GMP-AMP synthase (cGAS) (Amadio et al., 2021; Motwani et al., 2019), leading to the activation of innate immune responses. In plants, extracellular self-DNA fragments also trigger typical PTI responses, although the responsible PRRs have not been identified yet (Barbero et al., 2016; Duran-Flores and Heil, 2014; Wen et al., 2009). Interestingly, only DNA fragments from conspecifics, but not those from heterologous plants or insects, are able to elicit PTI responses, indicating a species-specific distinction between extracellular self-DNA and foreign-DNA in plants (Duran-Flores and Heil, 2018; Mazzoleni et al., 2015). It should be noted, however, that self-DNA fragments have versatile functions besides merely acting as DAMPs. After tissue damage, mammalian neutrophils can eject their DNA fragments along with histones and some antimicrobial proteases into the extracellular space to prevent the spread of pathogens and assist in eliminating the threat (Denning et al., 2019; Iba et al., 2014; Vorobjeva and Chernyak, 2020). Although a similar function has not been demonstrated in plants, *Arabidopsis* root border cells also rapidly export DNA into extracellular space, which is likely due to the constant exposure of the root tips to mechanical stress (Wen et al., 2017). These extracellular self-DNA fragments may have a protective function, as their degradation by DNase I impaired *Arabidopsis* resistance to pathogen infection (Cannesan et al., 2011).

1.2 Negative regulation of plant immunity by pathogens

1.2.1 Sequestering PAMPs

Host-adapted plant pathogens secrete numerous effector proteins into the apoplast or inside host cells to promote virulence activity. To dampen or manipulate the sophisticated plant immune system, pathogen effectors evolved diversified functions. One activity of pathogen effectors is to interfere with PTI responses. An example of this is ECP6 (for extracellular protein 6) from *Cladosporium fulvum*, which sequesters the fungus-derived chitin from being perceived by the PRRs as PAMPs (de Jonge et al., 2010). ECP6 has three LysM domains as observed in plant LysM-PRRs. In contrast to LysM-PRRs which typically use LysM2 for chitin binding, LysM1 and LysM3 of ECP6 form a groove that binds chitin with much higher affinity. Thus, ECP6 outcompetes plant PRRs in binding chitin and consequently neutralizes LysM-PRRs-mediated PTI (de Jonge et al., 2010; Sanchez-Vallet et al., 2013). Similarly, *Cf*Avr4 from *C. fulvum* binds chitin and shields the fungal cell wall to prevent chitin hydrolysis by host chitinases (Hurlburt et al., 2018; Pusztahelyi, 2018).

1.2.2 Targeting important hubs in plant immunity

As the frontline of plant immunity, PTI components are targeted by various pathogen effectors through different mechanisms. AvrPtoB from *P. syringae* is a multi-functional PTI suppressor. The N-terminal region of AvrPtoB inhibits the activity of *At*CERK1 and *At*CERK1-like PRR Bti9 (for AvrPtoB-tomato interacting protein 9) from tomato (Zeng et al., 2012); the central region blocks BAK1 function through interacting with the activation segment of the intracellular kinase domain (Cheng et al., 2011; Shan et al., 2008); the C-terminal region functions as an E3 ligase and directly degrades FLS2 and *At*CERK1 (Gohre et al., 2008; Janjusevic et al., 2006). Degradation of PTI signaling components appear to be a common effector strategy for interfering with host immune responses. Other examples include the cysteine protease effector AvrRpt2 from *P. syringae* which proteolytically cleaves the *Arabidopsis* protein RIN4 (for RPM1-interacting protein 4). The cleavage products in turn function as hyperactive suppressors of PTI signaling (Afzal et al., 2011). Moreover, RIN4 is phosphorylated by a host RLCK RIPK (for RPM1-induced protein kinase) in the presence of *P. syringae* effector AvrB. Phosphorylated RIN4 serves to promote more widely opened stomata on the plant surface, which facilitates pathogen entry (Lee et al., 2015).

Xanthomonas campestris pv. *campestris* (Xcc) effector AvrAC uridylylates two *Arabidopsis* RLCKs, RIPK and BIK1 (for botrytis-induced kinase 1), both of which play critical roles in PTI responses (Feng et al., 2012; Veronese et al., 2006). Interestingly, BIK1 can be proteolytically cleaved by *P. syringae* effector AvrPphB (Zhang et al., 2010), suggesting that the same PTI component can be targeted by multiple effectors through different mechanisms. Likewise, *P. syringae* effectors HopF2, HopAI1 and HopZ1a inactivate the mitogen-activated protein kinases (MAPKs) signaling pathway to suppress plant immunity (Rufian et al., 2021; Wang et al., 2010; Zhang et al., 2007). In addition to blocking MAPK activation, HopF2, like AvrPtoB, also directly targets BAK1 (Zhou et al., 2014), further supporting the notion that one pathogen effector can possess multiple PTI suppressing strategies.

1.2.3 Hijacking plant immune signals

Pathogen effectors can also hijack the immune signaling cascade once host immune response has been initiated. Some pathogen effectors negatively regulate plant immunity by acting as Nudix hydrolases, which typically hydrolyze nucleotide-derived substrates. *Xanthomonas campestris* pv. *vesicatoria* Nudix effector XopQ (for *Xanthomonas* outer protein Q) suppresses cell death in *Nicotiana* species which is dependent on EDS1 (for enhanced disease susceptibility 1), the signaling node downstream of TNLs (Adlung and Bonas, 2017). *Arabidopsis* expressing *Ralstonia. solanacearum* Nudix effector RipN exhibited higher susceptibility to pathogen infection compared to WT *Arabidopsis* or transgenic plants expressing a catalytically inactive *ripN* mutant (Sun et al., 2019). Immunosuppressive activity was also detected for the *Phytophthora sojae* Nudix effector Avr3b, but not its catalytically inactive mutant, in *Nicotiana. benthamiana* (Kong et al., 2015). These results suggest that Nudix effectors can metabolize some nucleotide-derived molecules with roles in plant immunity, to confer their virulence functions.

1.2.4 Manipulating plant cell death

To ensure accommodation with their hosts, pathogens that establish long-term parasitism must be highly effective in suppressing plant immunity. To this end, biotrophic pathogens usually secrete a large array of candidate secreted effector proteins (CSEPs) during infection, with approximately 25% of them being RNase-like effector proteins associated with haustoria (RALPH) effectors in *Blumeria graminis* (Pedersen et al., 2012). Transient expression of CSEP0139 or CSEP0182, effectors from *B. graminis*, inhibits barley cell death mediated by the pro-apoptotic animal protein, BAX (Xue et al., 2021). A similar inhibitory effect on cell death was also detected for other pathogen effecters, such as *Fusarium oxysporum* Six6 (for small proteins into the xylem sap 6) (Gawehns et al., 2014), *P. infestans* SNE1 (for suppressor of necrosis 1) (Kelley et al., 2010), *P. sojae* Avr1b (Dou et al., 2008) and *Puccinia striiformis* Pst_8713 (Zhao et al., 2018), suggesting that plant cell death suppression is a common virulence activity of pathogen effectors to establish parasitism in plants.

In contrast to biotrophic pathogens, necrotrophic pathogens destroy plant cells by secreting toxins and feed on dying host cells (Friesen et al., 2008; Laluk and Mengiste, 2010). *Cochliobolus victoriae* toxin victorin is a mixture of cyclic hexapeptides that confer host-specific pathogenicity to certain oat cultivars (Kessler et al., 2020). Victorin activates the *Arabidopsis* CNL encoded by *locus orchestrating victorin effects* 1 (LOV1) to trigger plant cell death and facilitate infection (Lorang et al., 2012). Another group of toxins encompasses the pathogen derived RNase effectors which cleave host ribosomal RNA (rRNA), disturbing host transcriptional homeostasis, and eventually leading to cell death (Gluck and Wool, 1996; Kettles et al., 2018; Olombrada et al., 2017). In many cases, their cytotoxic activities showed no host specificity. For example, *Zymoseptoria tritici* RNase effector Zt6 exhibited toxicity to plants, fungi and bacteria (Kettles et al., 2018). Similarly, RNase T1 from *Aspergillus oryzae* could also cause severe growth inhibition when overexpressed in yeast (Nonaka et al., 2000).

1.3 Plant immunity activated by intracellular immune receptors (ETI)

To discriminate the ‘enemies inside’, plants recruit intracellular NLR proteins to specifically detect pathogen effectors or effector modified targets. A canonical plant NLR protein has a tripartite domain structure, consisting of a C-terminal LRR domain normally responsible for effector recognition; a central NOD for oligomerization; and an N-terminal CC or TIR domain for the activation of immune signaling. Remarkable variation exists in the NLR domain-composition. For example, some NLRs harbor additional integrated domains (ID) (Grund et al., 2019), while others lack the LRR domain or both the LRR and NOD domains (Meyers et al., 2002; Xiao et al., 2001).

1.3.1 Direct recognition of pathogen effector by plant NLRs

The effector recognition mechanism was first explained by the ‘gene-for-gene’ model (Flor, 1942), showing that resistance or susceptibility to disease is controlled by pairs of matching host and pathogen genes, which were later known as NLRs and effectors, respectively. In the ‘gene-for-gene’ model, NLRs recognize effectors through direct interaction. This leads to a co-evolutionary arms race, with rapidly evolving polymorphic alleles and positive selection of both NLR and AVR genes to expand recognition specificity or to escape recognition (Karasov et al., 2014; Ravensdale et al., 2011). This hypothesis has been fulfilled in many cases. For example, the flax L resistance locus consists of a single gene encoding 13 allelic protein variants (L, L1 to L11, and LH) sharing >90% sequence identity. Through specific recognition of different matching effectors, AvrL567s (A-K). TNLs from L family confer resistance to the flax rust fungus, *Melampsora lini* (Ravensdale et al., 2012).

CNLs encoded by barley *Mildew locus a* (*Mla*) confer isolate-specific immunity against *B. graminis* forma specialis *hordei* (*Bgh*) fungus, the causative agent of powdery mildew disease (Bauer et al., 2021; Lu et al., 2016). Co-expression of MLAs and their cognate AVR$_{A}$ effectors triggered cell death in *N. benthamiana* leaves and barley protoplasts (Saur et al., 2019a), suggesting that the activation of MLAs is initiated by AVR$_{A}$ effectors. Furthermore, the sequence identity between MLAs is more than 90% with the positively selected amino acid residues concentrated in the LRRs, implying direct recognition of *Bgh* AVR$_{A}$ effectors by the LRRs of MLAs (Seeholzer et al., 2010; Shen et al., 2003). Whether MLA receptors recognize AVR$_{A}$ effectors through direct interaction is still an open question.

1.3.2 Indirect recognition of pathogen effectors by plant NLRs

Plant NLRs also recognize effectors indirectly by monitoring pathogen-modified host proteins that typically associate with the NLRs. When the host proteins modified by effectors are involved in plant immunity, and their interaction with effectors can be recognized by NLRs, these host proteins are referred to as ‘guardees’ and the NLRs ‘guards’ (Jones and Dangl, 2006; van Wersch et al., 2020). In contrast, when the host proteins only protect real effector targets but have no immune functions, they are called ‘decoys’ (van der Hoorn and Kamoun, 2008; van Wersch et al., 2020; Zhou and Chai, 2008). In both cases, these host proteins enable NLRs to detect virulence activities rather than the proteins of the effectors, thus allowing a relatively small repertoire of NLRs to protect against diverse pathogen effectors.

Arabidopsis RIN4 is a target of several different pathogen effectors and is guarded by two CNLs RPM1 (for resistance to *Pseudomonas syringae* pv. *maculicola* 1) and RPS2 (for resistance to *Pseudomonas syringae* protein 2) (Axtell and Staskawicz, 2003; Mackey et al., 2002). Phosphorylation of RIN4 by AvrRpm1 or AvrB activates RPM1 (Liu et al., 2011), whereas degradation of RIN4 by AvrRpt2 activates RPS2 (Coaker et al., 2005). In some cases, the status of one guardee can be monitored by multiple NLRs. For example, *Arabidopsis* senescence-associated E3 ubiquitin ligase 1 (SAUL1) is guarded by two TN-TNL pairs TN2-SOC3 (for suppressor of chs1-2, 3) and CHS1(for chilling sensitive 1) -SOC3, depending on the SAUL1 levels (Liang et al., 2018).

An example of the decoy model is pathogen recognition by the *Arabidopsis* CNL ZAR1 (for HOPZ-activated resistance 1). ZAR1 is activated by pathogen-modified modification of several host RLCKs, such as RKS1, ZED1 (for Hopz-effector-triggered immunity deficient 1) or ZRK3 (for ZED1-related kinase 3) among others (Martel et al., 2020), which form a a pre-activation receptor complex with ZAR1 via a conserved mechanism (Wang et al., 2015; Wang et al., 2019b). The *Xanthomonas campestris* effector AvrAC is a uridylase and uridylation of

Arabidopsis RLCK BIK1 by AvrAC dampens PTI and promotes bacterial virulence (Feng et al., 2012). PBL2 (for AvrPphB susceptible1-like protein 2), a paralogue of BIK1, can be similarly uridylated by AvrAC (Wang et al., 2015). Uridylated PBL2 (PBL2^{UMP}) is not required for AvrAC-mediated virulence but binds to another kinase RKS1 and activates the ZAR1-RKS1 precomplex. Like RKS1, ZED1 and ZRK3 are modified by the effectors HopZ1a (Lewis et al., 2013) and HopF2 (Bonardi et al., 2011), and are required for ZAR1 to mediate ETI. Thus, ZAR1 functions as a versatile signaling platform to monitor the homeostasis of important immune components (Dangl and Jones, 2019).

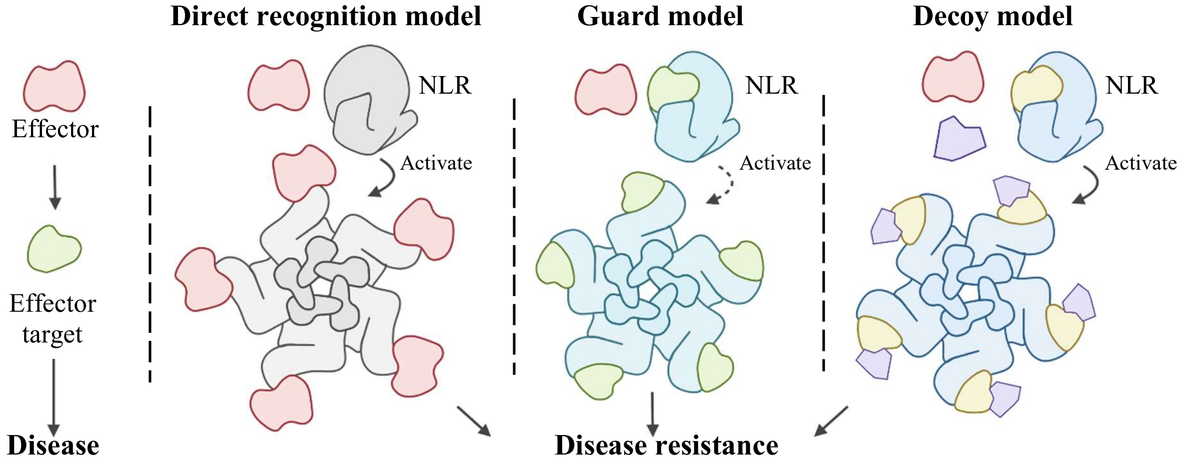

Figure 3. Schematic view of the activation mechanisms of plant NLRs. In the susceptible plants, effectors (pink) confer their virulence functions via targeting host proteins (green) and eventually lead to plant disease. NLRs recognize their cognate effectors indirectly (cyan and blue) or directly (grey) and form oligomeric resistosomes (CNL resistosomes are used as examples. The decoy and direct recognition models are illustrated by ZAR1 and Sr35, respectively). In the indirect recognition model, NLRs guard the effector targets (green) or the decoys (purple) which mimic the real targets. Activated NLRs initiate ETI responses and lead to plant disease resistance.

1.3.3 Activation mechanism of plant NLRs

Structural studies have provided significant insights into the biochemical function of CNLs. As in inactive NLRC4 (for NLR family CARD domain-containing protein 4) (Hu et al., 2013) and Apaf-1(for apoptotic protease activating factor 1) (Riedl et al., 2005), an ADP molecule binds to ZAR1 (Wang et al., 2019b). Upon infection, PBL2 becomes uridylated and interacts with RKS1, causing steric clashes with the ADP-bound ZAR1^{NBD}. As a consequence, the ZAR1^{NBD} rotates outward about 60°, releasing ADP and allowing exchange with ATP/dATP in the nucleotide-binding pocket. ATP/dATP binding induces structural remodeling in the WHD-LRR domains for full activation of ZAR1. Although a full-length structure of the inactive TNL is yet unavailable, a modelling study suggests that activation of TNLs also requires allosteric conformational changes similar to those in ZAR1 and Sr35 (Alexander et al., 2022a). Thus, effector-mediated steric clashes with the NBD and the subsequent ADP-ATP/dATP exchanges may be a pivotal step for the activation of plant NLRs.

1.3.4 Ion channel activity of activated CNLs

Fully activated ZAR1 assembles into the pentameric resistosome, in which the buried very N-terminal α helix (α1) of the ZAR1 CC domain flips out and forms a funnel-shaped structure (Wang et al., 2019a). The ZAR1 resistosome displays Ca^{2+}-permeable ion channel activity as demonstrated by two-electrode voltage clamp recording assays in both *Xenopus* oocytes and in planar lipid-bilayers (Bi et al., 2021). This activity is dependent on a conserved acidic residue Glu11 in α1, which is important for the formation of a central cavity for the ion permeation path (Bi et al., 2021). Recently, the wheat CNL Sr35 was also reported to form a pentameric resistosome and displays Ca^{2+}-permeable ion channel activity in *Xenopus* oocytes (Alexander et al., 2022b), suggesting that this activity is evolutionarily conserved among CNLs in distantly related plant species. Consistent with this, the N-terminal α1 is conserved in many CNLs from different plant species (Adachi et al., 2019). Importantly, a channel activity was also shown for the *Arabidopsis* helper NLR NRG1, as auto-active NRG1 facilitated Ca^{2+}, but not Cl^- influx when expressed in human HeLa cells (Jacob et al., 2021).

1.3.5 NADase activity of TIR domain proteins

Studies of human sterile alpha and TIR motif containing 1 (hSARM1) provided significant clues for the biochemical function of plant TNLs. hSARM1 was shown to possess NADase activity that promotes pathological axonal degeneration (Essuman et al., 2017). Plant TIR domain proteins were also demonstrated to have NADase activity, which is dependent on a highly conserved catalytic glutamic residue (Horsefield et al., 2019; Wan et al., 2019a). Wan et al., showed that the lysates of *Escherichia. coli* expressing WT plant TIR proteins, but not their catalytic glutamic mutants, depletes NAD^+ and produces a variant of cyclic ADP-ribose (v-cADPR) that has the same mass with distinct chromatography retention time compared with standard cADPR. Accumulation of v-cADPR was detected in *N. benthamiana* transiently expressing WT plant TIRs, but not their catalytic mutants (Wan et al., 2019a). Importantly, expression of TIR proteins with attenuated NADase activity also abolished TIR-mediated cell death in plants, suggesting that plant TIR NADase activity is required for TIR-induced HR cell death (Horsefield et al., 2019; Wan et al., 2019a).

The *N. benthamiana* TNL ROQ1 (for recognition of XopQ 1) directly binds XopQ and forms a tetrameric resistosome, exposing the catalytic site of the NADase cavity formed by two asymmetric TIR dimers (Martin et al., 2021). However, the low protein yield of the ROQ1 resistosome purified from *N. benthamiana* hindered the measurement of its NADase activity (R, Martin. personal communication at IS-MPMI 2021). In addition, the Nudix hydrolase activity of XopQ in the ROQ1 resistosome may potentially affect the NADase activity assay of ROQ1. Therefore, it remained an open question whether the assembly of TNL resistosomes is required for their NADase activity.

1.3.6 Function of truncated TNLs

Besides TNLs, plant genomes encode many truncated TNLs, such as TIR-only proteins (known as TX) and TNLs lacking the C-terminal LRR domain (known as TNs) (Meyers et al., 2002; Nandety et al., 2013). Although canonical TNLs have only been reported in dicotyledonous plant species, the TXs and TNs are found in both dicotyledons and monocotyledons, basal angiosperms, and magnoliids (Oliver et al., 2021). Similar to TNLs, TXs and TNs have been shown to function in plant defense (Collier et al., 2011; Meyers et al., 2002; Nandety et al., 2013; Nishimura et al., 2017). Transgenic expression of TX and TN proteins in *Arabidopsis* led to sustained activation of plant defense responses and resistance against pathogen infection (Nandety et al., 2013). Similarly, transient expression of several *Arabidopsis* TX and TN proteins in *N. tabacum* triggered *EDS1*-dependent cell death (Nandety et al., 2013), indicating that they and TNLs shared a conserved signaling mechanism. However, only a small number of TIR proteins exhibited cell death activity when expressed in *N. tabacum*. The precise reason for this remains to be examined (Nandety et al., 2013).

Interestingly, despite the lack of the LRR domain, some TIR-only proteins are able to respond to pathogen effectors. For example, *P. syringae* effector HopBA1 coimmunoprecipitates *Arabidopsis* TIR-only protein RBA1 and enhances RBA1 self-association, which is required for the activation of *EDS1*-dependent cell death in *N. benthamiana* (Nishimura et al., 2017). HopBA1 can also activate ZAR1 (Laflamme et al., 2020; Martel et al., 2020), implying a crosstalk between CNL- and TIR-mediated immune signaling *in planta.*

1.3.7 Products of TIR/TNL NADase activity activate downstream EDS1 signaling pathway

TNL/TIR signaling converges on the lipase-like protein EDS1 and its two direct partners PAD4 (for phytoalexin deficient 4) and SAG101 (for senescence-associated gene 101), and the helper NLRs ADR1 (for activated disease resistance 1) and NRG1 (for N requirement gene 1) of the CNL class (Lapin et al., 2019). All tested plant TNLs and TIRs are inactive in triggering immune responses in *eds1* mutant plants (Horsefield et al., 2019; Nandety et al., 2013; Oliver et al., 2021), supporting a central role of EDS1 in the TNL/TIR signaling pathway. Genetic studies have established a co-functioning relationship between EDS1-PAD4 and ADR1, and EDS1-SAG101 and NRG1 (Sun et al., 2021; Wu et al., 2021). In *Arabidopsis*, the EDS1-PAD4-ADR1 and EDS1-SAG101-NRG1 signaling modules function in parallel pathways but differentially contribute to immune outputs. The former module has a major role in basal immunity that slows pathogen growth, whereas the latter one predominantly contributes to TNL-mediated HR cell death. Contributions of the two signaling branches to immune outputs mediated by TNL/TIR vary among in different plant species (Lapin et al., 2019).

Since TIR NADase is required for TNL/TIR signaling, it was widely hypothesized that products of this enzymatic activity function to prime the EDS1-PAD4 and EDS1-SAG101 heterodimers (Wan et al., 2019a). The 'primed' EDS1-PAD4 and EDS1-SAG101 complexes then associate with and activate downstream helper NLRs (RNLs) ADR1 and NRG1, respectively (Huang et al., 2022; Jia et al., 2022). Both ADR1 and NRG1 are characterized by an N-terminal four-helix bundle domain with homology to the CC domain of the *Arabidopsis* CC-only protein RPW8 (for resistance to powdery mildew 8) and the HELO domains of *At*MLKLs (for mixed lineage kinase domain-like) (Daskalov et al., 2016; Jacob et al., 2021; Mahdi et al., 2020). Similar to the ZAR1 resistosome, auto-active forms of RNLs also function as Ca^{2+}-permeable cation channels to directly transduce cell death signals (Jacob et al., 2021). Thus, a model on TNL/TIR signaling would be that EDS1 integrates TIR-catalyzed products to activate the Ca^{2+} channel activity of ADR1 and NRG1. Supporting this model, the identities of several TIR-catalyzed products have recently been determined (Huang et al., 2022; Jia et al., 2022). The data from these two studies also showed that EDS1 heterodimers are direct receptors for these TIR-catalyzed small molecules. Binding of these small molecules allosterically promotes EDS1-PAD4 interaction with ADR1 and EDS1-SAG101 interaction with NRG1. In addition to NADase activity, the study by Jia et al. also discovered that the ADP-ribosylation activity of the TIR domain proteins is required for production of these small molecules.

1.3.8 Suppression of *EDS1*-dependent cell death in plants

In addition to the aforementioned pathogen Nudix effectors, *At*NUDT7 (also named *At*NUDX7), an *Arabidopsis* Nudix domain containing protein, also has well-documented ability in suppressing *EDS1*-dependent immunity (Bartsch et al., 2006; Ge et al., 2007). *Atnudt7* mutant plants display growth retardation as a result of exquisite sensitivity to environmental stimuli and enhanced resistance to *P. syringae* infection (Ge et al., 2007; Jambunathan and Mahalingam, 2006).

Atnudt7 mutant plants also accumulate higher levels of SA (Ge et al., 2007). In the same study, Ge et al crossed *Atnudt7* mutants with *Arabidopsis* overexpressing *NahG*, a bacterial SA hydroxylase. These double transgenic plants supported significantly more bacterial growth than *Atnudt7*, but are still more resistant than the *NahG* expressing plants (Ge et al., 2007). This suggests that *At*NUDT7 modulates two branches of defense response pathways: one independent of and the other dependent on SA accumulation.

Biochemical assays suggested that *At*NUDT7 can metabolize NADH and ADPR as preferred substrates and that the hydrolysis activity of *At*NUDT7 is essential for its biological function (Ge et al., 2007). However, there was no clear difference in the levels of NADH or ADPR between uninfected leaves of *Atnudt7* mutant and WT plants, although the NADH level in *Atnudt7* mutant was significantly higher than that in WT plants at 6 hours after *P. syringae* infiltration (Ge et al., 2007; Ge and Xia, 2008). Therefore, the authors speculated that neither of these nucleotide analogs likely is the physiological substrate of *At*NUDT7. Identification of additional substrates of *At*NUDT7 may provide further insights into how Nudix hydrolase inhibits *EDS1*-dependent immunity.

1.3.9 NADase activity is essential but not sufficient for full TIR signaling

NADase activity is required for TNL/TIR function. However, mounting evidence suggests that this enzymatic activity is not sufficient to fully mount TNL/TIR-mediated immunity. One piece of unexpected data came from estradiol-induced expression of AvrRps4, the cognate effector of the paired TNL RRS1 (for resistance to *Ralstonia solanacearum* 1) -RPS4 (for resistance to *Pseudomonas syringae* 4) (Sarris et al., 2015). While induced expression of the effector protein induces electrolyte leakage, no macroscopic cell death was observed in the AvrRps4-expressing *Arabidopsis* leaves (Ngou et al., 2020). This suggests the existence of additional components required for AvrRps4-induced TNL signaling. Consistently, overexpression of TIR^{AbTir}, a bacterial TIR protein that similarly produces v-cADPR, failed to trigger cell death in tobacco (Duxbury et al., 2020; Horsefield et al., 2019; Wan et al., 2019a). *At*TN3-mediated cell death in tobacco was enhanced by exogenous application of flg22 (Nandety et al., 2013), suggesting that flg22-induced components can facilitate TN3-mediated cell death. In concert with this idea, PTI signaling was recently show to potentiate RPS4-mediated ETI signaling (Ngou et al., 2021). These data collectively suggest that the *in situ* generation of plant TIR NADase products, is not sufficient to fully activate TIR immune signaling pathways.

1.4 TIR domain proteins in non-plant species

1.4.1 TIR domain proteins in animal

TIR domains are widely present in different species, including archaeal, bacterial and eukaryotic organisms, constituting a large protein family integral to immune systems (Essuman et al., 2018). In mammals, TIRs are the signature scaffolding domains of immune receptors, including the aforementioned TLRs, interleukin-1 receptors (IL-1Rs), and some downstream adaptor proteins. The TIR-TIR interaction between TLR4 and the signaling adaptor myeloid differentiation primary response 88 (MYD88) and MYD88 adaptor-like (MAL) is also required for immune and inflammatory responses (Fitzgerald et al., 2001; Ve et al., 2017).

In addition to acting as scaffolds for immune signal transduction, TIR proteins can also function as NADases. Animal TIR domain-containing protein SARM1, possesses intrinsic NADase activity and plays a key role in neuronal destruction following axonal injury. SARM1 consists of an N-terminal ARM domain; two central SAM domains; and a C-terminal TIR domain. The TIR domain of SARM1 ($SARM1^{TIR}$) cleaves NAD^+ into ADPR, cADPR, and NAM (Essuman et al., 2018; Li et al., 2022). Mutants of the catalytic residue E642 in $SARM1^{TIR}$ abolished the NADase activity of FL SARM1 *in vitro* and inactivated its pro-degenerative function *in vivo* (Essuman et al., 2018; Geisler et al., 2019; Horsefield et al., 2019). These results suggest that NADase activity is required for SARM1-mediated axonal degeneration. Unlike plant TNLs, SARM1 activation is not dependent on ligand binding but on the increased ratio of cytosolic NMN/NAD^+ (Waller and Collins, 2021). Axon injury first reduces cellular NAD^+ concentrations by decreasing levels of the enzyme responsible for its biosynthesis, nicotinamide mononucleotide adenylyltransferase 2 (NMNAT2) (Gilley and Coleman, 2010). As a result, NMN molecules, which accumulate as the precursors of NAD^+, bind to the ARM domain of SARM1 and release its autoinhibition (Figley et al., 2021; Shen et al., 2021; Shi et al., 2022). Activated SARM1 further reduces cellular NAD^+ levels, which in turn promote more SARM1 activation, suggesting that the NADase activity of SARM1 may have a self-amplifying role in its axonal degeneration function.

1.4.2 TIR domain proteins in bacteria

In bacteria, TIR domain proteins act as part of the Thoeris anti-phage immune system (Doron et al., 2018). Two bacterial TIR proteins act synergistically to restrict phage infection in bacteria (Ofir et al., 2021). Upon phage infection, the bacterial TIR protein ThsB uses NAD^+ as substrate and catalyzes the production of a signaling molecule, which in turn activates another TIR protein, ThsA, to deplete NAD^+. Mutations impairing ThsA NADase activity led to a complete loss of anti-phage protection (Ofir et al., 2021), linking NAD^+ degradation in bacteria to the anti-phage activity of ThsA (Ka et al., 2020; Ofir et al., 2021).

The identity of the ThsB-catalyzed product was recently determined (Azita et al., 2022). Interestingly, it shares similarity with the products of plant TIR NADase activity (2022; Jia et al., 2022), indicating the existence of possible ancestral forms of immune processes in bacteria and plants. Azita et al. also identified a large family of phage-encoded proteins that sequester and hinder the immune signaling molecule produced by ThsB from being sensed by ThsA, thereby inactivating bacterial antiviral immunity (Azita et al., 2022; Ofir et al., 2021). This suggests that hijacking key signaling molecules is a conserved strategy of invading pathogenic microorganisms.

1.5 Non-canonical cyclic nucleotides, 2′,3′-cNMPs

1.5.1 2′,3′-cNMPs are intermediates of RNA turnover

2′,3′-cyclic AMP (2′,3′-cAMP) is a naturally occurring regioisomer of 3′,5′-cAMP which acts as a second messenger in numerous signal transduction pathways. However, it was not until 2009 that the non-canonical cNMP family was identified in rat kidney (Ren et al., 2009). Since then, 2′,3′-cAMP and other 2′,3′-cNMPs (2′,3′-cGMP, 2′,3′-cCMP, and 2′,3′-cUMP) were detected in bacteria, human and plant cells (Jackson et al., 2009; Van Damme et al., 2014; Verrier et al., 2012).

Unlike 3’,5’-cAMP, which is produced from ATP by adenylyl cyclase, 2′,3′-cNMPs are mainly derived from RNA turnover (Ren 2019). In bacteria, 2′,3′-cNMPs are produced by RNase I-catalyzed RNA degradation. Fungal RNase T1 and RNase from other species were also shown to be capable of synthesizing 2′,3′-cNMPs through RNA hydrolysis (Abel et al., 1989; Deshpande and Shankar, 2002; Fontaine et al., 2018; Meador et al., 1990). 2′,3′-cNMPs are regarded as intermediates of RNA hydrolysis catalyzed by these RNases. In addition to 2′,3′-cNMPs, 2′,3′-cyclophosphate-terminated RNA oligonucleotides are also produced during RNA hydrolysis. Currently, enzymes responsible for the production of 2′,3′-cNMPs remain elusive.

1.5.2 2′,3′-cAMP can function both outside and inside animal cells

Studies in animals support a physiological role for 2′,3′-cAMPs in the response to injury. Traumatic injury to the brain increased the level of 2′,3′-cAMP in human cerebrospinal fluid (Verrier et al., 2012), implying that this non-canonical cAMP can be released into the extracellular space. Indeed, renal venous secretion of 2′,3′-cAMP was detected in rats after treatment with rapamycin (activator of mRNA turnover) (Jackson, 2017; Jackson et al., 2009). These data collectively suggest that 2′,3′-cAMP transporters may exist in cell membranes and that 2′,3′-cAMP may have a function outside cells. Function of 2′,3′-cAMP inside animal cells have also been reported. 2′,3′-cAMP treatment promoted permeability transition (PT) development on rat mitochondria, a key process in initiation of apoptotic cell death (Azarashvili et al., 2009). Interestingly, a follow up study demonstrated that PT is enhanced upon aging because older rats harbor significantly lower levels of 2', 3'-cNMP phosphodiesterase (PDE) compared to younger ones, resulting in increased 2’, 3'-cAMP concentrations inside cells (Krestinina et al., 2015). Taken together, these data suggest that 2′,3′-cAMP can function both inside and outside animal cells.

Thus, the function of 2', 3'-cAMP is reminiscent of 2′,3′-cGAMP, a well-known animal second messenger, which not only activates ER-localized signaling effector stimulator of interferon genes (STINGs), but can also be transferred to bystander cells in a process that involves transporters and anion channels (Luteijn et al., 2019; Zhou et al., 2020).

1.5.3 Function of 2′,3′-cAMP in plants

In *Arabidopsis*, wounding (Van Damme et al., 2014), heat and dark stress conditions (Kosmacz et al., 2018) induced the accumulation of cellular 2′,3′-cAMP/cGMP, demonstrating a correlation of increased 2′,3′-cNMP levels with plant stress responses. Remarkably, treatment with Br-2′,3′-cAMP, a cell-permeable 2′,3′-cAMP analogue, mimics the abiotic stress response in *Arabidopsis* (Chodasiewicz et al., 2022). In the same study, the authors employed multi-omics approaches to explore proteins co-migrating with 2′,3′-cAMP during size exclusion chromatography (SEC) and identified three TIR-domain proteins and twelve Nudix hydrolases including *At*NUDT7 as 2′,3′-cAMP interacting partners (Chodasiewicz et al., 2022).

Arabidopsis RNA-binding protein Rbp47b was also reported to directly associate with 2′,3′-cAMP but not 3′,5′-cAMP (Kosmacz et al., 2018). Under stress conditions, cytosolic 2′,3′-cAMP accumulate and bind to Rbp47b, promoting Rbp47b self-assembly and SG formation, a form of protein-mRNA aggregates. The assembled SGs, in turn, selectively store mRNA for use in response to stress (Kosmacz et al., 2019; Kosmacz et al., 2018).

2. Published Studies

2.1 Direct pathogen-induced assembly of an NLR immune receptor complex to form a holoenzyme

Shoucai Ma*, Dmitry Lapin*, Li Liu*, Yue Sun*, Wen Song*, Xiaoxiao Zhang, Elke Logemann, Dongli Yu, Jia Wang, Jan Jirschitzka, Zhifu Han, Paul Schulze-Lefert+, Jane E. Parker+, Jijie Chai+

Published in Science *370* (2020)

Author contributions:
Experimental design: J.C., J.E.P., P.S.-L., S.M., D.L.; recombinant protein expression assays, purification, structure determinations, modeling, and data analysis: S.M., X.Z., Y.S., W.S., J.W., and J.C.; biochemical assays: S.M., W.S., D.Y., J.J., Z.H.; plant expression and cell death assays: L.L., D.L., E.L.; HMM building: D.L.; data analysis: all authors; manuscript writing: J.C., J.E.P., P.S.-L. with contributions from other authors.

Specific contributions:
In this study, I collected evidence showing that $\mathrm{RPP1}^{\mathrm{TIR}}$ conferred NADase activity in a protein concentration-dependent manner. Furthermore, I co-crystalized $\mathrm{RPP1}^{\mathrm{TIR}}$ with NAD^+ and found that it formed an NADase-active tetrameric structure which was almost identical to the TIR domains in the RPP1 resistosome, further supporting the importance of TIR tetramerization in their NADase activity. In the $\mathrm{RPP1}^{\mathrm{TIR}}$ tetramer, the NAD^+ has been cleaved into ADPR and nicotinamide, and the C1″ position of the ADPR ribose sugar ring faced the catalytic glutamic residue of $\mathrm{RPP1}^{\mathrm{TIR}}$. My work illustrates the mechanism of the TIR NADase activity, which is substantial for this paper.

RESEARCH ARTICLE SUMMARY

PLANT SCIENCE

Direct pathogen-induced assembly of an NLR immune receptor complex to form a holoenzyme

Shoucai Ma*, Dmitry Lapin*, Li Liu*, Yue Sun*, Wen Song*, Xiaoxiao Zhang, Elke Logemann, Dongli Yu, Jia Wang, Jan Jirschitzka, Zhifu Han, Paul Schulze-Lefert†, Jane E. Parker†, Jijie Chai†

INTRODUCTION: Discrimination of self from nonself is pivotal for cellular organisms, as it allows the perception of pathogenic invaders that might otherwise multiply unchecked and cause disease in the host. To recognize nonself and to repel intruders, multicellular organisms deploy complex immune systems, in which repertoires of dedicated immune receptors play a central role. Innate immunity is an evolutionarily ancient arm of immunity in plants and animals that relies on structurally related, germline-encoded receptors. One class of these immune receptors inside cells, called the NLR protein family, shares a nucleotide-binding domain and leucine-rich repeats (LRRs). Plant sensor NLRs are classified into two main groups that are defined by different N-terminal domains: a coiled-coil (CC) domain in CC-NLRs (CNLs) and a Toll–interleukin-1 receptor (TIR) domain in TIR-NLRs (TNLs). A deeper understanding of the principles that govern nonself recognition by NLRs and their activation of innate immune responses necessitates protein structure–based approaches and reconstitution of signaling-active receptor complexes.

RATIONALE: Host-adapted plant pathogens secrete numerous effectors into the host extracellular spaces or inside cells. These effectors promote virulence, often by interfering with defense responses. Plant NLRs typically detect strain-specific pathogen virulence factors (effectors) delivered into host cells. This triggers immune responses that curtail pathogen proliferation and often culminate in localized host cell death. During plant host-pathogen coevolution, positive selection of random mutations in effector genes that abrogate NLR recognition drives the diversification of NLR repertoires at the population level. A well-studied coevolved pathosystem involves *Arabidopsis thaliana* and the downy mildew pathogen *Hyaloperonospora arabidopsidis* (*Hpa*). The *A. thaliana* TNL receptor RPP1 confers strain-specific immunity through recognition of *Hpa* effector ATR1. Specific allelic variants of ATR1 in *Hpa* populations activate only certain RPP1 variants in particular *A. thaliana* accessions. Previous work detected a nicotinamide adenine dinucleotide (NAD$^+$)–consuming enzymatic activity mediated by the N-terminal TIR domains of TNLs. How the TIR-associated NAD$^+$ hydrolase (NADase) activity and downstream signaling is enabled by TNL effector recognition is unknown.

RESULTS: We coexpressed a naturally occurring *A. thaliana* RPP1 receptor variant with its matching *Hpa* effector ATR1 in insect cells. Protein purification revealed an oligomeric protein complex of ~600 kD consisting of RPP1 and ATR1, which we term the "RPP1 resistosome." Biochemical assays showed that the RPP1 resistosome displays much higher Mg^{2+}/Ca^{2+}-dependent NADase activity than RPP1 alone. Using cryo–electron microscopy, we resolved a structure of the oligomeric complex that contains four RPP1 and four ATR1 molecules and reveals a tetrameric assembly mediated entirely by RPP1 subdomains. In contrast to other adenosine triphosphate (ATP)–bound NLRs in their active forms, RPP1 in the resistosome is adenosine diphosphate–bound, probably because of the lack of a motif required for ATP binding. The structure also reveals direct binding of ATR1 to a C-terminal jelly roll/Ig-like domain (C-JID) and the LRRs of the RPP1 receptor. Protein sequences corresponding to contact regions between the receptor and the pathogen effector are polymorphic in naturally occurring RPP1 and ATR1 variants, explaining why only certain RPP1 variants can detect strain-specific ATR1 molecules. The sequence-diversified RPP1$^{\text{C-JID}}$ is shared by many other TNLs, but not CNLs, in diverse plant species and might serve a role in the detection of other pathogen effectors. Receptor tetramerization creates two potential NADase active sites, each formed by an asymmetric TIR homodimer. Structure-guided substitutions of residues at this homodimeric TIR interface abolished ATR1-induced cell death in planta, supporting an essential role of the TIR-TIR interface in RPP1 function. Our combined biochemical and in planta assays show that assembly of two asymmetric TIR homodimers by the tetrameric receptor complex is responsible for NAD$^+$ hydrolysis and RPP1-mediated immune signaling.

CONCLUSION: Our findings indicate that the RPP1 resistosome acts as a pathogen effector–inducible holoenzyme for NAD$^+$ hydrolysis. The tetrameric RPP1 oligomeric structure provides an example of direct pathogen effector recognition by a plant NLR receptor and uncovers the mechanism of strain-specific recognition leading to NLR conformational activation. Our work suggests a multilayered regulation of RPP1 tetramerization, including ATR1 binding, RPP1 oligomerization driven by interactions among nucleotide-binding domains, and RPP1$^{\text{TIR}}$ self-association. The analysis provides a structural insight to induced NAD$^+$ hydrolysis mediated by the RPP1 holoenzyme and a framework for TNL receptor signaling. As a holoenzyme, the RPP1 resistosome bears similarity to the animal apoptosome and inflammasome, which form holoenzymes after the recruitment of procaspases. ■

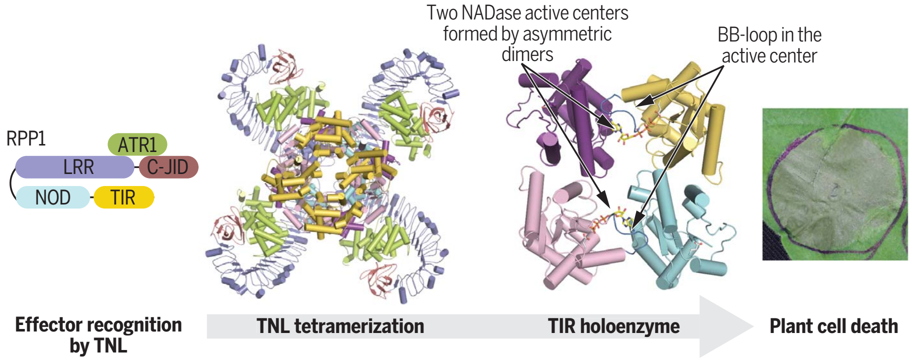

Pathogen activation of an NLR holoenzyme. Recognition of pathogen effector ATR1 via the C-JID and LRR domains of the plant TNL receptor RPP1 triggers the assembly of a tetrameric receptor complex with two asymmetric N-terminal TIR domain homodimers. This tetramer-induced TIR asymmetry creates, via two centrally located BB-loops, active sites for NAD$^+$ hydrolysis, which is essential for RPP1 signaling leading to host cell death.

The list of author affiliations is available in the full article online.
*These authors contributed equally to this work.
†Corresponding author. Email: chai@mpipz.mpg.de (J.C.); parker@mpipz.mpg.de (J.E.P.); schlef@mpipz.mpg.de (P.S.-L.)
Cite this article as S. Ma *et al.*, *Science* **370**, eabe3069 (2020). DOI: 10.1126/science.abe3069

READ THE FULL ARTICLE AT
https://doi.org/10.1126/science.abe3069

Ma *et al.*, *Science* **370**, 1184 (2020) 4 December 2020 **1 of 1**

RESEARCH ARTICLE

PLANT SCIENCE

Direct pathogen-induced assembly of an NLR immune receptor complex to form a holoenzyme

Shoucai Ma[1]*, Dmitry Lapin[2]*, Li Liu[2]*, Yue Sun[1]*, Wen Song[3]*, Xiaoxiao Zhang[1], Elke Logemann[2], Dongli Yu[2,3], Jia Wang[1], Jan Jirschitzka[3], Zhifu Han[1], Paul Schulze-Lefert[2,4]†, Jane E. Parker[2,4]†, Jijie Chai[1,2,3,4]†

Direct or indirect recognition of pathogen-derived effectors by plant nucleotide-binding leucine-rich repeat (LRR) receptors (NLRs) initiates innate immune responses. The *Hyaloperonospora arabidopsidis* effector ATR1 activates the N-terminal Toll–interleukin-1 receptor (TIR) domain of *Arabidopsis* NLR RPP1. We report a cryo–electron microscopy structure of RPP1 bound by ATR1. The structure reveals a C-terminal jelly roll/Ig-like domain (C-JID) for specific ATR1 recognition. Biochemical and functional analyses show that ATR1 binds to the C-JID and the LRRs to induce an RPP1 tetrameric assembly required for nicotinamide adenine dinucleotide hydrolase (NADase) activity. RPP1 tetramerization creates two potential active sites, each formed by an asymmetric TIR homodimer. Our data define the mechanism of direct effector recognition by a plant NLR leading to formation of a signaling-active holoenzyme.

Intracellular nucleotide-binding leucine-rich repeat immune receptors (NLRs) have evolved independently in plants and animals to detect pathogen disturbance. Plant sensor NLRs are classified into two main groups that are defined by different N-terminal domains: a coiled-coil (CC) domain in CC-NLRs (CNLs) and a Toll–interleukin-1 receptor (TIR) domain in TIR-NLRs (TNLs). Direct or indirect recognition of pathogen effector proteins by plant NLRs triggers an immune response termed effector-triggered immunity (*1*–*6*), often characterized by rapid host cell death (a hypersensitive response) at sites of attempted infection. In addition to the C-terminal LRR domain, noncanonical integrated domains of plant NLRs play a critical role in conferring specific effector recognition (*7*). Although modes of effector recognition vary, ligand sensing is widely believed to induce oligomerization of NLRs for signaling. For example, a recent structural study of the CNL ZAR1 in *Arabidopsis* showed that the ZAR1 resistosome induced by bacterial effector AvrAC assumes a wheel-like structure similar to that of NLR inflammasomes in animals (*8*). A body of evidence suggests that the CC domains of CNLs and the TIR domains of TNLs mediate signaling upon NLR activation (*9*–*14*). A TIR domain signaling role is further supported by biochemical assays that detected NADase activity required for TNL-mediated immunity (*15*, *16*). Structural and functional studies with individual TIR domains revealed their capacity for self-association as homo- or heterodimers, which is important for immunity induction (*5*, *9*, *17*, *18*). How TIR domain signaling activity is enabled by TNL effector recognition in the context of full-length receptors is unknown.

Members of the *Arabidopsis* RPP1 (Recognition of *Peronospora parasitica* 1) TNL family specifically recognize cognate ATR1 (*Arabidopsis thaliana* Recognized 1) effector variants produced by the foliar oomycete pathogen *Hyaloperonospora arabidopsidis* (*Hpa*) (*19*, *20*). In host and pathogen populations, both *RPP1* from *Arabidopsis* accessions and *ATR1* from *Hpa* strains are highly polymorphic. Recognition of different ATR1 forms by RPP1 variants is *Hpa* race–specific, indicative of host-pathogen coevolution (*12*, *21*). Specific RPP1-ATR1 recognition in *Arabidopsis* leading to leaf macroscopic host cell death was recapitulated in tobacco transient gene expression assays. Coupled with biochemical data, these studies showed a requirement for the RPP1 C-terminal LRR domain in direct binding of recognized ATR1 forms (*20*, *22*).

Reconstitution and cryo-EM structure of the RPP1 resistosome

We coexpressed Strep-RPP1_WsB (residues 61 to 1221) with His-ATR1_Emoy2 (residues 52 to 311) as a matching TNL-effector pair (*12*, *21*) in insect cells. We used a tandem affinity purification procedure to isolate the complex. Gel filtration analysis showed that comigration of the RPP1 and ATR1 proteins corresponded to a molecular weight of ~600 kD (fig. S1), indicating that they form an oligomeric complex, which we term the "RPP1 resistosome." The complex obtained from gel filtration was used for structural analysis by cryo–electron microscopy (cryo-EM). After three-dimensional (3D) classification, a subset of 409,348 particles was used for image reconstruction, generating a map with a global resolution of 3.16 Å, as determined with a gold-standard Fourier shell correlation (Fig. 1A and fig. S2). Resolution of the core complex without inclusion of the LRR portion was 2.99 Å.

The cryo-EM structure of the RPP1 resistosome contains four RPP1 and four ATR1 molecules, which assemble into a tetrameric complex measuring 160 Å × 160 Å × 120 Å (Fig. 1B, fig. S3, A and B, and table S1). Tetramerization of the resistosome is mediated entirely by RPP1 subdomains. We discovered in the resistosome structure that RPP1 has a C-terminal domain in addition to the canonical TNL domains TIR, nucleotide-binding domain (NBD), helix domain 1 (HD1), winged helix domain (WHD), and LRRs (Fig. 1B and fig. S3, C to F). Structural searches of the Protein Data Bank (PDB) revealed that the C-terminal domain adopts a classical β–jelly roll and Ig-like fold (fig. S4A), which we designate C-JID (C-terminal jelly roll and Ig-like domain). The $\mathrm{RPP1^{C\text{-}JID}}$ structure is similar to that of the TNL Roq1 (*23*) (fig. S4B). Whereas all canonical TNL-type domains of RPP1 are involved in resistosome assembly, $\mathrm{RPP1^{C\text{-}JID}}$ mediates interaction with ATR1, assisted by the inner surface of $\mathrm{RPP1^{LRR}}$ (Fig. 1B). The RPP1 resistosome is organized into a three-layered ring structure, with the top, middle, and bottom formed by the TIR domain, the NOD (nucleotide-binding oligomerization domain) module (i.e., NBD-HD1-WHD domains), and ATR1-bound LRR–C-JID, respectively (Fig. 1B). $\mathrm{RPP1^{NBD}}$, $\mathrm{RPP1^{HD1}}$, and $\mathrm{RPP1^{WHD}}$ are positioned similarly to the corresponding domains of activated ZAR1, NLRC4, and Apaf-1 (fig. S4C), indicating that RPP1 adopts an active conformation in the resistosome.

$\mathrm{RPP1^{C\text{-}JID}}$ is an essential structural determinant for ATR1-specific recognition

RPP1-bound ATR1 is nearly identical to a crystal structure of the ATR1 monomer alone (*24*) (fig. S4D). $\mathrm{RPP1^{LRR}}$ and $\mathrm{RPP1^{C\text{-}JID}}$ are comparatively less well defined than other RPP1 domains (fig. S2C). The cryo-EM density of $\mathrm{RPP1^{LRR}}$ and $\mathrm{RPP1^{C\text{-}JID}}$ was substantially improved by local refinement, sufficient for model building (figs. S2C and S3, G to I). ATR1 obliquely contacts $\mathrm{RPP1^{C\text{-}JID}}$ and $\mathrm{RPP1^{LRR}}$ via its N-terminal segment (residues 67 to 190) (Fig. 2A), consistent with an earlier report that residues 68 to 222 of ATR1 are sufficient

---

[1]Beijing Advanced Innovation Center for Structural Biology, Tsinghua-Peking Center for Life Sciences, Centre for Plant Biology, School of Life Sciences, Tsinghua University, 100084 Beijing, China. [2]Max Planck Institute for Plant Breeding Research, 50829 Cologne, Germany. [3]Institute of Biochemistry, University of Cologne, 50674 Cologne, Germany. [4]Cluster of Excellence in Plant Sciences (CEPLAS), 40225 Düsseldorf, Germany.
*These authors contributed equally to this work.
†Corresponding author. Email: chai@mpipz.mpg.de (J.C.); parker@mpipz.mpg.de (J.E.P.); schlef@mpipz.mpg.de (P.S.-L.)

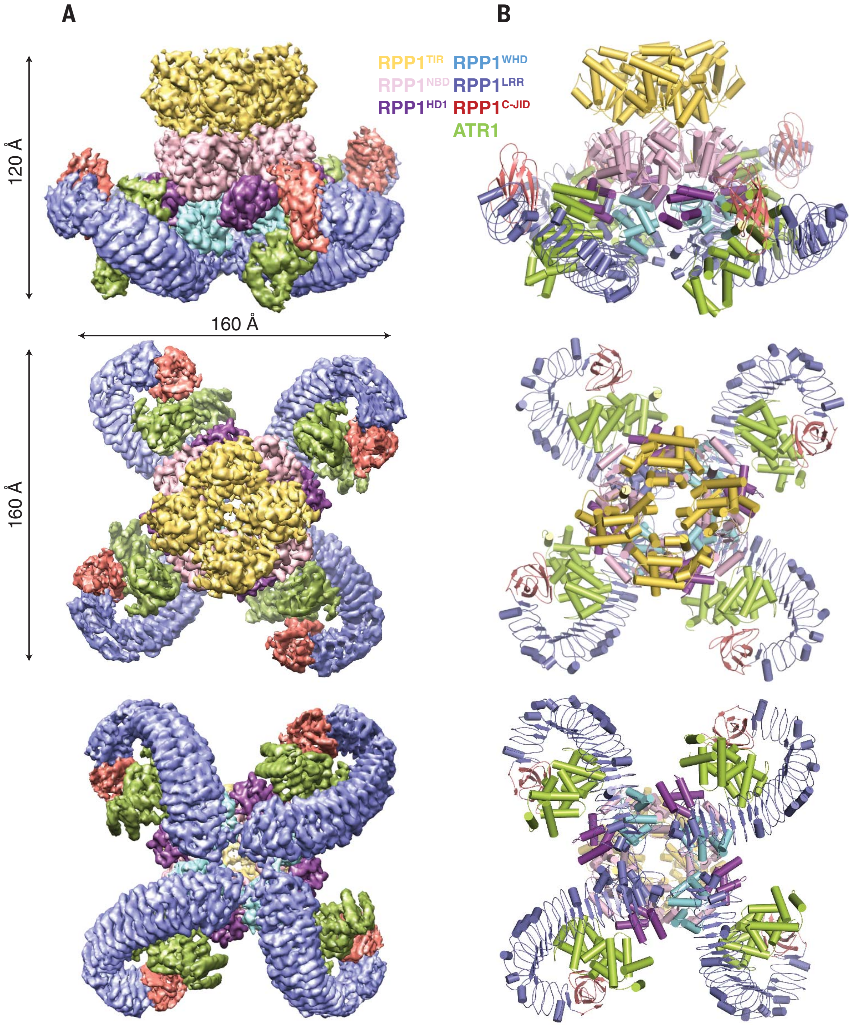

Fig. 1. Tetrameric assembly of the RPP1 resistosome. (**A**) Final 3D reconstruction of the RPP1 resistosome (oligomeric RPP1-ATR1 complex) in three orientations. (**B**) Final model of the RPP1 resistosome in three orientations. The reconstruction and model in each row are shown in the same orientation. Color codes for ATR1 and subdomains of RPP1 are indicated.

for RPP1 recognition (*24*). ATR1 interacts mainly with a flat exposed anti–β sheet surface of RPP1$^{\text{C-JID}}$ (interface 1), establishing hydrogen-bonding and hydrophobic interactions (Fig. 2B and fig. S5A). Contacts with nonconserved residues from the inner surface of the curved RPP1$^{\text{LRR}}$ further contribute to ATR1 interaction with RPP1 (interface 2) (Fig. 2C and figs. S5B and S6).

To verify the cryo-EM structure, we made substitutions of residues in ATR1 and RPP1 from interface 1 or 2, or both together. The various mutants were coexpressed in insect cells. Asp^{140} of ATR1_Emoy2 (ATR1$^{\text{D140}}$) that is conserved in RPP1_WsB-recognized ATR1_Maks9 and ATR1_Emco5, but not in nonrecognized ATR1_Cala2 and ATR1_Emwa1 (fig. S7), is located at the center of interface 1 (Fig. 2B). Substitution of this residue with a tyrosine present at the equivalent position of ATR1_Cala2 and ATR1_Emwa1 substantially reduced ATR1-Emoy2 binding to RPP1 in vitro (fig. S8A), indicating that interaction with RPP1$^{\text{C-JID}}$ is important for ATR1 recognition. This result also explains why the ATR1_Cala2 and ATR1_Emwa1 alleles are not recognized by RPP1_WsB (*12*, *21*). In further support of the cryo-EM structure, alanine substitutions of five residues from the loop region (E117A/L122A/D124A/T125A/Y126A) of ATR1 at interface 2 resulted in loss of interaction with RPP1 (fig. S8A). Substitutions of RPP1 residues at either of the two interfaces with amino acids at equivalent positions in other RPP1 variants (fig. S6) impaired interaction with ATR1_Emoy2 (fig. S8A).

We tested whether the above RPP1 and ATR1 substitutions affected ATR1-induced RPP1-dependent host cell death by using *Agrobacterium tumefaciens*–mediated transient gene expression to coexpress untagged RPP1 and hemagglutinin (HA)/StrepII (HS)–tagged ATR1 forms in leaves of *Nicotiana benthamiana*. Expectedly, coexpression of wild-type (WT) RPP1 with WT ATR1-HS resulted in cell death of infiltrated leaf zones (Fig. 2D). Epitope-tagged WT RPP1-HS also produced ATR1-dependent cell death in *N. benthamiana* and was detectable as a ~140-kD protein by immunoblotting (fig. S8, B and C). By contrast, cell death was strongly impaired with ATR1 proteins bearing substitutions that abolished or reduced interaction with RPP1 (Fig. 2, C and D, and fig. S8D). The loss of cell death induction by ATR1$^{\text{E117A/L122A/D124A/T125A/Y126A}}$ with multiple substitutions at interface 2 (Fig. 2, C and D) showed that in addition to RPP1$^{\text{C-JID}}$, RPP1$^{\text{LRR}}$ is important for ATR1 recognition, in agreement with previous data (*20*, *22*). Coexpression of RPP1 with ATR1$^{\text{R177A/Y179A}}$ that had no detectable interaction with RPP1 in vitro (fig. S8A) caused WT-like cell death (Fig. 2, C and D). The reason for the discrepancy remains unclear, but it is possible that a weak interaction between this ATR1 mutant and RPP1 was undetectable in vitro but was sufficient to support cell death. The RPP1 substitutions RPP1$^{\text{S1123K/S1125Y/N1181R/S1183R}}$ from interface 1 retained WT-like cell death activity when coexpressed with ATR1, but cell death was abolished with RPP1$^{\text{Y869D/R895S/Y935E/R937M}}$ substitutions from interface 2 (Fig. 2E). Collectively, our data indicate that RPP1$^{\text{C-JID}}$ and RPP1$^{\text{LRR}}$ are structural determinants for ATR1-specific binding and recognition of naturally occurring ATR1 variants. In support of this conclusion, a structure-guided RPP1 sequence alignment revealed that residues from these two domains, in particular those from RPP1$^{\text{C-JID}}$, are variable between different RPP1 proteins (fig. S6).

Assembly of the RPP1 resistosome is required for NADase activity

As observed in oligomerization of other NLR proteins (*8*, *25*–*27*), the RPP1 central NOD module (NBD-HD1-WHD domains) participates in tetramerization (Fig. 3A and fig. S9, A and B). In contrast to other NLRs, however, the loop region between β2 and α2 of RPP1$^{\text{NBD}}$ mediates RPP1 tetramerization by interacting with a groove between RPP1$^{\text{NBD}}$ and RPP1$^{\text{WHD}}$ of the adjacent protomer around the P-loop region (Fig. 3B and fig. S9C). Besides self-association (discussed below), the RPP1$^{\text{TIR}}$ stacks against RPP1$^{\text{NBD}}$ from an adjacent protomer (Fig. 3C and fig. S9, A, D, and E). Two adjacent RPP1$^{\text{TIR}}$s are positioned differently to engage in distinct interactions with RPP1$^{\text{NBD}}$ (Fig. 3A). A similar observation was reported for N-terminal CARD domains in the CED-4 apoptosome (*28*). In the RPP1 tetramer, the TIR loop region N-terminal to RPP1$^{\text{NBD}}$ (TIRa) is better defined than that of its neighboring TIR (TIRb). RPP1$^{\text{TIRa}}$ packs tightly against the top

Fig. 2. Structural mechanism of ATR1 recognition by RPP1. (**A**) Structure of ATR1 (in cartoon) bound by the RPP1$^{LRR-C-JID}$ fragment (in surface) showing two interfaces with ATR1. (**B**) Detailed interactions between RPP1^{C-JID} and ATR1 at interface 1 [blue frame in (A)]. Red dashed lines indicate polar interactions. (**C**) Detailed interactions between RPP1^{LRR} and ATR1 at interface 2 [purple frame in (A)]. Red dashed lines indicate polar interactions. (**D**) Host cell death triggered by coexpression of untagged RPP1_WsB and HS-tagged ATR1_Emoy2 variants in leaves of *N. benthamiana*. WT, wild type. Cell death was quantified by a leaf disk ion leakage (conductivity) assay at 3 days after agro-infiltration (dai). Data are normalized to the mean value for samples with RPP1_WsB and WT ATR1_Emoy2 in each experiment. Results from three independent experiments are displayed on the plot (*n* = 18; Tukey's HSD test, α = 0.01; data points of the same color were recorded in one experiment; shared lowercase letters indicate no significant difference). (**E**) Top: Ion leakage assay of RPP1_WsB mutations at RPP1-ATR1 interfaces 1 and 2 on ATR1_Emoy-induced cell death in *N. benthamiana*. The assay was performed as described in (D) after agro-infiltration of C-terminally HA-StrepII–tagged RPP1_WsB (RPP1_WsB-HS) with ATR1_Emoy2-HS. Statistical analysis via Tukey's HSD test is based on data from three independent experiments (*n* = 18, α = 0.001; data points of the same color were recorded in one experiment; shared lowercase letters indicate no significant difference). Below are photographs of representative agro-infiltrated leaf zones at 4 dai. Bottom: Western blot analysis of total *N. benthamiana* leaf protein extracts at 2 dai probed with antibody to HA. Expression of RPP1_WsB-HS WT and mutant proteins produces a signal of the expected molecular weight (~140 kD). Ponceau S staining indicates equal loading of total leaf proteins on the blot.

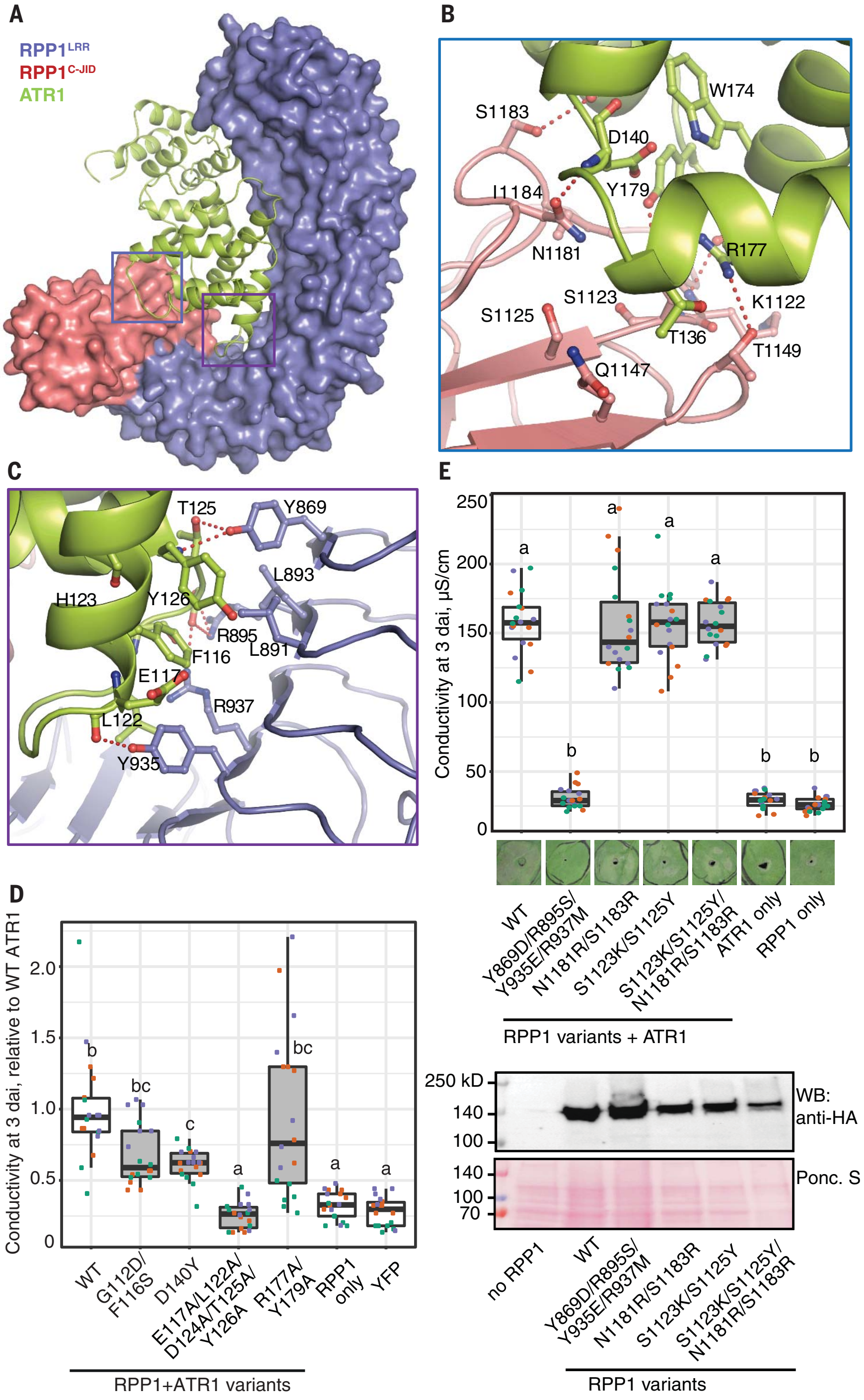

of RPP1^{NBD} from an adjacent protomer via extensive interactions of C-terminal parts of helices αA and αE (Fig. 3C and fig. S5C). Less tight interactions are formed between TIRb and its adjacent RPP1^{NBD} (fig. S9D). As observed in the ZAR1 resistosome, interactions between two neighboring LRR domains (fig. S9, A and E) likely further stabilize the RPP1 tetrameric resistosome.

We next investigated whether formation of the RPP1 resistosome is required for NADase activity. A high-performance liquid chromatography (HPLC) assay with recombinant proteins purified from insect cells showed that the RPP1-ATR1 complex, but not RPP1 alone, hydrolyzed nicotinamide adenine dinucleotide (NAD^+) at 1.0 μM protein (Fig. 3D). Divalent ions were shown to be important for nucleoside hydrolase activities (*29*). We therefore tested whether Mg^{2+} or Ca^{2+} changed RPP1-ATR1 tetramer NAD^+ hydrolysis. Addition of 10 mM Mg^{2+} strongly promoted consumption of NAD^+ by RPP1 (Fig. 3D). The same concentration of Ca^{2+} had a weaker effect. By contrast, Mg^{2+} or Ca^{2+} did not increase the negligible NADase activity of RPP1 alone (Fig. 3D). These data show that assembly of the RPP1 tetramer is necessary for NAD^+ hydrolysis. Notably, the same concentration (1.0 μM) of RPP1^{TIR} (residues 60 to 254) purified from insect cells was much less efficient in NAD^+ hydrolysis (fig. S10A). At a higher concentration (70 μM), RPP1^{TIR} NADase activity

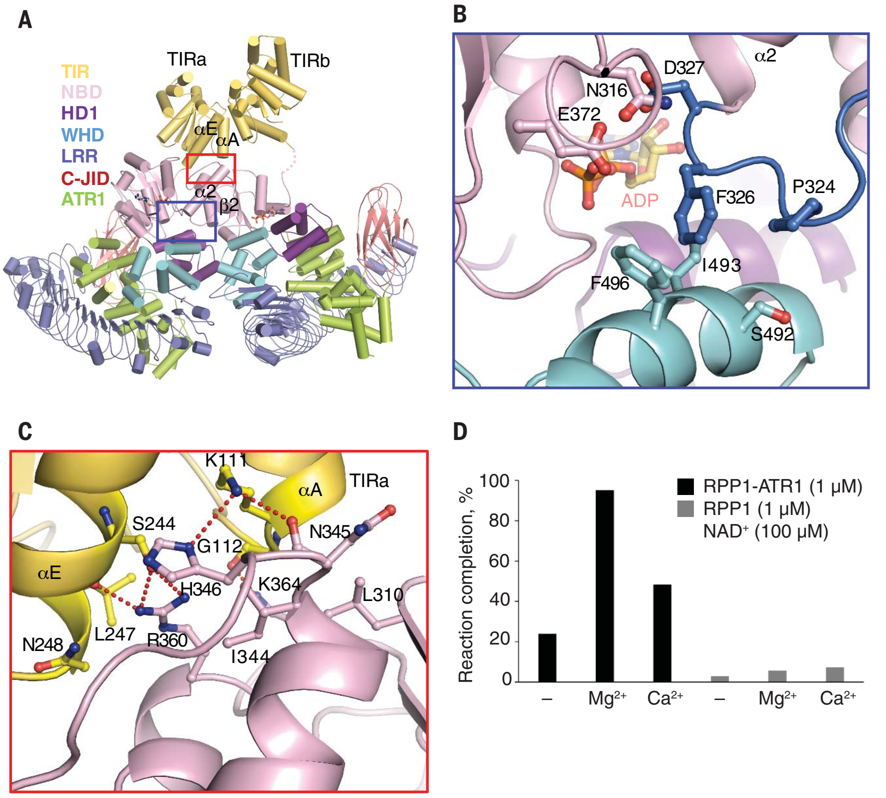

Fig. 3. The RPP1 resistosome, but not RPP1 alone, has Mg^{2+}/Ca^{2+}-dependent NADase activity. (**A**) A lateral RPP1 homodimer shown in cartoon. αA and αE are helices from the TIR domain (TIRa) in the left RPP1 protomer that interact with $RPP1^{NBD}$ of the right protomer. The dashed line in the right RPP1 indicates the flexible region C-terminal to the TIR domains. (**B**) Detailed interactions of the β2-α2 loop from the right protomer with $RPP1^{NBD}$ and $RPP1^{WHD}$ from the left protomer highlighted within the blue frame in (A). (**C**) Detailed interactions between $RPP1^{TIRa}$ and $RPP1^{NBD}$ highlighted within the red frame in (A). (**D**) NADase activity assay of the ATR1-RPP1 complex and RPP1 alone. The purified ATR1-RPP1 complex or RPP1 only was incubated with 100 μM NAD^+ in buffer with or without 10 mM Mg^{2+}/Ca^{2+}. After incubation at 25°C for 16 hours, reaction mixtures were centrifuged and immediately used for HPLC analysis. Reaction completion (%) of each sample was calculated as [1 – (concentration of unhydrolyzed NAD^+)/(concentration of NAD^+ before reaction)] × 100%.

was increased and promoted by Mg^{2+} and Ca^{2+} (fig. S10A), which suggests that high concentrations of TIR alone may drive it into oligomers with enzymatic activity (*5*). This notion is further supported by an earlier finding of $RPP1^{TIR}$ in vivo autoactivity that correlated with its self-association in solution (*30*). Also, induced TIR domain proximity led to cell death in planta (*31*). Collectively, our data indicate that ATR1-induced assembly of the RPP1 resistosome is required for RPP1 NADase activity and host cell death induction. Thus, the RPP1 resistosome can be viewed as a pathogen-inducible holoenzyme for NAD^+ hydrolysis.

Active sites are formed by asymmetric TIR homodimers

Whereas the four $RPP1^{NOD}$ modules in the RPP1 resistosome are approximately related with C_4 symmetry, the four TIR domains are related with C_2 symmetry because of the different positioning of two neighboring $RPP1^{TIR}$s (Fig. 4A). Thus, the tetrameric $RPP1^{TIR}$s contain two symmetric TIR homodimers that are nearly identical to those observed in the crystal structure of $RPP1^{TIR}$ (fig. S11, A and B) (*18*). Each of three tested substitutions of residues at this homodimeric "AE" interface (*9*, *17*, *18*) abolished ATR1-induced cell death in *N. benthamiana* (fig. S11C), supporting an essential role of the AE interface in RPP1 function. Functional relevance of the AE interface has been observed for TIR domains of other plant TNLs (*9*, *17*, *18*). In the RPP1 tetramer, opposite packing of the two symmetric TIR homodimers led to formation of two asymmetric head-to-tail $RPP1^{TIR}$ homodimers (Fig. 4A). The two $RPP1^{TIR}$s in an asymmetric homodimer have different conformations in the loop between αA and αB (equivalent to the BB-loop of other TIR domains, hereafter called the BB-loop) (Fig. 4B). The BB-loop is well defined in $RPP1^{TIRa}$ but is disordered in $RPP1^{TIRb}$ (fig. S12A). Asymmetric head-to-tail $RPP1^{TIR}$-$RPP1^{TIR}$ interaction is primarily mediated by the BB-loop of TIRa that contacts the opposite side of TIRb (Fig. 4, A and C, and fig. S12B).

From a sequence alignment (fig. S12C), the predicted catalytic $RPP1^{E158}$ is located at one end of the groove formed within an asymmetric $RPP1^{TIR}$ homodimer (fig. S13A), which suggests that this groove is important for RPP1-catalyzed NAD^+ hydrolysis and RPP1 function. To test this hypothesis, we mutated residues from the interface of the asymmetric $RPP1^{TIR}$ homodimer and evaluated the impact of these substitutions on the NADase activity of the RPP1 resistosome and ATR1-induced cell death in *N. benthamiana*. Substitutions RPP1 I121E, S124E, A222E, or G223A, which are predicted to disrupt the asymmetric $RPP1^{TIR}$ homodimers, all interacted with ATR1 (fig. S10B) but were strongly compromised in NAD^+ hydrolysis (Fig. 4D and fig. S13B). By contrast, an RPP1R123A exchange had less effect on NADase activity (Fig. 4D). In support of an essential role of NADase activity in RPP1 function, we also found that RPP1 I121E, A222E, E158A, or E158Q, but not RPP1 R123A, S124E, E122A/R123A/S124A/K125A/S126A, or G223A, displayed almost undetectable cell death activity (Fig. 4E). Taken together, these data show that the assembly of two TIRa-TIRb active sites in the RPP1 resistosome is responsible for NAD^+ hydrolysis and RPP1-mediated signaling.

A previous study showed that many single mutations in the TIR domain of the canonical *Arabidopsis* TNL RPS4 ($RPS4^{TIR}$) disrupted the cell death activity of $RPS4^{TIR}$ in tobacco (*13*). Mapping the equivalent residues onto the RPP1 resistosome revealed that most of them cluster around the asymmetric TIRa-TIRb groove (fig. S13C). We found that adenosine triphosphate (ATP), which was supplemented during protein purification, bound to this groove in the absence of NAD^+ (fig. S13A) and that the ATP binding groove is conserved among *Arabidopsis* TNLs (fig. S12C). The bound ATP likely acts as an analog of NAD^+ at the groove. Supporting this possibility, a structural comparison revealed that NAD^+ phosphate ($NADP^+$) bound to the TIR domain of plant TNL RUN1 (*9*, *17*, *18*) at a position similar to that of ATP in the RPP1 TIRa-TIRb groove (fig. S13D). These results provide additional evidence for the biological relevance of the asymmetric $RPP1^{TIR}$ homodimers in the resistosome.

ADP binds to the P-loop region of RPP1 in the resistosome

Previous studies demonstrated that structures of the NOD module from plant and animal NLRs are highly conserved in both inactive and active states (*32*). This is underscored here by the similar structures of $RPP1^{NOD}$ in the

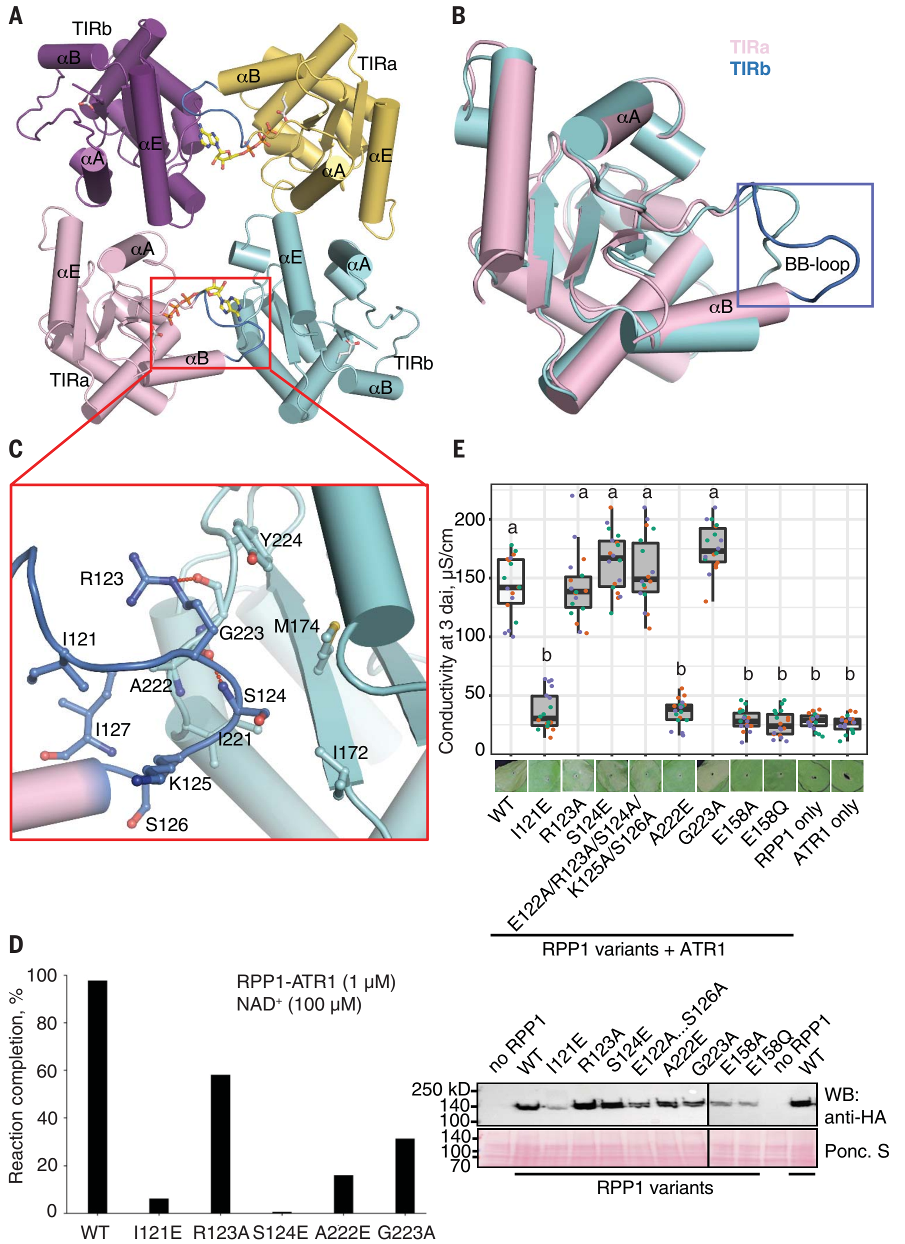

Fig. 4. Assembly of two active sites by two asymmetric RPP1^{TIR} dimers in the tetrameric RPP1 resistosome. (**A**) Tetrameric assembly of RPP1^{TIR}s in the resistosome. Some secondary structural elements are labeled. Two bound ATP molecules within the two asymmetric RPP1^{TIR} dimers (top and bottom dimer) are shown in stick. The loop region between αA and αB (BB-loop) from TIRa is framed in red and shown in blue. (**B**) Structural alignment of the two RPP1^{TIR} monomers from the asymmetric homodimer. The BB-loop from TIRa and TIRb is shown in blue and gray, respectively. The BB-loop is highlighted. (**C**) Detailed interactions of the BB-loop from TIRa with TIRb in the asymmetric dimer. (**D**) Mutagenesis analysis of the interactions shown in (C) using the NADase activity assay described in Fig. 3D. (**E**) Effects of mutations at sites mediating TIRa-TIRb interactions (AE interface) on RPP1_WsB-HS and ATR1_Emoy2-dependent cell death in *N. benthamiana* leaves. Host cell death was measured in a quantitative electrolyte leakage assay as described in Fig. 2, D and E. Top: Host cell death triggered by coexpression of RPP1_WsB-HS variants and ATR1_Emoy2-HS in leaves of *N. benthamiana*. Statistical analysis via Tukey's HSD test is based on data from three independent experiments (n = 18, α = 0.001; data points of the same color were recorded in one experiment; shared lowercase letters indicate no significant difference). RPP1 mutants E158A and E158Q were included as additional negative controls. Below are photographs of representative agro-infiltrated leaf zones at 4 dai. Bottom: Western blot analysis of total *N. benthamiana* leaf protein extracts at 2 dai probed with antibody to HA. Expression of RPP1_WsB-HS WT and mutant proteins produces a signal of the expected molecular weight (~140 kD). Ponceau S staining indicates equal loading of total leaf proteins in the tested samples.

RPP1 tetramer and ZAR1^{NOD} in the ZAR1 pentamer (fig. S4C). Furthermore, NLR activation involves conformational changes in the NBD relative to its C-terminal WHD, whereas no conformational change occurs in the WHD relative to its C-terminal portion, as demonstrated in activation of ZAR1, Apaf-1, and NLRC4 (8, 25–27). A modeling study using the inactive ZAR1^{NOD} structure (33) as a template suggested that the LRR domain, in its pre-activation state, sequesters RPP1 from oligomerization, consistent with other NLR autoinhibition models (fig. S14). The modeled inactive RPP1 structure also suggested that ATR1 binding would sterically clash with RPP1^{NBD} (fig. S14B), inducing conformational changes in RPP1^{NBD} for activation. Positioning of inactive RPP1^{TIR} is difficult to predict because of the lack of a reliable template. However, overexpression of RPP1^{TIR}, but not RPP1$^{TIR\text{-}NBD}$, induced cell death in *N. benthamiana* (12, 30). These data point to inhibition of RPP1^{TIR} by RPP1^{NOD}, presumably through interdomain interaction similar to that observed for the inactive ZAR1^{CC} (33). An inhibitory interaction between the TIR and NBD domains was also suggested for TNLs L6 and L7 from flax (34).

On the basis of current models (5, 32), we expected an ATP molecule to be bound by the NBD of activated RPP1. Surprisingly, an adenosine diphosphate (ADP) molecule, which is unambiguously defined by the cryo-EM density, binds to the P-loop of RPP1 in the resistosome (Fig. 5A and fig. S5D). The ADP is recognized via RPP1 residues that are highly conserved in other NLR proteins (33, 35–37). Recognition of the γ-phosphate group of deoxyadenosine triphosphate (dATP)/ATP in the ZAR1 resistosome (8) and Apaf-1 apoptosome (27) is mediated through an arginine residue in a "TT/SR" motif that is essential for their activation. The arginine is highly conserved in plant CNLs and animal NLRs (38) but is substituted with a differently charged or polar residue, creating "TTE/Q" in many known TNLs including RPP1 (fig. S15, A and B). In contrast to ZAR1 and Apaf-1, however, RPP1 tolerates such substitutions, which suggests that other interactions might compensate for loss of ATP-mediated stabilization of the RPP1 resistosome. Indeed, the β2-α2 loop contributes to RPP1 oligomerization by mediating NOD-NOD interactions (Fig. 3B and Fig. 5B). In further support of this hypothesis, the TNL Roq1 with the TT/SR motif has ATP bound in its activated form and the β2-α2 loop is not involved in formation of the Roq1 resistosome (23), similar to what was observed in the ZAR1 resistosome (Fig. 5, B and C). Besides Roq1, some other TNLs also carry the TT/SR motif (fig. S15A). Most of these TNLs have a shorter β2-α2 loop relative to those without the motif (fig. S15A), providing

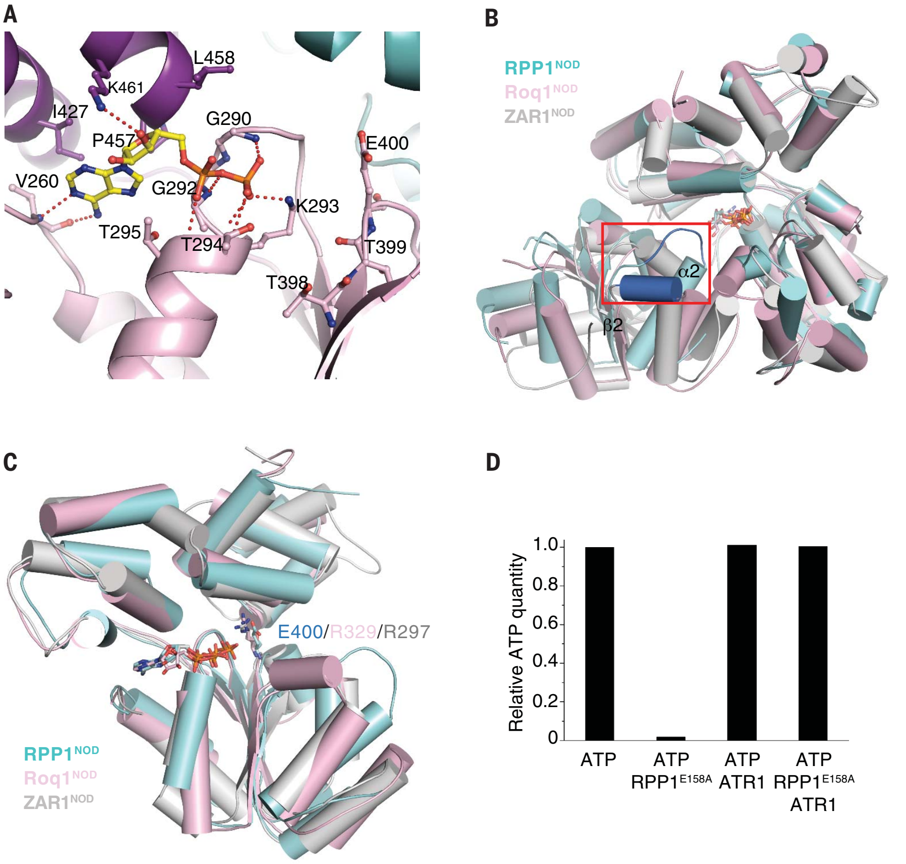

Fig. 5. Activation of RPP1 by ATR1. (**A**) ADP is bound between the NBD and HD1 domains in the cryo-EM structure of RPP1-ATR1. Red dashed lines represent polar interactions. A corresponding structure with EM density around the ADP-bound molecule is shown in fig. S5D. (**B**) Structural superposition of a lateral RPP1$^{\text{NOD}}$ (cyan), Roq1$^{\text{NOD}}$ (pink), and ZAR1$^{\text{NOD}}$ (gray) homodimer. For clarity, only the NBD from the left NOD monomer is shown. The β2-α2 loop is shown in blue and framed in red. (**C**) Structural superposition of RPP1$^{\text{NOD}}$ (cyan), Roq1$^{\text{NOD}}$ (pink), and ZAR1$^{\text{NOD}}$. Arg^{329} and Arg^{297} from the TTR motif of Roq1 and ZAR1, respectively, and Glu^{400} from the equivalent position of RPP1 are indicated. The bound ADP in RPP1 and ATP in Roq1 and ZAR1 are shown in stick. (**D**) ATPase activity assay for RPP1$^{\text{E158A}}$ and the RPP1$^{\text{E158A}}$-ATR1 complex with ATR1. The recombinant proteins were individually incubated with ATP (1.0 mM) in buffer containing 10 mM Mg^{2+}. After incubation at 25°C for 1 hour, samples were centrifuged and immediately used for HPLC analysis to measure ATP content. The vertical axis represents the ATP ratio after versus before the reaction.

additional evidence for the above hypothesis. Collectively, these results might explain why ADP is bound in the RPP1 tetramer, although exchange of ADP with ATP during RPP1 activation remains possible.

Bound ADP in the RPP1 resistosome might result from RPP1 intrinsic ATPase activity. To test this possibility, we used HPLC to measure the ATPase activity of the RPP1$^{\text{E158A}}$ resistosome or nonactivated RPP1$^{\text{E158A}}$ (to avoid potential interference from RPP1 NADase activity). In the presence of 10 mM Mg^{2+}, RPP1$^{\text{E158A}}$ alone displayed ATPase activity that was more potent than that of Apaf-1 by a factor of ~3 to 4 (Fig. 5D and fig. S16) (*35*, *39*). In contrast, the ATR1-activated RPP1$^{\text{E158A}}$ resistosome had much lower ATPase activity under the same conditions. Similar results were obtained with the Apaf-1 apoptosome (*39*). Hence, we propose that RPP1 ATPase activity also contributes to an ADP-bound resistosome.

Discussion

We reconstituted the RPP1 resistosome and solved its structure using cryo-EM at 3.16 Å. The structure reveals the mechanism of race-specific recognition of ATR1 by RPP1, leading to NLR conformational activation. We have presented evidence for the multilayered regulation of RPP1 tetramerization, including ATR1 binding (Fig. 2), RPP1$^{\text{NOD}}$ oligomerization (fig. S9), and RPP1$^{\text{TIR}}$ self-association (Fig. 4). RPP1 tetramerization results in the formation of two asymmetric RPP1$^{\text{TIR}}$ homodimers, creating active sites for NAD^{+} hydrolysis. Therefore, ATR1-induced receptor tetramerization links effector binding to the regulation of RPP1 NADase activity. Structural and biochemical characteristics of the activated RPP1 tetramer provide a template for understanding canonical plant TIR-type NLRs.

Besides the canonical TNL domains, the C-JID that could not be predicted by primary sequence was revealed in the cryo-EM structure of the RPP1 resistosome. Biochemical and functional data show that this novel structural domain is a major determinant for specific ATR1 recognition (Fig. 2). In contrast to integrated domains of plant NLRs that are sufficient for effector recognition (*7*), RPP1$^{\text{C-JID}}$ functions together with RPP1$^{\text{LRR}}$ for specific recognition of ATR1. The sequence-diversified RPP1$^{\text{C-JID}}$ is predicted by a hidden Markov model (HMM) to be shared by many TNLs in dicotyledonous plant species (fig. S17, A to F). It comprises part of a C-terminal domain in *Arabidopsis* TNL receptor RPS4 that confers effector-triggered immunity as a heterodimer with TNL RRS1 (*17*, *40*). Mutations within the predicted RPS4$^{\text{C-JID}}$ (fig. S17E) disabled RRS1/RPS4 immunity (*40*, *41*), pointing to broader importance of the C-JID for TNL function. It is possible that the C-JID serves as a decoy that mimics common virulence targets of pathogen effectors (*7*). However, using HMM, we failed to detect the RPP1$^{\text{C-JID}}$ in CNLs and non-NLR plant proteins (fig. S17, B to D). We therefore speculate that the C-JID in different TNLs plays a more generic role, together with LRRs, in TNL-specific detection of unrelated pathogen effectors. Although direct RPP1 recognition of ATR1 leads to resistosome formation, many plant NLRs perceive their cognate effectors in an indirect manner typically involving other host proteins (*2*).

Assembly of NADase active sites is mediated principally by the TIR BB-loop, which undergoes a major conformational change after RPP1 tetramer formation (fig. S18A). The BB-loop of RRS1$^{\text{TIR}}$ (four residues) is shorter than that of RPP1$^{\text{TIR}}$ and other TNL TIR domains (>9 residues; fig. S18B). The RRS1$^{\text{TIR}}$ BB-loop in the symmetric RRS1$^{\text{TIR}}$ homodimer or the RPS4$^{\text{TIR}}$-RRS1$^{\text{TIR}}$ heterodimer (*17*) cannot support an RPP1$^{\text{TIR}}$-like asymmetric homodimer (fig. S18B). Therefore, RRS1$^{\text{TIR}}$ would sequester the symmetric RPS4$^{\text{TIR}}$ homodimer from self-associating into asymmetric homodimers, potentially explaining RRS1$^{\text{TIR}}$-mediated in planta suppression of RPS4$^{\text{TIR}}$-triggered cell death (*17*). Structural alignment reveals that the asymmetric RPP1$^{\text{TIR}}$ homodimer is similar to that of filaments formed by MAL$^{\text{TIR}}$ in animals (fig. S18C) (*42*). However, there is no experimental evidence for a filament-forming activity of RPP1$^{\text{TIR}}$ or other plant TIR domains. Notably, MAL$^{\text{TIR}}$ can form cofilaments with TIR domains of other proteins such as human TLR4 and MyD88 (*42*). Many TIR-only genes are encoded in the genome of *Arabidopsis* (*43*), and TNLs have been proposed to recruit TIR-only proteins for signaling (44, 45). It will be interesting to determine whether the RPP1 resistosome can serve as a platform for interactions with TIR-only proteins or other oligomerized TNLs to amplify TNL-mediated immune signals.

Like the ZAR1 resistosome (8), the Apaf-1 apoptosome (27), and the NLRC4 inflammasome (25, 26, 46), the RPP1 tetramer forms a ring-like structure, despite the different oligomerization states of its components. The ZAR1 and RPP1 resistosomes contain, respectively, a stabilized funnel-shaped structure for plasma membrane targeting and a stabilized tetrameric RPP1$^{\mathrm{TIR}}$ for NADase activity. This contrasts with relatively flexible apoptosome and inflammasome N-terminal CARD domains. Hence, the N-terminal domains of plant and animal NLRs likely engage different mechanisms for immune signaling. Nonetheless, a shared principle in signaling mediated by the ZAR1 resistosome and NLRC4 inflammasome was proposed (8). The ZAR1 resistosome and probably many other CNLs with an N-terminal "MADA" motif (47) might form a membrane-resident pore or channel to mediate immunity. This is conceptually analogous to signaling mediated by the NLRC4 inflammasome that activates the pore-forming protein GSDMD for immune responses through the protease caspase-1 (48). The RPP1 resistosome, as a holoenzyme, bears similarity to both the apoptosome and the inflammasome, which form holoenzymes after recruitment of procaspase-9 and procaspase-1, respectively. Building on current models of TNL-mediated immune signaling, the RPP1 resistosome NADase activity is responsible for activation of HeLo domain–containing signaling (helper) NLRs via the EDS1 family of lipase-like proteins (49–51). It was speculated that HeLo-NLRs function similarly to ZAR1 at host membranes (8, 11, 47). Thus, the RPP1 resistosome and NLRC4 inflammasome might represent comparable paradigms in innate immunity signaling.

Materials and methods

Protein expression and purification

Sequence alignment of RPP1_WsB with its alleles RPP1_WsA, RPP1_NdA, RPP1_EstA, and RPP1_ZdrA by Clustal Omega (52) indicated that the N-terminal 60 amino acids of RPP1_WsB are not conserved. Therefore, an N-terminally truncated form of WT RPP1_WsB (61-1221) was constructed for protein expression in insect cells. ATR1_Emoy2 with an N-terminal truncation of 51 residues used for crystallization in a previous study (24) was used for protein expression. ATR1_Emoy2 (residues 52 to 311) was sufficient for recognition by RPP1, as demonstrated (24). For purification of the RPP1-ATR1 complex, a codon-optimized RPP1_WsB (61-1221; GENEWIZ Inc.) construct was cloned into the pFastBac 1 vector (Invitrogen) with a C-terminal twin-StrepII tag. A codon-optimized ATR1_Emoy2 construct (52-311; GENEWIZ) was cloned into the pFastBac 1 vector with a C-terminal 10 × HIS tag. These constructs were coexpressed in Sf21 insect cells (Invitrogen) at 28°C. After recombinant baculovirus infection for 48 hours, infected cells were harvested and resuspended in buffer A (25 mM Tris-HCl, pH 8.0, 150 mM NaCl, 1 mM $MgCl_2$, and 0.3 mM ATP). After sonication and centrifugation, the RPP1-ATR1 complex was purified using Strep-Tactin resin (IBA Lifesciences) from the supernatant. Proteins bound to resin were eluted with buffer A supplemented with 2.5 mM D-desthiobiotin. The eluent from Strep-Tactin was loaded onto Ni-NTA resin (Novagen) and the resin was washed with buffer A containing 20 mM imidazole. Proteins bound to the Ni-NTA resin were eluted with buffer A plus 250 mM imidazole. The eluent was concentrated through a 30-kD MWCO Vivaspin 500 concentrator (GE Healthcare) to 100 μl and loaded onto a Superose 6 increase 5/150 column (GE Healthcare) with buffer E (10 mM Tris-HCl pH 8.0, 100 mM NaCl, and 1 mM DTT). Peak fractions were concentrated to 0.45 mg/ml for cryo-EM sample preparation. A similar procedure was used for purification of the RPP1$^{\mathrm{E158A}}$ (61-1221)-ATR1 (52-311) complex.

Cryo-EM sample preparation and data collection

An aliquot of 3 μl of purified RPP1-ATR1 was applied to holey carbon grids (Quantifoil Au 1.2/1.3, 300 mesh) glow-discharged for 30 s at high level in Harrick Plasma after 2 min evacuation. Grids were then blotted on filter paper (Ted Pella Inc.) for 2.5 s at 8°C with 100% humidity and flash-frozen in liquid ethane using FEI Vitrobot Marked IV.

Two datasets of the WT RPP1-ATR1 complex were collected: one on a Titan Krios2 electron microscope operated at 300 kV, equipped with Gatan K3 Summit direct electron detector and a Gatan Quantum energy filter, the other on a Titan Krios3 electron microscope operated at 300 kV, equipped with a Cs-corrector, Gatan K3 Summit direct electron detector, and a Gatan Quantum energy filter. A total of 5701 and 3834 micrograph stacks were collected on Titan 2 and Titan 3, respectively. The micrograph stacks were automatically recorded using AutoEMation in superresolution mode (53), at a nominal magnification of 64,000× on Titan 2 and 81,000× on Titan 3. Defocus values varied from −1.0 μm to −2.0 μm for both datasets. Exposure rate of data collection on Titan 2 and Titan 3 was 23 and 24 electrons per pixel per second, respectively. The exposure time for both datasets was 2.56 s dose-fractionated into 32 subframes, leading to a total electron exposure of ~50 electrons per Å^2 for each stack.

Image processing and 3D reconstruction

The raw stacks of RPP1-ATR1 recorded in superresolution mode were motion-corrected by MotionCor2 and binned twofold, resulting in a physical pixel size of 1.0742 Å per pixel for Titan 2 motion-corrected micrographs and 1.0979 Å per pixel for Titan 3 motion-corrected micrographs (54). In the meantime, exposure rate for the summed micrographs was performed (55). Contrast transfer function (CTF) parameters were estimated by CTFFIND4 (56). Based on the CTF estimations, 5117 (Titan 2)/3123 (Titan 3) micrographs were manually picked, respectively, and were further processed in RELION3.1.

About 10,000 Laplacian-of-Gaussian auto-picked particles were subjected to 2D classification to generate initial templates for further auto-picking. For the dataset collected on Titan 2, 1,395,913 auto-picked particles were subjected to five rounds of 2D classification, which performed 25 iterations with regularization parameter $T = 2$ and number of classes = 100 to remove bad particles. Similar parameters were applied in three rounds of 2D classification of 1,125,203 auto-picked RPP1-ATR1 particles from Titan 3. After removal of bad particles, the remaining 661,434 particles on Titan 2 and 516,036 on Titan 3 for the RPP1-ATR1 complex were subjected to 3D classification with C_1 symmetry, using initial 3D reference models obtained by ab initio calculation from RELION3.1.

Particles (276,146 from Titan 2 and 133,202 from Titan 3 for RPP1-ATR1) from good 3D classes with clear overall structural features were selected for 3D refinement. At this stage, the 3D reconstructions clearly showed four RPP1 molecules in the complex. C_4 symmetry was therefore tested in the following 3D refinement. Resulting reconstructions showed that the global density, particularly that corresponding to the TIR part, became worse, indicating that lower or no symmetry exists in the RPP1-ATR1 complex. Subsequent 3D refinement with C_2 symmetry greatly improved the density quality and global resolution. After global 3D refinement with C_2 symmetry, CTF refinement, and postprocessing, the resolution of the RPP1-ATR1 reconstruction from the Titan 2 and Titan 3 datasets was 3.65 Å and 3.16 Å, respectively. Refined RPP1-ATR1 particles (409,348) from the two datasets were joined and subjected to a further round of 3D reconstruction, yielding a final cryo-EM map with 3.16 Å resolution.

A core region mask including the TIR, NBD, HD1, and WHD domains of RPP1 and ATR1 was generated by Chimera and then applied to 3D auto-refinement using C_2 symmetry and 409,348 particles from the final reconstruction with the merged datasets. In the end, the resolution of RPP1 core part reconstruction was 2.99 Å after postprocess.

The LRR and C-JID portions in the final EM map were more flexible relative to the other parts of the RPP1-ATR1 complex. To improve resolution of the local density, C_4 symmetry was first used to refine the joined particles, and the refined particles were expanded with C_4 symmetry for focused 3D classification. A local mask for LRR, C-JID, and ATR1 was generated using Chimera and then applied for focused 3D classification without alignment as described (57). After the focused 3D classification, a total of 222,015 particles were selected for C_1 focused 3D refinement, finally yielding a local reconstruction for LRR, C-JID, and ATR1 with 3.19 Å after postprocess.

2D classification, 3D classification, and 3D autorefinement were all performed with RELION3.1 (58–60). The resolutions were determined by gold-standard Fourier shell correlation (61). Local resolution distribution was evaluated using RELION (62).

Model building and refinement

The final RPP1-ATR1 EM map was generated by merging the global map and local LRR, C-JID, and ATR1 map, using combine_focused_map in PHENIX (63). For model building of the whole RPP1-ATR1 complex, the RPP1 TIR domain (PDB: 5TEB) (18) and ATR1 (PDB: 3RMR) were docked into the EM map in Chimera (64). The models of the NBD, HD1, and WHD domains of RPP1 were manually built in COOT based on the global EM map of RPP1-ATR1, and the LRR and C-JID domains in COOT using the local refined EM map (65). All the domains were then combined, generating a model containing four ATR1 molecules and four RPP1 molecules. The generated model was refined against the combined RPP1-ATR1 EM density using real-space refinement in PHENIX with secondary structure and geometry restraints (63). The final model after refinement was validated using MolProbity and EMRinger in the PHENIX package (63). Table S1 summarizes the model statistics.

In vitro NADase assays

Purified RPP1, RPP1-ATR1, mutant RPP1-ATR1, or $RPP1^{TIR}$ were used for NADase assays at the indicated concentrations. Proteins were individually incubated with 100 μM NAD^+ (final concentration) and 10 mM $MgSO_4$ or $CaCl_2$ in buffer containing 100 mM NaCl, 25 mM Tris-HCl pH 8.0. The total volume for each reaction was 100 μl. Reactions were performed in a thermoshaker at 25°C for 16 hours. After reaction, samples were centrifuged and immediately applied for HPLC analysis.

In vitro ATPase assays

Purified $RPP1^{E158A}$, $RPP1^{E158A}$-ATR1 complex, and ATR1 were used for ATPase assays with a protein concentration of 5 μM. Each protein was incubated with 100 μM ATP (final concentration) in buffer containing 10.0 mM $MgSO_4$, 100 mM NaCl, 25.0 mM Tris-HCl pH 8.0 at 25°C for the indicated times. The volume for reaction was 100 μl. After reaction, samples were centrifuged and immediately applied for HPLC analysis. 1.0 μM $RPP1^{E158A}$ was used to quantify its ATPase activity. Reactions were carried out as described above. Samples (50 μl) taken at different time points (1, 2, 3, 4, and 5 hours) were analyzed on an HPLC system to detect the formed ADP. By comparison with reference samples (ADP), the respective integrated ADP peak area was converted into concentration. The ATPase activity was calculated by five data points–based linear regression.

HPLC measurements

HPLC was performed on an Agilent 1260 bioinert HPLC system using a Synergi Fusion-RP 80 Å (4.6 × 150 mm, 4 μm) (Phenomenex) column. The samples were measured via an 8-min method. Samples (10 μl) were injected at 550 μl/min with ammonium formate (5 mM) in water and methanol used as mobile phases A and B, respectively. The elution profile was as follows: 0 to 3 min, 10 to 70% B; 3 to 6 min, 70% B; 6 to 6.1 min, 70 to 10% B; 6.1 to 8 min, 10% B. The autosampler temperature was maintained at 4°C and the column temperature at 25°C. UV signals were detected at 260 nm. Reference standards were used to determine respective retention times. The integrations of peak area were used to calculate relative concentrations.

Site-directed mutagenesis of RPP1_WsB and ATR1_Emoy2 for in planta analyses

For *N. benthamiana* transient expression analyses, the RPP1_WsB gene body (exons and introns) was PCR-amplified from the pENTR/D-TOPO pRPP1:gRPP1 construct provided by K. Krasileva (12, 19) and cloned into pENTR/D-TOPO vector (Thermo Fisher Scientific, K240020). The ATR1_Emoy2 sequence starts with a codon corresponding to T19 in NCBI accession AAX51198 ATR1_Emoy2, thereby removing a signal peptide. Mutagenesis was performed using a QuikChange II site-directed mutagenesis kit (Agilent, 200523) or KOD-Plus-Mutagenesis kit (CosmoBio, SMK-101). Sequences of oligonucleotides are provided in table S2. Obtained pENTR/D-TOPO RPP1_WsB and pDONR207 ATR1_Emoy2 plasmids were LR-recombined (Thermo Fisher Scientific, 11791020) into pXCSG vectors (66) to allow expression of untagged $RPP1^{WsB}$, C-terminally tagged RPP1_WsB-3xHA-StrepII, and ATR1_Emoy2-3xHA-StrepII proteins under a 35S promoter. All constructs were verified by DNA sequencing. Generated binary constructs were transformed into *Agrobacterium tumefaciens* (*Rhizobium radiobacter*) GV3101 pMP90RK via electroporation.

Protein expression in N. benthamiana and Western blot analysis

RPP1_WsB-HS and ATR1_Emoy2-HS were expressed in *N. benthamiana* using agrobacteria-mediated transient expression assays in the presence of the P19 suppressor of RNAi silencing as in (49). The final OD_{600} for each strain was set to 0.2. To detect ATR1 variants, two 8-mm leaf discs per sample were harvested at 2 dai and boiled at 95°C in Laemmli buffer for 5 min. The ATR1-HS fusions were blotted onto nitrocellulose membranes and detected using primary α-HA antibodies (Sigma Aldrich, 11867423001 or H6908; Cell Signaling Technology, #3724) and secondary horseradish peroxidase (HRP)–conjugated antibodies (Santa Cruz, sc-2006; Sigma Aldrich, A5164) at dilution 1:5000 (3% milk powder in TBST). Detection was performed using enhanced chemiluminescence assays Clarity, Clarity Max Western ECL (Bio-Rad, #1705061 and #1705062). To detect RPP1_WsB-HS variants, infiltrated *N. benthamiana* leaves were collected at 2 dai, frozen in liquid nitrogen, and ground to a fine powder. Powder (~100 μl in a tube) was resuspended in 100 μl of urea-SDS sample buffer [50 mM Tris-HCl pH 6.8, 2% SDS, 8 M urea, 2% β-mercaptoethanol, 5% glycerol, protease inhibitor cocktail (Roche), and 0.004% Bromophenol Blue] and vortexed for 10 min at room temperature. No boiling step was included. After centrifugation at 16,000*g* for 10 min, 10 μl of the supernatant was loaded onto 8% SDS-PAGE and proteins were blotted onto a PVDF membrane. Immunoblot assay was performed using monoclonal rat anti-HA antibody (Sigma Aldrich, 11867423001) diluted 1:4000 and rabbit anti-rat antibody (Sigma Aldrich, A5164) diluted 1:5000 in 1× TBS, 0.1% Tween-20 with 3.5% w/v nonfat dry milk. RPP1_WsB-HS fusion proteins were detected using ECL SuperSignal West Femto Maximum Sensitivity Substrate and ECL Western Blotting substrate (Thermo Scientific) in a ratio of 2:1.

Cell death quantification in N. benthamiana

RPP1_WsB-HS and ATR1_Emoy2-HS WT and mutant protein combinations were transiently expressed in *N. benthamiana* as described above (49) and agrobacteria-infiltrated leaf zones used for cell death (ion leakage) assays at 3 dai as described (49). Statistical analysis was performed on conductivity data normalized to the mean level in samples containing WT RPP1_WsB and ATR1_Emoy2 samples via Tukey's HSD (honestly significant difference) test after checking normality of residuals distribution and homogeneity of variance using visual examination of the plots and Shapiro-Wilcoxon and Levene tests ($P > 0.05$). Images of agrobacteria-infiltrated leaf spots were taken at 4 to 5 dpi.

RPP1_WsB jelly roll/Ig-like (JID) sequence distribution across plants

Protein sequences of 32 representative plant species from green algae to *Arabidopsis thaliana* were obtained as in (*49*). Sequences similar to the jelly roll domain of RPP1_WsB (amino acids 1075 to 1195) were initially searched with BLASTP (-evalue 0.01). The jelly roll–like sequences were detected at this step only in *Brassicaceae* plants. The match sequences were extracted and aligned via the Muscle method. A hidden Markov model was built from the resulting alignment [hmmbuild in HMMER 3.1b2 (*67*), default settings]. This model (v1) identified 622 matches mainly in Brassicales but also in Fabales, Malpighiales, and Rosales (Reference Proteomes 2020_04, hmmsearch at EMBL-EBI–incE 0.01). To improve sensitivity of the search, a next version of the HMM model was prepared. For that, the v1 HMM was run against the 32 species protein database above (hmmsearch in HMMER 3.1b2,–incE 0.01) and not against public databases to avoid with redundancy and skewing toward *Brassicaceae* in public databases. The resulting matches were again extracted, aligned with Clustal Omega, and the obtained alignment served as an input for building the version 2 HMM, available as data S1. The v2 HMM run against Uniprot database (2019-10-03) at EMBL-EBI (hmmsearch -E1–domE 1–incE 0.001–incdomE 0.03–seqdb uniprotkb) identified 2711 hits, only in eudicots. The majority of found proteins have a typical TNL domain architecture, other hits have different arrangements/combinations of NBARC, LRR, TIR domains and occasionally other domains. Finally, to assess distribution of the RPP1_WsB-like JID across plants, the v2 HMM (data S1) was scanned against the above custom non-redundant database of protein sequences from 32 representative plant species (hmmsearch–incE 0.01).

REFERENCES AND NOTES

1. H. Burdett, B. Kobe, P. A. Anderson, Animal NLRs continue to inform plant NLR structure and function. *Arch. Biochem. Biophys.* **670**, 58–68 (2019). doi: 10.1016/j.abb.2019.05.001; pmid: 31071301
2. J. D. Jones, R. E. Vance, J. L. Dangl, Intracellular innate immune surveillance devices in plants and animals. *Science* **354**, aaf6395 (2016). doi: 10.1126/science.aaf6395; pmid: 27934708
3. S. Lolle, D. Stevens, G. Coaker, Plant NLR-triggered immunity: From receptor activation to downstream signaling. *Curr. Opin. Immunol.* **62**, 99–105 (2020). doi: 10.1016/j.coi.2019.12.007; pmid: 31958770
4. T. Maekawa, T. A. Kufer, P. Schulze-Lefert, NLR functions in plant and animal immune systems: So far and yet so close. *Nat. Immunol.* **12**, 817–826 (2011). doi: 10.1038/ni.2083; pmid: 21852785
5. S. Nimma, T. Ve, S. J. Williams, B. Kobe, Towards the structure of the TIR-domain signalosome. *Curr. Opin. Struct. Biol.* **43**, 122–130 (2017). doi: 10.1016/j.sbi.2016.12.014; pmid: 28092811
6. J. Wang, J. Chai, Molecular actions of NLR immune receptors in plants and animals. *Sci. China Life Sci.* **63**, 1–14 (2020). doi: 10.1007/s11427-019-1687-6; pmid: 32613490
7. E. Grund, D. Tremousaygue, L. Deslandes, Plant NLRs with Integrated Domains: Unity Makes Strength. *Plant Physiol.* **179**, 1227–1235 (2019). doi: 10.1104/pp.18.01134; pmid: 30530739
8. J. Wang *et al.*, Reconstitution and structure of a plant NLR resistosome conferring immunity. *Science* **364**, eaav5870 (2019). doi: 10.1126/science.aav5870; pmid: 30948527
9. M. Bernoux *et al.*, Structural and functional analysis of a plant resistance protein TIR domain reveals interfaces for self-association, signaling, and autoregulation. *Cell Host Microbe* **9**, 200–211 (2011). doi: 10.1016/j.chom.2011.02.009; pmid: 21402359
10. S. Cesari *et al.*, Cytosolic activation of cell death and stem rust resistance by cereal MLA-family CC-NLR proteins. *Proc. Natl. Acad. Sci. U.S.A.* **113**, 10204–10209 (2016). doi: 10.1073/pnas.1605483113; pmid: 27555587
11. S. M. Collier, L. P. Hamel, P. Moffett, Cell death mediated by the N-terminal domains of a unique and highly conserved class of NB-LRR protein. *Mol. Plant Microbe Interact.* **24**, 918–931 (2011). doi: 10.1094/MPMI-03-11-0050; pmid: 21501087
12. K. V. Krasileva, D. Dahlbeck, B. J. Staskawicz, Activation of an Arabidopsis resistance protein is specified by the in planta association of its leucine-rich repeat domain with the cognate oomycete effector. *Plant Cell* **22**, 2444–2458 (2010). doi: 10.1105/tpc.110.075358; pmid: 20601497
13. M. R. Swiderski, D. Birker, J. D. Jones, The TIR domain of TIR-NB-LRR resistance proteins is a signaling domain involved in cell death induction. *Mol. Plant Microbe Interact.* **22**, 157–165 (2009). doi: 10.1094/MPMI-22-2-0157; pmid: 19132868
14. T. Maekawa *et al.*, Coiled-coil domain-dependent homodimerization of intracellular barley immune receptors defines a minimal functional module for triggering cell death. *Cell Host Microbe* **9**, 187–199 (2011). doi: 10.1016/j.chom.2011.02.008; pmid: 21402358
15. L. Wan *et al.*, TIR domains of plant immune receptors are NAD$^+$-cleaving enzymes that promote cell death. *Science* **365**, 799–803 (2019). doi: 10.1126/science.aax1771; pmid: 31439793
16. S. Horsefield *et al.*, NAD$^+$ cleavage activity by animal and plant TIR domains in cell death pathways. *Science* **365**, 793–799 (2019). doi: 10.1126/science.aax1911; pmid: 31439792
17. S. J. Williams *et al.*, Structural basis for assembly and function of a heterodimeric plant immune receptor. *Science* **344**, 299–303 (2014). doi: 10.1126/science.1247357; pmid: 24744375
18. X. Zhang *et al.*, Multiple functional self-association interfaces in plant TIR domains. *Proc. Natl. Acad. Sci. U.S.A.* **114**, E2046–E2052 (2017). doi: 10.1073/pnas.1621248114; pmid: 28159890
19. M. A. Botella *et al.*, Three genes of the Arabidopsis RPP1 complex resistance locus recognize distinct Peronospora parasitica avirulence determinants. *Plant Cell* **10**, 1847–1860 (1998). doi: 10.1105/tpc.10.11.1847; pmid: 9811793
20. A. D. Steinbrenner, S. Goritschnig, B. J. Staskawicz, Recognition and activation domains contribute to allele-specific responses of an Arabidopsis NLR receptor to an oomycete effector protein. *PLOS Pathog.* **11**, e1004665 (2015). doi: 10.1371/journal.ppat.1004665; pmid: 25671309
21. A. P. Rehmany *et al.*, Differential recognition of highly divergent downy mildew avirulence gene alleles by RPP1 resistance genes from two Arabidopsis lines. *Plant Cell* **17**, 1839–1850 (2005). doi: 10.1105/tpc.105.031807; pmid: 15894715
22. S. Goritschnig, A. D. Steinbrenner, D. J. Grunwald, B. J. Staskawicz, Structurally distinct Arabidopsis thaliana NLR immune receptors recognize tandem WY domains of an oomycete effector. *New Phytol.* **210**, 984–996 (2016). doi: 10.1111/nph.13823; pmid: 26725254
23. R. Martin *et al.*, Structure of the activated Roq1 resistosome directly recognizing the pathogen effector XopQ. bioRxiv 246413 [preprint]. 14 August 2020.
24. S. Chou *et al.*, Hyaloperonospora arabidopsidis ATR1 effector is a repeat protein with distributed recognition surfaces. *Proc. Natl. Acad. Sci. U.S.A.* **108**, 13323–13328 (2011). doi: 10.1073/pnas.1109791108; pmid: 21788488
25. Z. Hu *et al.*, Structural and biochemical basis for induced self-propagation of NLRC4. *Science* **350**, 399–404 (2015). doi: 10.1126/science.aac5489; pmid: 26449475
26. L. Zhang *et al.*, Cryo-EM structure of the activated NAIP2-NLRC4 inflammasome reveals nucleated polymerization. *Science* **350**, 404–409 (2015). doi: 10.1126/science.aac5789; pmid: 26449474
27. M. Zhou *et al.*, Atomic structure of the apoptosome: Mechanism of cytochrome c- and dATP-mediated activation of Apaf-1. *Genes Dev.* **29**, 2349–2361 (2015). doi: 10.1101/gad.272278.115; pmid: 26543158
28. S. Qi *et al.*, Crystal structure of the Caenorhabditis elegans apoptosome reveals an octameric assembly of CED-4. *Cell* **141**, 446–457 (2010). doi: 10.1016/j.cell.2010.03.017; pmid: 20434985
29. T. Ogawa, Y. Ueda, K. Yoshimura, S. Shigeoka, Comprehensive analysis of cytosolic Nudix hydrolases in Arabidopsis thaliana. *J. Biol. Chem.* **280**, 25277–25283 (2005). doi: 10.1074/jbc.M503536200; pmid: 15878881
30. K. J. Schreiber, A. Bentham, S. J. Williams, B. Kobe, B. J. Staskawicz, Multiple Domain Associations within the Arabidopsis Immune Receptor RPP1 Regulate the Activation of Programmed Cell Death. *PLOS Pathog.* **12**, e1005769 (2016). doi: 10.1371/journal.ppat.1005769; pmid: 27427964
31. Z. Duxbury *et al.*, Induced proximity of a TIR signaling domain on a plant-mammalian NLR chimera activates defense in plants. *Proc. Natl. Acad. Sci. U.S.A.* **117**, 18832–18839 (2020). doi: 10.1073/pnas.2001185117; pmid: 32709746
32. Y. Xiong, Z. Han, J. Chai, Resistosome and inflammasome: Platforms mediating innate immunity. *Curr. Opin. Plant Biol.* **56**, 47–55 (2020). doi: 10.1016/j.pbi.2020.03.010; pmid: 32554225
33. J. Wang *et al.*, Ligand-triggered allosteric ADP release primes a plant NLR complex. *Science* **364**, eaav5868 (2019). doi: 10.1126/science.aav5868; pmid: 30948526
34. M. Bernoux *et al.*, Comparative Analysis of the Flax Immune Receptors L6 and L7 Suggests an Equilibrium-Based Switch Activation Model. *Plant Cell* **28**, 146–159 (2016). doi: 10.1105/tpc.15.00303; pmid: 26744216
35. Z. Hu *et al.*, Crystal structure of NLRC4 reveals its autoinhibition mechanism. *Science* **341**, 172–175 (2013). doi: 10.1126/science.1236381; pmid: 23765277
36. H. Sharif *et al.*, Structural mechanism for NEK7-licensed activation of NLRP3 inflammasome. *Nature* **570**, 338–343 (2019). doi: 10.1038/s41586-019-1295-z; pmid: 31189953
37. J. F. C. Steele, R. K. Hughes, M. J. Banfield, Structural and biochemical studies of an NB-ARC domain from a plant NLR immune receptor. *PLOS ONE* **14**, e0221226 (2019). doi: 10.1371/journal.pone.0221226; pmid: 31461469
38. X. Yang, G. Lin, Z. Han, J. Chai, Structural Biology of NOD-Like Receptors. *Adv. Exp. Med. Biol.* **1172**, 119–141 (2019). doi: 10.1007/978-981-13-9367-9_6; pmid: 31628654
39. T. F. Reubold, S. Wohlgemuth, S. Eschenburg, A new model for the transition of APAF-1 from inactive monomer to caspase-activating apoptosome. *J. Biol. Chem.* **284**, 32717–32724 (2009). doi: 10.1074/jbc.M109.014027; pmid: 19801675
40. Y. Ma *et al.*, Distinct modes of derepression of an *Arabidopsis* immune receptor complex by two different bacterial effectors. *Proc. Natl. Acad. Sci. U.S.A.* **115**, 10218–10227 (2018). doi: 10.1073/pnas.1811858115; pmid: 30254172
41. K. H. Sohn *et al.*, The nuclear immune receptor RPS4 is required for RRS1SLH1-dependent constitutive defense activation in Arabidopsis thaliana. *PLOS Genet.* **10**, e1004655 (2014). doi: 10.1371/journal.pgen.1004655; pmid: 25340333
42. T. Ve *et al.*, Structural basis of TIR-domain-assembly formation in MAL- and MyD88-dependent TLR4 signaling. *Nat. Struct. Mol. Biol.* **24**, 743–751 (2017). doi: 10.1038/nsmb.3444; pmid: 28759049
43. B. C. Meyers, M. Morgante, R. W. Michelmore, TIR-X and TIR-NBS proteins: Two new families related to disease resistance TIR-NBS-LRR proteins encoded in Arabidopsis and other plant genomes. *Plant J.* **32**, 77–92 (2002). doi: 10.1046/j.1365-313X.2002.01404.x; pmid: 12366802
44. R. S. Nandety *et al.*, The role of TIR-NBS and TIR-X proteins in plant basal defense responses. *Plant Physiol.* **162**, 1459–1472 (2013). doi: 10.1104/pp.113.219162; pmid: 23735504
45. M. T. Nishimura *et al.*, TIR-only protein RBA1 recognizes a pathogen effector to regulate cell death in *Arabidopsis*. *Proc. Natl. Acad. Sci. U.S.A.* **114**, E2053–E2062 (2017). doi: 10.1073/pnas.1620973114; pmid: 28137883
46. J. L. Tenthorey *et al.*, The structural basis of flagellin detection by NAIP5: A strategy to limit pathogen immune evasion. *Science* **358**, 888–893 (2017). doi: 10.1126/science.aao1140; pmid: 29146805
47. H. Adachi *et al.*, An N-terminal motif in NLR immune receptors is functionally conserved across distantly related plant species. *eLife* **8**, e49956 (2019). doi: 10.7554/eLife.49956; pmid: 31774397
48. L. Wang, H. Wu, Keeping the Death Protein in Check. *Immunity* **51**, 1–2 (2019). doi: 10.1016/j.immuni.2019.06.011; pmid: 31315028

49. D. Lapin *et al*., A Coevolved EDS1-SAG101-NRG1 Module Mediates Cell Death Signaling by TIR-Domain Immune Receptors. *Plant Cell* **31**, 2430–2455 (2019). doi: 10.1105/tpc.19.00118; pmid: 31311833
50. B. Castel *et al*., Diverse NLR immune receptors activate defence via the RPW8-NLR NRG1. *New Phytol.* **222**, 966–980 (2019). doi: 10.1111/nph.15659; pmid: 30582759
51. Z. Wu *et al*., Differential regulation of TNL-mediated immune signaling by redundant helper CNLs. *New Phytol.* **222**, 938–953 (2019). doi: 10.1111/nph.15665; pmid: 30585636
52. F. Sievers *et al*., Fast, scalable generation of high-quality protein multiple sequence alignments using Clustal Omega. *Mol. Syst. Biol.* **7**, 539 (2011). doi: 10.1038/msb.2011.75; pmid: 21988835
53. J. Lei, J. Frank, Automated acquisition of cryo-electron micrographs for single particle reconstruction on an FEI Tecnai electron microscope. *J. Struct. Biol.* **150**, 69–80 (2005). doi: 10.1016/j.jsb.2005.01.002; pmid: 15797731
54. S. Q. Zheng *et al*., MotionCor2: Anisotropic correction of beam-induced motion for improved cryo-electron microscopy. *Nat. Methods* **14**, 331–332 (2017). doi: 10.1038/nmeth.4193; pmid: 28250466
55. T. Grant, N. Grigorieff, Measuring the optimal exposure for single particle cryo-EM using a 2.6 Å reconstruction of rotavirus VP6. *eLife* **4**, e06980 (2015). doi: 10.7554/eLife.06980; pmid: 26023829
56. J. A. Mindell, N. Grigorieff, Accurate determination of local defocus and specimen tilt in electron microscopy. *J. Struct. Biol.* **142**, 334–347 (2003). doi: 10.1016/S1047-8477(03)00069-8; pmid: 12781660
57. X. C. Bai, E. Rajendra, G. Yang, Y. Shi, S. H. Scheres, Sampling the conformational space of the catalytic subunit of human γ-secretase. *eLife* **4**, e11182 (2015). doi: 10.7554/eLife.11182; pmid: 26623517
58. S. H. Scheres, RELION: Implementation of a Bayesian approach to cryo-EM structure determination. *J. Struct. Biol.* **180**, 519–530 (2012). doi: 10.1016/j.jsb.2012.09.006; pmid: 23000701
59. S. H. Scheres, A Bayesian view on cryo-EM structure determination. *J. Mol. Biol.* **415**, 406–418 (2012). doi: 10.1016/j.jmb.2011.11.010; pmid: 22100448
60. J. Zivanov, T. Nakane, S. H. W. Scheres, Estimation of high-order aberrations and anisotropic magnification from cryo-EM data sets in *RELION*-3.1. *IUCrJ* **7**, 253–267 (2020). doi: 10.1107/S2052252520000081; pmid: 32148853
61. P. B. Rosenthal, R. Henderson, Optimal determination of particle orientation, absolute hand, and contrast loss in single-particle electron cryomicroscopy. *J. Mol. Biol.* **333**, 721–745 (2003). doi: 10.1016/j.jmb.2003.07.013; pmid: 14568533
62. A. Kucukelbir, F. J. Sigworth, H. D. Tagare, Quantifying the local resolution of cryo-EM density maps. *Nat. Methods* **11**, 63–65 (2014). doi: 10.1038/nmeth.2727; pmid: 24213166
63. P. D. Adams *et al*., PHENIX: A comprehensive Python-based system for macromolecular structure solution. *Acta Crystallogr. D* **66**, 213–221 (2010). doi: 10.1107/S0907444909052925; pmid: 20124702
64. E. F. Pettersen *et al*., UCSF Chimera—A visualization system for exploratory research and analysis. *J. Comput. Chem.* **25**, 1605–1612 (2004). doi: 10.1002/jcc.20084; pmid: 15264254
65. P. Emsley, B. Lohkamp, W. G. Scott, K. Cowtan, Features and development of Coot. *Acta Crystallogr. D* **66**, 486–501 (2010). doi: 10.1107/S0907444910007493; pmid: 20383002
66. C. P. Witte, L. D. Noël, J. Gielbert, J. E. Parker, T. Romeis, Rapid one-step protein purification from plant material using the eight-amino acid StrepII epitope. *Plant Mol. Biol.* **55**, 135–147 (2004). doi: 10.1007/s11103-004-0501-y; pmid: 15604670
67. S. R. Eddy, Accelerated Profile HMM Searches. *PLOS Comput. Biol.* **7**, e1002195 (2011). doi: 10.1371/journal.pcbi.1002195; pmid: 22039361

ACKNOWLEDGMENTS

We thank J. Lei, X. Li, X. Fan, and N. Liu at Tsinghua University for data collection. We acknowledge the Tsinghua University Branch of the China National Center for Protein Sciences (Beijing) for providing the cryo-EM facility support and the computational facility support on the cluster of Bio-Computing Platform. **Funding:** Supported by the National Natural Science Foundation of China (31421001 to J.C. and 31971119 to Z.H.), the Alexander von Humboldt Foundation (a Humboldt professorship to J.C.), the Max-Planck-Gesellschaft (J.E.P. and P.S.-L., and a Max Planck fellowship to J.C.), Deutsche Forschungsgemeinschaft SFB-1403-414786233 (J.C., J.E.P., and P.S.-L.) and Germany's Excellence Strategy CEPLAS (EXC-2048/1, Project 390686111) (J.C., J.E.P., and P.S.-L.). **Author contributions:** Experimental design: J.C., J.E.P., P.S.-L., S.M., D.L.; recombinant protein expression assays, purification, structure determinations, modeling, and data analysis: S.M., X.Z., Y.S., W.S., J.W., and J.C.; biochemical assays: S.M., W.S., D.Y., J.J., Z.H.; plant expression and cell death assays: L.L., D.L., E.L.; HMM building: D.L.; data analysis: all authors; manuscript writing: J.C., J.E.P., P.S.-L. with contributions from other authors. **Competing interests:** The authors declare no competing interests. **Data and materials availability:** Plasmids for in planta expression of RPP1_WsB and ATR1_Emoy2 variants (table S2) are available from J.E.P. or P.S.-L. under a material agreement with Max Planck Institute for Plant Breeding Research. All data are available in the main text, supplementary materials, or the listed Protein Data Bank (PDB) files. For the RPP1 resistosome and RPP1LRR-C-JID-ATR1, the atomic coordinates have been deposited in the PDB with accession codes 7CRC and 7CRB, respectively. The EM maps have been deposited in the Electron Microscopy Database with accession codes EMD-30450 and EMD-30449, respectively.

SUPPLEMENTARY MATERIALS

science.sciencemag.org/content/370/6521/eabe3069/suppl/DC1
Figs. S1 to S18
Tables S1 and S2
Data S1
References (*68*–*71*)

13 August 2020; accepted 22 October 2020
10.1126/science.abe3069

2.2 TIR domains of plant immune receptors are 2′,3′-cAMP/cGMP synthetases mediating cell death

Dongli Yu*, Wen Song*, Eddie Yong Jun Tan*, Li Liu, Yu Cao, Jan Jirschitzka, Ertong Li, Elke Logemann, Chenrui Xu, Shijia Huang, Aolin Jia, Xiaoyu Chang, Zhifu Han, Bin Wu[+], Paul Schulze-Lefert[+] and Jijie Chai[+]

Published in Cell *185* (2022)

Author contributions:
Conceptualization, J.C., P.S.-L., D.Y.; Formal Analysis, B.W., E.T., C.X.; Investigation, D.Y., W.S., L.L., Y.C., J.J., E.Li., E.Logemann., S.H., A.J., X.C, Z.H.; Writing, J.C., D.Y., P.S.-L. with input from all authors; Resources, J.C., P.S.-L., B.W.; Funding Acquisition, J.C., P.S.-L., B.W.; Supervision, J.C., P.S.-L.

Specific contributions:
In this study, I identified TIR domain proteins as a novel group of 2′,3′-cAMP/cGMP synthetases. Structural comparison of the dsDNA-bound L7^{TIR} filament with the ADPR-bound L7^{TIR} showed that TIR domain proteins adopt two mutually exclusive oligomers to confer 2′,3′-cAMP/cGMP synthetases and NADase activities. Biological experiments showed that these two enzyme activities act together to activate plant immune responses.

Page numbers in the attached paper are not counted in the pagination of the thesis.

Cell

Article

TIR domains of plant immune receptors are 2′,3′-cAMP/cGMP synthetases mediating cell death

Graphical abstract

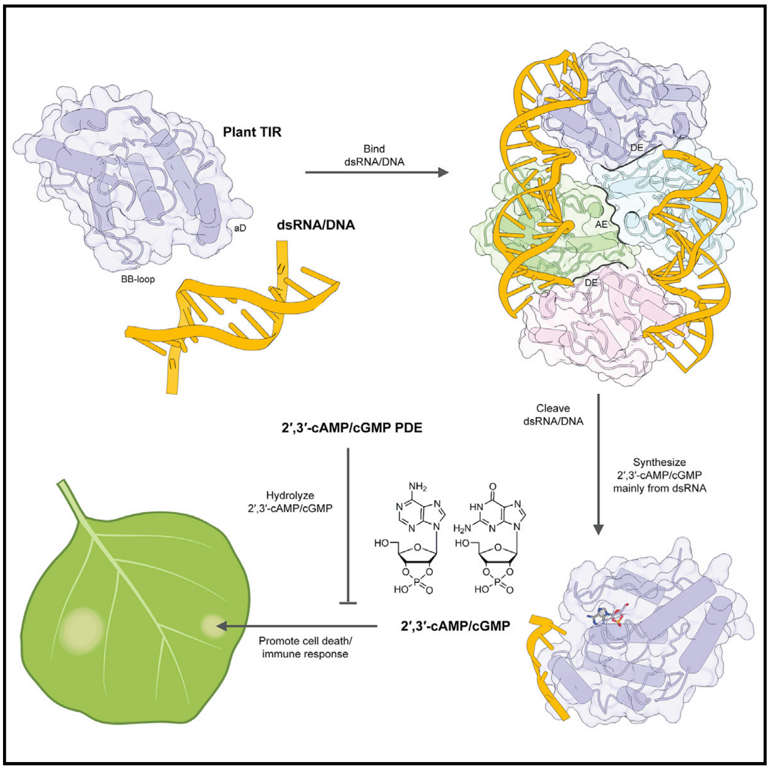

Highlights

- Plant TIR proteins act as 2′,3′-cAMP/cGMP synthetases by hydrolyzing dsRNA/dsDNA
- Cryo-EM structure reveals the mechanism of plant TIRs as bifunctional enzymes
- 2′,3′-cAMP/cGMP are required for TIR-mediated cell death in plants
- 2′,3′-cAMP/cGMP PDE negatively regulate TIR-mediated cell death in plants

Authors

Dongli Yu, Wen Song,
Eddie Yong Jun Tan, ..., Bin Wu,
Paul Schulze-Lefert, Jijie Chai

Correspondence

wubin@ntu.edu.sg (B.W.),
schlef@mpipz.mpg.de (P.S.-L.),
chai@mpipz.mpg.de (J.C.)

In brief

Plant TIR domain-containing proteins are bifunctional enzymes with NADase and cyclic nucleotide monophosphate synthetase activity. Combinations of these activities may cooperate to control cell death and immune signaling processes in plants.

Yu et al., 2022, Cell *185*, 1–17
June 23, 2022 © 2022 Elsevier Inc.
https://doi.org/10.1016/j.cell.2022.04.032

Please cite this article in press as: Yu et al., TIR domains of plant immune receptors are 2′,3′-cAMP/cGMP synthetases mediating cell death, Cell (2022), https://doi.org/10.1016/j.cell.2022.04.032

Cell

CellPress

Article

TIR domains of plant immune receptors are 2′,3′-cAMP/cGMP synthetases mediating cell death

Dongli Yu,[1,2,6] Wen Song,[1,6] Eddie Yong Jun Tan,[3,6] Li Liu,[2] Yu Cao,[1,2] Jan Jirschitzka,[1] Ertong Li,[1] Elke Logemann,[2] Chenrui Xu,[3] Shijia Huang,[4] Aolin Jia,[4] Xiaoyu Chang,[4] Zhifu Han,[4] Bin Wu,[3,5,*] Paul Schulze-Lefert,[2,*] and Jijie Chai[1,2,4,7,*]
[1]Institute of Biochemistry, University of Cologne, Cologne, Germany
[2]Max Planck Institute for Plant Breeding Research, Cologne, Germany
[3]School of Biological Sciences, Nanyang Technological University, Singapore, Singapore
[4]Beijing Advanced Innovation Center for Structural Biology, Tsinghua-Peking Joint Center for Life Sciences, Center for Plant Biology, School of Life Sciences, Tsinghua University, Beijing, China
[5]NTU Institute of Structural Biology, Nanyang Technological University, Singapore, Singapore
[6]These authors contributed equally
[7]Lead contact
*Correspondence: wubin@ntu.edu.sg (B.W.), schlef@mpipz.mpg.de (P.S.-L.), chai@mpipz.mpg.de (J.C.)
https://doi.org/10.1016/j.cell.2022.04.032

SUMMARY

2′,3′-cAMP is a positional isomer of the well-established second messenger 3′,5′-cAMP, but little is known about the biology of this noncanonical cyclic nucleotide monophosphate (cNMP). Toll/interleukin-1 receptor (TIR) domains of nucleotide-binding leucine-rich repeat (NLR) immune receptors have the NADase function necessary but insufficient to activate plant immune responses. Here, we show that plant TIR proteins, besides being NADases, act as 2′,3′-cAMP/cGMP synthetases by hydrolyzing RNA/DNA. Structural data show that a TIR domain adopts distinct oligomers with mutually exclusive NADase and synthetase activity. Mutations specifically disrupting the synthetase activity abrogate TIR-mediated cell death in *Nicotiana benthamiana* (*Nb*), supporting an important role for these cNMPs in TIR signaling. Furthermore, the *Arabidopsis* negative regulator of TIR-NLR signaling, NUDT7, displays 2′,3′-cAMP/cGMP but not 3′,5′-cAMP/cGMP phosphodiesterase activity and suppresses cell death activity of TIRs in *Nb*. Our study identifies a family of 2′,3′-cAMP/cGMP synthetases and establishes a critical role for them in plant immune responses.

INTRODUCTION

2′,3′-cyclic adenosine monophosphate (2′,3′-cAMP) is a regioisomer of the canonical second messenger 3′,5′-cAMP, but little is known about the noncanonical cyclic nucleotide monophosphate (cNMP). It was not until recently that 2′,3′-cAMP was identified in animals (Ren et al., 2009) and in plants (Van Damme et al., 2014). The occurrence of 2′,3′-cAMP and other 2′,3′-cNMPs has now been shown in different kingdoms (Jackson, 2017). mRNA turnover by RNases can produce 2′,3′-cNMPs (Jackson, 2017). Studies in animals support a physiological role for 2′,3′-cNMPs in response to injury (Azarashvili et al., 2009; Jackson et al., 2014). In *Arabidopsis*, wounding (Van Damme et al., 2014), heat, and dark stress (Kosmacz et al., 2018) induce the accumulation of cellular 2′,3′-cAMP and 2′,3′-cyclic guanosine monophosphate (2′,3′-cGMP) (2′,3′-cAMP/cGMP, unless defined otherwise). 2′,3′-cAMP mediates stress granule (SG) formation (Kosmacz et al., 2018) and mimics the abiotic stress response in *Arabidopsis* (Chodasiewicz et al., 2022). The metabolization of 2′,3′-cNMPs to 2′-NMPs and 3′-NMPs has been demonstrated (Trapp et al., 1988; Genschik et al., 1997; Tyc et al., 1987), suggesting negative regulation of the noncanonical cNMPs.

Plant defense against microbial pathogens is built on a two-tiered immune system that consists of an interdependent pathogen-associated molecular pattern (PAMP)-triggered immunity (PTI) and effector-triggered immunity (ETI) (Ngou et al., 2021; Yuan et al., 2021). ETI is typically mediated by intracellular nucleotide-binding (NB) leucine-rich repeat (NLR) receptors, which recognize strain-specific pathogen effectors delivered inside plant cells. NLRs can be largely divided into two groups, with N-terminal coiled-coil (CC) or N-terminal Toll/interleukin-1 receptor (TIR) domains. Recognition of pathogen effectors induces oligomeric NLR complexes termed resistosomes (Xiong et al., 2020). Activation of NLR resistosomes induces ETI responses, often including a hypersensitive response (HR), a form of regulated cell death that is localized to sites of attempted pathogen infection. Whereas the CC-NLR (CNL) ZAR1 resistosome is a Ca^{2+}-permeable cation channel (Bi et al., 2021; Wang et al., 2019), the TIR-NLRs (TNLs) RPP1 and Roq1 resistosomes function as holoenzymes of TIR-encoded NADase (Horsefield et al., 2019; Ma et al.,

Please cite this article in press as: Yu et al., TIR domains of plant immune receptors are 2′,3′-cAMP/cGMP synthetases mediating cell death, Cell (2022), https://doi.org/10.1016/j.cell.2022.04.032

2020; Martin et al., 2020; Wan et al., 2019). The NADase activity is required for the activation of two immune signaling nodes, EDS1-SAG101 and EDS1-PAD4 heterodimers and the "helper" NLRs (RNLs), ADR1s, and NRG1s (Castel et al., 2019; Lapin et al., 2019; Peart et al., 2005; Qi et al., 2018; Wu et al., 2019). Once TNLs are activated, EDS1-PAD4 and EDS1-SAG101 form hetero complexes with ADR1s and NRG1s, respectively (Sun et al., 2021; Wu et al., 2021), inducing Ca^{2+}-channel activity of the RNLs (Jacob et al., 2021). ADR1 is also important for the defense responses of some CNLs (Bhandari et al., 2019; Bonardi et al., 2011; Castel et al., 2019; Venugopal et al., 2009; Wu et al., 2019). EDS1 signaling is also involved in abiotic stress responses of plants (Suzuki et al., 2012; Wiermer et al., 2005). In *Arabidopsis*, EDS1 signaling is negatively regulated by *AtNUDT7*, a nucleoside diphosphate-linked moiety X (Nudix) hydrolase, and its closest homolog *AtNUDT6* (Bartsch et al., 2006; Ge et al., 2007), although the underlying mechanism remains elusive.

In addition to canonical TNLs, plant genomes encode many TIR proteins consisting only of a TIR domain (TIR-only or TX) or TIR-NB (TN) (Collier et al., 2011; Gao et al., 2018; Meyers et al., 2002; Nandety et al., 2013; Nishimura et al., 2017). For example, the TIR-only protein RBA1 in *Arabidopsis* Ag-0 triggers EDS1-dependent immune signaling in response to the bacterial pathogen effector HopBA1 (Nishimura et al., 2017). Overexpression of several other TIR-only genes also induces EDS1-dependent signaling (Bayless and Nishimura, 2020; Meyers et al., 2002; Nandety et al., 2013; Nishimura et al., 2017; Santamaría et al., 2019; Staal et al., 2008; Zhao et al., 2015), indicating that TIR-containing members share a conserved signaling pathway to mediate immune responses. Cell death mediated by TIR-containing proteins depends on a conserved putative catalytic glutamate (Wan et al., 2019). TIR NADase activity is essential but not sufficient for cell death and defense activation (Duxbury et al., 2020; Horsefield et al., 2019; Wan et al., 2019), suggesting that additional signaling components are needed to fully activate TIR-mediated immune responses.

Here, we show that plant TIR domain proteins produce 2′,3′-cAMP/cGMP via hydrolysis of RNA and probably DNA (RNA/DNA unless defined otherwise). Nuclease activity was not sufficient for TIR-mediated cell death, as TIR mutants retaining both nuclease and NADase activity but lacking the 2′,3′-cAMP/cGMP synthetase (referred to synthetase hereafter) activity failed to trigger cell death in *Nicotiana benthamiana* (*Nb*). The structural basis of TIR proteins as bifunctional enzymes was revealed by cryoelectron microscopy (cryo-EM) structures of the double-stranded DNA (dsDNA)-bound TIR domain of flax TNL L7 ($L7^{TIR}$) that recognizes the flax rust fungus effector AvrL567 (Dodds et al., 2006). Specific disruption of the synthetase activity *in vitro* greatly suppressed TIR-mediated cell death in *Nb*, indicating that this enzymatic activity is required for TIR signaling. Moreover, *At*NUDT7 and the oomycete pathogen effector Avr3b function as 2′,3′-cAMP/cGMP phosphodiesterases (PDEs) *in vitro*. Furthermore, co-expression of wild-type (WT) *AtNUDT7*, but not its catalytic mutant, suppressed RBA1-mediated cell death in *Nb*. As Nudix hydrolases are highly conserved throughout all organisms (McLennan, 2006), our findings open opportunities for the study of 2′,3′-cNMPs beyond plants.

RESULTS

TIR proteins exhibit nuclease and 2′,3′-cAMP/cGMP synthetase activity *in vitro*

When assaying RBA1 NADase activity, we found that the TIR-only protein hydrolyzed many metabolites besides nicotinamide adenine dinucleotide in its oxidized form (NAD^+) (Figures S1A and S1B). All these *in vitro* RBA1 substrates contain phosphodiester bonds, prompting us to test if DNA and RNA are RBA1 substrates. The purified RBA1 protein exhibited activity of degrading PCR product (Figure 1A, left), plasmid DNA (Figure 1A, right) or *Arabidopsis* genomic DNA (gDNA) (Figure 1B). RBA1 displayed a much higher nuclease activity when *Arabidopsis* total RNA (*At*RNA) was used as the substrate (Figures 1A–1C, S1C, and S1D). The nuclease activity appears to be a general feature of TIR proteins, as several TIR proteins tested including $L7^{TIR}$ also displayed the activity of degrading *Arabidopsis* gDNA and total RNA (Figures 1B and 1C). Furthermore, RBA1 and several other TIR proteins exhibited clear cleavage activity toward a fluorescent DNA probe (Figure 1D). Unlike DNase I, TIR-catalyzed production of the fluorescent product appears not to obey Michaelis-Menten kinetics.

We then investigated whether the nuclease activity is associated with TIR-mediated cell death *in planta*. Cys132 of $L7^{TIR}$ is highly conserved among plant TIR proteins (Figure S1E) (Lapin et al., 2022; Johanndrees et al., 2021). The equivalent cysteine residue is important for cell death mediated by grape $RPV1^{TIR}$ (Williams et al., 2016) and $L6^{TIR}$ (Bernoux et al., 2011) in *N. tabacum* (*Nt*). The residue at this position is substituted with Thr in the bacterial *Acinetobacter baumannii* TIR (*Ab*TIR) (Figure S1E), which possesses NADase activity but has no cell death activity in *Nt* (Duxbury et al., 2020). These results suggest that the phenotype caused by mutation of the conserved cysteine residue in $L6^{TIR}$ and $RPV1^{TIR}$ *in planta* is probably not due to the absence of their NADase activity. Indeed, $L7^{TIR}$ C132A had little impact on the NADase activity of $L7^{TIR}$ (Figure S1F). Unexpectedly, however, the $L7^{TIR}$ mutant protein also retained nuclease activity comparable with that of the WT protein (Figure S1F). These results suggest that the nuclease activity, if important, is not sufficient for the cell death activity of TIRs *in planta*.

The data above suggest that there are unknown molecules generated by TIR-mediated degradation of RNA/DNA for the cell death activity. To probe this possibility, we analyzed products of *At*RNA or gDNA incubated with $L7^{TIR}$ using liquid chromatography-mass spectrometry (LC-MS). Incubation of $L7^{TIR}$ with *At*RNA or gDNA, but not $L7^{TIR}$, the RNA, or DNA alone, gave rise to two distinct peaks, one with a parent ion of 330 *m/z* (Figures 1E, 1F, S1G, and S1H) and the other 346 *m/z* (Figures 1G, 1H, S1G, and S1H), corresponding to the molecular weight of 3′,5′-cAMP and 3′,5′-cGMP, respectively. However, the retention time of these two unknown substances matches that of neither standard 3′,5′-cAMP nor standard 3′,5′-cGMP (Figures 1E, 1G, and S1G). LC-MS assays showed that the retention time of 330 and 346 *m/z* was identical to that of the standard 2′,3′-cAMP and 2′,3′-cGMP, respectively (Figures 1E, 1G, and S1G). The identities of the two unknown substances were further confirmed by multiple reaction monitoring (MRM) (Figures 1E

Please cite this article in press as: Yu et al., TIR domains of plant immune receptors are 2′,3′-cAMP/cGMP synthetases mediating cell death, Cell (2022), https://doi.org/10.1016/j.cell.2022.04.032

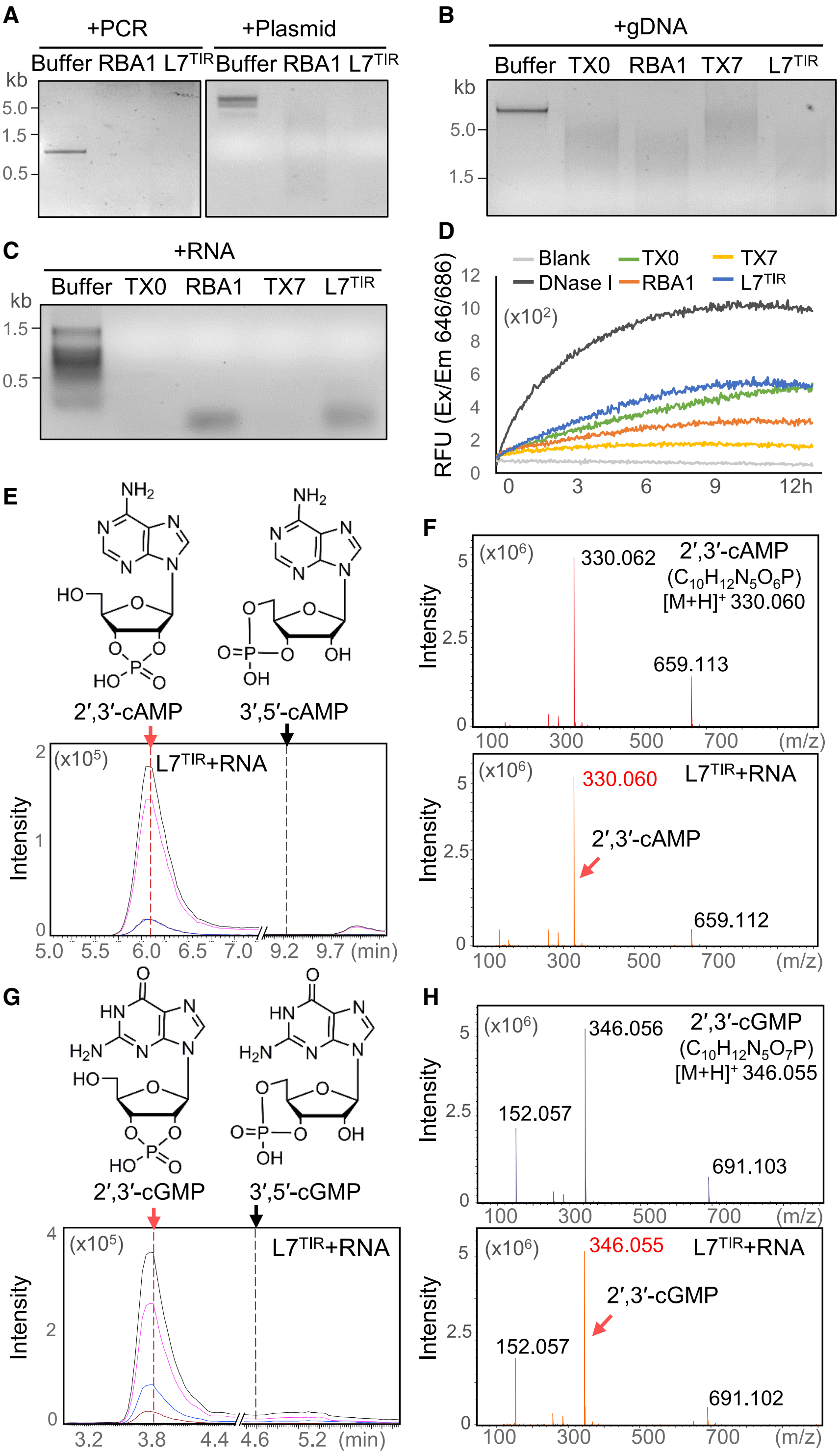

Figure 1. TIR proteins catalyze the production of 2′,3′-cAMP/cGMP using RNA/DNA as substrates

(A–C) TIRs have DNase and RNase activity *in vitro*. TIR proteins indicated were incubated with 100 ng PCR product (A, left), plasmid (A, right), *Arabidopsis* genomic DNA (gDNA) (B), and total RNA (C). After incubation at 25°C for 16 h, the reaction mixtures were visualized by agarose gel electrophoresis. L: DNA ladder (Thermo Scientific 11581625). Data are depicted as representative gels of three independent experiments.

(D) TIR proteins display DNase activity toward a fluorescent probe. The TIR proteins indicated were individually incubated with a fluorescent DNA probe. The fluorescent product yielded was meaured at 646/686 nm (extinction/emission). Data are depicted as a representative line graph of two independent experiments.

(E–H) L7^{TIR} has 2′,3′-cAMP/cGMP synthetase activity using RNA as the substrate. Top of (E) and (G): molecular structures of 2′,3′-cAMP/3′,5′-cAMP and 2′,3′-cGMP/3′,5′-cGMP, respectively. Bottom of (E) and (G): L7^{TIR} protein was incubated with *At*RNA at 25°C for 16 h, and the reaction products were analyzed by LC-MS in multiple reaction monitoring (MRM) mode. A representative chromatogram of MRM analyses is shown for 2′,3′-cAMP (E) and 2′,3′-cGMP (G). (F) and (H): comparison of the high-resolution MS spectra of the standard 2′,3′-cAMP (F) or 2′,3′-cGMP (H) and the L7^{TIR}-generated products. 2′,3′-cAMP theoretical $[M + H]^+$: 330.0597, standard $[M + H]^+$: 330.0615, assay product $[M + H]^+$: 330.0600. 2′,3′-cGMP theoretical $[M + H]^+$: 346.0547, standard $[M + H]^+$: 346.0558, assay product $[M + H]^+$: 346.0552. Data are depicted as a representative chromatograph of three independent experiments.

See also Figure S1.

and 1G) and high-resolution MS analyses (Figures 1F and 1H). Similar results were obtained with the products from RBA1 incubated with *At*RNA or gDNA as the substrate (Figure S1I). The synthetase activity of L7^{TIR} appears to be conserved among TIR proteins, as several *Arabidopsis* TIR proteins, including RBA1, produced these two cNMPs when *Arabidopsis* gDNA (Figure S1K) or *At*RNA (Figure S1L) was used as the substrate. As a control, fungal RNase T1, but not DNase I, showed similar activity in producing 2′,3′-cAMP/cGMP (Figure S1J). These data demonstrate that TIR domains act as synthetases with RNA/DNA as substrates.

Cryo-EM structure of L7^{TIR} bound by dsDNA

During protein purification, we found that several TIR proteins, including L7^{TIR}, were eluted at the void position of a Superose 6 gel filtration column, suggesting the formation of large “aggregates” of these TIR proteins. The aggregates appeared to contain nucleic acids as evidenced by UV absorbance at the wavelength of 260 nm (Figures S2A and S2B). Visualization of the negatively stained large molecular weight species

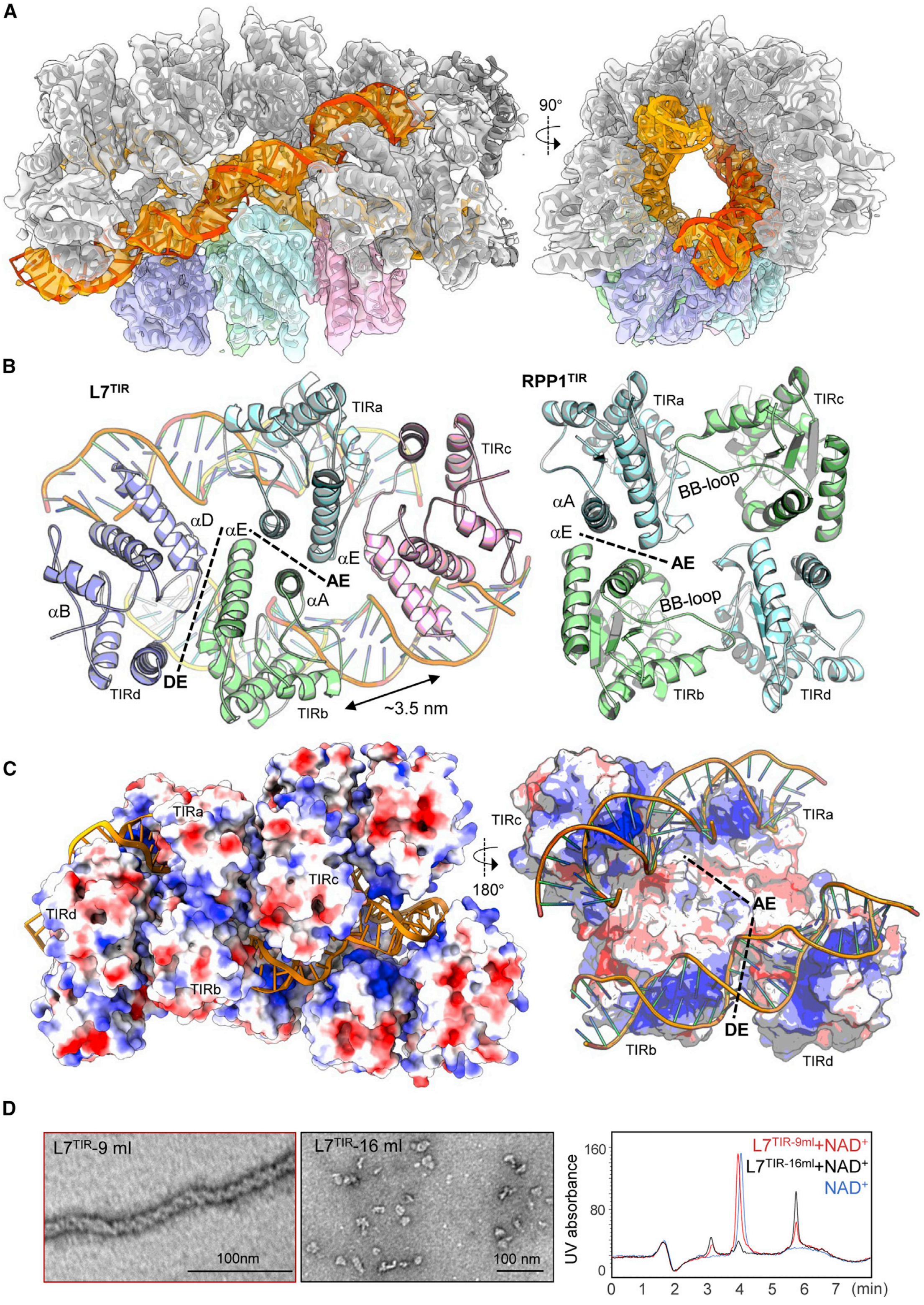

Figure 2. Cryo-EM structure of L7^{TIR} in the complex with dsDNA

(A) Different views of the final cryo-EM map of L7^{TIR} filaments at an initial dsDNA-binding state. The cryo-EM density of L7^{TIR} and dsDNA is shown in gray and orange/orange red, respectively.

(legend continued on next page)

Please cite this article in press as: Yu et al., TIR domains of plant immune receptors are 2′,3′-cAMP/cGMP synthetases mediating cell death, Cell (2022), https://doi.org/10.1016/j.cell.2022.04.032

revealed filament or filament-like structures (Figure S2A). Notably, the filaments formed by L7^{TIR} following the removal of the maltose-binding protein (MBP) tag were more uniform (Figure S2A). Then, we solved the cryo-EM structures of the L7^{TIR} filaments (Figures S2C–F), representing an initial dsDNA/dsRNA binding state, an intermediate state, and an end state of DNA/RNA hydrolysis, with a resolution of 3.3, 2.7, and 2.6 Å, respectively (Figures S2G–S2J; Table S1).

In the initial dsDNA/RNA binding state, the L7^{TIR} filament is composed of 4 protofilaments with the two outer ones being made of L7^{TIR} (Figure 2A). Sandwiched between the two L7^{TIR} protofilaments are two thinner protofilaments, which clearly come from dsDNA or dsRNA (Figure 2A), although the density does not allow a distinction. dsDNA was modeled to the helical-shaped density because it was more resistant to TIR degradation compared with RNA *in vitro* (Figures 1A, 1B, S1C, and S1D). Nonetheless, dsDNA cleavage can be found in part of the L7^{TIR}-dsDNA complex, as represented by the structures of the intermediate (~3 base pairs of dsDNA bound) and the end state (0–1 base pair of dsDNA bound) of L7^{TIR} filaments (Figures S2I–S2K). Interactions of the two L7^{TIR} protofilaments mediated by the two dsDNA protofilaments result in the formation of a superhelical structure (Figures 2A and S2N).

The L7^{TIR} protofilaments contain two types of symmetric homodimers. One is mediated by the interface involving helices αA and αE (AE interface) (Figure 2B) seen in the crystal structures of TIR domains (Bernoux et al., 2011; Horsefield et al., 2019; Williams et al., 2014, 2016; Zhang et al., 2017) and cryo-EM structures of TNL resistosomes (Ma et al., 2020; Martin et al., 2020). The functional significance of the AE interface is well established (Ma et al., 2020; Martin et al., 2020; Nimma et al., 2017). Propagation of the AE dimers through the interaction of two L7^{TIR} monomers of two adjacent AE dimers forms the second type of the L7^{TIR} dimer (Figure 2B) that is nearly identical to the dimer in the crystal structure of L6^{TIR} mediated by the interface involving helices αD and αE (DE interface) (Figure S2L). This interface is conserved in many TIR proteins and is required for their cell death activities (Nishimura et al., 2017; Zhang et al., 2017). The L7^{TIR} protofilaments are reminiscent of a structural model of the L6^{TIR} domain higher order assembly (Zhang et al., 2017). Parallel packing of the two AE dimers via the DE interface generates a tetrameric L7^{TIR}, which is different from the closed tetrameric TIR in the RPP1 resistosome (Figure 2B). Asymmetric L7^{TIR} dimers similar to those important for the NADase activity of the TNL resistosomes are absent in the tetrameric L7^{TIR}. Along each L7^{TIR} protofilament are two positively charged surfaces sandwiching two dsDNAs (Figure 2C). We cannot assign the sequence of the modeled dsDNA due to its limited quality of cryo-EM density. However, the L7^{TIR} makes no base-specific contacts with the dsDNA, indicating non-sequence-specific binding to dsDNA/dsRNA by L7^{TIR}. This is consistent with sequence-independent cleavage of *Arabidopsis* or barley total RNA *in vitro* (Figure S1C).

The formation of asymmetric TIR dimers is required for NADase activity of TNLs (Ma et al., 2020; Martin et al., 2020). The lack of such dimers suggests that L7^{TIR} in the filaments cannot hydrolyze NAD$^+$. This was confirmed by the NADase activity assay of the L7^{TIR} protein eluted at the void position in gel filtration (Figure 2D, left) with high-performance liquid chromatography (HPLC) (Figure 2D, right). By contrast, the L7^{TIR} protein at the position with lower molecular weight species (Figure 2D, middle) fully consumed NAD$^+$ under the same conditions. These results suggest that L7^{TIR} forms distinct oligomers for its synthetase and NADase activity.

Nucleic acid binding, AE and DE interfaces are important for synthetase activity of L7^{TIR}

The distance between two adjacent L7^{TIR} along the two outer protofilaments is ~3.5 nm (Figure 2B), close to the length of one turn of dsDNA (3.4 nm). This allows L7^{TIR} αD from one side of the outer protofilaments to periodically interact with the major groove of the dsDNA via electrostatic interaction (Figures 2A and 3A), which is characteristic of major groove binders of dsDNA (Eckel et al., 2003). A cluster of basic residues from αD is solvent exposed and largely conserved among TIR proteins (Figure S1E). Additionally, the loop connecting αB and βB (called the BB-loop) of L7^{TIR}, with different conformation from that of its equivalent of L6^{TIR} (Figure S3A), also contacts the backbones of dsDNA (Figure 3A). BB-loops are also critical to mediate the formation of asymmetric dimerization of RPP1^{TIR} (Ma et al., 2020) and Roq1^{TIR} (Martin et al., 2020). These results suggest that the BB-loop is likely important for both NADase and synthetase activity of TIR proteins. The AE interface in L7^{TIR} filaments is highly conserved in other TIRs (Figure S2L). As in the crystal structure of L6^{TIR} (Bernoux et al., 2011), the DE interface in the L7^{TIR} filaments is mainly mediated by van der Waals and hydrophobic contacts (Figure 3B). Hydrophobic residues are also conserved at this corresponding position in other TIRs (Figure S2L).

To investigate whether the dsDNA-αD interaction is important for the synthetase activity of L7^{TIR}, we made a simultaneous mutation K171A/K172A/R175A (KKR^{AAA}) for the basic residues from this helix. In contrast to WT L7^{TIR}, the KKR^{AAA} protein was eluted only at the position of the low molecular species in gel filtration (Figure 3C), indicating that the mutant has lost its filament-forming activity. Similar effects were also observed with K176A/K180A (KK^{AA}) and K100A/G101A/K102A/E103A

(B) Left: packing of L7^{TIR} protomers (in different colors) in the cryo-EM structure of (A). Dashed lines indicate L7^{TIR} dimerization interfaces. Right: packing of the four RPP1^{TIR} domains in the RPP1 resistosome (PDB: 7CRC).

(C) Different views of the cryo-EM structure of (A) are shown in surface representation, with electrostatic potential mapped to the surface. Left: overall structure of L7^{TIR} filaments shown in surface representation with electrostatic potential mapped to the surface. Right: longitudinal cut of the dsDNA-L7^{TIR} electrostatic interface.

(D) dsDNA-bound L7^{TIR} has little NADase activity. Left and middle: negative staining images of L7^{TIR} (tag free) eluted at 9 and 16 mL in Superose 6 gel filtration column, respectively. Right: NADase activity of L7^{TIR} protein eluted at different elution volumes. Horizontal axis: retention time of the samples (min). Vertical aixs: UV absorbance at 260 nm. Data are depicted as a representative chromatograph of three independent experiments.

See also Figure S2.

Please cite this article in press as: Yu et al., TIR domains of plant immune receptors are 2′,3′-cAMP/cGMP synthetases mediating cell death, Cell (2022), https://doi.org/10.1016/j.cell.2022.04.032

(KGKE^{AAAA}) mutations predicted to disrupt αD and BB-loop interactions with dsDNA, respectively (Figure 3C). Furthermore, KKR^{AAA} significantly diminished the activity of L7^{TIR} nuclease (Figures 3D and S3D) and synthetase (Figures 3E, S3B, and S3C). These basic residues are not involved in the formation of the AE dimer and the predicted asymmetric L7^{TIR} dimer. Indeed, the KKR^{AAA} mutation had little impact on the NADase activity of the TIR protein (Figure 3F).

Supporting an essential role of the DE interface in the filament-forming activity of L7^{TIR}, L7^{TIR} K200E at this interface (Figure 3B) was eluted only at the low molecular species position (Figure 3C). As expected, the mutation greatly reduced L7^{TIR} nuclease (Figures 3D and S3D) and synthetase (Figures 3E and S3C) activity but not its NADase activity (Figure 3F). By comparison, all three L7^{TIR} enzymatic activities were reduced by F79A/E209A (FE^{AA}) from the AE interface (Figures 3C–3F). Taken together, these data show that TIR oligomers mediated by different interface combinations confer synthetase or NADase activity.

TIR proteins generate no 2′,3′-cyclophosphate-terminated RNA oligonucleotides

In addition to 2′,3′-cNMPs, RNA cleavage by RNases also generates 2′,3′-cyclophosphate-terminated RNA oligonucleotides (Jackson, 2017). In fact, this type of RNA oligonucleotides generated by RNase T2 act as PAMPs recognized by Toll-like receptor 8 (TLR8) to stimulate innate immune responses in humans (Greulich et al., 2019; Ostendorf et al., 2020). We tested whether TIRs produce similar RNA oligonucleotides. LC-MS assay of *At*RNA incubated with L7^{TIR} showed that the products contained no chemical species with a molecular weight corresponding to 2′,3′-cAMP- or 2′,3′-cGMP-terminated RNA dinucleotides (Figure 4A). By contrast, fungal RNase T1, a guanine base-specific RNase (Yoshida, 2001), strongly promoted the production of compounds with molecular weights corresponding to 2′,3′-cGMP terminated UMP and 2′,3′-cGMP terminated CMP (UGp and CGp, respectively).

The cryo-EM structure of L7^{TIR} filaments in the end state revealed that the packing of the tetrameric TIR domains (Figure 2B, left) is similar to that in the initial and intermediate states (Figure S4A). Compared with the other two states, the end state displays less conformational heterogeneity, yielding the best resolution density (Figure S2H) that allowed us to build a detailed atomic model of the TIR domain (Figures 4B and S4B). No clear density for dsDNA is present in the end state, suggesting that nucleic acid hydrolysis is complete (Figure 4C). There is an extra density blob inside the predicted NAD$^+$-binding pocket of L7^{TIR} roughly the size of a single nucleotide (Figure 4C). Interestingly, the conformation of the BB-loop of L7^{TIR} is nearly identical to that of RUN1^{TIR} bound by NADP$^+$ and bis-Tris (Figure S4C). The quality of the density does not allow us to unambiguously determine the identity of the molecule bound in the pocket, but docking of nucleotides and nucleotide derivatives showed that a 2′,3′-cNMP (2′,3′-cAMP modeled) best fits the topology of the density (Figure 4D). The modeled 2′,3′-cAMP completely overlaps with bis-Tris bound in RUN1^{TIR} and is buried in that pocket (Figures 4D and S4C). By comparison, the active sites of RNase T1 (Ishikawa et al., 1996) and RNase MC1 (Numata et al., 2003) are largely solvent exposed, making it possible for them to bind an oligonucleotide for cyclization of the 3′-phosphate group (Figure 4E). The smaller size of the binding pocket of L7^{TIR} can only allow the binding of a mononucleotide for cyclization reaction.

2′,3′-cAMP/cGMP synthetase activity is required for TIR-mediated cell death

Next, we asked whether the synthetase activity is required for TIR signaling. Although the conserved Cys132 was dispensable for the NADase and nuclease activity of L7^{TIR} (Figure S1F), the equivalent residue is important for the cell death activity of L6^{TIR} (Bernoux et al., 2011) and RPV1^{TIR} (Williams et al., 2016) in *Nt*. These results suggest that this conserved residue may be specifically important for the synthetase activity of TIRs. Indeed, C132A abrogated much of L7^{TIR} synthetase activity (Figure S5A). Similarly, RBA1 C83A greatly impaired the synthetase activity (Figures 5A and S5B), but had no detectable effect on the NADase (Figure 5B) and a modest effect on the nuclease activity (Figure S5C) of RBA1. Like mutations of the equivalent residues of L6^{TIR} and RPV1^{TIR}, RBA1 C83A substantially suppressed the cell death activity of RBA1 in *Nb* (Figure 5C). Together, these results support an essential and conserved role of synthetase activity in TIR-mediated cell death, confirming the idea that nuclease activity is not sufficient for TIR-mediated cell death.

Like the mutation of basic residues in L7^{TIR} (Figures 3F–3H), a simultaneous mutation K122A/K123A/K130A (KKK^{AAA}) of the equivalent residues from αD in RBA1 nearly abrogated the synthetase (Figures 5A and S5C) and nuclease (Figure S5B) activities, however, only slightly affected the NADase (Figure 5B) activity of RBA1. By contrast, the catalytic mutation E86A resulted in the loss of these three enzymatic activities of RBA1 (Figures 5A, 5B, S5B, and S5C). We then employed RBA1 KKK^{AAA} to further confirm whether the synthetase activity is important for TIR-mediated cell death. The cell death phenotype by RBA1 in *Nb* was completely suppressed by the catalytic E86A mutation (Figures 5B and 5C), further confirming an essential role for the NADase activity in TIR signaling. Importantly, the cell death phenotype was similarly suppressed by the KKK^{AAA} mutation (Figure 5C). Together, these results support a critical and conserved role for the cluster of basic residues from αD in the cell death activity of TIRs.

We next investigated if TIR expression promotes the accumulation of 2′,3′-cAMP/cGMP *in planta*. Levels of these two non-canonical 2′,3′-cNMPs in *RBA1*-expressing *Nb* plants were assayed by LC-MS. Expression of WT *RBA1*, but not empty vector (EV) and catalytic mutant E86A, significantly enhanced accumulation of both 2′,3′-cAMP and 2′,3′-cGMP (Figures 5D and S5D). Similarly, KKK^{AAA} with reduced RBA1-mediated cell death also reduced the accumulation of 2′,3′-cAMP/cGMP. These results indicate that RBA1-mediated cell death in *Nb* is accompanied by increased 2′,3′-cAMP/cGMP levels.

*Ab*TIR has NADase activity (Essuman et al., 2018) but fails to induce cell death when expressed in *Nt* (Duxbury et al., 2020). The cluster of basic residues conserved in plant TIRs is not conserved in *Ab*TIR (Figure S1E), suggesting that *Ab*TIR lacks synthetase activity. Indeed, while *Ab*TIR had comparable NADase activity to L7^{TIR} as previously reported (Duxbury et al.,

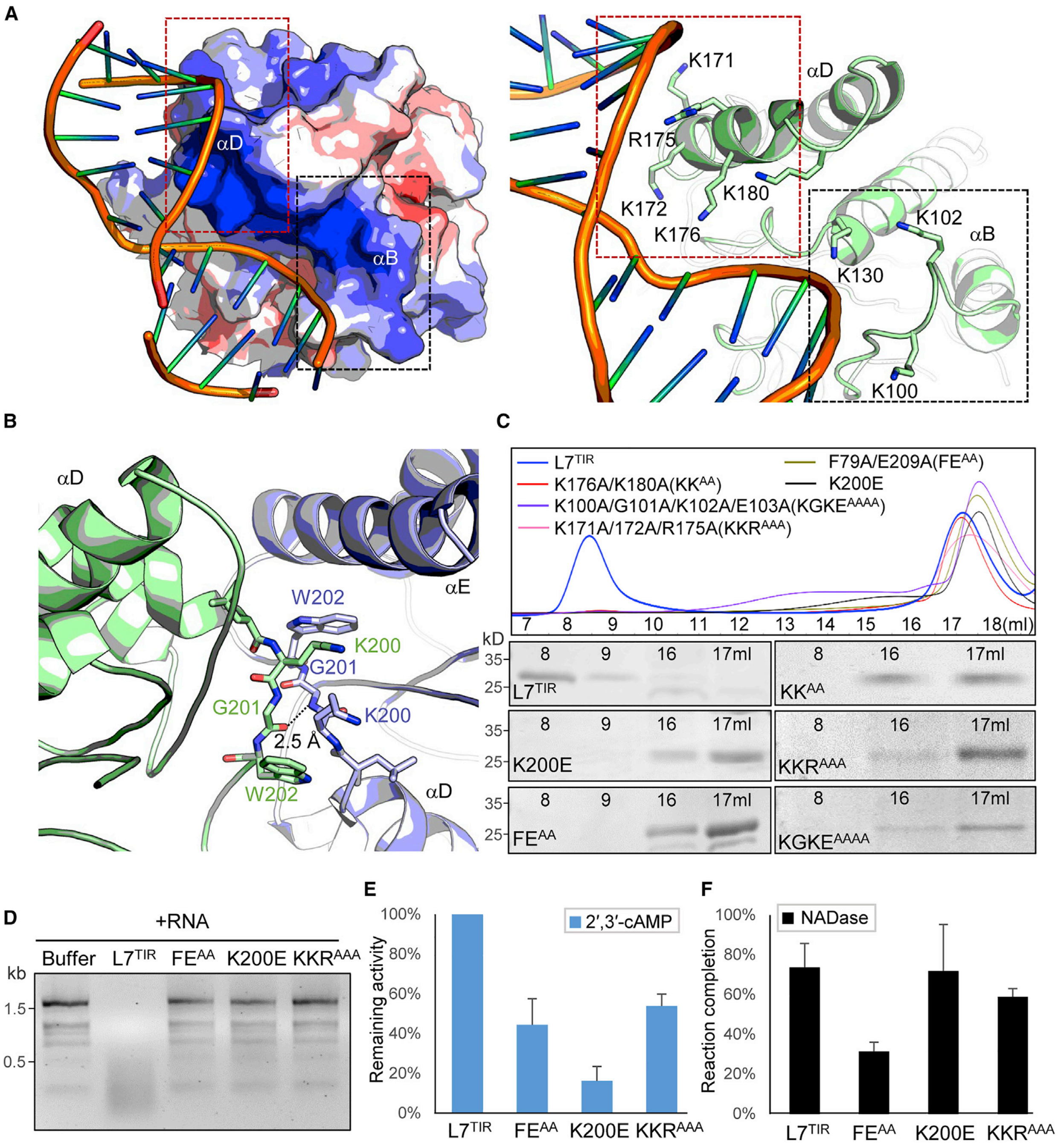

Figure 3. RNA/DNA binding and dimerization are required for 2′,3′-cAMP/cGMP synthetase activity of L7^{TIR}

(A) Left: a close-up view of the interaction between αD helix of L7^{TIR} and dsDNA. Right: detailed interactions of αD (red dashed frame) and the BB-loop (black dashed frame) with dsDNA.

(B) A close-up view of detailed interactions of the DE interface.

(C) Gel filtration analyses of WT and mutant L7^{TIR} proteins. Top and Bottom: gel filtration profiles and SDS-PAGE analyses of WT and mutant L7^{TIR} proteins, respectively. FE^{AA}, K200E, and KKR^{AAA} are from the AE, DE, and dsDNA binding interfaces of L7^{TIR} filaments, respectively.

(D–F) Effect of L7^{TIR} mutations on nuclease (D), 2′,3′-cAMP synthetase (E), and NADase (F) activity of L7^{TIR}. The assays for the nuclease and 2′,3′-cAMP synthetase activity were performed as described in Figures 1C and 1E, respectively. The remaining activity was calculated as (MS intensity [area] of each sample/MS intensity [area] of WT L7^{TIR})×100%. The 2′,3′-cAMP synthetase activity of WT L7^{TIR} was normalized to 100%. Reaction completion (%) of each sample was calculated as [concentration of unhydrolyzed NAD$^+$]/[concentration of NAD$^+$ before reaction]) × 100%. Data are depicted as the average peak intensity or a representative gel of three independent experiments.

See also Figure S3.

Please cite this article in press as: Yu et al., TIR domains of plant immune receptors are 2′,3′-cAMP/cGMP synthetases mediating cell death, Cell (2022), https://doi.org/10.1016/j.cell.2022.04.032

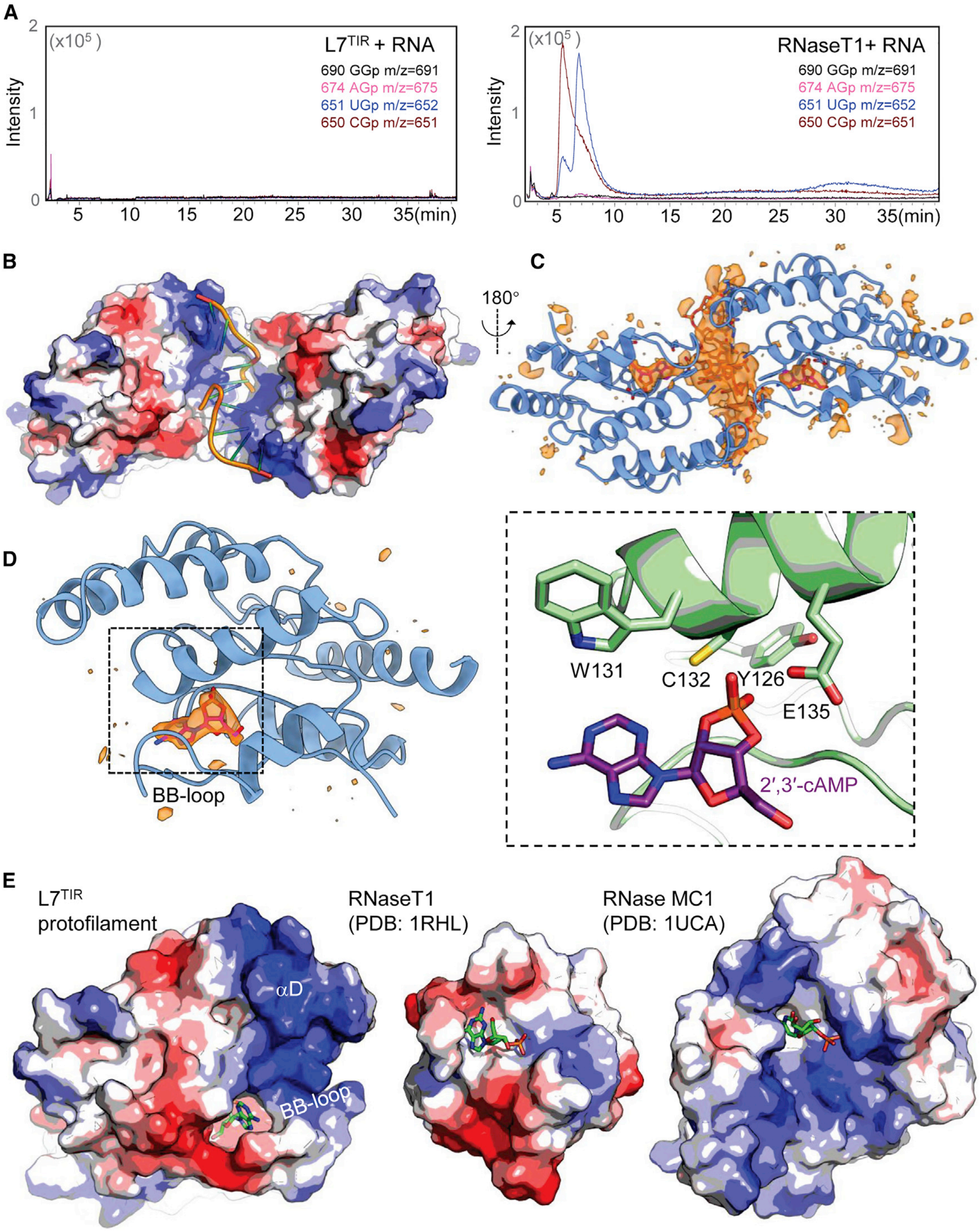

Figure 4. Hydrolysis of RNA by L7^{TIR} produces no 2′,3′-cyclophosphate-terminated RNA oligonucleotides

(A) Analysis of RNA hydrolyzed products by L7^{TIR} (left) and fungal RNase T1 (right) by LC-MS. *At*RNA was incubated with RNase T1 or L7^{TIR} and the reaction products were quantified by LC-MS. Data are depicted as a representative chromatograph of two independent experiments.

(B) The interaction of the distorted ssDNA (cartoon representation) with L7^{TIR} (surface representation, with electrostatic potential mapped to the surface).

(C) Cryo-EM density (orange) not accounted for by L7^{TIR} in the 3D reconstruction of L7^{TIR} filaments at the end state. One 2′,3′-cAMP was built into the NAD$^+$-binding pocket of each L7^{TIR}, to annotate two significant blobs of the difference in density.

(D) Left: cryo-EM density (orange) within the active site of L7^{TIR}. Right: detailed interactions of the modeled 2′,3′-cAMP with L7^{TIR}.

(E) Structural comparison of L7^{TIR} (left), RNase T1 (middle, PDB: 1RHL), and uridine base-specific RNase from bitter gourd, RNase MC1 (right, PDB: 1UCA). 2′,3′-cAMP bound by L7^{TIR} and 2′-GMP, 2′-UMP bound by RNase T1, RNase MC1 are shown in stick representation.

See also Figure S4.

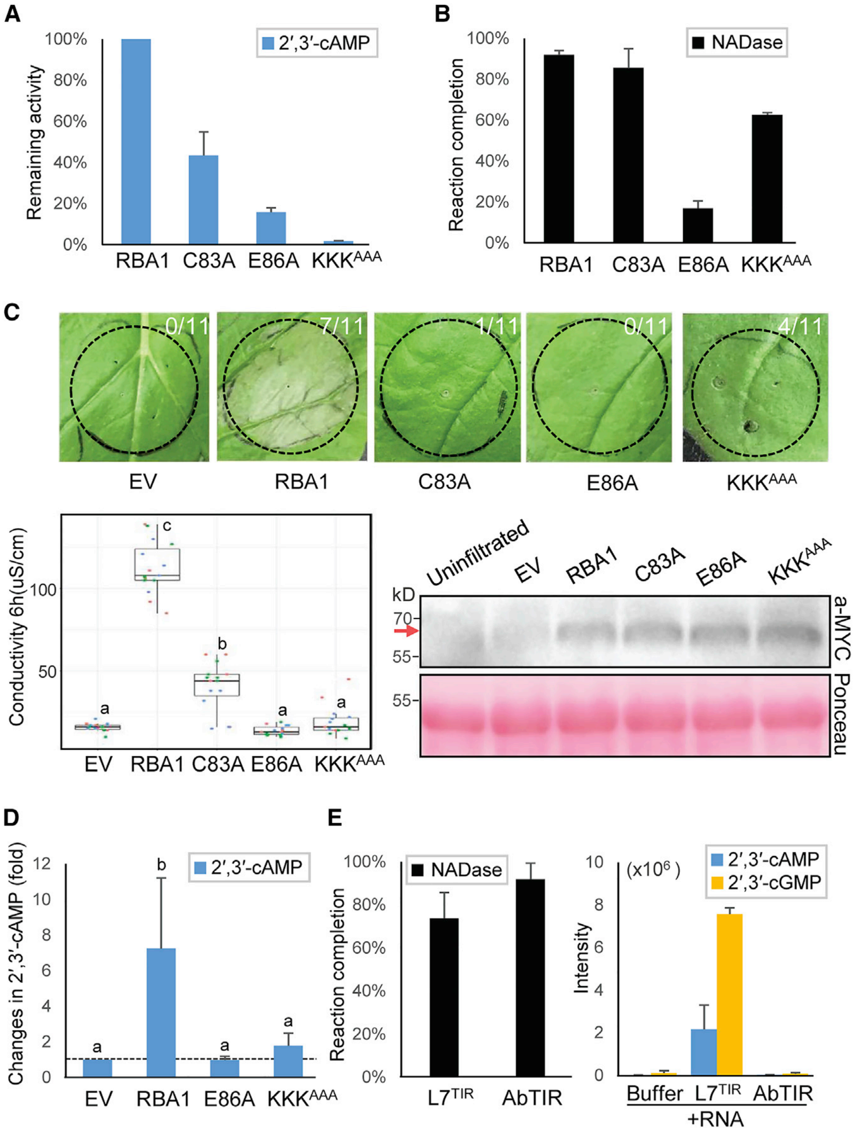

Figure 5. 2′,3′-cAMP/cGMP synthetase activity is required for RBA1-mediated cell death

(A and B) 2′,3′-cAMP synthetase (left) and NADase (right) activity of WT and mutant RBA1 proteins. Vertical axis: MS intensity (area) of 2′,3′-cAMP produced by mutant protein compared with WT RBA1 protein (A) and percentage of NAD$^+$ consumed (B). The 2′,3′-cAMP synthetase activity of WT RBA1 was normalized to 100%. The assays for 2′,3′-cAMP synthetase and NADase activity of different RBA1 proteins were performed as described in Figures 3E and 3F, respectively. Data are depicted as the average peak intensity of three independent experiments.

(C) Cell death phenotype of *Nb* plants transiently expressing WT and *RBA1* mutants. Top: cell death was visually assessed and photographed at 4 days post infection (dpi). The numbers in parentheses indicate the numbers of leaves displaying cell death out of the total number of leaves infiltrated. The representative images from a single replicate of three independent experiments are shown. Bottom left: cell death was quantified by the electrolyte leakage assay at 3 dpi. Colors indicate biological replicates. Significance was calculated with Tukey's HSD test (n = 15, α = 0.05; shared lowercase letters indicate no significant difference). Data are depicted as the average electrolyte leakage value of three independent experiments. Bottom right: protein blots for WT and *RBA1* mutants. Total protein was extracted from 2 dpi leaves and subjected to immunoblot using the indicated antibodies. Ponceau staining is shown to indicate loading. The red arrow points to the expected size of RBA1.

(D) 2′,3′-cAMP levels in *N. benthamiana* plants expressing WT and *RBA1* mutants. The leaf extract of *Nb* plants expressing the indicated constructs was analyzed by LC-MS. Vertical axis: MS intensity of 2′,3′-cAMP of each construct. Significance was calculated with Tukey's HSD test (n = 3, α = 0.05; shared lowercase letters indicate no significant difference). The level of 2′,3′-cAMP in *N. benthamiana* expressing EV was normalized to 1.0. Data are depicted as the average peak intensity of three independent experiments.

(E) *Ab*TIR has NADase but no detectable 2′,3′-cAMP/cGMP synthetase activity. NADase (left), 2′,3′-cAMP/cGMP synthetase activity (right) of L7^{TIR} and *Ab*TIR were performed as described in Figures 3F and 3E, respectively. Data are depicted as the average peak intensity of three independent experiments.

See also Figure S5.

2020), the bacterial TIR protein displayed no nuclease and synthetase activity (Figures 5E and S5E). These results may explain why *Ab*TIR has no cell death activity *in planta* and provide additional evidence for a critical role of synthetase activity in TIR-mediated cell death.

2′,3′-cAMP/cGMP PDEs inhibit TIR-mediated cell death

Our results support a crucial role of 2′,3′-cAMP/cGMP in TIR-mediated cell death. Conceivably, the intracellular homeostasis of these noncanonical cNMPs has to be maintained in the absence of biotic or abiotic stress conditions. Although *in vivo* substrates of *At*NUDT6 and *At*NUDT7 remain unknown, the catalytic residue Glu154 is required for *At*NUDT7 inhibition of EDS1 signaling (Ge et al., 2007). Therefore, we hypothesized that *At*NUDT7 acts as a 2′,3′-cAMP/cGMP PDE to negatively regulate EDS1-dependent signaling. HPLC analyses showed that purified *At*NUDT7 protein exhibited PDE activity toward 2′,3′-cAMP/cGMP but not 3′,5′-cAMP/cGMP (Figures 6A, S6A, and S6B). Furthermore, the substitution of the catalytic residue Glu154 with Gln abolished the PDE activity (Figures 6A and S6A). These results demonstrate that *At*NUDT7 acts as a 2′,3′-cAMP/cGMP PDE *in vitro*. Further supporting this

Please cite this article in press as: Yu et al., TIR domains of plant immune receptors are 2′,3′-cAMP/cGMP synthetases mediating cell death, Cell (2022), https://doi.org/10.1016/j.cell.2022.04.032

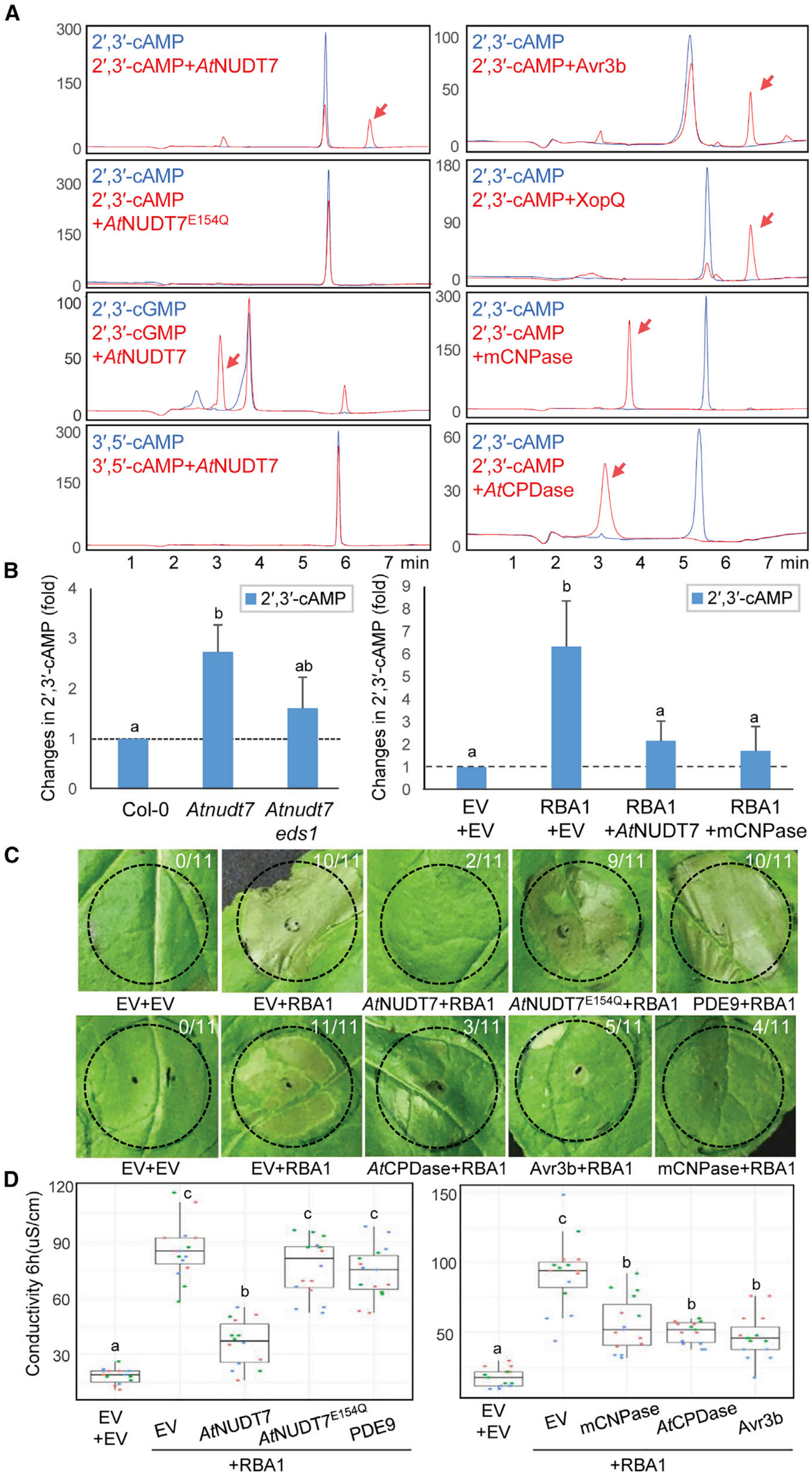

(legend on next page)

Please cite this article in press as: Yu et al., TIR domains of plant immune receptors are 2′,3′-cAMP/cGMP synthetases mediating cell death, Cell (2022), https://doi.org/10.1016/j.cell.2022.04.032

conclusion, the *At*NUDT7 protein hydrolyzed 2′,3′-cAMP/cGMP produced by L7^{TIR} but had no effect on L7^{TIR}-mediated degradation of *At*RNA (Figures S6A and S6C).

Next, we investigated if the 2′,3′-cAMP/cGMP PDE activity is required for *AtNUDT7* inhibition of EDS1 signaling. Supporting previous data (Bartsch et al., 2006; Ge et al., 2007), *Atnudt7 Arabidopsis* plants exhibited a stunted growth phenotype (Figure S6D). Quantification with LC-MS showed that levels of both 2′,3′-cAMP (Figure 6B, left) and 2′,3′-cGMP (Figure S6E, left) were markedly elevated in the *Atnudt7* plants as compared with those of WT plants, suggesting that the absence of *At*NUDT7 reduces hydrolysis of these cNMPs. Although not statistically significant, the levels of 2′, 3′-cAMP/cGMP in *Atnudt7 eds1* double-mutant plants appear to be higher than those of WT plants (Figures 6B and S6E), suggesting an EDS1-dependent and an EDS1-independent role in promoting the production of these cNMPs. These results support *At*NUDT7 as a 2′,3′-cAMP/cGMP PDE *in vivo* and reinforce our conclusion that synthetase activity is required for TIR-mediated and EDS1-dependent signaling.

We next assessed the effect of *AtNUDT7* on *RBA1*-mediated cell death in *Nb*. Co-expression with *AtNUDT7* strongly suppressed the cell death activity of *RBA1* (Figures 6C, 6D, and S6F). This suppressing activity of *AtNUDT7* was nearly abrogated by the catalytic mutation E154Q, indicating that *At*NUDT7 inhibition of RBA1-mediated cell death is dependent on 2′,3′-cAMP/cGMP PDE activity. In support of this conclusion, 2′,3′-cAMP/cGMP levels were significantly reduced in *Nb* expressing *RBA1* and *AtNUDT7* compared with *Nb* expressing *RBA1* and EV (Figures 6B, right and S6E, right). By contrast, co-expression with 3′,5′-cGMP-specific *PDE9* (Hanna et al., 2012) had little effect on RBA1-mediated cell death (Figures 6C, 6D, and S6F). Taken together, these data indicate that *At*NUDT7 suppresses RBA1-mediated cell death by acting as a 2′,3′-cAMP/cGMP PDE.

We then asked whether 2′,3′-cNMP PDEs can generally inhibit RBA1-mediated cell death. 2′,3′-cyclic-nucleotide 3′-PDE (CNPase) is an animal enzyme that hydrolyzes 2′,3′-cNMPs to their respective 2′-nucleotides (Myllykoski et al., 2016). The enzymatic activity of mouse CNPase (mCNPase) was confirmed by HPLC (Figures 6A and S6A). Like *At*NUDT7, mCNPase had no activity of hydrolyzing 3′,5′-cAMP/cGMP *in vitro* (Figures S6A and S6B). Co-expression with *mCNPase* in *Nb* greatly compromised RBA1-mediated cell death (Figures 6C, 6D, and S6F). Similar observations were made with an *Arabidopsis* 2′,3′-cyclic PDE (*At*CPDase) (Figures 6A, 6C, 6D, S6A, S6B, and S6F).

Our data above show that Nudix hydrolases can act as 2′,3′-cAMP/cGMP PDEs to suppress EDS1 signaling. Nudix hydrolases are present in many pathogens (Dong and Wang, 2016) and some Nudix effectors like *Xanthomonas euvesicatoria* XopQ (Adlung and Bonas, 2017) and *Phytophthora sojae* Avr3b (Kong et al., 2015) are critical for pathogen virulence activity, suggesting that these two effectors may have 2′,3′-cAMP/cGMP PDE activity. Assays by HPLC showed that purified XopQ and Avr3b displayed activity to hydrolyze 2′,3′- but not 3′,5′-cAMP/cGMP (Figures 6A, S6A, and S6B). Furthermore, co-expression with *Avr3b* compromised RBA1-mediated cell death in *Nb* (Figures 6C, 6D, and S6F). A similar experiment was not performed for XopQ because the effector is recognized by the endogenous *Nb* TNL Roq1 (Schultink et al., 2017). Nonetheless, these results support pathogen-mediated negative regulation of 2′,3′-cAMP/cGMP-induced signaling by PDEs. The metabolization of 2′,3′-cAMP/cGMP by XopQ also provides an explanation for XopQ-mediated inhibition of EDS1-dependent cell death in *Nicotiana* species (Adlung and Bonas, 2017).

Model on the role of 2′,3′-cAMP/cGMP in TIR signaling

Next, we asked whether upregulation of 2′,3′-cAMP/cGMP promotes RBA1 cell death activity. Treatment of *Nb* plants with 8-Br-2′,3′-cAMP, a cell-permeable analog of 2′,3′-cAMP, had no effect on the cell death activity of RBA1, likely because the analog is unable to mimic all functions of 2′,3′-cAMP in plants and/or both 2′,3′-cAMP and 2′,3′-cGMP are needed to promote RBA1 signaling. We then tested if HopBA1-induced cell death in *Arabidopsis* Ag-0 is accompanied by increased levels of 2′,3′-cAMP/cGMP. Supporting a previous study, delivery of HopBA1 by *Pseudomonas fluorescens* Pf0-1 in leaves induced visible cell death in *Arabidopsis* Ag-0 48 h post infection (hpi) (Figure S7A). 2′,3′-cAMP/cGMP levels in these plants were higher than those in EV carrying Pf0-1 infiltrated plants (Figure 7A). Together with previous data (Nishimura et al., 2017), these results indicate a positive correlation between 2′,3′-cAMP/cGMP levels and RBA1-mediated immune signaling.

Figure 6. 2′,3′-cAMP/cGMP PDEs suppress RBA1-mediated cell death

(A) Hydrolysis of 2′,3′-cAMP/cGMP by the indicated proteins. Peaks from the absorbance of the hydrolyzed products of 2′,3′-cAMP/cGMP are indicated by red arrows. Vertical axis: UV absorbance at 260 nm. Data are depicted as a representative chromatograph of three independent experiments.

(B) 2′,3′-cAMP/cGMP PDEs reduce the levels of 2′,3′-cAMP *in planta*. Left: *Atnudt7* displays a higher level of 2′,3′-cAMP than WT plants. Leaf extract of the indicated 4-week-old *Arabidopsis* plants was analyzed by LC-MS as described in Figure 5D. The level of 2′,3′-cAMP in *Arabidopsis* Col-0 was normalized to 1.0. Right: expression of 2′,3′-cAMP/cGMP PDEs reduces the 2′,3′-cAMP levels of *Nb* plants expressing *RBA1*. Empty vector (EV) or constructs indicated were co-expressed with *RBA1* in *Nb* plants and leaf extract was analyzed by LC-MS as described in Figure 5D. The level of 2′,3′-cAMP in *Nb* expressing EV+EV was normalized to 1.0. For quantification, internal standard 8-Br-2′,3′-cAMP was used. Significance was calculated with Tukey's HSD test ($n = 3$, $\alpha = 0.05$; shared lowercase letters indicate no significant difference). Data are depicted as the average peak intensity of three independent experiments.

(C) Co-expression with *AtNUDT7* (top) or other 2′,3′-cAMP/cGMP PDEs (bottom) suppress RBA1-mediated cell death in *Nb*. EV or indicated constructs were co-expressed with *RBA1* in *Nb* plants. Cell death was visually assessed and photographed at 4 dpi. The assays were performed as described in Figure 5C. Representative images from a single replicate of three independent experiments are shown.

(D) Electrolyte leakage assay of *Nb* plants transiently co-expressing *RBA1* with various constructs indicated. The assays were performed as described in Figure 5C. Colors indicate biological replicates. Significance was calculated with Tukey's HSD test ($n = 15$, $\alpha = 0.05$; shared lowercase letters indicate no significant difference). Data are depicted as the average electrolyte leakage value of three independent experiments.

See also Figure S6.

Please cite this article in press as: Yu et al., TIR domains of plant immune receptors are 2′,3′-cAMP/cGMP synthetases mediating cell death, Cell (2022), https://doi.org/10.1016/j.cell.2022.04.032

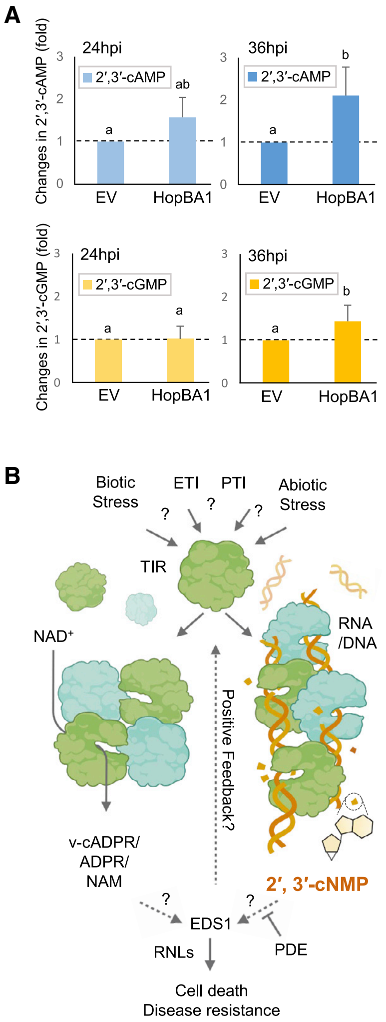

Figure 7. Working model of TIR-mediated signaling

(A) 2′,3′-cAMP (top) and 2′,3′-cGMP (bottom) levels are enhanced by HopBA1 in *Arabidopsis* Ag-0 plants. Pf0-1 carrying HopBA1 was infiltrated into *Arabidopsis* accession Ag-0. Leaf extract was analyzed by LC-MS at 24 hpi (left) and 36 hpi (right). Significance was calculated with Tukey's HSD test ($n = 3$, $\alpha = 0.05$; shared lowercase letters indicate no significant difference). The levels of 2′,3′-cAMP/cGMP extracted from EV carrying Pf0-1 infiltrated leaves at each time point were normalized to 1.0. Data are depicted as the average peak intensity of three independent experiments.

(B) Model on signaling mechanism of 2′,3′-cAMP/cGMP. In response to different stimuli, TIR proteins can form oligomers for NADase and 2′,3′-cAMP/cGMP synthetase activity. Products such as variant of cyclic ADP-ribose (v-cADPR) from the NADase activity and 2′,3′-cAMP/cGMP might act cooperatively to trigger the initiation of EDS1-dependent immune signaling.

See also Figure S7.

Our results suggest that the production of 2′,3′-cNMPs by TIRs is upstream of EDS1. Unexpectedly, however, expression of *RBA1* in *eds1* mutants of *Nb* induced no pronounced accumulation of 2′,3′-cAMP/cGMP (Figure S7B). This is consistent with the observation that 2′,3′-cAMP/cGMP levels in *Atnudt7 eds1* plants were comparable with those of WT *Arabidopsis* (Figures 6B and S6E). However, downregulation of these two cNMPs by 2′,3′-cAMP/cGMP PDEs greatly compromised EDS1-dependent immune signaling in *Nb* (Figures 6C and 6D). A model reconciling these data is positive feedback between TIR-catalyzed 2′,3′-cAMP/cGMP and EDS1, which is negatively regulated by 2′,3′-cAMP/cGMP PDEs (Figure 7B). The model agrees with the observation that the strength of TIR-mediated HR-like cell death is strongly correlated with protein levels (Zhang et al., 2004). Since TIR signaling is activated during PTI (Pruitt et al., 2021; Roth et al., 2017; Tian et al., 2021), this model may also explain why PTI activation potentiates HR cell death in transgenic *Arabidopsis* plants expressing AvrRps4 (Ngou et al., 2020) and flg22 enhances HR-like cell death mediated by *At*TN3 in *Nb* (Nandety et al., 2013). Thus, 2′,3′-cAMP/cGMP-promoted EDS1 signaling appears to involve a self-amplification mechanism.

DISCUSSION

Enzymes engaging in the specific production of 2′,3′-cNMPs remained unidentified. Here, we provide evidence that plant TIR proteins are bifunctional enzymes with both NADase and synthetase activity. TIR mutants lacking either enzymatic activity lost their cell death activity, indicating that the dual enzymatic activity is important for TIR function. Furthermore, downregulation of 2′,3′-cAMP/cGMP levels by 2′,3′-cyclic PDEs from different origins suppressed TIR-mediated cell death; conversely, upregulation of 2′,3′-cAMP/cGMP in *Atnudt7* plants or the delivery of HopBA1 into RBA1-containing host cells was associated with cell death. These results collectively support an important role for the synthetase activity in TIR-mediated immune signaling. This study not only identified an enzyme family for the production of 2′,3′-cNMPs but also established an essential role for them in mediating EDS1-dependent signaling.

Catalytic mechanism of TIR

Both DNA and RNA were hydrolyzed by TIR proteins to produce 2′,3′-cAMP/cGMP *in vitro*, but whether DNA, RNA, or both are substrates of TIR synthetases remains unknown. *In vitro*, RNA appears to be a much more favorable substrate. It is rather surprising that DNA acts as a substrate for 2′,3′-cAMP/cGMP production since it does not have a 2′-hydroxyl group. The mechanism of TIR-catalyzed 2′,3′-cNMPs remains undefined, but our data (Figures 4B, S1F, and S5A) suggest a two-step mechanism for their production: RNA/DNA cleavage could result in the flipping and binding of a nucleotide to the catalytic site of TIRs for the cyclization reaction. Consistently, a patch of density in the catalytic pocket of the intermediate state appears to come from a flipped nucleotide (Figure S2K). This model would explain why ATP and guanosine triphosphate (GTP) were not substrates of TIRs to produce 2′,3′-cAMP/cGMP (Figure S7C). Thus, plant TIRs are different from human DNase/RNase endonuclease G that directly cleaves RNA/DNA for apoptotic cell death (Cregan et al., 2004). However, we cannot exclude a role of TIR nuclease activity in other processes than plant cell death.

Mechanism of TIR proteins as bifunctional enzymes

In contrast to canonical bifunctional enzymes that generally harbor two structural domains with separate catalytic sites (Moore, 2004), the dual enzymatic activity of TIR proteins is

Please cite this article in press as: Yu et al., TIR domains of plant immune receptors are 2′,3′-cAMP/cGMP synthetases mediating cell death, Cell (2022), https://doi.org/10.1016/j.cell.2022.04.032

encoded by the same structural domain. TIRs form different oligomers for their NADase and synthetase activities (Figures 2B and 2D). In addition to the AE and DE interfaces, RNA/DNA substrates clearly have an important role in forming TIR oligomers for synthetase activity, because mutations predicted to disrupt DNA binding activity resulted in the loss of the enzymatic activity (Figures 3D and 3E).

The formation of the L7^{TIR}-dsDNA complex is mediated by both AE and DE interfaces (Figure 2B), revealing the mechanism underlying the simultaneous requirement of the two interfaces for TIR functions (Nishimura et al., 2017; Williams et al., 2016; Zhang et al., 2017). Although the AE interface is highly conserved among TIRs, variations exist in the DE interface. These variations, as seen in the crystal structure of RPP1^{TIR}, allow no propagation of the DE and AE interfaces to form a filament-like structure (Zhang et al., 2017). However, the RPP1^{TIR} protein was active in producing 2′,3′-cAMP/cGMP albeit with lower activity (Figure S7D), suggesting that filament formation is not absolutely required for the synthetase activity. This can be explained by the observation that a L7^{TIR} tetramer mediated by the AE and DE interfaces is sufficient for binding one complete turn of dsDNA/dsRNA (Figure 3A). The tetramer is incompatible with the tetrameric TIR that is important for the NADase activity (Ma et al., 2020; Martin et al., 2020), suggesting that synthetase and NADase activity are exclusive in a given oligomeric TIR. Consistent with this conclusion, the L7^{TIR}-dsDNA complex had little NADase activity (Figure 2D). NADase activity of TIR domain proteins from different kingdoms has been demonstrated (Essuman et al., 2018; Horsefield et al., 2019; Wan et al., 2019; Ofir et al., 2021). Our data with *Ab*TIR could be a hint that TIR synthetase activity did not evolve universally in all kingdoms.

2′,3′-cNMPs-promoted self-amplification of EDS1 signaling

Both synthetase and NADase activities are essential for RBA1-mediated HR cell death in *Nb* but whether and how the two activities interact remain unknown. Triggering initiation of TIR immune signaling may require the dual enzymatic activity. Once initiated, TIR signaling can promote the production of 2′,3′-cNMPs, which in turn further amplify TIR signaling. Initiation of EDS1 signaling may cause alterations, for example, in structures and/or stability of DNA/RNA, which allow a TIR protein to access the otherwise poor substrates. This model agrees with the observations that some TNLs require nuclear localization (Wirthmueller et al., 2007; Zhu et al., 2010) for function and NLR activation induces EDS1-dependent DNA damage (Rodriguez et al., 2018). Furthermore, cytosolic or membrane localization has been reported for other TIRs (Nandety et al., 2013; Roth et al., 2017; Nishimura et al., 2017). Thus, different cellular localization may enable TIRs to guard the integrity of RNA/DNA. This would provide an explanation of how TIR-only proteins sense the presence of pathogen effectors despite the lack of the pathogen-sensing leucine-rich repeat (LRR) as demonstrated in both CNLs and TNLs (Ma et al., 2020; Martin et al., 2020). Clearly, more studies, including the identification of predicted 2′,3′-cAMP/cGMP receptors, are needed to unveil the signaling mechanism of these noncanonical cNMPs. These studies may also aid to determine whether these cNMPs act as second messengers or not.

Negative regulation of 2′,3′-cAMP/cGMP levels

Although several small molecules were shown to be substrates of *At*NUDT7 *in vitro*, changes in their levels were not detected in *Atnudt7* mutant plants (Ge et al., 2007). Accumulation of 2′,3′-cAMP (Figure 6B, left) and 2′,3′-cGMP (Figure S6E, left) were strongly enhanced in *Atnudt7* leaves, supporting the role of these two cNMPs in immune signaling. However, the phenotypes of *Atnudt7-1* plants are largely abolished under conditions of reduced stress (Straus et al., 2010), suggesting that 2′,3′-cNMPs alone are insufficient for EDS1 activation. This is consistent with the idea that both 2′,3′-cNMP synthetase and NADase activities are required for TIR-mediated signaling. Notably, the Nudix effector XopQ and Avr3b also exhibited 2′,3′- but not 3′,5′-cAMP/cGMP PDE activity *in vitro*, with the latter effector suppressing RBA1-mediated cell death in *Nb* (Figures 6C and 6D). These results suggest that pathogens have evolved strategies for targeting 2′,3′-cAMP/cGMP-induced signaling to defeat plant immunity.

Nudix hydrolases belong to a highly conserved family of enzymes across all organisms and have broad substrate specificities (McLennan, 2006). Our finding that *At*NUDT7, XopQ, and Avr3b act as 2′,3′-cAMP/cGMP PDEs opens opportunities for investigations of this enzyme family and the two noncanonical cNMPs beyond plants. In addition to Nudix hydrolases, plant 2′,3′-AMP/cGMP PDEs were also found in *Triticum aestivum* germ and shown to possess the ability to hydrolyze 2′,3′-cNMPs into 2′-NMPs (Tyc et al., 1987). Two homologs of this group of PDEs are present in *Arabidopsis*. Biochemical data showed that *At*4g18930 has similar enzymatic activity (Genschik et al., 1997). It will be of interest to know whether these non-Nudix 2′,3′-cAMP/cGMP PDEs have a role in regulating EDS1-dependent signaling. Given the diversity of TIR and Nudix hydrolase-encoding gene families in plant genomes, the accumulation of these non-canonical cNMPs might be differentially regulated in other plant organs and tissues.

Multiple potential functions of 2′,3′-cAMP/cGMP

The accumulation of RBA1 is induced by HopBA1 and broadly correlated with HR cell death triggered by canonical NLRs (Nishimura et al., 2017), including the role of RBA1 in immune signaling mediated by the CNL ZAR1 (Martel et al., 2020). Consistent with a contribution of TIRs in CNL-mediated ETI, more recent data revealed a direct functional link between *At*TN13 and RPS5 in *Arabidopsis* (Cai et al., 2021). These results agree with gene expression profiling analysis revealing biotic stress-induced expression of TIR-only and TN genes (Nandety et al., 2013). In addition to ETI, accumulating evidence supports the role of TIR signaling in PTI responses (Pruitt et al., 2021; Roth et al., 2017; Tian et al., 2021). Consistently, EDS1-dependent signaling is required for basal resistance to virulent pathogens (Bonardi et al., 2011; Rietz et al., 2011). These results suggest a broad role for TIR signaling in ETI and PTI responses. The role of 2′,3′-cAMP/cGMP in plant abiotic stresses was supported by recent data (Van Damme et al., 2014; Kosmacz et al., 2018). Moreover, 2′,3′-cAMP mediates SG formation (Kosmacz et al., 2018),

Please cite this article in press as: Yu et al., TIR domains of plant immune receptors are 2′,3′-cAMP/cGMP synthetases mediating cell death, Cell (2022), https://doi.org/10.1016/j.cell.2022.04.032

which mimics the abiotic response in *Arabidopsis* (Chodasiewicz et al., 2022). Interestingly, *AtNUDT7* is one of the most induced genes in response to 2′,3′-cAMP (Chodasiewicz et al., 2022). *AtNUDT7* transcripts are responsive to numerous abiotic and biotic stress conditions (Straus et al., 2010), suggesting a broad role for *AtNUDT7* and possibly 2′,3′-cAMP/cGMP in the regulation of plant stress responses. However, it remains unknown whether TIR signaling is directly involved in abiotic stress responses induced by 2′,3′-cAMP in plants. Future investigations are needed to determine whether and how 2′,3′-cNMPs are involved in the interplay between PTI and ETI, TNL- and CNL-triggered, and abiotic/biotic stress responses. Answering these questions may provide new signaling paradigms for stress biology.

Limitations of the study

In this study, we show that plant TIR proteins act as synthetases with RNA/DNA serving as substrates and provide evidence for the role of the two noncanonical cNMPs in TIR-mediated cell death. Thus, TIR proteins are bifunctional enzymes with NADase and 2′,3′-cAMP/cGMP synthetase activities. We propose that products such as the previously identified v-cADPR from the NADase activity and 2′,3′-cAMP/cGMP act cooperatively to trigger the initiation of TIR-dependent immune signaling, but the underlying mechanism remains unknown. In the future, identification and characterization of 2′,3′-cAMP/cGMP targets will reveal whether the two mutually exclusive TIR enzyme activities converge on the same or act on different host targets. Finally, chemical synthesis of the cell-permeable prodrug analogs that can be hydrolyzed to 2′,3′-cAMP/cGMP in plant cells will be useful to provide further evidence for their biological function and to explore a broader role of these cNMPs in plant stress biology.

STAR★METHODS

Detailed methods are provided in the online version of this paper and include the following:

- KEY RESOURCES TABLE
- RESOURCE AVAILABILITY
    - Lead contact
    - Materials availability
    - Data and code availability
- EXPERIMENTAL MODEL AND SUBJECT DETAILS
    - Bacteria strain
    - Insect cell line
    - Plant materials
- METHOD DETAILS
    - Recombinant protein expression and purification
    - *In vitro* NADase assay
    - Site-directed mutagenesis
    - *In vitro* nuclease activity assay
    - *In vitro* 2′,3′-cNMP PDE activity assay
    - Production and detection of 2′,3′-cNMP *in vitro*
    - Negative-stain electron microscopy
    - Cryo-EM sample preparation and data collection
    - Cryo-EM data processing
    - Model building
    - Protein expression in *N. benthamiana* and western blot analysis
    - Cell death quantification in *N. benthamiana*
    - HopBA delivery assay
    - *In vivo* 2′,3′-cNMP extraction and detection
    - Metabolite measurement by LC-MS/MS
- QUANTIFICATION AND STATISTICAL ANALYSIS

SUPPLEMENTAL INFORMATION

Supplemental information can be found online at https://doi.org/10.1016/j.cell.2022.04.032.

ACKNOWLEDGMENTS

We thank Jian Shi, Yue Sun, and Xiaoxiao Zhang for their advice and help with the cryo-EM data collection; Jane E. Parker's lab for their *Nb epss* quadruple mutant, *Arabidopsis Atnudt7*, and *Atnudt7 eds1* mutant seeds; Ruben Garrido Oter, Frederickson Entila, and Yuang Wu for their advice with statistical analysis; Sabine Metzger for her help on the 2′,3′-cAMP and 2′,3′-cGMP confirmation of standard and assays; Ulla Neumann for her advice and help with the negative staining EM. We acknowledge the Tsinghua University Branch of the China National Center for Protein Sciences (Beijing) and the National University of Singapore for providing the cryo-EM facility support and the computational facility support on the cluster of Bio-Computing Platform; the Biocenter, University of Cologne, for providing MS facilities; and the greenhouse facility of the Max Planck Institute for Plant Breeding Research for providing *Nb* plants. This work was supported by the Alexander von Humboldt Foundation (a Humboldt professorship to J.C.), the Max-Planck-Gesellschaft (a Max Planck fellowship to J.C.), the Deutsche Forschungsgemeinschaft SFB-1403-414786233 (J.C. and P.S.-L.), Germany's Excellence Strategy CEPLAS (EXC-2048/1, project 390686111) (J.C. and P.S.-L.), and the Ministry of Health – Singapore, NMRC-OFIRG grant (MOH-000382-00 to B.W.).

AUTHOR CONTRIBUTIONS

Conceptualization, J.C., P.S.-L., D.Y., and W.S.; formal analysis, B.W., E.Y.J.T., and C.X.; investigation, D.Y., W.S., L.L., Y.C., J.J., E. Li, E. Logemann, S.H., A.J., X.C., and Z.H.; writing, J.C., D.Y., and P.S.-L. with input from all the authors; resources, J.C., P.S.-L., and B.W.; funding acquisition, J.C., P.S.-L., and B.W.; supervision, J.C. and P.S.-L.

Received: November 8, 2021
Revised: March 8, 2022
Accepted: April 26, 2022
Published: May 20, 2022

REFERENCES

Adlung, N., and Bonas, U. (2017). Dissecting virulence function from recognition: cell death suppression in Nicotiana benthamiana by XopQ/HopQ1-family effectors relies on EDS1-dependent immunity. Plant J. Cell Mol. Biol. *91*, 430–442.

Azarashvili, T., Krestinina, O., Galvita, A., Grachev, D., Baburina, Y., Stricker, R., Evtodienko, Y., and Reiser, G. (2009). Ca^{2+}-dependent permeability transition regulation in rat brain mitochondria by 2′,3′-cyclic nucleotides and 2′,3′-cyclic nucleotide 3′-phosphodiesterase. Am. J. Physiol. Cell Physiol. *296*, C1428–C1439.

Bartsch, M., Gobbato, E., Bednarek, P., Debey, S., Schultze, J.L., Bautor, J., and Parker, J.E. (2006). Salicylic acid-independent enhanced disease susceptibility1 signaling in *Arabidopsis* immunity and cell death is regulated by the monooxygenase FMO1 and the Nudix hydrolase NUDT7. Plant Cell *18*, 1038–1051.

Please cite this article in press as: Yu et al., TIR domains of plant immune receptors are 2′,3′-cAMP/cGMP synthetases mediating cell death, Cell (2022), https://doi.org/10.1016/j.cell.2022.04.032

Bayless, A.M., and Nishimura, M.T. (2020). Enzymatic functions for toll/interleukin-1 receptor domain proteins in the plant immune system. Front. Genet. *11*, 539.

Bernoux, M., Ve, T., Williams, S., Warren, C., Hatters, D., Valkov, E., Zhang, X., Ellis, J.G., Kobe, B., and Dodds, P.N. (2011). Structural and functional analysis of a plant resistance protein TIR domain reveals interfaces for self-association, signaling, and autoregulation. Cell Host Microbe *9*, 200–211.

Bhandari, D.D., Lapin, D., Kracher, B., von Born, P., Bautor, J., Niefind, K., and Parker, J.E. (2019). An EDS1 heterodimer signalling surface enforces timely reprogramming of immunity genes in *Arabidopsis*. Nat. Commun. *10*, 772.

Bi, G., Su, M., Li, N., Liang, Y., Dang, S., Xu, J., Hu, M., Wang, J., Zou, M., Deng, Y., et al. (2021). The ZAR1 resistosome is a calcium-permeable channel triggering plant immune signaling. Cell *184*, 3528–3541. e12.

Bonardi, V., Tang, S., Stallmann, A., Roberts, M., Cherkis, K., and Dangl, J.L. (2011). Expanded functions for a family of plant intracellular immune receptors beyond specific recognition of pathogen effectors. Proc. Natl. Acad. Sci. USA *108*, 16463–16468.

Cai, H., Wang, W., Rui, L., Han, L., Luo, M., Liu, N., and Tang, D. (2021). The TIR-NBS protein TN13 associates with the CC-NBS-LRR resistance protein RPS5 and contributes to RPS5-triggered immunity in *Arabidopsis*. Plant J *107*, 775–786.

Castel, B., Ngou, P.M., Cevik, V., Redkar, A., Kim, D.S., Yang, Y., Ding, P., and Jones, J.D.G. (2019). Diverse NLR immune receptors activate defence via the RPW8-NLR NRG1. New Phytol *222*, 966–980.

Chodasiewicz, M., Kerber, O., Gorka, M., Moreno, J.C., Sampathkumar, A., and Skirycz, A. (2022). 2′,3′-cAMP treatment mimics abiotic stress response. Plant Physiol *188*, 1966–1978.

Collier, S.M., Hamel, L.P., and Moffett, P. (2011). Cell death mediated by the N-terminal domains of a unique and highly conserved class of NB-LRR protein. Mol. Plant. Microbe Interact. *24*, 918–931.

Cregan, S.P., Dawson, V.L., and Slack, R.S. (2004). Role of AIF in caspase-dependent and caspase-independent cell death. Oncogene *23*, 2785–2796.

Dodds, P.N., Lawrence, G.J., Catanzariti, A.M., Teh, T., Wang, C.I., Ayliffe, M.A., Kobe, B., and Ellis, J.G. (2006). Direct protein interaction underlies gene-for-gene specificity and coevolution of the flax resistance genes and flax rust avirulence genes. Proc. Natl. Acad. Sci. USA *103*, 8888–8893.

Dong, S., and Wang, Y. (2016). Nudix effectors: a common weapon in the arsenal of plant pathogens. PLoS Pathog *12*, e1005704.

Duxbury, Z., Wang, S., MacKenzie, C.I., Tenthorey, J.L., Zhang, X., Huh, S.U., Hu, L., Hill, L., Ngou, P.M., Ding, P., et al. (2020). Induced proximity of a TIR signaling domain on a plant-mammalian NLR chimera activates defense in plants. Proc. Natl. Acad. Sci. USA *117*, 18832–18839.

Eckel, R., Ros, R., Ros, A., Wilking, S.D., Sewald, N., and Anselmetti, D. (2003). Identification of binding mechanisms in single molecule-DNA complexes. Biophys. J. *85*, 1968–1973.

Essuman, K., Summers, D.W., Sasaki, Y., Mao, X., Yim, A.K.Y., DiAntonio, A., and Milbrandt, J. (2018). TIR domain proteins are an ancient family of NAD$^+$-consuming enzymes. Curr. Biol. *28*, 421–430. e4.

Gantner, J., Ordon, J., Ilse, T., Kretschmer, C., Gruetzner, R., Löfke, C., Dagdas, Y., Bürstenbinder, K., Marillonnet, S., and Stuttmann, J. (2018). Peripheral infrastructure vectors and an extended set of plant parts for the Modular Cloning system. PLoS One *13*, e0197185.

Gao, Y., Wang, W., Zhang, T., Gong, Z., Zhao, H., and Han, G.Z. (2018). Out of water: the origin and early diversification of plant R-genes. Plant Physiol *177*, 82–89.

Ge, X., Li, G.J., Wang, S.B., Zhu, H., Zhu, T., Wang, X., and Xia, Y. (2007). *At*NUDT7, a negative regulator of basal immunity in *Arabidopsis*, modulates two distinct defense response pathways and is involved in maintaining redox homeostasis. Plant Physiol *145*, 204–215.

Genschik, P., Hall, J., and Filipowicz, W. (1997). Cloning and characterization of the *Arabidopsis* cyclic phosphodiesterase which hydrolyzes ADP-ribose 1′′,2′′-cyclic phosphate and nucleoside 2′,3′-cyclic phosphates. J. Biol. Chem. *272*, 13211–13219.

Gong, Q., Robinson, K., Xu, C., Huynh, P.T., Chong, K.H.C., Tan, E.Y.J., Zhang, J., Boo, Z.Z., Teo, D.E.T., Lay, K., et al. (2021). Structural basis for distinct inflammasome complex assembly by human NLRP1 and CARD8. Nat. Commun. *12*, 188.

Greulich, W., Wagner, M., Gaidt, M.M., Stafford, C., Cheng, Y., Linder, A., Carell, T., and Hornung, V. (2019). TLR8 is a sensor of RNase T2 degradation products. Cell *179*, 1264–1275. e13.

Hanna, C.B., Yao, S., Wu, X., and Jensen, J.T. (2012). Identification of phosphodiesterase 9A as a cyclic guanosine monophosphate-specific phosphodiesterase in germinal vesicle oocytes: a proposed role in the resumption of meiosis. Fertil. Steril. *98*, 487–495.e1.

Horsefield, S., Burdett, H., Zhang, X., Manik, M.K., Shi, Y., Chen, J., Qi, T., Gilley, J., Lai, J.S., Rank, M.X., et al. (2019). NAD(+) cleavage activity by animal and plant TIR domains in cell death pathways. Science *365*, 793–799.

Ishikawa, K., Suzuki, E., Tanokura, M., and Takahashi, K. (1996). Crystal structure of ribonuclease T1 carboxymethylated at Glu58 in complex with 2′-GMP. Biochemistry *35*, 8329–8334.

Jackson, E.K. (2017). Non-canonical cyclic Nucleotides: discovery and roles of 2,3-cAMP in biological systems. Handb. Exp. Pharmacol. *238*, 229–252.

Jackson, E.K., Gillespie, D.G., Mi, Z., Cheng, D., Bansal, R., Janesko-Feldman, K., and Kochanek, P.M. (2014). Role of 2′,3′-cyclic nucleotide 3′-phosphodiesterase in the renal 2′,3′-cAMP-adenosine pathway. Am. J. Physiol. Ren. Physiol. *307*, F14–F24.

Jacob, P., Kim, N.H., Wu, F., El-Kasmi, F., Chi, Y., Walton, W.G., Furzer, O.J., Lietzan, A.D., Sunil, S., Kempthorn, K., et al. (2021). Plant “helper” immune receptors are Ca^{2+}-permeable nonselective cation channels. Science *373*, 420–425.

Johanndrees, O., Baggs, L.E., Uhlmann, C., Locci, F., Läßle, L.H., Melkonian, K., Käufer, K., Dongus, A.J., Nakagami, H., Krasileva, V.K., Parker, E.J., and Lapin, D. (2021). Differential EDS1 requirement for cell death activities of plant TIR-domain proteins. Preprint at bioRxiv. https://doi.org/10.1101/2021.11.29.470438.

Kong, G., Zhao, Y., Jing, M., Huang, J., Yang, J., Xia, Y., Kong, L., Ye, W., Xiong, Q., Qiao, Y., et al. (2015). The activation of Phytophthora effector Avr3b by plant cyclophilin is required for the Nudix hydrolase activity of Avr3b. PLoS Pathog *11*, e1005139.

Kosmacz, M., Luzarowski, M., Kerber, O., Leniak, E., Gutiérrez-Beltrán, E., Moreno, J.C., Gorka, M., Szlachetko, J., Veyel, D., Graf, A., et al. (2018). Interaction of 2′,3′-cAMP with Rbp47b plays a role in stress granule formation. Plant Physiol *177*, 411–421.

Lapin, D., Johanndrees, O., Wu, Z., Li, X., and Parker, J.E. (2022). Molecular innovations in plant TIR-based immunity signaling. Plant Cell *00*, 1–18.

Lapin, D., Kovacova, V., Sun, X., Dongus, J.A., Bhandari, D., von Born, P., Bautor, J., Guarneri, N., Rzemieniewski, J., Stuttmann, J., et al. (2019). A coevolved EDS1-SAG101-NRG1 module mediates cell death signaling by TIR-domain immune receptors. Plant Cell *31*, 2430–2455.

Ma, S., Lapin, D., Liu, L., Sun, Y., Song, W., Zhang, X., Logemann, E., Yu, D., Wang, J., Jirschitzka, J., et al. (2020). Direct pathogen-induced assembly of an NLR immune receptor complex to form a holoenzyme. Science *370*, eabe3069.

Martel, A., Laflamme, B., Seto, D., Bastedo, D.P., Dillon, M.M., Almeida, R.N.D., Guttman, D.S., and Desveaux, D. (2020). Immunodiversity of the *Arabidopsis* ZAR1 NLR is conveyed by receptor-like cytoplasmic kinase sensors. Front. Plant Sci. *11*, 1290.

Martin, R., Qi, T., Zhang, H., Liu, F., King, M., Toth, C., Nogales, E., and Staskawicz, B.J. (2020). Structure of the activated ROQ1 resistosome directly recognizing the pathogen effector XopQ. Science *370*, eabd9993.

McLennan, A.G. (2006). The Nudix hydrolase superfamily. Cell. Mol. Life Sci. *63*, 123–143.

Meyers, B.C., Morgante, M., and Michelmore, R.W. (2002). TIR-X and TIR-NBS proteins: two new families related to disease resistance TIR-NBS-LRR proteins encoded in *Arabidopsis* and other plant genomes. Plant J *32*, 77–92.

Moore, Bd. (2004). Bifunctional and moonlighting enzymes: lighting the way to regulatory control. Trends Plant Sci *9*, 221–228.

Myllykoski, M., Seidel, L., Muruganandam, G., Raasakka, A., Torda, A.E., and Kursula, P. (2016). Structural and functional evolution of 2′,3′-cyclic nucleotide 3′-phosphodiesterase. Brain Res *1641*, 64–78.

Nandety, R.S., Caplan, J.L., Cavanaugh, K., Perroud, B., Wroblewski, T., Michelmore, R.W., and Meyers, B.C. (2013). The role of TIR-NBS and TIR-X proteins in plant basal defense responses. Plant Physiol *162*, 1459–1472.

Ngou, B.P.M., Ahn, H.K., Ding, P., and Jones, J.D.G. (2021). Mutual potentiation of plant immunity by cell-surface and intracellular receptors. Nature *592*, 110–115.

Ngou, B.P.M., Ahn, H.K., Ding, P., Redkar, A., Brown, H., Ma, Y., Youles, M., Tomlinson, L., and Jones, J.D.G. (2020). Estradiol-inducible AvrRps4 expression reveals distinct properties of TIR-NLR-mediated effector-triggered immunity. J. Exp. Bot. *71*, 2186–2197.

Nimma, S., Ve, T., Williams, S.J., and Kobe, B. (2017). Towards the structure of the TIR-domain signalosome. Curr. Opin. Struct. Biol. *43*, 122–130.

Nishimura, M.T., Anderson, R.G., Cherkis, K.A., Law, T.F., Liu, Q.L., Machius, M., Nimchuk, Z.L., Yang, L., Chung, E.H., El Kasmi, F., et al. (2017). TIR-only protein RBA1 recognizes a pathogen effector to regulate cell death in *Arabidopsis*. Proc. Natl. Acad. Sci. USA *114*, E2053–E2062.

Numata, T., Suzuki, A., Kakuta, Y., Kimura, K., Yao, M., Tanaka, I., Yoshida, Y., Ueda, T., and Kimura, M. (2003). Crystal structures of the ribonuclease MC1 mutants N71T and N71S in complex with 5′-GMP: structural basis for alterations in substrate specificity. Biochemistry *42*, 5270–5278.

Ofir, G., Herbst, E., Baroz, M., Cohen, D., Millman, A., Doron, S., Tal, N., Malheiro, D.B.A., Malitsky, S., Amitai, G., and Sorek, R. (2021). Antiviral activity of bacterial TIR domains via immune signalling molecules. Nature *600*, 116–120.

Ostendorf, T., Zillinger, T., Andryka, K., Schlee-Guimaraes, T.M., Schmitz, S., Marx, S., Bayrak, K., Linke, R., Salgert, S., Wegner, J., et al. (2020). Immune sensing of synthetic, bacterial, and protozoan RNA by toll-like receptor 8 requires coordinated processing by RNase T2 and RNase 2. Immunity *52*, 591–605. e6.

Peart, J.R., Mestre, P., Lu, R., Malcuit, I., and Baulcombe, D.C. (2005). NRG1, a CC-NB-LRR protein, together with N, a TIR-NB-LRR protein, mediates resistance against tobacco mosaic virus. Curr. Biol. *15*, 968–973.

Pruitt, R.N., Gust, A.A., and Nürnberger, T. (2021). Plant immunity unified. Nat. Plants *7*, 382–383.

Qi, T., Seong, K., Thomazella, D.P.T., Kim, J.R., Pham, J., Seo, E., Cho, M.J., Schultink, A., and Staskawicz, B.J. (2018). NRG1 functions downstream of EDS1 to regulate TIR-NLR-mediated plant immunity in *Nicotiana benthamiana*. Proc. Natl. Acad. Sci. USA *115*, E10979–E10987.

Ren, J., Mi, Z., Stewart, N.A., and Jackson, E.K. (2009). Identification and quantification of 2′,3′-cAMP release by the kidney. J. Pharmacol. Exp. Ther. *328*, 855–865.

Rietz, S., Stamm, A., Malonek, S., Wagner, S., Becker, D., Medina-Escobar, N., Corina Vlot, A., Feys, B.J., Niefind, K., and Parker, J.E. (2011). Different roles of Enhanced Disease Susceptibility1 (EDS1) bound to and dissociated from Phytoalexin Deficient4 (PAD4) in Arabidopsis immunity. New Phytol *191*, 107–119.

Rodriguez, E., Chevalier, J., El Ghoul, H., Voldum-Clausen, K., Mundy, J., and Petersen, M. (2018). DNA damage as a consequence of NLR activation. PLoS Genet *14*, e1007235.

Roth, C., Ludke, D., Klenke, M., Quathamer, A., Valerius, O., Braus, G.H., and Wiermer, M. (2017). The truncated NLR protein TIR-NBS13 is a MOS6/IMPORTIN-alpha3 interaction partner required for plant immunity. Plant J. Cell Mol. Biol. *92*, 808–821.

Santamaría, M.E., Martínez, M., Arnaiz, A., Rioja, C., Burow, M., Grbic, V., and Díaz, I. (2019). An *Arabidopsis* TIR-lectin two-domain protein confers defense properties against tetranychus urticae. Plant Physiol *179*, 1298–1314.

Schultink, A., Qi, T., Lee, A., Steinbrenner, A.D., and Staskawicz, B. (2017). Roq1 mediates recognition of the *Xanthomonas* and *Pseudomonas* effector proteins XopQ and HopQ1. Plant J *92*, 787–795.

Staal, J., Kaliff, M., Dewaele, E., Persson, M., and Dixelius, C. (2008). RLM3, a TIR domain encoding gene involved in broad-range immunity of *Arabidopsis* to necrotrophic fungal pathogens. Plant J *55*, 188–200.

Straus, M.R., Rietz, S., Ver Loren van Themaat, E., Bartsch, M., and Parker, J.E. (2010). Salicylic acid antagonism of EDS1-driven cell death is important for immune and oxidative stress responses in *Arabidopsis*. Plant J *62*, 628–640.

Sun, X., Lapin, D., Feehan, J.M., Stolze, S.C., Kramer, K., Dongus, J.A., Rzemieniewski, J., Blanvillain-Baufumé, S., Harzen, A., Bautor, J., et al. (2021). Pathogen effector recognition-dependent association of NRG1 with EDS1 and SAG101 in TNL receptor immunity. Nat. Commun. *12*, 3335.

Suzuki, N., Koussevitzky, S., Mittler, R., and Miller, G. (2012). ROS and redox signalling in the response of plants to abiotic stress. Plant Cell Environ *35*, 259–270.

Tian, H., Wu, Z., Chen, S., Ao, K., Huang, W., Yaghmaiean, H., Sun, T., Xu, F., Zhang, Y., Wang, S., et al. (2021). Activation of TIR signalling boosts pattern-triggered immunity. Nature *598*, 500–503.

Trapp, B.D., Bernier, L., Andrews, S.B., and Colman, D.R. (1988). Cellular and subcellular distribution of 2′,3′-cyclic nucleotide 3′-phosphodiesterase and its mRNA in the rat central nervous system. J. Neurochem. *51*, 859–868.

Tyc, K., Kellenberger, C., and Filipowicz, W. (1987). Purification and characterization of wheat germ 2′,3′-cyclic nucleotide 3′-phosphodiesterase. J. Biol. Chem. *262*, 12994–13000.

Van Damme, T., Blancquaert, D., Couturon, P., Van Der Straeten, D., Sandra, P., and Lynen, F. (2014). Wounding stress causes rapid increase in concentration of the naturally occurring 2′,3′-isomers of cyclic guanosine- and cyclic adenosine monophosphate (cGMP and cAMP) in plant tissues. Phytochemistry *103*, 59–66.

Venugopal, S.C., Jeong, R.D., Mandal, M.K., Zhu, S., Chandra-Shekara, A.C., Xia, Y., Hersh, M., Stromberg, A.J., Navarre, D., Kachroo, A., et al. (2009). Enhanced disease susceptibility 1 and salicylic acid act redundantly to regulate resistance gene-mediated signaling. PLoS Genet *5*, e1000545.

Wan, L., Essuman, K., Anderson, R.G., Sasaki, Y., Monteiro, F., Chung, E.H., Osborne Nishimura, E., DiAntonio, A., Milbrandt, J., Dangl, J.L., et al. (2019). TIR domains of plant immune receptors are NAD(+)-cleaving enzymes that promote cell death. Science *365*, 799–803.

Wang, J., Hu, M., Wang, J., Qi, J., Han, Z., Wang, G., Qi, Y., Wang, H.W., Zhou, J.M., and Chai, J. (2019). Reconstitution and structure of a plant NLR resistosome conferring immunity. Science *364*, eaav5870.

Wiermer, M., Feys, B.J., and Parker, J.E. (2005). Plant immunity: the EDS1 regulatory node. Curr. Opin. Plant Biol. *8*, 383–389.

Williams, S.J., Sohn, K.H., Wan, L., Bernoux, M., Sarris, P.F., Segonzac, C., Ve, T., Ma, Y., Saucet, S.B., Ericsson, D.J., et al. (2014). Structural basis for assembly and function of a heterodimeric plant immune receptor. Science *344*, 299–303.

Williams, S.J., Yin, L., Foley, G., Casey, L.W., Outram, M.A., Ericsson, D.J., Lu, J., Boden, M., Dry, I.B., and Kobe, B. (2016). Structure and function of the TIR domain from the grape NLR protein RPV1. Front. Plant Sci. *7*, 1850.

Wirthmueller, L., Zhang, Y., Jones, J.D., and Parker, J.E. (2007). Nuclear accumulation of the Arabidopsis immune receptor RPS4 is necessary for triggering EDS1-dependent defense. Curr. Biol. *17*, 2023–2029.

Wu, Z., Li, M., Dong, O.X., Xia, S., Liang, W., Bao, Y., Wasteneys, G., and Li, X. (2019). Differential regulation of TNL-mediated immune signaling by redundant helper CNLs. New Phytol *222*, 938–953.

Wu, Z., Tian, L., Liu, X., Zhang, Y., and Li, X. (2021). TIR signal promotes interactions between lipase-like proteins and ADR1-L1 receptor and ADR1-L1 oligomerization. Plant Physiol *187*, 681–686.

Xiong, Y., Han, Z., and Chai, J. (2020). Resistosome and inflammasome: platforms mediating innate immunity. Curr. Opin. Plant Biol. *56*, 47–55.

Yoshida, H. (2001). The ribonuclease T1 family. Methods Enzymol *341*, 28–41.

Yuan, M., Jiang, Z., Bi, G., Nomura, K., Liu, M., Wang, Y., Cai, B., Zhou, J.M., He, S.Y., and Xin, X.F. (2021). Pattern-recognition receptors are required for NLR-mediated plant immunity. Nature *592*, 105–109.

Zhang, X., Bernoux, M., Bentham, A.R., Newman, T.E., Ve, T., Casey, L.W., Raaymakers, T.M., Hu, J., Croll, T.I., Schreiber, K.J., et al. (2017). Multiple functional self-association interfaces in plant TIR domains. Proc. Natl. Acad. Sci. USA *114*, E2046–E2052.

Zhang, Y., Dorey, S., Swiderski, M., and Jones, J.D. (2004). Expression of RPS4 in tobacco induces an AvrRps4-independent HR that requires EDS1, SGT1 and HSP90. Plant J. Cell Mol. Biol. *40*, 213–224.

Zhao, T., Rui, L., Li, J., Nishimura, M.T., Vogel, J.P., Liu, N., Liu, S., Zhao, Y., Dangl, J.L., and Tang, D. (2015). A truncated NLR protein, TIR-NBS2, is required for activated defense responses in the exo70B1 mutant. PLoS Genet *11*, e1004945.

Zhu, Y., Qian, W., and Hua, J. (2010). Temperature modulates plant defense responses through NB-LRR proteins. PLoS Pathog *6*, e1000844.

Please cite this article in press as: Yu et al., TIR domains of plant immune receptors are 2′,3′-cAMP/cGMP synthetases mediating cell death, Cell (2022), https://doi.org/10.1016/j.cell.2022.04.032

STAR★METHODS

KEY RESOURCES TABLE

REAGENT or RESOURCE	SOURCE	IDENTIFIER
Antibodies		
anti-Myc antibody	Thermo Scientific	Cat# R950-25; RRID: AB_2556560
anti-GFP antibody	Chromtek	Cat# pabg1-100; RRID: AB_2749857
anti-HA antibody (monoclonal)	Sigma-Aldrich	Cat# 11867423001; RRID: AB_390918
anti-HA antibody (polyclonal)	Abcam	Cat# 9110; RRID: AB_307019
Bacterial and Virus Strains		
Escherichia coli (E. coli) DH5α competent cell	Lab stock / Invitrogen	N/A
E. coli BL21 (DE3) competent cell	Novagen	Cat# 69450
E. coli DH10Bac competent cell	Invitrogen	Cat# 10361-012
Spodoptera frugiperda (sf21) insect cell line	Lab stock / Invitrogen	Cat# 11497013
Rhizobium radiobacter (Agrobacterium tumefaciens) GV3101 pMP90RK competent cell	Lab stock / DSMZ	Cat# 12365
Pseudomonas fluorescens Pf0-1-HopBA1	This study	N/A
Chemicals, Peptides, and Recombinant Proteins		
2′,3′-cAMP	Sigma-Aldrich	Cat# A9376
2′,3′-cGMP	SCBT	Cat# sc-481308
3′,5′-cAMP	Sigma-Aldrich	Cat# A9501
3′,5′-cGMP	Sigma-Aldrich	Cat# G7504
8-Br-2′,3′-cAMP	BioLog	Cat# B280
NAD^+	Sigma-Aldrich	Cat# N7004
ATP	CarlRoth	Cat# HN35
GTP	CarlRoth	Cat# K056
CTP	CarlRoth	Cat# K057
TTP (dTTP)	CarlRoth	Cat# K036
3-isobutyl-1-methylxanthine (IBMX)	Sigma-Aldrich	Cat# 28822-58-4
Cellfectin II	Thermo Scientific	Cat# 10362100
TGX stain-free fastcast acrylamide kit	Bio-Rad	Cat# 1610183
PreScission protease	Lab stock	N/A
Isopropyl-β-D-thiogalactoside (IPTG)	CarlRoth	Cat# 367-93-1
Ni Sepharose 6 fast flow (Ni^{2+} resin)	GE Healthcare / Cytiva	Cat# 17531802
Glutathione Sepharose 4B (GST resin)	GE Healthcare / Cytiva	Cat# 17075605
RNase T1	Thermo Scientific	Cat# EN0541
DNase I	Jena Bioscience	Cat# EN-173S
Critical Commercial Assays		
Q5 site-directed mutagenesis kit	NEB	Cat# E0554S
DNase I assay kit (Fluorometric)	Abcam	Cat# ab234056
Deposited Data		
$L7^{TIR}$ with 2′,3′-cAMP bound in the catalytic pocket	This paper	PDB ID: 7VU8
$L7^{TIR}$-dsDNA initial state complex	This paper	PDB ID: 7X5K
$L7^{TIR}$-dsDNA intermediate state complex	This paper	PDB ID: 7X5L
$L7^{TIR}$-dsDNA end state complex	This paper	PDB ID: 7X5M
Recombinant DNA		
Plasmid: pMAL(pMAL C2X)-$L6^{TIR}$	This paper	N/A

(*Continued on next page*)

Please cite this article in press as: Yu et al., TIR domains of plant immune receptors are 2′,3′-cAMP/cGMP synthetases mediating cell death, Cell (2022), https://doi.org/10.1016/j.cell.2022.04.032

Continued

REAGENT or RESOURCE	SOURCE	IDENTIFIER
Plasmid: pMAL-L7^{TIR}	This paper	N/A
Plasmid: pMAL-L7^{TIR} K176A/K180A(KK^{AA})	This paper	N/A
Plasmid: pMAL-L7^{TIR} K171A/172A/R175A(KKR^{AAA})	This paper	N/A
Plasmid: pMAL-L7^{TIR} K100A/G101A/K102A/E103A (KGKE^{AAAA})	This paper	N/A
Plasmid: pMAL-L7^{TIR} K200E	This paper	N/A
Plasmid: pMAL-L7^{TIR} F79A	This paper	N/A
Plasmid: pMAL-L7^{TIR} F79A/E209A(FE^{AA})	This paper	N/A
Plasmid: pMAL-L7^{TIR} C132A	This paper	N/A
Plasmid: pMAL-L7^{TIR} E135A	This paper	N/A
Plasmid: pFastBac (pFastBac 1)-RBA1	This paper	N/A
Plasmid: pFastBac-RBA1 C83A	This paper	N/A
Plasmid: pFastBac-RBA1 E86A	This paper	N/A
Plasmid: pFastBac-RBA1 S80A	This paper	N/A
Plasmid: pFastBac-RBA1 K149E	This paper	N/A
Plasmid: pFastBac-RBA1 K122A/K123A/K130A (KKK^{AAA})	This paper	N/A
Plasmid: pMAL-TX0	This paper	N/A
Plasmid: pMAL-TX7	This paper	N/A
Plasmid: pMAL-*Ab*TIR	This paper	N/A
Plasmid: pGEX6p-1-PreScission Protease	This paper	N/A
Plasmid: pGEX6p-1-*At*NUDT7	This paper	N/A
Plasmid: pGEX6p-1-*At*NUDT7 E154Q	This paper	N/A
Plasmid: pGEX6p-1-XopQ	This paper	N/A
Plasmid: pGEX6p-1-Avr3b	This paper	N/A
Plasmid: pGEX6p-1-mCNPase	This paper	N/A
Plasmid: pGEX6p-1-*At*CPDase	This paper	N/A
Plasmid: pXCSG-RBA1	This paper	N/A
Plasmid: pXCSG-RBA1 C83A	This paper	N/A
Plasmid: pXCSG-RBA1 E86A	This paper	N/A
Plasmid: pXCSG-RBA1 K122A/K123A/K130A (KKK^{AAA})	This paper	N/A
Plasmid: pXCSG-Avr3b	This paper	N/A
Plasmid: pXCSG-mCNPase	This paper	N/A
Plasmid: pXCSG-*At*CPDase	This paper	N/A
Plasmid: pEGAD-PDE9	This paper	N/A
Plasmid: pEGAD-*At*NUDT7	This paper	N/A
Plasmid: pEGAD-*At*NUDT7 E154Q	This paper	N/A
Software and Algorithms		
PyMOL	Molecular Graphics System, Version 1.8 Schrödinger	https://pymol.org/2/
Chimera X	UCSF	https://www.cgl.ucsf.edu/chimerax/
RELION	University of Cambridge	https://www3.mrc-lmb.cam.ac.uk/relion
Cryosparc	Structura Biotechnology Inc.	https://cryosparc.com/
Phenix	UC Berkeley	https://phenix-online.org/

RESOURCE AVAILABILITY

Lead contact

Further information and requests for resources and reagents should be directed to and will be fulfilled by the lead contact Jijie Chai (chai@mpipz.mpg.de).

Please cite this article in press as: Yu et al., TIR domains of plant immune receptors are 2′,3′-cAMP/cGMP synthetases mediating cell death, Cell (2022), https://doi.org/10.1016/j.cell.2022.04.032

Materials availability

Constructs and reagents in this study will be made available upon request, but a completed Materials Transfer Agreement may be required if there is potential for commercial application.

Data and code availability

The structures of the L7^{TIR}-dsDNA initial state complex, intermediate state complex and end state complex were deposited in the Protein Data Bank (PDB) with PDB code: 7X5K, 7X5L, 7X5M, respectively. In the end state complex, a 2',3'-cAMP bound L7^{TIR} protomer was deposited in PDB with PDB code: 7VU8. This paper does not report original code. Any additional information required to reanalyze the data reported in this work paper is available from the lead contact upon request.

EXPERIMENTAL MODEL AND SUBJECT DETAILS

Bacteria strain

Bacteria strain *Escherichia coli* BL21 (DE3) was used in this work for protein purification. Bacteria were cultured in LB medium (CarlRoth) at 37°C until OD_{600} reached 0.6, protein expression was induced by addition of 0.8 mM Isopropyl-β-D-thiogalactoside (IPTG) at 18°C for 16 h with 180 rpm in shaking incubator (MaxQ 6000, Thermo Scientific).

Insect cell line

Insect cell strain *Spodoptera frugiperda* (Sf21) was used in this work for protein purification. Cells were cultured in Sf-900 II SFM medium (Gibco) at 28°C with 120 rpm in shaking incubator (Innova 44, Eppendorf). Baculovirus infected cells were cultured at 28°C with 120 rpm for 48 h.

Plant materials

Arabidopsis thaliana accession Ag-0, Col-0 and *Nicotiana benthamiana* were used in this work. The *N. benthamiana* quadruple mutant *epss* (*eds1, pad4, sag101a, sag101b*), *Arabidopsis* single mutant *Atnudt7* and double mutant *Atnudt7 eds1* were described previously (Lapin et al.,2019; Straus et al., 2010). All plants were grown on soil in walk-in growth chambers, the greenhouse, the Max Planck Institute for Plant Breeding Research, Cologne.

METHOD DETAILS

Recombinant protein expression and purification

TX0 (*At*1g57630, residues 1-172) was cloned into pMAL C2X vector and expressed in *E. coli* as MBP-fusion protein with an additional C-terminal GST tag, TX7 (*At*1g57850, residues 1-192), *Ab*TIR (residues 1-269), L6^{TIR} (residues 26-231) and L7^{TIR} (residues 26-231) were cloned into pMAL C2X vector and expressed in *E. coli* as MBP-fusion proteins with additional C-terminal 6 × His tags. The constructs were transformed into the *E. coli* strain BL21 (DE3) (Novagen) at 42°C with 90 s heat shock and the cell cultures were grown at 37°C to OD_{600} of 0.6. Isopropyl-β-D-thiogalactoside (IPTG, Sigma) was added to induce protein expression at 18°C for 16 h. The *E. coli* cells were harvested and lysed by sonification in buffer containing 25 mM Tris-HCl at pH 8.0, 150 mM NaCl, and 15 mM imidazole. The cell lysates were centrifuged at 30,000 *g* for 1.5 h. The supernatant containing soluble proteins was collected and allowed to flow through Ni-NTA resin (GE Healthcare). After washing with three column volumes of sonification buffer, the fusion proteins were eluted in the buffer containing 25 mM Tris-HCl at pH 8.0, 150 mM NaCl, and 150 mM imidazole. For TX0 and TX7, tags could not be completely removed by PreScission protease. *Arabidopsis* NUDT7 (residues 1-322), NUDT7^{E154Q} (residues 1-322), *Phytophthora sojae* Avr3b^{p6497} (residues 19-314), *Xanthomonas euvesicatoria* XopQ (residues 85-465), mouse CNPase1 (mCNPase1, residues 161-380) and *Arabidopsis* CPDase (AtCPDase, residues 1-181) were cloned into pGEX6p-1 vector and expressed in *E. coli* as N-terminal GST-fused proteins. The same protocol as described above was used for *E. coli* culturing. The *E. coli* cells were harvested and lysed by sonification in buffer containing 25 mM Tris-HCl pH 8.0, 150 mM NaCl. The cell lysates were centrifuged at 30,000 *g* for 1.5 h. The supernatant containing soluble proteins were collected and allowed to flow through GST4B resin (GE Healthcare). After washing with three column volumes of sonification buffer, the fusion proteins were incubated with PreScission at 4°C overnight to remove the N-terminal GST tag and the digested proteins flowed through the columns in the buffer containing 25 mM Tris-HCl pH 8.0, and 150 mM NaCl. WT RBA1 (residues 1-363) and RBA1 mutant proteins were cloned into the pFastBac 1 vector (Invitrogen) with an N-terminal SUMO-6×His tag. The constructs were used for generating recombinant baculovirus in Sf21 insect cells (Invitrogen). RBA1 and RBA1 mutant proteins were expressed in Sf21 insect cells with recombinant baculovirus infection at 28 °C for 48 h. The infected cells were harvested and lysed by sonification in buffer containing 25 mM Tris-HCl pH 8.0, 150 mM NaCl, and 15 mM imidazole. The cell lysates were centrifuged at 30,000 *g* for 1.5 h. The supernatant containing soluble proteins were collected and allowed to flow through Ni-NTA resin. After washing with three column volumes of sonification buffer, the fusion proteins were incubated with PreScission protease at 4°C overnight to remove the N-terminal SUMO-6×His tag and the digested proteins flowed through the columns in the buffer containing 25 mM Tris-HCl pH 8.0, and 150 mM NaCl.

Please cite this article in press as: Yu et al., TIR domains of plant immune receptors are 2′,3′-cAMP/cGMP synthetases mediating cell death, Cell (2022), https://doi.org/10.1016/j.cell.2022.04.032

In vitro NADase assay

Purified WT and mutant L7^{TIR} proteins (20 μM), *Ab*TIR (20 μM), WT RBA1 and mutant proteins (10 μM) were used for NADase assays. Proteins were individually incubated with 100 μM NAD$^+$ (final concentration) and 10 mM $MgCl_2$ in buffer containing 100 mM NaCl, 25 mM Tris-HCl pH 8.0. The total volume for each reaction was 100 μl. Reactions were performed in a thermoshaker (CellMedia) at 25°C for 16 h. After reaction, samples were centrifuged and immediately applied for high-performance liquid chromatography (HPLC) analysis.

HPLC was performed on an Agilent 1260 bioinert HPLC system using a Synergi Fusion-RP 80 Å (4.6 × 150 mm, 4 μm) (Phenomenex) column. The samples were measured via an 8-min method. Samples (10 μl) were injected at 550 μl/min with ammonium formate (5 mM) in water and methanol used as mobile phases A and B, respectively. The elution profile was as follows: 0 to 3 min, 10 to 70% B; 3 to 6 min, 70% B; 6 to 6.1 min, 70 to 10% B; 6.1 to 8 min, 10% B. The autosampler temperature was maintained at 4°C and the column temperature at 25°C. UV signals were detected at 260 nm. Reference standards were used to determine respective retention times. The integrations of peak area were used to calculate relative concentrations.

Site-directed mutagenesis

*At*NUDT7^{E154Q} construct was introduced using overlap extension PCR. All other mutations of the constructs used for *in vitro* and *in vivo* assays were introduced using a Q5 site-directed mutagenesis kit (NEB). All constructs were verified by DNA sequencing.

In vitro nuclease activity assay

Arabidopsis genomic DNA, *Arabidopsis* total RNA, PCR product and plasmid (100 ng for each) were individually incubated with purified RBA1 and RBA1 mutant proteins (200 nM for each), TX0, TX7, *Ab*TIR, L7^{TIR} and L7^{TIR} mutant proteins (1 μM for each) in the buffer containing 25 mM Tris-HCl pH 8.0 and 150 mM NaCl at 25°C for 16 h if not mentioned otherwise. After reaction, the products were mixed with DNA loading buffer and visualized by agarose gel electrophoresis. Reaction products were visualized 6 h after reaction when RNA was used as substrate.

Nuclease activity was further measured by DNase I Assay Kit (Fluorometric, Abcam) with a fluorescent DNA probe as the substrate. The purified TIR proteins (5 μM) individually were incubated with the fluorescent DNA probe (25 μM, Abcam). The samples were measured by microplate reader SynergyH1 (BioTek) with excitation/emission 646/686 nm fluorescence.

In vitro 2′,3′-cNMP PDE activity assay

Purified *At*NUDT7, *At*NUDT7^{E154Q}, Avr3b, XopQ, mCNPase and *At*CPDase (2 μM for each) were used for 2′,3′-cAMP/cGMP PDE assay. Proteins were individually incubated with 100 μM 2′,3′-cAMP, 2′,3′-cAMP cGMP, 3′,5′-cAMP or 3′,5′-cGMP (final concentration) and 10 mM $MgCl_2$ in buffer containing 100 mM NaCl, 25 mM Tris-HCl pH 8.0. The total volume for each reaction was 50 μl. Reactions were performed in a thermoshaker (CellMedia) at 25°C for 16 h. After reaction, samples were centrifuged and immediately applied for high-performance liquid chromatography (HPLC) analysis.

Production and detection of 2′,3′-cNMP *in vitro*

The purified RBA1 and RBA1 mutant proteins (5 μM for each), TX0, TX7 *Ab*TIR, L7^{TIR} and L7^{TIR} mutant proteins (1 μM for each) were incubated with 100 ng *Arabidopsis* genomic DNA or *Arabidopsis* total RNA in the buffer containing 25 mM Tris-HCl pH 8.0 and 150 mM NaCl. 2.5 μL of RNase T1 (Thermo Scientific) or DNase I (Jena Bioscience) was incubated with 100 ng *Arabidopsis* total RNA or gDNA. The total volume for each reaction was 100 μl. After incubation at 25°C for 16 h, the samples were centrifuged at 12,000 *g* for 10 min, and the supernatant was applied to LC-MS/MS for metabolite identification and quantification.

Negative-stain electron microscopy

For quality examination and overall structure analysis, TX0, RBA1, L6^{TIR}, L7^{TIR} and MBP tagged L7^{TIR} were subjected to Superose 6 10/300 gel filtration column (GE Healthcare). Fractions eluted at void volume were collected. 3 μl of each protein (0.1mg/ml) was applied to formvar carbon grids glow-discharged for 45 s at high level in Harrick Plasma after 2 min evacuation. The sample stayed on grid for 1 min at room temperature and dried by touching the edge of a filter paper. 3 μl 2% uranyl acetate was then applied to the grid for 45 s. The excess stain was removed. Grids were dried at room temperature for 2 min. Samples were imaged using Hitachi H-7650 120 kV transmission electron microscope (TEM) and images were recorded with an AMT XR-41 camera.

Cryo-EM sample preparation and data collection

For structure determination, MBP tagged L7^{TIR} was incubated with PreScission protease at 4°C or 22°C for 12 h to remove the MBP tag. The L7^{TIR} protein was further purified by size-exclusion chromatography using Superose6 10/300 gel filtration column in buffer containing 10 mM Tris-HCl pH 8.0, 100 mM NaCl. 2.5 μl L7^{TIR} protein (1mg/ml) was applied to holey carbon grids (Quantifoil Cu 1.2/1.3, 300 mesh) glow-discharged for 30 s at high level in Harrick Plasma after 2 min evacuation. Grids were then blotted on filter paper (Ted Pella Inc.) for 3 s at 4°C with 100% humidity and plunge-frozen in liquid ethane using FEI Vitrobot Marked IV. Several other conditions were tested with the hope to capture intermediate states, MBP-L7^{TIR} samples were cleaved by PreScission protease at room temperature (22°C) for 4 h, then further purified and blotted following similar protocol.

Please cite this article in press as: Yu et al., TIR domains of plant immune receptors are 2′,3′-cAMP/cGMP synthetases mediating cell death, Cell (2022), https://doi.org/10.1016/j.cell.2022.04.032

Two datasets of the L7^{TIR} filaments were collected: 4°C processed dataset on a Titan Krios2 electron microscope operated at 300 kV, equipped with Gatan K2 Summit direct electron detector and a Gatan Quantum energy filter, and the 22°C processed dataset on Titan Krios2 with Gatan K3 detector later on.

Cryo-EM data processing

Processing of the cryo-EM data followed a previous workflow used for reconstructing thin flexible helical complexes (Gong et al., 2021). Firstly, Motion Correction and CTF determination were carried out using corresponding modules in RELION. An in-house picking script designed specifically for filament picking was then used to select end-to-end filament coordinates (https://github.com/Alexu0/Cryo-EM-filament-picker). After segment extraction, coordinates and raw images were imported to cryoSPARC for binned 2D classification. Then selected particle coordinates were transferred back to RELION for helical 2D and 3D classification, 3D helical refinement, and final refinement and masked polishing.

In preliminary non-helical 2D analysis, 150 Å appeared to be the basic repeat unit of the physical rise after rotating the filament by either 180° or 360°. In addition, it appeared that there was a smaller helical unit around 35 Å. Then we exhausted and tested all the potential combinations of helical parameters that fit with these two observations. The preliminary helical parameter hits emerged to be +/-43°, and 34 Å. After iterative 3D classification and optimization, it turned out that the initial state Complex had helical parameters of 159.2°, 16.56 Å (mathematically equivalent to -41.6°, 33.12 Å). The intermediate state complex was -48.6°, 33.51 Å. The end state complex was -49.3°, 33.43 Å. Based on Gold Standard FSC = 0.143 measurement, the initial complex, intermediate complex and the end state complex maps were refined to the resolution of 3.4 Å, 3.5 Å and 3.0 Å, respectively.

Model building

Previous TIR domain crystal structure was used as initial model. Model refinement was achieved by fitting PDB 6O0W into a single TIR domain density of the end state complex (PDB code: 7VU8). Phenix real space refinement module was used to optimize the model fitting. Final model to density FSC (0.143) = 2.95 Å, while mask to density CC values (CC-mask, volume, peak, box) were within the range of 0.718 to 0.791. An extra blob of density was identified inside the nucleotide binding pocket. Extensive small molecule docking identified 2′,3′-cAMP as the best fit to accommodate this extra density. 16 refined L7^{TIR} models were docked into initial state complex, and the remaining dsDNA like density was fitted with 43 bp A-form dsDNA (PDB code: 7X5K), model generated by Chimera. For every 11bp DNA, there was 2-3 base pairs found to be stretched, and possessing high slide and twist values, after Phenix real space optimization of the model fitting. This 43bp-16 TIR model was used to analyze how TIR domains oligomerize and cooperatively recognize nucleic acids. From several intermediate state complex structures, one representative density, which showed all double stranded region hydrolyzed down to 3 remaining base pair, was selected for model building. Using Coot and Chimera, nucleotides were manually added in to best represent the density. A detailed four L7^{TIR} model with the bound nucleic acids was built (PDB code: 7X5L), with the aim of analyzing the nucleic acid-TIR interface during the progressive hydrolysis.

Two L7^{TIR} models together, with the bound single stranded DNA, was docked into the end state complex map to determine the complex conformation at the end of nucleic acid hydrolysis (PDB code: 7X5M). Nucleotides were manually docked in, using Coot and Chimeraand later optimized using Phenix real space refinement. This model highlighted additional TIR-TIR interactions and how the residual single stranded nucleic acids remaining associated with TIR after many nucleotides were cleaved and removed. At this conformation, the 2′,3′-cNMP density inside the TIR domain was most obvious among all complexes.

Protein expression in *N. benthamiana* and western blot analysis

For *N. benthamiana* transient expression, *RBA1* (residues 1-363), *AtNUDT7* (residues 1-322), *PDE9* (residues 1-533), *mCNPase1* (residues 161-380), *AtCPDase* (residues 1-181), *Avr3b* (residues 19-314), were cloned into the pENTR/D-TOPO vector (Thermo Fisher Scientific, K240020). The obtained pENTR/D-TOPO *RBA1* and *RBA1* mutant plasmids were LR-recombined into pXCSG vectors with a C-terminal MYC tag. *AtNUDT7* and *PDE9* were cloned into pEGAD vectors with a C-terminal GFP tag by ligation and the obtained pENTR/D-TOPO *mCNPase1*, *AtCPDase*, *Avr3b* plasmids were LR-recombined into pXCSG vectors with a C-terminal 3×HA tag. All the constructs were verified by DNA sequencing. Generated constructs were transformed into *Agrobacterium tumefaciens* (Rhizobium radiobacter) GV3101 pMP90RK via electroporation.

RBA1 and *RBA1* mutants were expressed in leaves of four weeks old *N. benthamiana* plants using *agrobacteria*-mediated transient expression assays in the presence of the P19 suppressor of RNAi silencing. The final OD_{600} for each strain was set to 0.8. For co-infiltration, *agrobacteria* carrying TIR and hydrolases expression constructs were mixed at 1:1 ratio. TIRs mixed with the EV were applied as a negative control to rule out the possibility that high titer of *agrobacteria* would affect infection efficiency. To detect RBA1, RBA1 mutants and the co-infiltrated *At*NUDT7, *At*NUDT7^{E154Q} and PDE9 protein expression, *N. benthamiana* leaves were collected at 2 dpi, snap-frozen in liquid nitrogen, and ground to fine powder. The powder (~100 μl in a tube) was resuspended in 100 μl of urea-SDS sample buffer [50 mM Tris-HCl pH 6.8, 2% SDS, 8 M urea, 2% β-mercaptoethanol, 5% glycerol, protease inhibitor cocktail (Roche), and 0.004% Bromophenol Blue] and vortexed for 10 min at room temperature. No boiling step was included. After centrifugation at 16,000 *g* for 10 min, 10 μl of the supernatant was loaded onto 8% SDS-PAGE and proteins were blotted onto a PVDF membrane.

To detect co-infiltrated mCNPase, *At*CPDase and Avr3b proteins expression, 300 mg *N. benthamiana* leaves were collected at 2 dpi and snap-frozen in liquid nitrogen. All further steps were performed at 4°C if not mentioned otherwise. Tissue samples were ground to fine powder and resuspended in 1 ml of IP buffer [100mM Tris-HCl pH 7.5, 150 mM NaCl, 5 mM EDTA, 2 mM EGTA, 5% (v/v) glycerol, 1% Triton, 2% (w/v) PVPP, 10mM Dithiothreitol (DTT) 2% (v/v), protease inhibitor cocktail (Roche), 0.5 mM PMSF] and incubated for 1 h with gentle rotation. Debris was removed by centrifugation at 21,000 *g* for 15 min. Immunoprecipitations were performed with 5 μl rabbit polyclonal anti-HA antibody (Abcam 9110) coupled to 50 μl bed volume Protein A agarose (Roche) per sample. After 4 h of incubation under constant rotation, beads were washed 5 times in 1 mL IP buffer (without PVPP) and eluted by boiling in 100 μL of 2× Laemmli sample buffer for 10 min at 95°C. 10 μl was loaded onto 10% SDS-PAGE and proteins were blotted onto a PVDF membrane.

Immunoblot assays were performed using monoclonal rat anti-HA antibody (Sigma Aldrich, 11867423001), mouse anti-Myc antibody (ThermoScientific R950-25), and rabbit anti-GFP antibody (Chromtek.pabg1-100) diluted 1:3000 in 1× TBS, 0.1% Tween-20 with 5% non-fat milk powder. Proteins were detected with a Gel Doc XR+ Gel Documentation System by using ECL SuperSignal West Femto Maximum Sensitivity Substrate and ECL Western Blotting substrate (Thermo Scientific) in a ratio of 2:1.

Cell death quantification in *N. benthamiana*

RBA1 and *RBA1* mutants and combinations with 2′,3′-cAMP/cGMP hydrolase *AtNUDT7*, *PDE9*, *mCNPase*, *AtCPDase* and *Avr3b* were transiently expressed in *N. benthamiana* as described above and three individual *agrobacteria*-infiltrated leaf zones were used for electrolyte leakage assays. Five 8-mm leaf discs from *N. benthamiana* agroinfiltrated leaves were taken at 3 dpi, washed in 10 to 20 mL of milliQ water (18.2 MΩ*cm, mQ) for 30 to 60 min, transferred to a 24-well plate with 1 mL mQ in each well, and incubated at room temperature. Electrolyte leakage was measured at 0 and 6 h with a conductometer Horiba Twin Model B-173. Statistical analysis was performed on conductivity data via Tukey′s HSD (honestly significant difference) test (a=0.05). Images of *agrobacteria*-infiltrated leaf spots were taken at 4 -5 dpi.

HopBA delivery assay

Cloning of the HopBA1 effector into bacterial type III secretion vector pCK014 to mobilize into the *Pseudomonas fluorescens* strain Pf0-1was performed as described (Gantner et al., 2018). Overnight grown Pf0-1 carrying HopBA-1 or EV bacteria were resuspended in 10 mM $MgCl_2$ to OD_{600} of 0.2 and infiltrated with a needleless syringe into rosette leaves of 5-6 weeks old *Arabidopsis* Ag-0 plants before noon. 3 infiltrated leaves were harvested from each pot, leaves from 3 pots were harvested and snap-frozen at 24 or 36 hpi for 2′,3′-cAMP/cGMP detection. Images of infiltrated leaves were taken at 48 hpi.

In vivo 2′,3′-cNMP extraction and detection

2′,3′-cNMP were extracted from *N. benthamiana* or *Arabidopsis* as described (Van Damme et al., 2014). For WT and *RBA1* mutants infiltrated or *RBA1*-hydrolase co-infiltrated *N. benthamina* leaves, 3 individual infiltrated zones were harvested and snap-frozen at 3 dpi. For 4 weeks old Col-0 and *Atnudt7 eds1 Arabidopsis*, 3 leaves were harvested from each pot; for 4 weeks old *Atnudt7* leaves, due to the dwarf phenotype, 2 leaves were harvested from each pot. Leaves from 4 pots were harvested and snap-frozen. Frozen plant leaves were homogenized manually with a precooled mortar and pestle with liquid nitrogen. 100 (±5) mg ground tissue was transferred to precooled 2 ml. Eppendorf tubes. 600 μl 4% acetic acid with 20 μl 1mM phosphodiesterase inhibitor 3-isobutyl-1-methylxanthine (IBMX, Sigma) and 0.6 μl 1mM spike control 8-Br-2′,3′-cAMP (BioLog) were added to per 100 mg sample. The samples were vortexed for 2 min and subsequently centrifuged for 9 min at 9000 *g*. The supernatant was transferred into new precooled tubes. 800 μl chloroform was added to each tube. The tubes were gently inverted 6 times and then centrifuged at 6000 *g* for 6 min. Aqueous phase were collected and extracted again by chloroform. The samples were dried at 30°C in speed vacuum concentrator and reconstituted in 50 μl of water and vortexed for 1 min. The samples were centrifuged 12,000 *g* for 10 min, and the supernatant was applied to the LC-MS/MS for metabolite identification and quantification.

Metabolite measurement by LC-MS/MS

Chromatography was performed on a Nexera XR 40 series HPLC (Shimadzu) using a Synergi 4 μM Fusion-RP 80 Å 150×2mm column (Phenomenex). The column temperature was maintained at 40°C and the sample tray at 4°C. Samples (10 μl) were injected at a flow rate of 0.2 ml/min using 10 mM ammonium formate at pH 4.2 and methanol as mobile phases A and B, respectively. Metabolites were eluted using the profile 0-8 min, 8-90% B; 8-10 min, 90% B; 10-10.1 min 90-8% B; 10.1-20 min, 8% B. The LCMS-8060 triple quadrupole mass spectrometer with electro spray ionization (Shimadzu) was operated in positive mode. Scheduled multiple reaction monitoring (MRM) was used to monitor analyte parent ion to product ion formation. MRM conditions were optimized using authentic standard chemicals including: 2′,3′-cAMP ($[M+H]^+$ 330.00>136.20, 330.00>99.15, 330.00>119.15), 2′,3′-cGMP ($[M+H]^+$ 346.00>152.15, 346.00 >135.20, 346.00>110.15), 2′,3′-cCMP ($[M+H]^+$ 306.00>112.15, 306.00>95.20, 306.00>178.20), 2′,3′-cUMP ($[M+H]^+$ 307.00>113.15, 307.00>195.10, 307.00>136.15), 8-Br-2′,3′-cAMP ($[M+H]^+$ 407.90 >214.00, 407.90>99.20, 407.90>69.25), 3′,5′-cAMP ($[M+H]^+$ 329.80>135.95, 329.80>311.90, 329.80>96.95), 3′,5′-cGMP ($[M+H]^+$ 345.90>151.95, 345.90>135.05, 345.90>110.20), 3′,5′-cCMP ($[M+H]^+$ 306.00>112.20, 306.00>95.20, 306.00>69.20), 3′,5′-cUMP ($[M+H]^+$ 307.00>97.15, 307.00>148.15, 307.00>113.15). Both Q1 and Q3 quadrupoles were maintained in unit resolution. LabSolutions LCMS v5.97 software was used for data acquisition and LabSolutions Postrun for processing (both Shimadzu). Metabolites were quantified by scheduled MRM peak integration using external calibration curves of standard chemicals.

2.3 The leucine-rich repeats in allelic barley MLA immune receptors define specificity towards sequence-unrelated powdery mildew avirulence effectors with a predicted common RNase-like fold

Saskia Bauer, Dongli Yu, Aaron W. Lawson, Isabel M. L. Saur, Lamprinos Frantzeskakis, Barbara Kracher, Elke Logemann, Jijie Chai, Takaki Maekawa, Paul Schulze-Lefert

Published in PLoS Pathogens *17* (2021)

Author contributions:
Conceptualization: S.B., I.M.L.S., P.S.-L. Data curation: S.B., I.M.L.S., L.F., B.K., T.M., P.S.-L. Formal analysis: S.B., D.Y., A.W.L, I.M.L.S., L.F., E.L. Funding acquisition: I.M.L.S., P.S.-L. Investigation: S.B., D.Y., A W.L, I.M.L.S., L.F., E.L., T.M., P.S.-L. Methodology: S.B., D.Y., E.L. Project administration: P.S.-L. Resources: I.M.L.S., T.M., P.S.-L. Software: B.K. Supervision: I.M.L.S., J.C., P.S.-L. Validation: I.M.L.S. Visualization: S.B., I.M.L.S., L.F., B.K. Writing – original draft: S.B, I.M.L.S, P.S.-L. Writing – review & editing: S.B, I.M.L.S, L.F, B.K., J.C., P.S.-L.

Specific contributions:
In this study, I showed that AVR_A effectors have no RNase activity *in vitro*. This pseudo-enzyme activity of AVR_A effectors was further supported by testing AVR_A effectors purified from different expression systems. These data exclude a potential enzymatic activity of the AVR_A effectors, therefore my work is substantial for this paper.

Page numbers in the attached paper are not counted in the pagination of the thesis.

PLOS PATHOGENS

RESEARCH ARTICLE

The leucine-rich repeats in allelic barley MLA immune receptors define specificity towards sequence-unrelated powdery mildew avirulence effectors with a predicted common RNase-like fold

Saskia Bauer[1], **Dongli Yu**[1,2], **Aaron W. Lawson**[1], **Isabel M. L. Saur**[1], **Lamprinos Frantzeskakis**[3¤a], **Barbara Kracher**[1], **Elke Logemann**[1], **Jijie Chai**[2,4], **Takaki Maekawa**[1¤b], **Paul Schulze-Lefert**[1,4]*

1 Department of Plant Microbe Interactions, Max Planck Institute for Plant Breeding Research, Cologne, Germany, **2** Institute of Biochemistry, University of Cologne at Max Planck Institute for Plant Breeding Research, Cologne, Germany, **3** DOE Joint Genome Institute, Berkeley, California, United States of America, **4** Cluster of Excellence on Plant Sciences, Düsseldorf, Germany

¤a Current address: Bayer Crop Science, West Sacramento, California, United States of America
¤b Current address: Institute for Plant Science, University of Cologne, Cologne, Germany, Cluster of Excellence on Plant Sciences, Düsseldorf, Germany
* schlef@mpipz.mpg.de

Citation: Bauer S, Yu D, Lawson AW, Saur IML, Frantzeskakis L, Kracher B, et al. (2021) The leucine-rich repeats in allelic barley MLA immune receptors define specificity towards sequence-unrelated powdery mildew avirulence effectors with a predicted common RNase-like fold. PLoS Pathog 17(2): e1009223. https://doi.org/10.1371/journal.ppat.1009223

Editor: Bostjan Kobe, University of Queensland, AUSTRALIA

Received: June 23, 2020

Accepted: December 7, 2020

Published: February 3, 2021

Data Availability Statement: RNA-seq data can be found in the National Center for Biotechnology Information Gene Expression Omnibus (GEO) database (accession no. GSE110266, GSE106282 and GSE83237). Primary data and intermediate files of the phylogenetic analysis can be found at https://github.com/lambros-f/avra6_2019 All other relevant datasets are shown within the manuscript and its Supporting Information files.

Abstract

Nucleotide-binding domain leucine-rich repeat-containing receptors (NLRs) in plants can detect avirulence (AVR) effectors of pathogenic microbes. The *Mildew locus a* (*Mla*) NLR gene has been shown to confer resistance against diverse fungal pathogens in cereal crops. In barley, *Mla* has undergone allelic diversification in the host population and confers isolate-specific immunity against the powdery mildew-causing fungal pathogen *Blumeria graminis* forma specialis *hordei* (*Bgh*). We previously isolated the *Bgh* effectors AVR_{A1}, AVR_{A7}, AVR_{A9}, AVR_{A13}, and allelic AVR_{A10}/AVR_{A22}, which are recognized by matching MLA1, MLA7, MLA9, MLA13, MLA10 and MLA22, respectively. Here, we extend our knowledge of the *Bgh* effector repertoire by isolating the AVR_{A6} effector, which belongs to the family of catalytically inactive RNase-Like Proteins expressed in Haustoria (RALPHs). Using structural prediction, we also identified RNase-like folds in AVR_{A1}, AVR_{A7}, AVR_{A10}/AVR_{A22}, and AVR_{A13}, suggesting that allelic MLA recognition specificities could detect structurally related avirulence effectors. To better understand the mechanism underlying the recognition of effectors by MLAs, we deployed chimeric MLA1 and MLA6, as well as chimeric MLA10 and MLA22 receptors in plant co-expression assays, which showed that the recognition specificity for AVR_{A1} and AVR_{A6} as well as allelic AVR_{A10} and AVR_{A22} is largely determined by the receptors' C-terminal leucine-rich repeats (LRRs). The design of avirulence effector hybrids allowed us to identify four specific AVR_{A10} and five specific AVR_{A22} aa residues that are necessary to confer MLA10- and MLA22-specific recognition, respectively. This suggests that the MLA LRR mediates isolate-specific recognition of structurally related AVR_{A} effectors. Thus, functional diversification of multi-allelic MLA receptors may be driven by a common structural effector scaffold, which could be facilitated by proliferation of the RALPH effector family in the pathogen genome.

Author summary

Barley powdery mildew caused by the fungus *Blumeria graminis* forma specialis *hordei* (*Bgh*) can result in annual yield losses of 15% of this cereal crop. *Bgh* promotes virulence in plants through the secretion of diverse effector molecules, small proteins of which a subset enters into and modifies the immune status and physiology of the host leaf. In response, the host has evolved a multitude of disease resistance genes. The *Mildew locus a* (*Mla*) resistance gene stands out because diversification in the host population has generated numerous *Mla* variants encoding multi-domain receptors, each of which can directly recognize an isolate-specific *Bgh* effector, designated as avirulence (AVR_A) effectors. Recognition of AVR_A effectors by MLA triggers plant immune responses, a phenomenon known as isolate-specific resistance, which invariably results in localized host cell death. Here, we identify the powdery mildew effector AVR_{A6} and validate its specific interaction with its matching receptor MLA6. Furthermore, through the use of hybrid receptors constructed from MLA1 and MLA6 as well as MLA10 and MLA22 receptors, we provide insights into the specific domains and amino acid residues generally important for AVR_A recognition by MLA receptors. We find that sequence variation in the leucine-rich repeats (LRRs) of multi-allelic MLA receptors determines specific recognition of AVR_A effectors. These effectors are sequence-unrelated, but our analysis indicates that they may be structurally related. This data may assist in the future generation of synthetic immune receptors with pre-defined recognition specificities.

Introduction

Plants have evolved sophisticated innate immune systems to protect themselves against colonization by pathogenic microbes [1,2]. At the population level, a host-adapted pathogenic species is comprised of numerous isolates/races with distinctive genetic blueprints which determine their infection phenotypes on individual accessions (genotypes) of a plant host population. In isolate-specific resistance, individual host accessions often mount a hypersensitive immune response against a subset of pathogenic isolates [3,4]. Isolate-specific resistance is mediated by genetic interactions between plant host resistance (*R*) genes and matching pathogen avirulence (*AVR*) effector genes (gene-for-gene model) [5]. Plant *R* genes often encode intracellular nucleotide-binding domain leucine-rich repeat-containing receptors (NLRs) [6]. These receptors have a characteristic modular domain architecture, consisting of a variable N-terminal Coiled-Coil (CC), Toll-Interleukin (TIR) domain or HeLo domain (named after the fungal HET-S and LOPB proteins), a central NB-ARC (*nucleotide-binding* adaptor shared by APAF-1, certain *R* gene products, and CED-4) domain, and C-terminal leucine-rich repeats (LRRs) [7,8]. The LRRs often constitute a determinant for specific pathogen recognition. NLRs can detect AVRs by direct interaction [9–11], a receptor-integrated decoy [12], or indirectly detecting effector-mediated alterations of a host target [13]. Upon AVR recognition by NLRs, a localized host cell death is typically, but not invariably, associated with receptor-mediated immunity.

Funding: This work was supported by the Max Planck Society (SB and PSL), the Deutsche Forschungsgemeinschaft (DFG, German Research Foundation) in the Collaborative Research Centre Grant (SFB-1403 – 414786233 to JC, TM, PSL) and under Germany's Excellence Strategy – EXC-Number 2048/1 – project 390686111 (PSL), the Horizon 2020 Framework Programme (742263) and the Daimler and Benz Foundation (both to IMLS). Work conducted by the U.S. Department of Energy Joint Genome Institute, a DOE Office of Science User Facility, is supported by the Office of Science of the U.S. Department of Energy under Contract No. DE-AC02-05CH11231 (to LF). The funders had no role in study design, data collection and analysis, decision to publish, or preparation of the manuscript.

Competing interests: The authors have declared that no competing interests exist.

Here, we study the *NLR* gene *Mildew locus a* (*Mla*), which has the capacity to confer isolate-specific resistance against both biotrophic basidiomycete and ascomycete fungal pathogens in closely related host cereal species, including wheat and barley. The barley *Mla* locus contains a cluster of *NLR* genes and is orthologous to the *Stem Rust* (*Sr*) resistance loci *Sr33* and *Sr50* in wheat, which confer immunity against specific isolates of the barley powdery mildew *Blumeria graminis* f. sp. *hordei* (*Bgh*) and against the wheat rust pathogen *Puccinia graminis* f. sp. *tritici* (*Pgt*), respectively [14–16]. *Bgh* and *Pgt* are filamentous eukaryotic pathogens that belong to different phyla and diverged from each other approximately 500–650 million years ago [17]. Furthermore, *Resistance to Magnaporthe oryzae* (*RMo1*) confers immunity to the rice blast pathogen in barley, and also maps to the barley *Mla* locus [18].

In barley, the *Mla* gene has undergone tremendous diversification into over 30 different allelic resistance specificities in the host population [19,20]. This is the result of a co-evolutionary arms race in which each *Mla* allele recognizes a matching $\mathrm{AVR_A}$ effector encoded by a subset of *Bgh* isolates [14]. Prior to the molecular isolation of *Bgh* $\mathrm{AVR_A}$ effectors, domain swap experiments with MLA1 and MLA6 suggested that the LRR is a determinant of isolate-specific disease resistance, an idea which is further supported by the observation that most sites under positive selection map to the predicted solvent-exposed sites of the LRR [19,20]. A multi-allelic *Powdery mildew 3* (*Pm3*) resistance locus also evolved in wheat populations, in which it confers isolate-specific resistance against the wheat powdery mildew *Blumeria graminis* f. sp. *tritici* (*Bgt*) through recognition of sequence-unrelated but possibly structurally related *Bgt* AVRPM3 effectors [21,22]. Although barley *Mla* and wheat *Pm3* both encode CC-type NLRs, the receptors are sequence-unrelated and map to non-syntenic locations in the genomes of the sister host species. Most sites that are polymorphic between different *Pm3* resistance alleles localize to the LRR [23–26]. For other multi-allelic NLRs, yeast two-hybrid and co-immunoprecipitation experiments with matching effectors suggested that the LRRs determine isolate-specific resistance by direct effector binding [10,27]. However, it remains unclear whether AVRPM3 effectors directly bind to PM3 receptors and whether the LRRs of allelic variants of MLA or PM3 receptors are directly responsible for specific discrimination between powdery mildew avirulence effectors, and thereby for isolate-specific recognition.

Recently, we identified the sequence-unrelated *Bgh* effectors $\mathrm{AVR_{A1}}$, $\mathrm{AVR_{A7}}$, $\mathrm{AVR_{A9}}$, $\mathrm{AVR_{A13}}$, and allelic $\mathrm{AVR_{A10}}/\mathrm{AVR_{A22}}$ [11,28], which are recognized by barley MLA1, MLA7, MLA9, MLA13, MLA10 and MLA22, respectively [11]. Experiments in yeast, in the absence of other plant proteins, provided evidence for direct interaction of three receptor-effector pairs, namely MLA7/$\mathrm{AVR_{A7}}$, MLA10/$\mathrm{AVR_{A10}}$, and MLA13/$\mathrm{AVR_{A13}}$ [11]. However, it is not known how MLA receptors with >90% sequence identity can recognize the sequence-unrelated fungal *Bgh* effectors. Structural relatedness between effectors, which is needed for recognition by allelic variants of MLA, could explain this phenomenon. For instance, based on structural predictions, ~15% of candidate-secreted effector proteins (CSEPs) were predicted as RNase-Like Proteins expressed in Haustoria (RALPHs), among them, CSEP0064 [29–31]. The X-ray structure of *Bgh* CSEP0064 indeed revealed a ribonuclease-like fold. Structural overlay of CSEP0064 and the active fungal F1 RNase from *Fusarium moniliforme* demonstrated the absence of canonical catalytic residues in the predicted substrate-binding pocket of CSEP0064 [30]. Notably, $\mathrm{AVR_{A7}}$ and $\mathrm{AVR_{A13}}$ but not the other isolated *Bgh* $\mathrm{AVR_A}$ proteins were predicted by IntFOLD version 3.0 to also adopt a RNase-like fold. Here, we used a transcriptome-wide association study (TWAS) approach [11,28] to identify the effector recognized by the barley *Mla6* receptor. The protein which we identified as $\mathrm{AVR_{A6}}$, CSEP0254, is very likely structurally similar to the RALPH effector CSEP0064 [30]. By applying version 5.0 of the structural prediction algorithm IntFOLD [32], we found that all identified $\mathrm{AVR_A}$ effectors are predicted to share structural similarity with fungal RNases, but similar to all other *Bgh* ribonuclease-likes

CSEPs, the isolated AVR_A effectors also lack the residues critical for catalytic activity [30,31]. By taking advantage of previously engineered hybrid receptors of MLA1 and MLA6 we confirm that the molecular basis of isolate-specific disease resistance against *Bgh* isolates A6 and K1 lies in the specific recognition of AVR_{A6} and AVR_{A1} effectors by six and 12 C-terminal LRRs of MLA1 and MLA6 receptors, respectively. We find that the LRRs of allelic MLA10 and MLA22 are largely sufficient for specific perception of allelic AVR_{A10} and AVR_{A22} effector proteins. Co-expression of hybrid effectors generated from allelic AVR_{A10} and AVR_{A22} with MLA10 and MLA22 receptors revealed that multiple effector residues participate in AVR_A recognition specificities. Our findings imply a model in which co-evolution of the barley *Mla-Bgh* AVR_a pathogen interaction is driven MLA sequence diversification upon detection of a common structural effector scaffold. This co-evolutionary process may have contributed to the proliferation and sequence diversification of RALPH effectors in the powdery mildew genome.

Results

TWAS identifies *BLGH_00709* (*CSEP0254*) as an AVR_{a6} candidate

For the isolation of AVR_{a6}, we examined the gene-wise association of *Bgh* transcriptomes with the published infection phenotypes of 27 *Bgh* isolates on *Mla6* barley lines [11,28]. We used the previously described *in planta* fungal transcripts of the 27 *Bgh* isolates and their published infection phenotypes on barley *Mla6* near-isogenic lines (NILs) of the barley cultivars (*cv.*) Pallas and Manchuria [11]. In short, we integrated high-confidence non-synonymous variants over each annotated *Bgh* gene and considered absence of a transcript as a missing genotype to obtain gene-wise genotypes. We then tested the gene-wise genotypes for association with the observed avirulence phenotypes using Fisher's exact test [11]. Association mapping identified a number of genes encoding CSEPs. The *csep* encoding genes with the lowest *p*-values in this analysis were *BLGH_00709* (*CSEP0254*; gene-wise: p = 7,40E-07) and *BLGH_00697* (p = 7.25E-07), suggesting them to be top-ranking candidates for AVR_{a6} (Fig 1A, S1 and S2 Tables). To first determine which candidate is recognized by MLA6 in barley, we transiently co-expressed the AVR_a candidate gene and *Mla6* receptor gene in *cv*. Golden Promise barley protoplasts. Co-expression of matching AVR_a-*Mla* pairs in this system triggers a reduction in luciferase (LUC) reporter gene activity as a proxy for cell death [33]. Co-expression of *BLGH_00709* and *Mla6* led to a significant reduction of relative LUC activity in comparison to the empty vector (EV) control (98% reduction), while co-expression of *BLGH_00697* with *Mla6* did not reduce LUC activity (S1 Fig). This suggests that *BLGH_00709* is recognized by *Mla6* in barley, and we therefore subjected *BLGH_00709* to further analysis as the top AVR_{a6} candidate.

First, we analyzed the gene architecture of the AVR_{a6} candidate gene in the available genomes of the *Bgh* isolates DH14 and RACE1 (both avirulent on *Mla6* lines). The annotated near chromosome-level reference genome of the DH14 *Bgh* isolate harbors two more identical copies of *BLGH_00709*. These copies are annotated as *BLGH_00708* and *BLGH_07091* (Fig 1B). Additionally, DH14 harbors another *CSEP0254* paralog, called *BLGH_07092*. In comparison to *BLGH_00709*, *BLGH_07092* carries a frameshift mutation that predicts an altered sequence from aa 64 onwards in the *BLGH_07092* encoded protein (Fig 1D). *BLGH_00708* and *BLGH_00709* are located in close proximity to each other in a head-to-tail orientation next to the cyclin B1 gene on scaffold 16 of the DH14 genome, while *BLGH_07091* resides with *BLGH_07092* on scaffold 309 in a head-to-head orientation. In the genome of the *Mla6* avirulent RACE1 isolate, three identical copies of *BLGH_00709* can be found on tig00005311: *BLGHR1_15960* (syntenic position to *BLGH_00709*) is located next to the cyclin B1 gene and on the same scaffold *BLGHR1_15970* (syntenic position to *BLGH_07091*) and *BLGHR1_15971*

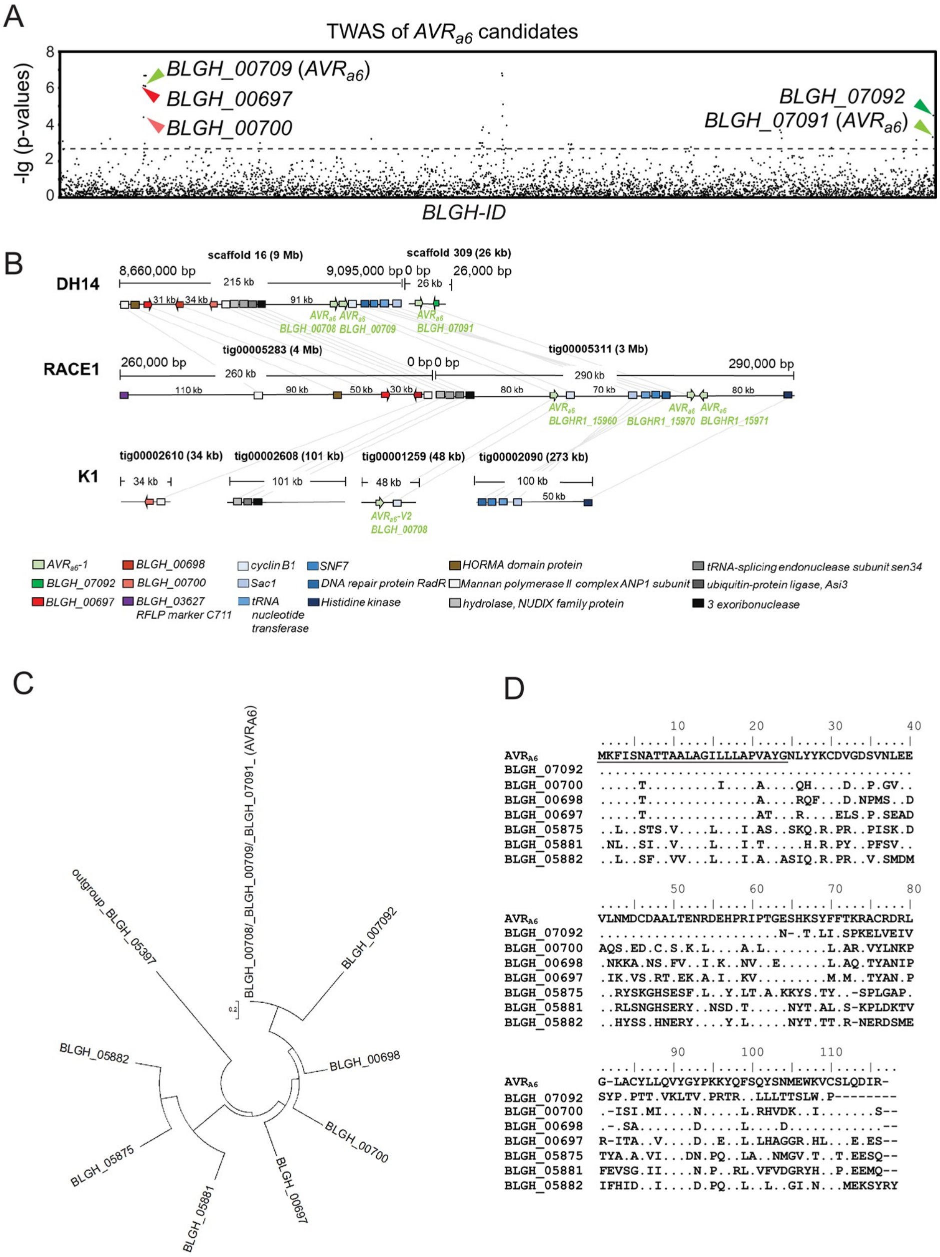

```
                   10        20        30        40
          ....|....|....|....|....|....|....|....|
AVRA6      MKFISNATTAALAGILLLAPVAYGNLYYKCDVGDSVNLEE
BLGH_07092 ........................................
BLGH_00700 .....T.........I....A....QH....D..P.GV..
BLGH_00698 .....T..............A....RQF...D.NPMS..D
BLGH_00697 .....T..............AT...R....ELS.P.SEAD
BLGH_05875 ..L..STS.V....L...I.AS..SKQ.R.PR..PISK.D
BLGH_05881 .NL..SI..V....L...I.T.....H.R.PY..PFSV..
BLGH_05882 ..L..SF..VV...L...I.A..ASIQ.R.PR..V.SMDM

                   50        60        70        80
          ....|....|....|....|....|....|....|....|
AVRA6      VLNMDCDAALTENRDEHPRIPTGESHKSYFFTKRACRDRL
BLGH_07092 ......................N-.T.LI.SPKELVEIV
BLGH_00700 AQS.ED.C.S.K.L....A.L.........L.AR.VYLNKP
BLGH_00698 .NKKA.NS.FV..I.K..NV..E......L.AQ.TYANIP
BLGH_00697 .IK.VS.RT.EK.A.I..KV.........M.M..TYAN.P
BLGH_05875 ..RYSKGHSESF.L..Y.LT.A.KKYS.TY..-SPLGAP.
BLGH_05881 ..RLSNGHSERY..NSD.T.....NYT.AL.S-KPLDKTV
BLGH_05882 ..HYSS.HNERY....Y.L.....NYT.TT.R-NERDSME

                   90       100       110
          ....|....|....|....|....|....|....|...
AVRA6      G-LACYLLQVYGYPKKYQFSQYSNMEWKVCSLQDIR-
BLGH_07092 SYP.PTT.VKLTV.PRTR..LLLTTSLW.P--------
BLGH_00700 .-ISI.MI....N.....L.RHVDK..I.......S--
BLGH_00698 .-.SA.......D.....L....D............--
BLGH_00697 R-ITA..V....D..E..L.LHAGGR.HL...E.ES--
BLGH_05875 TYA.A.VI...DN.PQ..LA..NMGV.T..T.EESQ--
BLGH_05881 FEVSG.II....N.P..RL.VFVDGRYH..P.EEMQ--
BLGH_05882 IFHID..I....D.PQ..L..L..GI.N...MEKSYRY
```

Fig 1. Identification of *BLGH_00709* (*CSEP0254*) as one of the top ranking *AVR$_{a6}$* candidates by association of *Bgh AVR$_a$* profiles on *Mla6* near-isogenic lines with transcript polymorphisms. (A) Manhattan plot summarizing the gene-wise association results for candidate *AVR$_{a6}$*. The x axis represents the *Bgh* DH14 genes, sorted by *Bgh* gene ID; the y axis shows −lg of p-values for all genes with at least one nonsynonymous coding SNP, indels as well as presence or absence of transcripts. CSEPs with a $p < 0.018$ (dotted line) are depicted by arrowheads. The candidate *AVR$_{a6}$* gene copies *BLGH_00709* (*CSEP0254*) and *BLGH_07091* are designated in the plot with bright green arrowheads. *BLGH_07092* is designated by a dark green arrowhead. The other candidates *BLGH_00697* (*CSEP0058*) and *BLGH_00700* are depicted with a dark red and a bright red arrowhead, respectively. (B) Schematic illustration of the chromosomal regions harboring the *AVR$_{a6}$* candidate *BLGH_00709* and its paralogues and family members with corresponding gene IDs in the genomes of *Bgh* isolates DH14, RACE1, and K1. All CSEPs are depicted by arrows. (C) Phylogeny of CSEP family 8 containing AVR$_{A6}$, which can be divided into clade 1 (BLGH_00709, BLGH_07092, BLGH_00700, BLGH_00698, BLGH_00697) and clade 2 (BLGH_05882, BLGH_05875, BLGH_05881), based on the protein sequences excluding the signal peptide and using BLGH_05397 as an outgroup. (D) Protein sequence alignment of AVR$_{A6}$ and CSEP family 8 members including their respective signal peptides.

https://doi.org/10.1371/journal.ppat.1009223.g001

(syntenic position to *BLGH_07092*) reside in a head-to-head orientation. Further analysis of genes surrounding the AVR_{a6} locus in DH14 and RACE1 suggests major genomic rearrangements: a gene cluster containing a tRNA nucleotide transferase and the DNA repair protein RadR is present in inverted orientation in scaffold 16 and tig00005311, and the *BLGH_00700* family member cannot be found on tig0005283 of the RACE1 genome (Fig 1B). For simplicity, from here on we will refer to the three sequence-identical paralogues *BLGH_00709*, *BLGH_00708*, and *BLGH_07091* as AVR_{a6}. $\mathrm{AVR_{A6}}$ is part of the CSEP family 8, which contains six additional members and can be subdivided into two clades: $\mathrm{AVR_{A6}}$, BLGH_07092, BLGH_00698 (CSEP0333), BLGH_00700, and BLGH_00697 (CSEP0058) belong to clade 1, whereas BLGH_05881 (CSEP0151), BLGH_05875 (CSEP0147), and BLGH_05882 (CSEP0148) belong to clade 2 (Fig 1C). The clade 1 CSEP family 8 members share a 48.3–60.4% sequence identity with $\mathrm{AVR_{A6}}$, while the clade 2 family members share a 32.9–39.7% sequence identity with the avirulence effector candidate. As *BLGH_07092* is most likely a nonfunctional copy of AVR_{a6}, and its expression is lower when compared to AVR_{a6} in every *Bgh* isolate (S2 Fig), we did not subject it to further analysis.

Analysis of transcriptomic data revealed that all isolates avirulent on the *cv*. Manchuria and *cv*. Pallas *Mla6* NILs express AVR_{a6}, which encodes a 115-aa-long protein with a predicted 24-aa-long signal peptide (SP) (S3 and S4 Figs). AVR_{a6} possesses one intron, which is spliced out in all transcripts of avirulent isolates. However, we identified transcripts of AVR_{a6} carrying this intron in all *Bgh* isolates virulent on *Mla6* NILs. The transcription of the AVR_{a6} intron may be facilitated by two different mechanisms (S4 Fig): The AVR_{a6} transcript variant expressed in the virulent isolates CC66 and CC148 exhibits a T270C mutation in the intron branch point consensus sequence, suggesting that intron retention may be caused by inefficient or nonexistent U2 spliceosome recognition (S4B Fig). If this is the case, the intron retention leads to a premature stop codon and a truncated protein, which is only 79 aa-long including the signal peptide. This deduced truncated protein variant, which we named $\mathrm{AVR_{A6}}$-V1, would also harbor A48S, A75T, and R79S amino acid substitutions. The isolates K1, K2, K3, B103, S15, S16, S22, and S25 are virulent on *Mla6* lines and contain a splice donor site mutation (S3 and S4B Figs) in the transcripts that maps to the AVR_{a6} gene of the reference genome. Genome analysis of isolate K1 [11] confirmed this splice-site mutation (Fig 1B). The predicted intron retention in the transcript of the AVR_{a6} variant expressed by the K1, K2, K3, B103, S15, S16, S22, and S25 isolates leads to a premature stop codon as well as to a predicted 79-aa-long truncated protein (S4B Fig). In addition, the encoded protein exhibits two amino acid substitutions when compared to $\mathrm{AVR_{A6}}$: A75T and R79I and we named this variant $\mathrm{AVR_{A6}}$-V2. Furthermore, the number of transcripts from virulent *Bgh* isolates that map to AVR_{a6} is approximately four-fold lower than the AVR_{a6} transcripts in the avirulent DH14 isolate (S2 Fig), which could be a consequence of nonsense-mediated mRNA decay. In conclusion, virulence of *Bgh* isolates on barley NILs harboring *Mla6* is likely conferred by SNPs in splice sites that may lead to intron retention in the respective genes. This is associated with reduced levels of the transcripts that map to the AVR_{a6} gene in *Bgh* isolates virulent on *Mla6* lines.

Transient co-expression assays provide evidence for specific recognition of AVR_{a6} by *Mla6*

To determine if the candidate $\mathrm{AVR_{A6}}$ is specifically recognized by MLA6, we first co-expressed AVR_{a6} and *Mla6* in a transient barley protoplast system containing leaf mesophyll cells [33]. Co-expression of matching AVR_{a6} or AVR_{a1} with *Mla6* or *Mla1*, respectively, triggered significant reductions in LUC activity, when compared to reference samples where the effector gene has been exchanged to an EV (98% and 85% reductions, respectively, Fig 2A). Co-expression

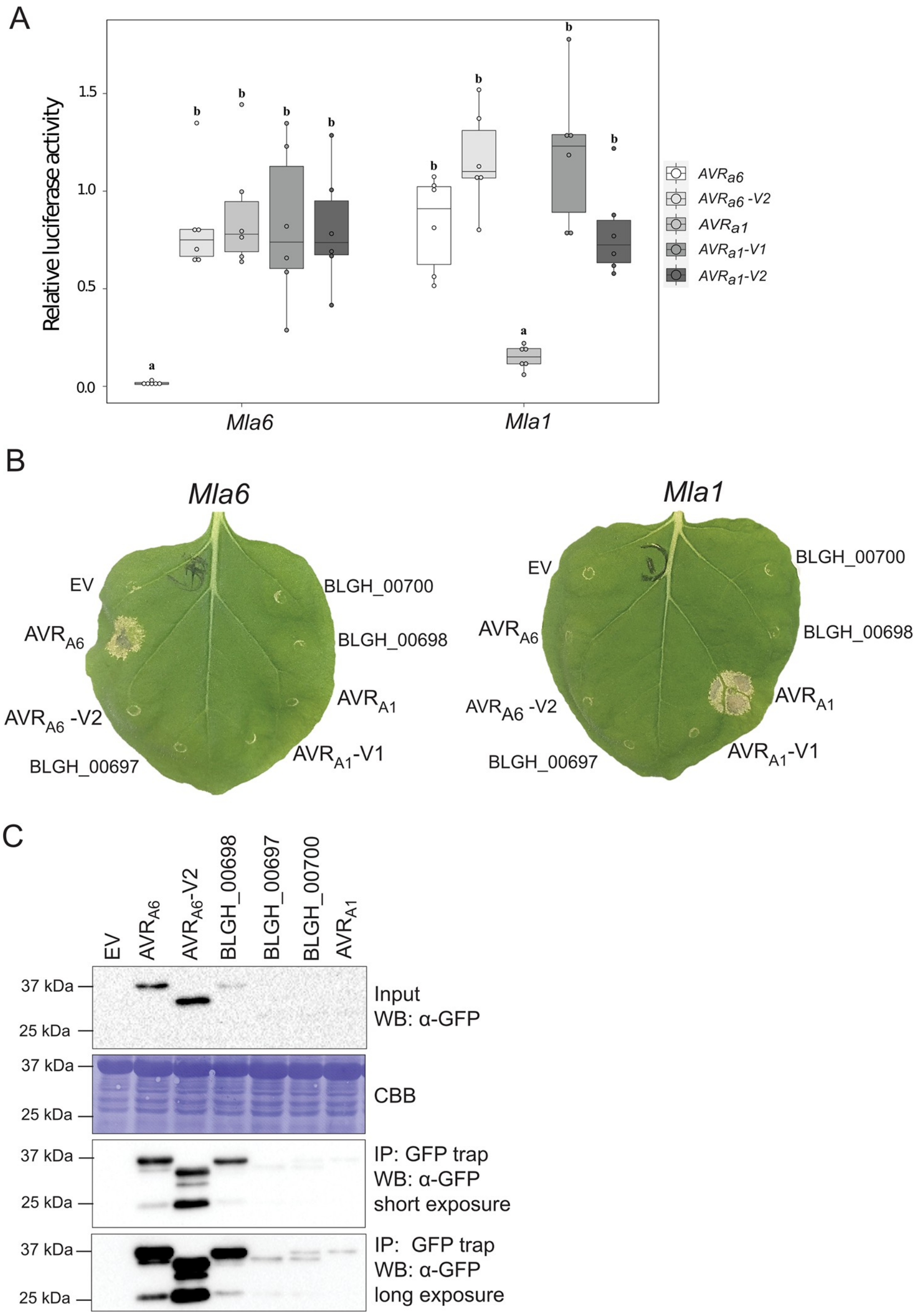

Fig 2. *Mla6* and AVR_{a6} co-expression in barley protoplasts and *N. benthamiana* causes a specific cell death response. (A) Barley *cv.* Golden Promise protoplasts were transfected with pIPKb002 vectors containing cDNAs of *Mla6* or *Mla1* and either an empty vector (EV), AVR_{a6}, AVR_{a6}-*V2*, AVR_{a1}, AVR_{a1}-*V1*, or AVR_{a1}-*V2* variants lacking their respective signal peptides together with a *pUBI:Luciferase* construct. The LUC activity relative to the EV sample was measured as a proxy for cell death 16 h post transfection. Box plot diagrams show median of the relative LUC activity of six independent transfections, which are represented by dots, while the box shows the interquartile range. Significant differences between samples were analyzed using non-parametric Kruskal-Wallis (KW) analysis followed by a Dunn's test. Calculated KW *p*-values are as follows: *Mla6*: $p = 0.007146$; *Mla1*: $p = 0.0007392$. Samples labeled with identical letters did not differ significantly ($p < 0.05$) in the Dunn's test for the corresponding *Mla* variant. (B) cDNAs of clade 1 AVR_{a6} family members *BLGH_00698*, *BLGH_00697*, *BLGH_00700*, AVR_{a6}, and AVR_{a1} variants were expressed without their respective signal peptides and stop codons and with a C-terminal mYFP fusion under the control of a 35S promotor in *N. benthamiana*. The effectors were co-expressed with *Mla1* and *Mla6* cDNAs fused C-terminally with a 4xmyc tag under the control of a 35S promotor. Cell death was scored five days post infiltration and

Figures show a representative of at least 15 co-transformations. (C) Protein levels of AVR_{A1}-mYFP, AVR_{A6}-mYFP, AVR_{A6}-V2-mYFP, BLGH_00698-mYFP, BLGH_00697-mYFP and BLGH_00700-mYFP. Samples for total protein extraction were harvested two days post infiltration. mYFP fusion proteins were enriched by an GFP-Trap. Proteins were separated using 10% or 12% polyacrylamide gels and proteins were detected using α-GFP and α-myc western blotting (WB). IP = immunoprecipitation. CBB = Coomassie Brilliant Blue.

https://doi.org/10.1371/journal.ppat.1009223.g002

of *Mla6* with a DNA sequence that encodes a truncated version of AVR_{a6} (likely encoded by AVR_{a6}*-V2*) or co-expression of AVR_{a6} with *Mla1* did not lead to significantly reduced LUC activity compared to samples co-expressing AVR_{a6} with *Mla6*, confirming the specificity of the recognition (Fig 2A).

To examine whether AVR_{A6} is recognized by MLA6 in a heterologous expression system without the presence of other barley proteins, we co-expressed the C-terminally mYFP-tagged effector fusion protein with the C-terminally 4xmyc-tagged receptor in *N. benthamiana*. Unlike the essentially complete cell death observed in the barley protoplast system (as evidenced by the very low levels of LUC activity), co-expression of AVR_{a6}*-mYFP* and *Mla6-4xmyc* triggered a cell death of varying confluence in *Agrobacterium tumefaciens* infiltrated tissue in independent *N. benthamiana* leaves compared to the cell death observed when co-expressing AVR_{a1} and *Mla1* (Figs 2B and S14). Co-expression of AVR_{a6}*-mYFP* with *Mla1-4xmyc* did not elicit cell death, confirming the specific recognition of candidate AVR_{A6} by MLA6 but not MLA1. No cell death was observed when *Mla6-4xmyc* was co-expressed with a DNA sequence that encodes a truncated version of AVR_{a6}*-mYFP* (here named AVR_{A6}-V2-mYFP), even though both AVR_{A} and MLA proteins are detectable in *N. benthamiana* leaf extracts (Figs 2B, 2C and 5C). Furthermore, co-expression of the clade 1 CSEP family 8 member *BLGH_00698-mYFP*, which shares the highest sequence similarity with AVR_{a6}, with *Mla6* did not lead to cell death, even though BLGH_00698-mYFP is detectable in *N. benthamiana* leaf extracts (Fig 2B and 2C). Detection of BLGH_00700 and BLGH_00697 proteins was possible only after enrichment with a GFP-Trap, suggesting that their protein stability is lower than those of AVR_{A6} and BLGH_00698 in this system. A faster-migrating protein band for BLGH_00697-mYFP and a double band visible after blotting for BLGH_00700-mYFP suggest that these proteins may either be cleaved post-translationally by proteases in heterologous *N. benthamiana* or that they are not stable in the plant extraction buffer (Fig 2C). Taken together, co-expression of AVR_{A6} with MLA6 in both homologous and heterologous plant expression systems triggers a significant and specific cell death response, indicating specific effector recognition by the matching MLA immune receptor.

AVR_{A} effectors have low sequence similarity, but show predicted structural homology to RNases

We subjected AVR_{A6} to a phylogenetic analysis including all annotated CSEPs in *B. graminis* formae speciales *poae*, *lolium*, *avenae*, *tritici* (isolate 96224), *hordei* DH14, *secalis* (isolate S1459), *triticale* (isolate T1-20), and *dactylidis*, but were unable to detect significant polypeptide sequence relatedness to other known *Bgh* AVR_{A} effector proteins or to the so far isolated wheat powdery mildew avirulence effectors, AVRPM2, $\text{AVRPM3}^{\text{A2/F2}}$, $\text{AVRPM3}^{\text{B2/C2}}$, and $\text{AVRPM3}^{\text{D3}}$ (Fig 3A). However, we noted that all the avirulence proteins isolated from barley and wheat powdery mildews belong to CSEPs with a length of approximately 80 to 130 amino acids when neglecting their respective signal peptides. The same is true for CSEP0064, which was shown to form a RNase-like protein structure. To determine potential structural similarity between AVR_{A6} and known *Bgh* effectors, we subjected AVR_{A6} to structural prediction using IntFOLD version 5.0 [32]. AVR_{A6} exhibited high predicted structural similarity to the RNase-

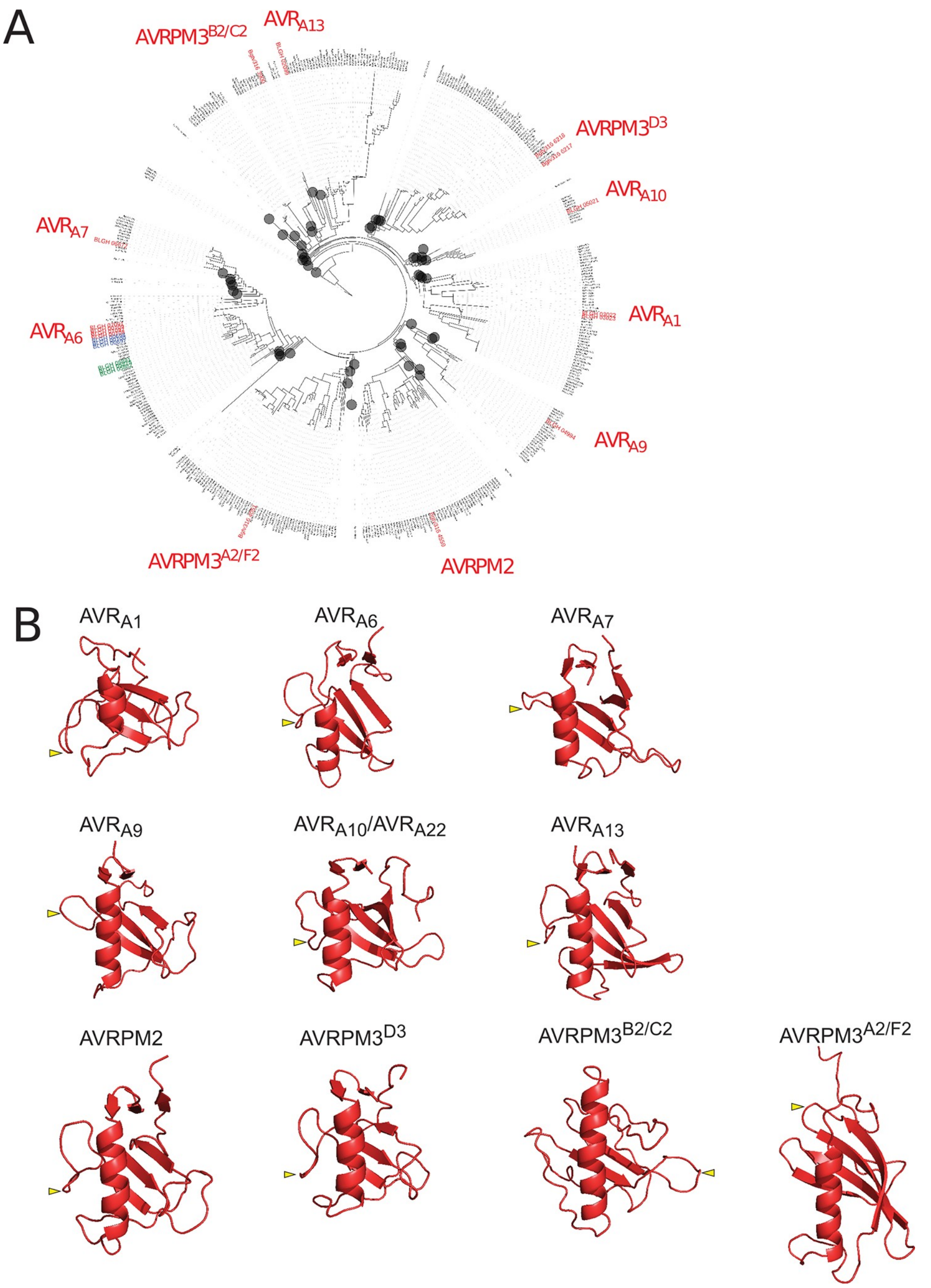

Fig 3. *Bgh* AVR$_A$ and *Bgt* AVRPM effectors are sequence-unrelated but exhibit predicted structural similarity to RNases. (A) Maximum likelihood phylogeny including all predicted CSEPs from *B. graminis* formae speciales *poae*, *lolium*, *avenae*, *tritici* 96224, *hordei* DH14, *secalis* S1459, *triticale* T1-20, and *dactylidis*. Depicted in red are the BLGH-IDs of all so far isolated *Bgh* AVR$_A$ and *Bgt* AVRPM effectors. Depicted in blue are the clade-1 family members of AVR$_{A6}$, while the clade-2 family members are colored in green. CSEP clades that were collapsed (grey circles) to improve legibility of the tree do not include AVR members and are indicated by grey circles. (B) Structural prediction of isolated AVR$_A$s and AVRPM by IntFOLD version 5.0 in red (p-values: AVR$_{A1}$ = 4.888e^{-4} most similar to PDB IDs 5gy6, 3who and 1rds, AVR$_{A6}$ = 3.293e^{-5} to 6fmb, AVR$_{A7}$ = 2.114e^{-4} to PDB ID 5gy6, AVR$_{A9}$ = 1.18e^{-5} most similar to PDB IDs 6fmb, 3who, and 1ch0, AVR$_{A10}$ = 9.759e^{-5} most similar to PDB ID 1fusa and to 3whoa, AVR$_{A13}$-1 = 7,359e^{-7} most similar to 6fmb, AVRPM2 = 8.741e^{-9} most similar to 6fmb, 1chOA, and 1rmsA, AVRPM3^{D3} = 8.82e^{-5} most similar to PDB 6fmb and 5gy6A, AVRPM3$^{A2/F2}$ = 1.145e^{-5} to 3ub1A2, AVRPM3$^{B2/C2}$ = 7.079e^{-2}, no structural similarities predicted). Yellow arrow depicts relative position of the characteristic RALPH intron in effector structures.

https://doi.org/10.1371/journal.ppat.1009223.g003

like fold observed for the X-ray structure, suggesting that $\mathrm{AVR}_{\mathrm{A6}}$ possesses a ribonuclease-like fold similar to $\mathrm{AVR}_{\mathrm{A13}}$ and $\mathrm{AVR}_{\mathrm{A7}}$ (S5 Fig). This prompted us to also reanalyze all isolated $\mathrm{AVR}_{\mathrm{A}}$ effectors using the with IntFOLD version 5.0. We found that $\mathrm{AVR}_{\mathrm{A1}}$, $\mathrm{AVR}_{\mathrm{A9}}$, and $\mathrm{AVR}_{\mathrm{A10}}$/$\mathrm{AVR}_{\mathrm{A22}}$ are also predicted to harbor a central α-helix directly facing three to four β-sheets with a topology characteristic of ribonucleases (Fig 3B). This is reminiscent of structural predictions for *Bgt* effectors AVRPM2 and $\mathrm{AVRPM3}^{\mathrm{D3}}$, which also suggested structural similarities to ribonucleases (Fig 3, [22,34–36]). Although the relationship to ribonucleases is less clear for *Bgt* $\mathrm{AVRPM3}^{\mathrm{A2/F2}}$ and $\mathrm{AVRPM3}^{\mathrm{B2/C2}}$, these two effectors were predicted to exhibit a central α-helix and two to four ß-sheets like $\mathrm{AVRPM3}^{\mathrm{D3}}$ ([22], Fig 3B). We examined AVR_a and *AvrPm* gene models for the presence of an intron, which is thought to be characteristic for RALPH effector-encoding genes [29,31] and identified one intron at position +163 to +201 bp after the end of the signal peptide (S6A and S7A Figs). The relative intron position in the structural predictions is in an unstructured loop between the first and the second ß-sheet, except in $\mathrm{AVR}_{\mathrm{A13}}$, $\mathrm{AVRPM3}^{\mathrm{A2/F2}}$, and $\mathrm{AVRPM3}^{\mathrm{B2/C2}}$ (Fig 3B). For the latter three effectors, the intron is positioned in a predicted unstructured loop C-terminal to the second ß-sheet (Figs 3B and S6). No common sequence motifs are detectable in the highly diverse intron sequences (S7B Fig). Thus, it remains unclear whether all known *Blumeria* avirulence effectors are descendants of one common "*ur*-RALPH" ancestor [29]. Irrespective of this, our analysis suggests that isolated *Bgh* and *Bgt* avirulence effectors are structurally related to fungal ribonucleases.

RNase-like $\mathrm{AVR}_{\mathrm{A}}$ effectors do not show ribonuclease activity

Using an RNase activity assay, we tested whether $\mathrm{AVR}_{\mathrm{A}}$ proteins are truly catalytically inactive as suggested for RNase-like *Bgh* effectors previously [29,30]. First, we expressed N-terminally GST-tagged $\mathrm{AVR}_{\mathrm{A6}}$, $\mathrm{AVR}_{\mathrm{A10}}$, and $\mathrm{AVR}_{\mathrm{A13}}$ in *Escherichia coli* and purified them by GST affinity chromatography. We then cleaved the GST tag and applied size-exclusion chromatography (S8A Fig). Successful protein expression and purification of the $\mathrm{AVR}_{\mathrm{A}}$ effector proteins was tested by SDS-PAGE (S8B Fig). We then incubated $\mathrm{AVR}_{\mathrm{A6}}$, $\mathrm{AVR}_{\mathrm{A10}}$, and $\mathrm{AVR}_{\mathrm{A13}}$ effectors with denatured *Hv*RNA or native rRNA to test for ribonuclease activity [37]. Using RNA gel electrophoresis, we observed a degradation of RNA when co-incubated with a commercially available T1 RNase, which has the same function as the *Fusarium* F1 RNase. We did not observe RNA degradation when incubating *Hv*RNA or rRNA with the $\mathrm{AVR}_{\mathrm{A}}$ effectors (Fig 4A and 4B). These results were independently validated with $\mathrm{AVR}_{\mathrm{A6}}$, $\mathrm{AVR}_{\mathrm{A10}}$, and $\mathrm{AVR}_{\mathrm{A13}}$ effector proteins that were produced in eukaryotic insect cells, followed by affinity chromatographic purification (S9A and S9B Fig). Taken together, the data indicate that $\mathrm{AVR}_{\mathrm{A}}$ effectors have no RNase activity, which is consistent with the previous prediction that ascribed pseudoenzymatic function to the RALPHs [29,30].

The C-terminal leucine-rich repeats of MLA1 and MLA6 receptors account for specific discrimination of structurally homologous $\mathrm{AVR}_{\mathrm{A1}}$ and $\mathrm{AVR}_{\mathrm{A6}}$ effectors *in planta*

A previous study showed that most of the residues under positive selection in allelic MLA resistance specificities in barley populations are located in the LRR region [19]. Using single-cell expression of MLA chimeras in barley leaf epidermal cells, C-terminal LRR regions of *Mla1* and *Mla6* were shown to encode determinants for isolate-specific immunity in barley to *Bgh* isolates K1 (carrying AVR_{a1}) and A6 (carrying AVR_{a6}) [38]. Here, we tested if the LRRs determine isolate-specific immunity by specifically recognizing $\mathrm{AVR}_{\mathrm{A}}$ effectors in barley. Therefore, we made use of the previously constructed intron-containing DNAs of the chimeric receptors *M16666*, *M11166*, *M61111*, and *M66111* ([38] (protein sequence shown in S10 Fig)

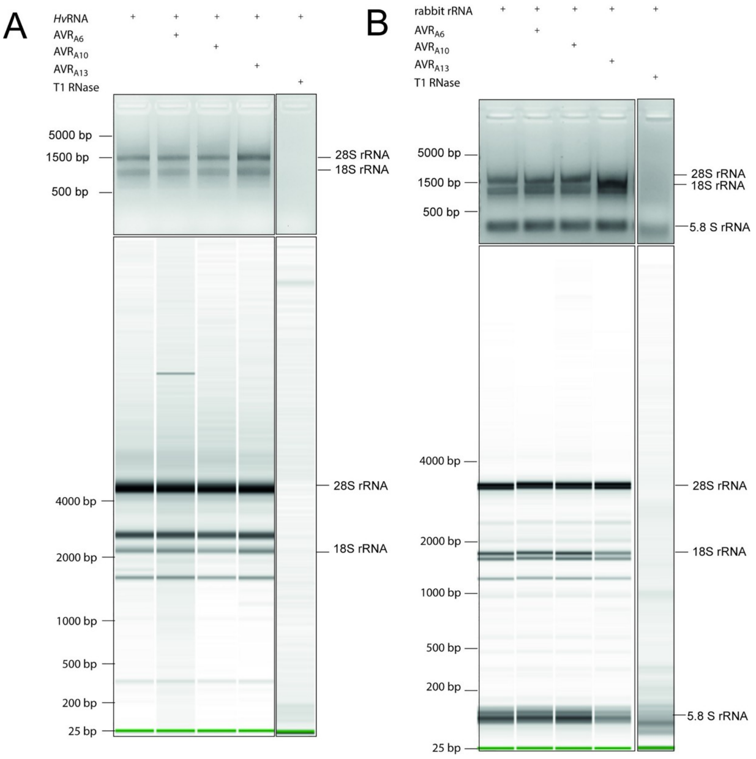

Fig 4. Recombinant AVR$_{A6}$, AVR$_{A10}$, and AVR$_{A13}$ effector proteins do not exhibit ribonuclease activity. To test for ribonuclease activity, heterologous AVR$_{A6}$, AVR$_{A10}$, and AVR$_{A13}$ proteins, purified upon expression of the respective genes in *E. coli*, or T1 RNase were co-incubated with (A) denatured *Hv*RNA and (B) native rabbit rRNA always. All samples were separated on non-denaturing 2% agarose gels (top panels) and analysed on a Bioanalyzer (lower panels) to check for RNA degradation.

https://doi.org/10.1371/journal.ppat.1009223.g004

and co-expressed them with matching *AVR$_{a6}$*, *AVR$_{a6}$-V2*, *AVR$_{a1}$*, and *AVR$_{a1}$-V1* cDNAs lacking the signal peptide (SP) in the pIPKb002 vector under the control of a strong maize ubiquitin promoter in barley protoplasts. Upon co-expression of *AVR$_{a6}$* with *M16666* or *M11166* we detected a significant 79% or 92% reduction in relative LUC activity when compared to the EV samples, respectively (Fig 5A). This reduction was not observed when *M16666* or *M11166* were co-expressed with *AVR$_{a6}$-V2*, *AVR$_{a1}$*, or *AVR$_{a1}$-V1*, respectively, suggesting that both chimeric receptors specifically recognize their matching effector (Fig 5A). These findings suggest that the last six C-terminal leucine-rich repeats of a total of 15 deduced LRRs in MLA6 account for the recognition specificity of AVR$_{A6}$ in barley. Furthermore, we discovered that co-expression of *AVR$_{a1}$* with *M61111* or *M66111* triggered a significant and specific 92% reduction of relative LUC activity in barley protoplasts indicative of a cell death response compared to the EV sample (Fig 5A). This suggests that, out of 15 predicted LRRs in the MLA1 receptor, the 12 C-terminal ones contribute to the specific recognition of AVR$_{A1}$. Together, these findings corroborate previous experiments that show a significant growth reduction of *Bgh* isolate A6 when barley cells express *M16666* and *M11166*, or growth reduction of *Bgh* isolate K1, when barley cells express *M61111* or *M66111* [38]. While our data does not exclude that other MLA domains contribute to the association with the *Bgh* AVR$_A$ effector proteins, we conclude that the MLA LRR regions confer *Bgh* recognition specificities to of the different *Mla* alleles in barley.

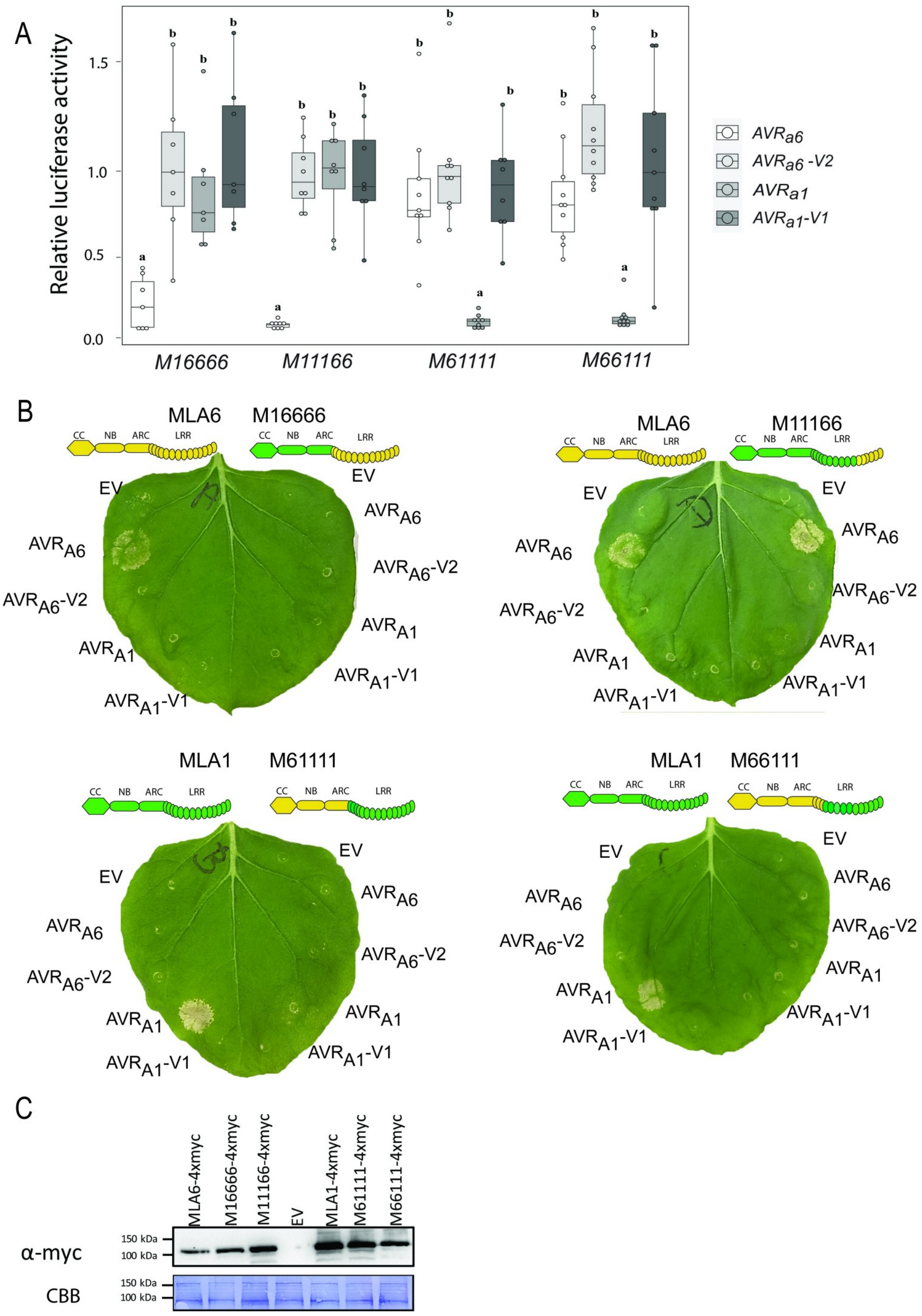

Fig 5. Specific recognition of AVR$_{A6}$ and AVR$_{A1}$ by MLA1/MLA6 chimeric constructs *in planta*. (A) Barley *cv.* Golden Promise protoplasts were transfected with a LUC reporter construct and pIPKb002 vectors containing cDNAs of *AVR$_{a6}$*, *AVR$_{a6}$-V2*, *AVR$_{a1}$*, *AVR$_{a1}$-V1* or an empty vector (EV) together with vectors harboring intron-containing DNA of receptor chimeras *M16666*, *M11166*, *M61111*, or *M66111* under the control of a *pZmUBI* promotor. Transfections were performed at least seven times independently. Significant differences between samples were analyzed using non-parametric Kruskal-Wallis (KW) analysis followed by a Dunn's test. Calculated KW p-values are as follows: *M16666*: $p = 0.001883$; *M11166*: $p = 0.000559$, *M61111*: $p = 0.0001582$, *M66111*: $p = 1.658e\text{-}05$. Samples labeled with identical letters did not differ significantly ($p < 0.05$) in the Dunn's test for the corresponding *Mla* variant. (B) Transient transformation of *N. benthamiana* leaves with empty vector (EV) or cDNAs of *AVR$_{a6}$* or *AVR$_{a1}$* variants fused C-terminally with a mYFP tag together with *Mla1* or *Mla6* cDNAs or *M16666*, *M11166*, *M61111*, or *M66111* intron-containing DNAs with a C-terminal 4xmyc fusion. All constructs were expressed from a 35S promotor. Figures show a representative of at least three independent co-transformations. (C) MLA-4xmyc proteins were extracted two

days post infiltration and separated using a 10% polyacrylamide gels and detected using α-myc western blotting, CBB = Coomassie Brilliant Blue.

https://doi.org/10.1371/journal.ppat.1009223.g005

To determine if these results can be independently validated in a heterologous system, we co-expressed C-terminally 4xmyc-tagged *M16666*, *M11166*, *M61111*, and *M66111* and C-terminally mYFP-tagged AVR_{a6} and AVR_{a1} variants in *N. benthamiana*. We observed a strong cell death response upon co-expression of *M11166-4xmyc* with AVR_{a6}*-mYFP*, suggesting that the last six C-terminal LRR repeats of MLA6 are sufficient for recognition of AVR_{a6} even in the absence of further barley-specific host proteins (Fig 5B). We detected weak recognition of AVR_{A1} by M61111 under UV light at 302 nm in *N. benthamiana* (indicative of accumulation of autofluorescent compounds in dying plant cells; S11 and S14 Figs), whereas the specific recognition of AVR_{A6} by M16666 and AVR_{A1} by M66111 seen in barley protoplasts was completely lost, suggesting that other barley-specific protein(s) might be necessary for the functionality of these chimeric receptors in the heterologous expression system.

The LRRs of the MLA10 and MLA22 receptors specifically recognize allelic AVR_{A10} and AVR_{A22}

To test if the LRRs of MLA NLRs are necessary to specifically recognize not only sequence unrelated, but also sequence related allelic AVR_A effectors, we designed two chimeric receptor genes encoding the MLA10 CC-NB fused with the MLA22 LRRs (MLA10LRR22) and the MLA22 CC-NB domain fused with the MLA10 LRRs (MLA22LRR10) (S12 Fig). Subsequently, *Mla10-4xmyc*, *Mla22-4xmyc*, *Mla10Lrr22-4xmyc* or *Mla22Lrr10-4xmyc* were co-expressed with AVR_{a10}*-mYFP*, AVR_{a10}*-V/*AVR_{a22}*-V-mYFP*, or AVR_{a22}*-mYFP* in heterologous *N. benthamiana*. Co-expression of *Mla10-4xmyc* or *Mla22Lrr10-4xmyc* with AVR_{a10}*-mYFP* led to cell death in *N. benthamiana* leaves, but no cell death was observed when these *Mla NLRs* were co-expressed with an empty vector (EV), AVR_{a10}*-V /* AVR_{a22}*-V-mYFP*, or AVR_{a22}*-mYFP* (Fig 6A). Additionally, expression of *Mla22-4xmyc* and *Mla10Lrr22-4xmyc* led to cell death when co-expressed with AVR_{a22}*-mYFP*, but not when these proteins were co-expressed with AVR_{a10}*-mYFP*, AVR_{a10}*-V/*AVR_{a22}*-V-mYFP*, or an EV control (Fig 6A). The MLA10LRR22 and MLA22LRR10 receptor chimeras were detectable in *N. benthamiana* leaf extracts at levels comparable with the MLA10 and MLA22 receptors (Fig 6B). To determine whether these results were reproducible in the homologous barley protoplast system, we expressed *Mla10Lrr22* or *Mla22Lrr10* together with AVR_{a10} and AVR_{a22} in leaf protoplasts and measured reduction of LUC activity as a proxy for cell death. In comparison to the EV reference sample, co-expression of AVR_{a22} with *Mla10Lrr22* and AVR_{a10} with *Mla22Lrr10* lead to an average 80% and 40% reduction of relative LUC activity, respectively, and this was not the case when AVR_{a10} was co-expressed with *Mla10Lrr22* or when AVR_{a22} was co-expressed with *Mla22Lrr10* (Fig 6C). Taken together, the results suggest that the 58 amino acid differences between the LRRs of *Mla10* and *Mla22* are major determinants of respective recognition specificities for the allelic AVR_{A10} and AVR_{A22} effectors.

An association between MLA10 and AVR_{A10} was previously shown to be detectable in plant extracts and in yeast [11]. Using a previously established split-LUC complementation assay, we therefore tested, whether the MLA22LRR10 hybrid receptor also specifically interacts with the AVR_{A10} effector when co-expressed *in planta*. We generated constructs expressing AVR_a variants fused C-terminally to the N-terminal part of the LUC reporter (AVR_a*-nLUC)*;

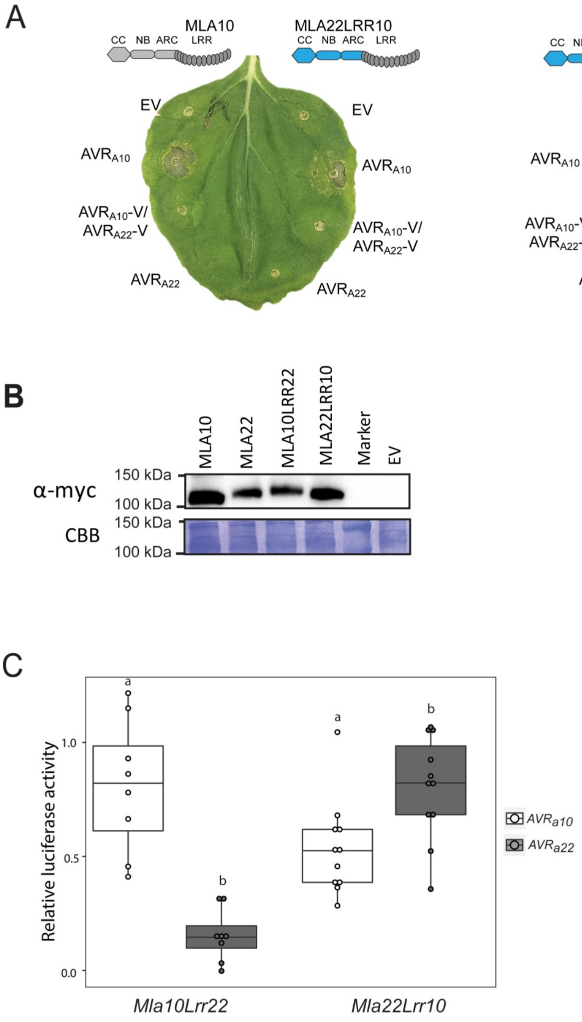

Fig 6. The LRR domains of MLA10 and MLA22 distinguish between AVR_{A10} and AVR_{A22}. (A) Transient transformation of *Nicotiana benthamiana* leaves with EV or cDNAs of AVR_{a10}, AVR_{a10}-V/AVR_{a22}-V, and AVR_{a22} fused C-terminally with mYFP together with *Mla10* or *Mla22* cDNAs fused C-terminally with a 4xmyc tag. All constructs were expressed from a 35S promotor. Cell death was scored five days post infiltration (dpi) and Figures show a representative of at least 15 co-transformations. (B) Protein levels of MLA-4xmyc after total protein extraction from *N. benthamiana* leaves at two dpi. Proteins were separated on a 10% polyacrylamide gel and a detected using α-myc western blotting (WB) (C) Barley *cv.* Golden Promise protoplasts were transfected with a LUC reporter construct and pIPKb002 vectors containing cDNAs of AVR_{a10} or AVR_{a22} together with *Mla10Lrr22* and *Mla22Lrr10* chimeras. Transfections were performed at least eight times independently. Significant differences between samples were analyzed using non-parametric Kruskal-Wallis (KW) one-way analysis of variance. Calculated KW *p*-values are as follows: Mla10Lrr22: $p = 0.0007775$; Mla22Lrr10: $p = 0.01654$. Samples labeled with different letters differed significantly ($p < 0.05$).

https://doi.org/10.1371/journal.ppat.1009223.g006

and *Mla* variants fused C-terminally to the C-terminal part of the LUC reporter (*Mla-cLUC*) [11]. We then performed *A. tumefaciens*-mediated transformation of *N. benthamiana* leaves to express AVR_{a10}-*nLUC* or AVR_{a10}-V/AVR_{a22}-V-*nLUC* (not recognized AVR_{a10} variant) together with either *Mla10-cLUC*, *Mla22Lrr10-cLUC* or *Mla10Lrr22-cLUC*. Forty hours post infiltration, we determined LUC activity as a proxy for AVR_A/MLA association, as described previously [11]. LUC activity was significantly higher in samples that co-expressed AVR_{a10}-*nLUC* with *Mla10-cLUC* or *Mla22Lrr10-cLUC*, when compared to samples where AVR_{a10}-

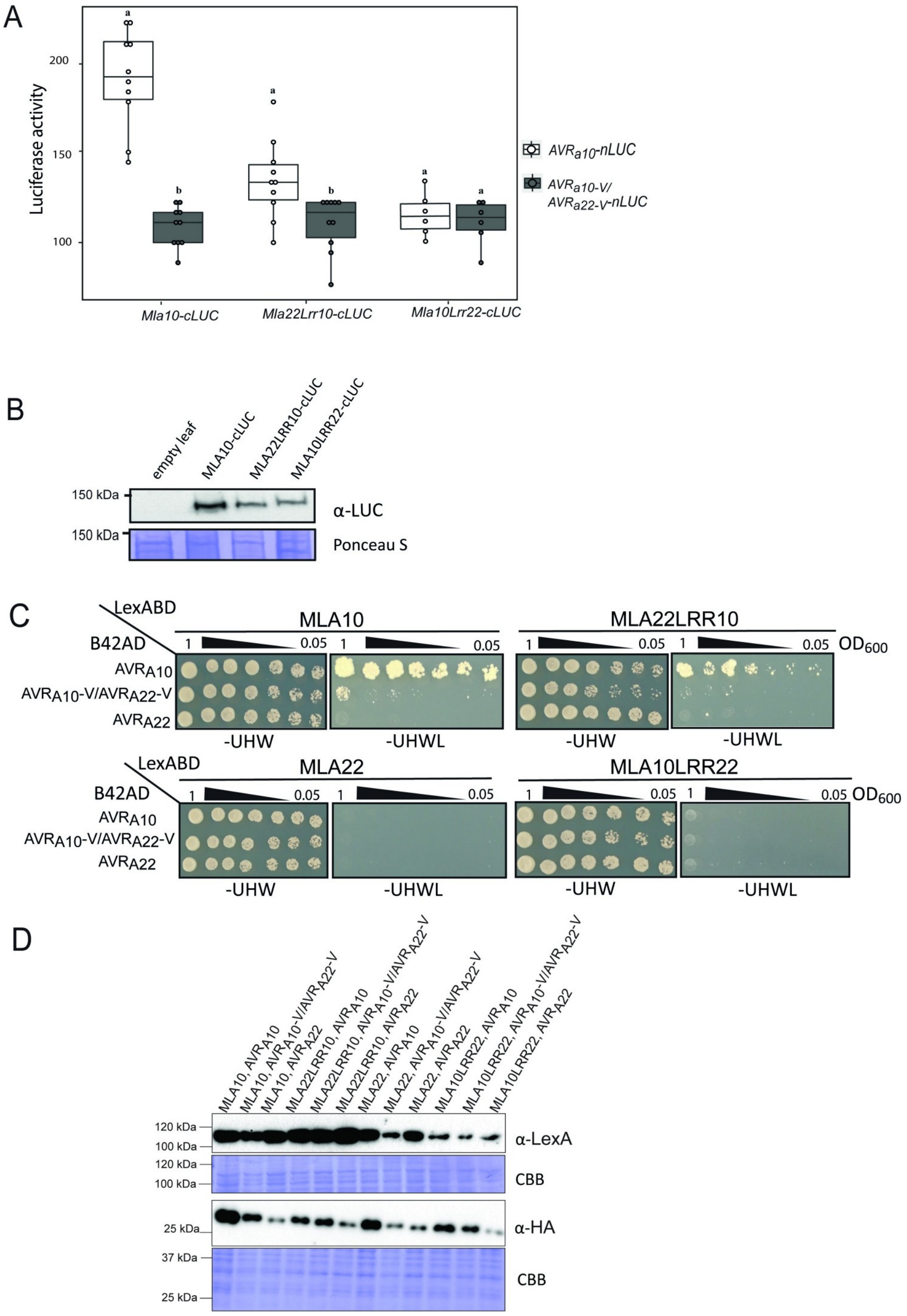

Fig 7. The LRR domain of MLA10 accounts for the specific interaction with AVR$_{A10}$ *in planta* and in yeast. (A) *Nicotiana benthamiana* leaves were transformed transiently with vectors containing cDNAs of *Mla10-cLUC*, *Mla10Lrr22-cLUC* or *Mla22Lrr10-cLUC* together with vectors containing cDNAs of *AVR$_{a10}$-nLUC* or *AVR$_{a10}$-V/ AVR$_{a22}$-V nLUC* lacking signal peptides (SPs), under the control of a 35S promoter. LUC activity was determined forty hours after transfection. The experiment was performed on at least three independent days with two to four replicates (independent set of plants) each day. Significant differences between *AVR$_{a10}$-nLUC* or *AVR$_{a10}$-V/ AVR$_{a22}$-V nLUC* were analyzed using one-way Kruskal-Wallis (KW) analysis. Calculated KW *p*-values are as follows: Mla10: $p = 0.0001491$; Mla22Lrr10: $p = 0.009035$; Mla10Lrr22: $p = 0.8079$. Samples labeled with different letters differed significantly ($p < 0.05$). (B) Protein levels of MLA10-cLUC, MLA22LRR10-cLUC and MLA10LRR22-cLUC in *N. benthamiana* leaf extracts. Proteins were separated on a 8% SDS-PAGE gel and a detected using anti-LUC western blot (WB). (C) Yeast was co-transformed with cDNAs of N-terminal LexABD-fused MLA and N-terminal B42AD-fused AVR$_A$ variants. Growth on media lacking Leucine indicates association of respective proteins fused to AD (activation

domain) and BD (Binding domain). (D) Protein levels of LexABD-MLA and B42AD-AVR$_{A}$ variants. Proteins were precipitated using an ammonium-acetate buffer and dissolved in a urea-SDS sample buffer before separation on a 10% or 12% polyacrylamide gel and detection by either α-LexA or α-HA WB.

https://doi.org/10.1371/journal.ppat.1009223.g007

nLUC was exchanged with its virulent variant *AVR$_{a10}$-V/AVR$_{a22}$-V*. This was not the case when the *AVR$_{a10}$-nLUC* variants were co-expressed with *Mla10Lrr22-cLUC* (Fig 7A and 7B). Our data suggests a reduced association of AVR$_{A10}$ with the MLA22LRR10 hybrid receptor compared to wild-type MLA10, which is in agreement with differences in cell death scores of *N. benthamiana* leaves co-expressing *AVR$_{a10}$-mYFP* with *Mla10-4xmyc* and *Mla22Lrr10-4xmyc* (S14D Fig).

We also tested whether AVR$_{A10}$ can interact with MLA22LRR10 in the absence of other plant proteins in yeast. We co-expressed *LexABD-Mla10Lrr22* or *LexABD-Mla22Lrr10* under the control of a constitutive ADH1 promoter with *B42AD-AVR$_{a10}$*, *B42AD-AVR$_{a10}$-V/AVR$_{a22}$-V*, or *B42AD-AVR$_{a22}$* under the control of a galactose (GAL1)-inducible promoter. Co-expressing *B42AD-AVR$_{a10}$* with *LexABD-Mla22Lrr10* or with *LexABD-Mla10* in a yeast two-hybrid assay (Y2H) led to yeast growth on leucine-deprived media (Fig 7C). Little growth was detectable when *LexABD-Mla22Lrr10* or *LexABD-Mla10* was co-expressed with *B42AD-AVR$_{a10}$-V/AVR$_{a22}$-V*, while no growth was detected when co-expressing *B42AD-AVR$_{a22}$* (Fig 7C), even though all effector and receptor fusion proteins were detectable in yeast extracts (Fig 7D). Taken together, our findings suggest that the MLA10 LRR domain is responsible for specific recognition of AVR$_{A10}$ and that this is dependent on effector-receptor association. However, we were unable to detect an interaction of *LexABD-Mla22* or *Lex-ABD-Mla10Lrr22* with *B42AD-AVR$_{a22}$* in this Y2H assays (Fig 7C).

Multiple residues in AVR$_{A10}$ and AVR$_{A22}$ are responsible for differential recognition specificities of MLA10 and MLA22

It has been proposed that direct fungal effector-plant NLR receptor interactions are mediated by cumulative binding of multiple effector aa residues to the surface of its corresponding NLR receptor [27,39]. We aimed to resolve which of the 11 amino acid residues that are polymorphic between AVR$_{A10}$ and AVR$_{A22}$ alleles (excluding the SP) are responsible for the specific recognition by the cognate MLA10 and MLA22 receptors. On the basis of AVR$_{A10}$ secondary structural predictions, we divided AVR$_{A10}$/AVR$_{A22}$ proteins into three equally long parts: an N-terminal (residues 22–54 aa, comprising ß1-ß2 sheets and the α1-helix, which included the two amino acid substitutions D45G, D53E), a central (55–86aa; comprising the ß3-ß4 sheet and cluster of most amino acid differences Q55H, D58N, G59D, Q61P, H64Y, and the residue F77Y), and a C-terminal part (87–118 aa; including the ß5-ß6 sheets and three amino acid differences V93L, W96L, I111N) (Fig 8A). These individual regions were exchanged between AVR$_{A10}$/AVR$_{A22}$ effector peptides and we then tested the interactions of the six resulting chimeric AVR$_{A10}$/AVR$_{A22}$ effector constructs (called chimera11, chimera12, chimera13, chimera14, chimera15 and chimera16) with MLA10 and MLA22, in *N. benthamiana* as described above. All chimeric proteins were detectable after GFP-Trap enrichment except for chimera16-mYFP, which was not consistently detectable (Fig 8C). Co-expression of *chimera14-mYFP* with *Mla22-4xmyc* led to cell death (Figs 8B, S13 and S14). These findings suggest that the C-terminal polymorphic residues V93, W96, and I111 are not responsible for the specific recognition by MLA22.

While in chimera14-mYFP, the three C-terminal residues of AVR$_{A22}$ are exchanged for the respective amino acids found at these positions in AVR$_{A10}$, in chimera12-mYFP the three C-terminal residues of AVR$_{A10}$ are exchanged for AVR$_{A22}$-specific amino acid residues (Fig 8A).

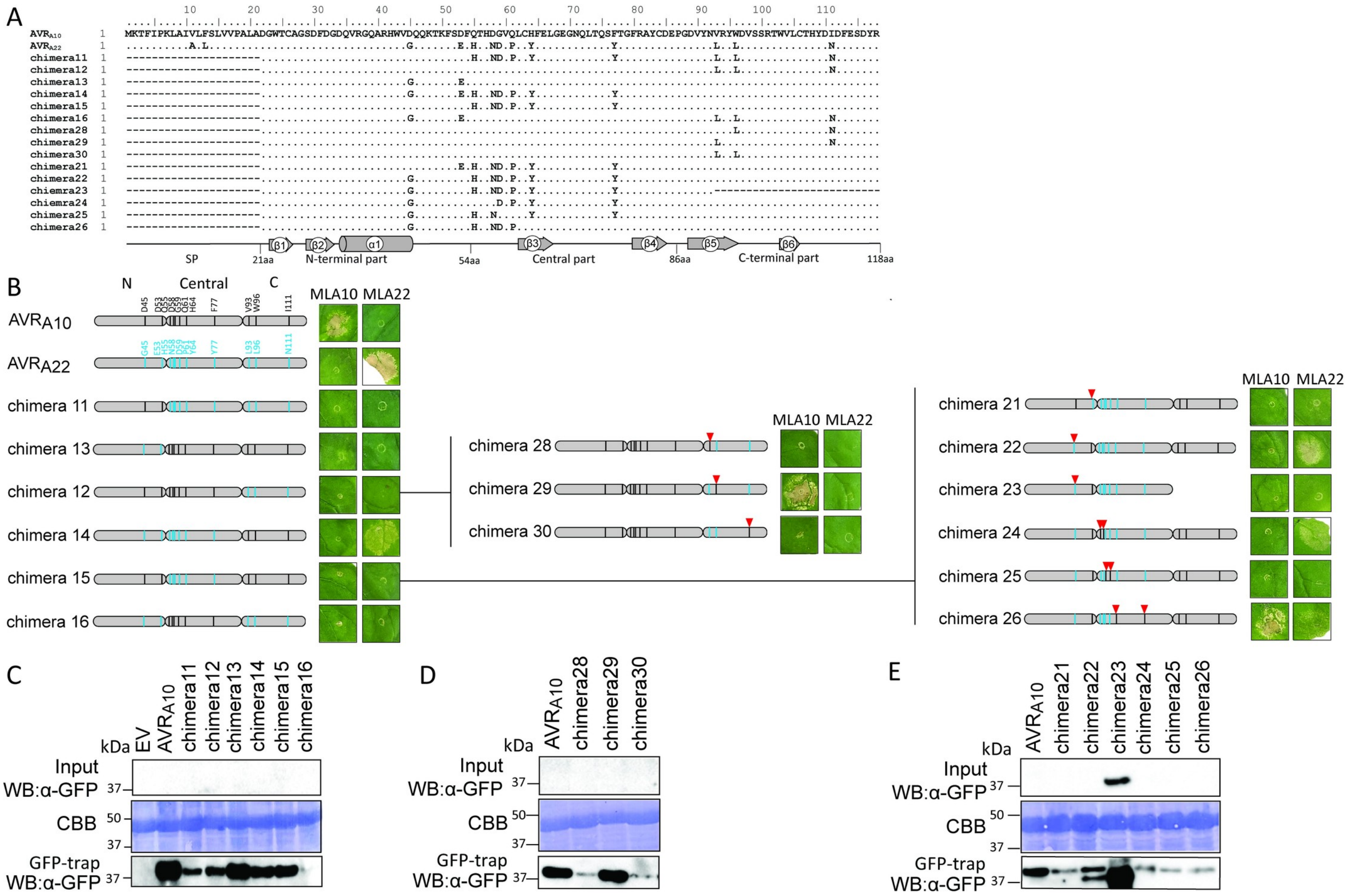

Fig 8. Co-expression of AVR$_{A10}$ and AVR$_{A22}$ chimeras with MLA10 and MLA22 in *N. benthamiana*. (A) Protein sequence alignment of the AVR$_{A10}$/AVR$_{A22}$ chimeric construct. Grey boxes below sequences show the length of the N-terminal, the central and the C-terminal effector part. Dashes represent missing/deletion of effector parts and points designate identical amino acid residues (B) Co-expression of *N. benthamiana* with cDNAs of *AVR$_{a10}$*, *AVR$_{a22}$*, or chimeric *AVR$_{a10}$/AVR$_{a22}$* constructs fused C-terminally with mYFP and *Mla10* or *Mla22* cDNAs fused C-terminally with a 4xmyc tag from the 35S promotor in *N. benthamiana* leaves. Cell death was scored five days post infiltration and Figures show a representative of at least seven co-transformations. (C-E) Protein levels of AVR$_{A}$-mYFP and chimeric AVR$_{A10}$/AVR$_{A22}$mYFP variants after total protein extraction from *N. benthamiana* leaves at two dpi. Proteins were separated on a 12% polyacrylamide gel and detected by α-mYFP western blotting.

https://doi.org/10.1371/journal.ppat.1009223.g008

Even though both effector chimeras were stable *in planta*, chimera12-mYFP was not recognized by MLA10-4xmyc (Figs 8B, 8C and S13 and S14). This suggests that single, double, or triple amino acid mutations at aa positions 93, 96, or 111 within the C-terminus of AVR$_{A10}$ can lead to a loss of MLA10-specific recognition. We sought to determine which amino acid residues at the C-terminus, if exchanged to the respective AVR$_{A22}$ residues, would result in abrogation of MLA10-specific recognition. To this end, we introduced L93V, L96W, or N111I single amino acid substitutions in chimera12-mYFP. The resulting *chimera28-mYFP* (L93V), *chimera29-mYFP* (L96W), and *chimera30-mYFP* (N111I) constructs were co-expressed with *Mla10-4xmyc* and with *Mla22-4xmyc*. Co-expression of *chimera29-mYFP* with *Mla10-4xmyc* led to cell death, while co-expression of *chimera28-mYFP* or *chimera30-mYFP* with *Mla10-4xmyc* did not (Figs 8B–8D and S13 and S14), suggesting that the tryptophan at position 96 in AVR$_{A10}$ is important for MLA10-specific recognition. However, we cannot exclude that differences in protein stability between mYFP fused chimera 29 and 28, or 30, accounts for the lack of cell death in samples co-expressing *chimera28-mYFP* and *chimera30-mYFP* together with *Mla10-4xmyc*.

Even though chimera14-mYFP and chimera15-mYFP differ by only two N-terminal amino acids at positions 45 and 53 and both proteins are detectable, co-expression of *chimera15-mYFP* with *Mla22-4xmyc* did not trigger cell death (Figs 8B, 8C and S13 and S14). This suggests that residues at one or both of these N-terminal positions are necessary for the specific recognition by MLA22. To test this hypothesis, we introduced single D45G or D53E substitutions into *chimera15-mYFP* (Fig 8A). The resulting *chimera21-mYFP* (D53E) and *chimera22-mYFP* (D45G) constructs were co-expressed with *Mla10-4xmyc* or *Mla22-4xmyc*. Co-expression of *chimera22-mYFP* but not *chimera21-mYFP* with *Mla22-4xmyc* led to cell death, while no cell death was observed upon co-expression of *chimera21-mYFP* with *Mla22-4xmyc*, suggesting that the glycine at position 45 but not the glutamic acid at position 53 is essential for MLA22-specific recognition (Fig 8A, 8B and 8E).

To test if the N-terminal and central parts of the AVR_{a22} effector are sufficient to trigger cell death when co-expressed with *Mla22*, we constructed a deletion construct (Δ93–118) of *chimera22*, which we termed *chimera23* (Fig 8A). Co-expression of *chimera23-mYFP* with *Mla10-4xmyc* or *Mla22-4xmyc* did not trigger cell death, although the chimera23-mYFP protein was seemingly more stable than AVR_{A10} and all other chimeric proteins (Figs 8B–8E and S13 and S14). Even though the C-terminal residues L93, L96, and N111 are not specifically recognized by MLA22, our findings suggest that the C-terminal region of the AVR_{A22} effector potentially stabilizes the conformation of the N-terminal and central regions, which are necessary for MLA22-specified recognition. In summary, the N-terminal glycine at position 45 and the C-terminal tryptophan at position 96 are important for MLA22- and MLA10-specific recognition, respectively.

In addition, we assessed the role of amino acids in the central positions 55, 58, 59, 61, 64, and 77 for MLA10- and MLA22-specific recognition. We introduced double mutations in *chimera22-mYFP* to generate *chimera24-mYFP* (H55Q and N58D), *chimera25-mYFP* (D59G and P61Q) and *chimera26-mYFP* (Y64H and Y77F), which were co-expressed with *Mla10-4xmyc* or *Mla22-4xmyc* (Fig 8A). While co-expression of *chimera24-mYFP* with *Mla22-4xmyc*, but not with *Mla10-4xmyc* led to a specific cell death response, co-expression of *chimera25-mYFP* with *Mla22-4xmyc* or with *Mla10-4xmyc* did not lead to cell death in *N. benthamiana* leaves (Figs 8B–8E and S13 and S14). Surprisingly, *chimera26-mYFP* triggered a strong cell death response when co-expressed with *Mla10-4xmyc* and a subtle but consistent cell death phenotype when co-expressed with *Mla22-4xmyc*, suggesting that it is recognized by both receptors (Fig 8B–8E).

To independently verify the data, we also co-expressed a selection of AVR_{a10}/AVR_{a22} chimeras (*chimera12*, *chimera14*, *chimera21*, *chimera22*, *chimera24*, *chimera26 and chimera29*) together with *Mla10* or *Mla22* in protoplasts of barley *cv*. Golden Promise and determined cell viability by LUC activity, as described above. LUC activity was approximately 50% lower in samples co-expressing *Mla10* with AVR_{a10} when compared to samples that co-express *Mla10* with AVR_{a22}, and this is in agreement with previously published data [11] (Fig 9A). We detected intermediate LUC activity when co-expressing *Mla10* together with *chimera26* or *chimera29*, but this reduced LUC activity did not differ significantly from the sample co-expressing *Mla10* and AVR_{a10} (Fig 9A). This was not the case for samples co-expressing *Mla10* together with *chimera12*, *chimera14*, *chimera21*, *chimera22*, or *chimera24* (Fig 9A).

LUC activity was on average 80% lower in samples co-expressing *Mla22* with AVR_{a22} when compared to samples that co-express *Mla22* with AVR_{a10}, and this is again in agreement with published data [11]. LUC activity of samples co-expressing *Mla22* together with *chimera14*, *chimera22*, *chimera24* and *chimera26* was not statistically different from the activity observed

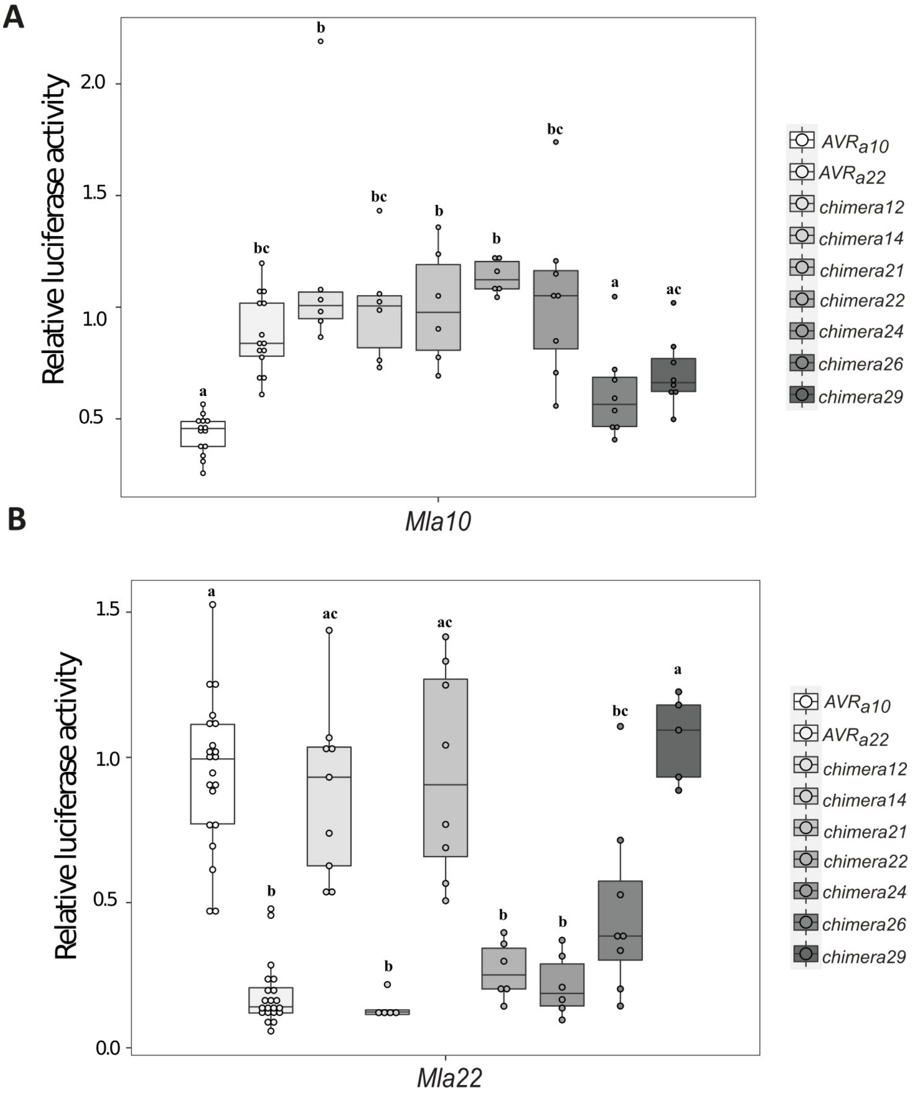

Fig 9. Co-expression of a selection of AVR$_{A10}$/AVR$_{A22}$ chimeras with MLA10 and MLA22 in barley protoplasts. Barley protoplasts of *cv*. Golden Promise were co-transfected with a LUC reporter assay and pIPKb002 vectors containing cDNAs of *AVR$_{a10}$*, *AVR$_{a22}$*, *chimera12*, *chimera14*, *chimera21*, *chimera22*, *chimera24*, *chimera26* or *chimera29* without signal peptide or with an empty vector (EV) together with either (A) *Mla10* or (B) *Mla22* in pipkb002. Transfections were performed at least six times independently. Significant differences between samples were analyzed using non-parametric Kruskal-Wallis (KW) analysis followed by the Dunn's test. Calculated KW *p*-value are as follows: *Mla10*: $p = 1.439\text{e-}07$, *Mla22*: $p = 5.374\text{e-}11$. Samples labeled with different letters differed significantly ($p < 0.05$) in the Dunn's test.

https://doi.org/10.1371/journal.ppat.1009223.g009

when co-expressing *Mla22* and *AVR$_{a22}$* (Fig 9B). This was not the case for samples co-expressing *Mla22* together with *chimera12*, *chimera21* or *chimera29*. Notably, we detected an intermediate relative LUC activity when co-expressing *Mla22* together with *chimera26* (Fig 9B). Similarly, cell death scores of *N. benthamiana* leaves co-expressing *Mla22-4xmyc* together with *chimera26-mYFP* were also lower than when co-expressing *Mla22-4xmyc* together with *AVR$_{a22}$-mYFP* (Figs 8 and S14). We thus conclude that the barley protoplast cell death data (Fig 9) overall recapitulate the MLA10 and MLA22 specificities towards AVR$_{A}$ chimeric constructs observed in the heterologous *N. benthamiana* system (Fig 8).

In summary, our findings suggest that for triggering MLA10-specific cell death, the four residues D53, H64, F77, and W96 of AVR_{A10} cannot be exchanged to the residues found in AVR_{A22}. In turn, to trigger MLA22-specific cell death, the five amino acid residues G45, H55, N58, D59, and P61 of AVR_{A22} cannot be exchanged to the residues found in $\text{AVR}_{\text{A22.}}$ Furthermore, deletion of the C-terminal third of the AVR_{A10} and AVR_{A22} effectors leads to loss of avirulence function (Fig 8).

To determine if MLA-mediated cell death initiated by recognition of the AVR_{A} effector also correlates with receptor-effector association in plant extracts, we again applied the split-LUC complementation assay. We transiently expressed *Mla10-cLUC* together with *AVR_{a10}-nLUC*, *chimera26-nLUC*, *chimera29-nLUC* and as a control, *chimera22-nLUC* in *N. benthamiana* leaves, followed by LUC measurements at 40 hours post infiltration of leaves with the *A.*

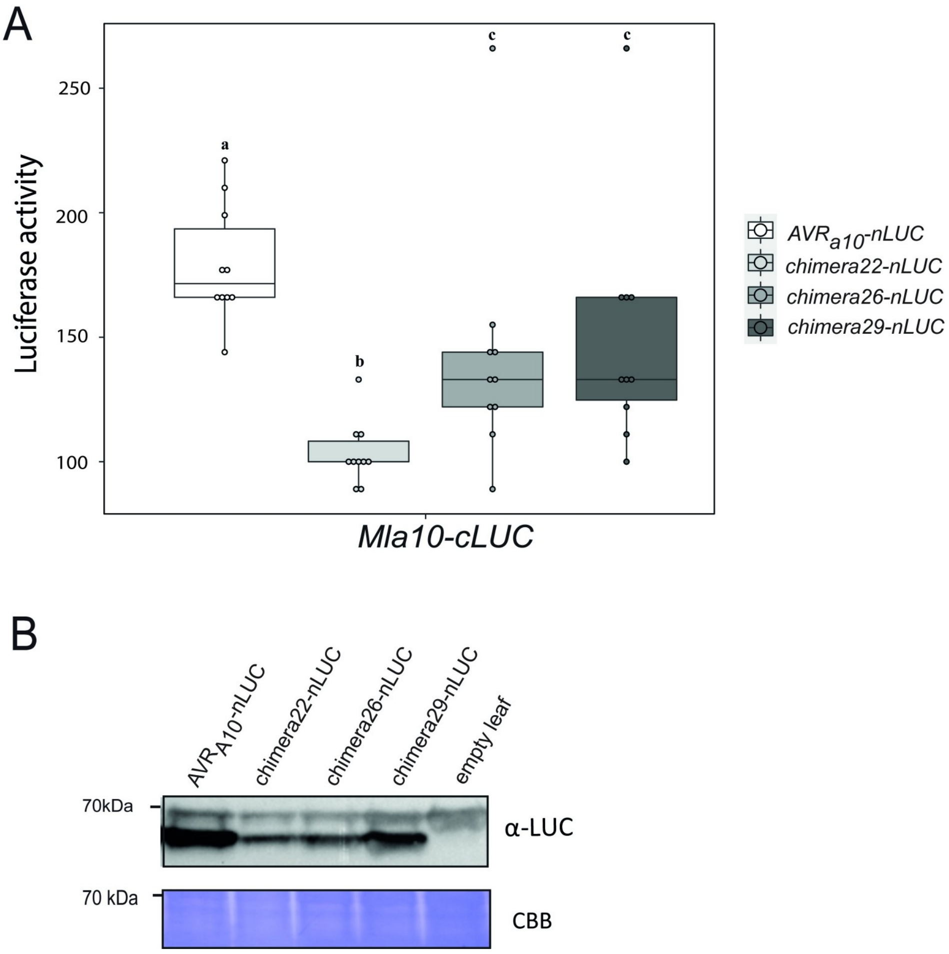

Fig 10. AVR_{A10} amino acid residues that are responsible for specific recognition correlate with residues that interact with the MLA10 receptor. (A) *N. benthamiana* plants were transformed transiently with vectors containing cDNAs of *Mla10-cLUC* together with cDNAs of *AVR_{a10}-nLUC* without signal peptide, *chimera22-nLUC*, *chimera26-nLUC* or *chimera29-nLUC* under the control of a 35S promoter. LUC activity was determined 40 h after *A. tumefaciens*-mediated transformation. The experiment was performed on at least four independent days with two to four replicates (independent set of plants) each day. Significant differences between samples were analyzed using non-parametric Kruskal-Wallis (KW) analysis followed by the Dunn's test. Calculated KW p-value = 5.03e-05. Samples labeled with different letters differed significantly ($p < 0.05$) in the Dunn's test. (B) Protein levels of AVR_{A10}-nLUC, chimera22-nLUC, chimera26-nLUC and chimera29-nLUC. Proteins were separated on a 8% SDS_PAGE gel and a detected using anti-LUC western blotting (WB).

https://doi.org/10.1371/journal.ppat.1009223.g010

tumefaciens carrying constructs of interest. LUC activity of samples co-expressing *Mla10-cLUC* with *AVR_{a10}-nLUC*, *chimera26-nLUC* and *chimera29-nLUC* was significantly higher than the LUC activity observed in the samples expressing *Mla10-cLUC* together with *chimera22-nLUC* (Fig 10A and 10B). Chimera26 and chimera29 but not chimera22, can trigger MLA10-mediated cell death in co-expression assays (Figs 8 and 9), and as such, we conclude that the recognition specificities mediated by MLA10 towards the AVR_A chimeric variants 26, 29 and 22 correlate with receptor-effector association. We again only observed intermediate levels of LUC activity in samples co-expressing *Mla10-cLUC* together with *chimera26-nLUC* or *chimera29-nLUC* (Fig 10A). This is in agreement with the quantitative cell death assay in barley protoplasts (Fig 9A), and suggests that when compared to *$AVR_{a10,}$* these constructs are impaired in their ability to activate and associate with MLA10 *in planta* and this may be associated with levels of protein expression (Fig 10B).

Two amino acids of AVR_{A10} that cannot be exchanged to respective AVR_{A22} residues are located in a predicted positively charged area that corresponds to the catalytic cleft of the fungal F1 RNase

Microscale thermophoresis assays suggested that CSEP0064 has some affinity to total RNA but its X-ray structure suggests that it lacks residues required for RNA hydrolysis [30]. Our data also suggests that the putative RNase-like fold of AVR_A effectors is not associated with RNase activity (Fig 4). Here, we examined the location of the AVR_{A10} and AVR_{A22} residues that are required for specific recognition by MLA10 and MLA22, and if the corresponding residues in the F1 RNase are required for RNA binding and hydrolysis. To do this, we superimposed AVR_{A10} and AVR_{A22} predicted structures on the structure of *Fusarium moniliformis* F1 RNase. Residues Y38, Y42, and Y45 of the F1 RNase are involved in binding the ribose and phosphate of 2' GMP and the respective amino acids found in AVR_{A10} (F51, F54, and H57) are identical to those of $AVR_{A22,}$ and as such, do not account for specific MLA recognition (Fig 11A–11C). The R77 residue in the F1 RNase, also forms a contact with the phosphate in 2' GMP. The corresponding residue can also be found in AVR_{A10} and AVR_{A22} (residue R81, Fig 11A–11C) but not in the CSEP0064 structure or the predicted structures of any other AVR_A effector isolated so far. The residues W96 and H64 of AVR_{A10} are L96 and Y64 in AVR_{A22} and have dissimilar properties to the corresponding residues (H92 and E58, respectively) in the F1 RNase. Electrostatic potential prediction using Adaptive Poisson-Boltzmann Solver (APBS) of surfaces suggests that H64, R77, and W96 in AVR_{A10} and L64, R77, and L96 in AVR_{A22} belong to a positively charged cleft (Fig 11B–11D). In AVR_{A10}, these residues are predicted to be part of the positively charged surface patch. For recognition by MLA10, H64 and W96 can indeed not be exchanged to the respective residues found in AVR_{A22} (Fig 11B). In contrast, the AVR_{A22} residues that cannot be exchanged to the respective AVR_{A10} residues without losing MLA22 avirulence activity, can be found in a negatively charged surface patch away from the positively charged area, presumably required for MLA10 recognition (Fig 11D). These results suggest that the AVR_A residues, which confer specific recognition by MLA10 and MLA22 receptors, are located in distinct predicted surface patches of the avirulence proteins encoded by allelic *AVR_{a10}* and *AVR_{a22}*.

Discussion

Identification of AVR_{A6}

Long-read DNA sequencing and high-quality genome assembly of the DH14 *Bgh* isolate recently recovered 30 Mb of previously unassembled repetitive regions of the *Blumeria*

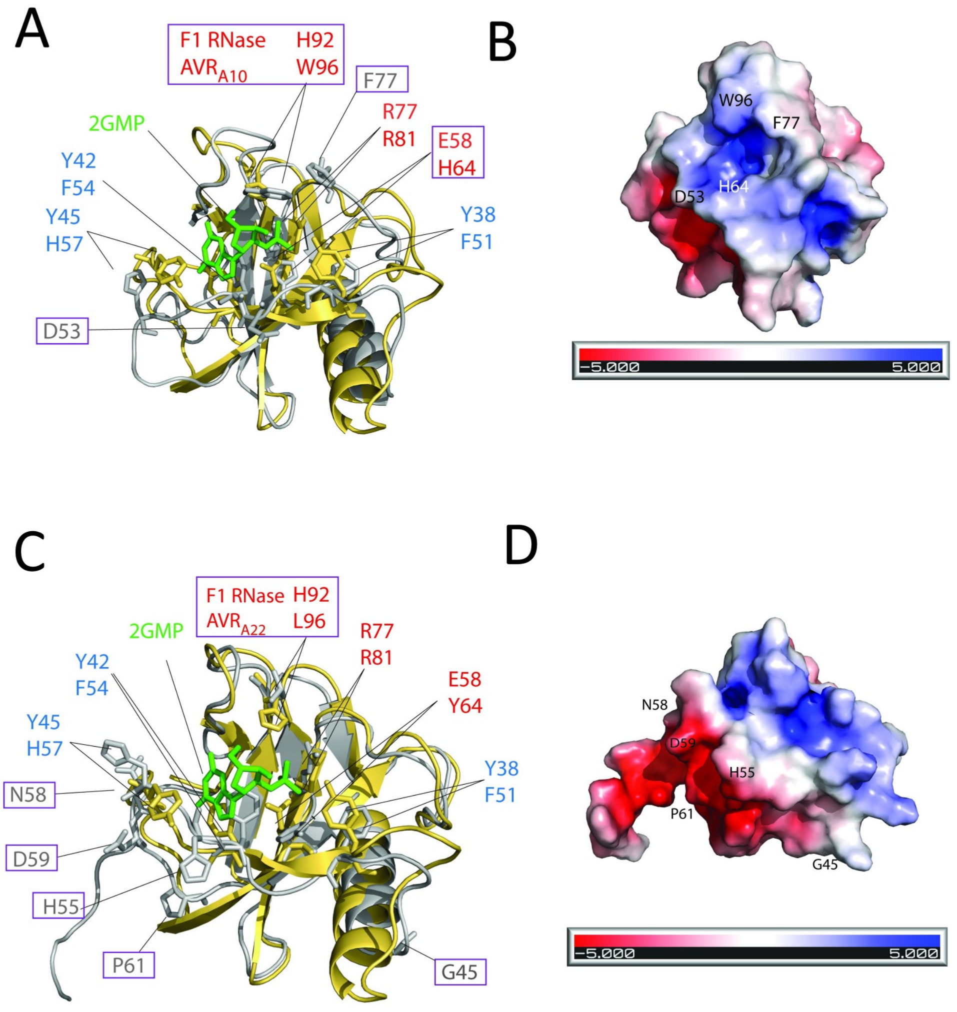

Fig 11. The location of amino acid residues in AVR$_{A10}$ and AVR$_{A22}$ that determine MLA10 and MLA22 recognition specificities. (A and C) show structural superimposition of the crystal structure of *Fusarium moniliformis* RNase F1 (yellow) and IntFOLD version 5.0 structural predictions of AVR$_{A10}$ or AVR$_{A22}$ (grey). Depicted in green is the F1 RNase ligand 2'-guanosine monophosphate (2' GMP); residues of the F1 RNase catalytic triad and corresponding AVR$_A$ residues are depicted in red; residues of the F1 RNase RNA binding pocket and corresponding AVR$_A$ residues are shown in blue. The residues of AVR$_{A10}$ and AVR$_{A22}$ required for specific MLA10 and MLA22 recognition as determined in Figs 8–10 are framed with a purple rectangle. (B and D) Predicted electrostatic surface potential of the AVR$_{A10}$ and AVR$_{A22}$ effector surface calculated using Adaptive Poisson Boltzmann Solver (APBS) [67]. The residues of AVR$_{A10}$ and AVR$_{A22}$ required for specific MLA10 and MLA22 recognition as determined in Figs 8–10 are indicated. Below is a scale bar of the electrostatic potential (red = negative charge, white = neutral charge, blue = positive charge).

https://doi.org/10.1371/journal.ppat.1009223.g011

genome, which linked together multiple non-contiguous series of genomic sequences, including scaffold 16 [40]. This may explain why we failed to identify BLGH_00708, BLGH_00709 and BLGH_07091 as AVR$_{A6}$ in our previous studies [11,28] and emphasizes the importance of high-quality *Blumeria* genome assemblies for identification of novel AVR$_A$ effectors. We found three *AVR$_{a6}$* paralogues in the RACE1 genome, and in line with this observation, three non-identical paralogues of *AVR$_{a7}$* have been described in RACE1 [11], indicating that these *AVR$_a$* effectors were duplicated [11]. Similarly, *BLGH_07092* is likely an *AVR$_{a6}$* copy with a frameshift mutation. This *AVR$_a$* duplication could facilitate the gain of new virulence functions.

Unlike other virulent variants of *Bgh* AVR_a effectors that carry SNPs in the coding region or transposon insertions, or are transcriptionally silent [11,28], here we report that virulence of *Bgh* isolates on *Mla6* NILs is possibly caused by splice site mutations in the intron of transcripts from isolates virulent on *Mla6* lines that map to the AVR_{a6} gene. The intron retention observed in most of these transcripts is potentially caused by either a splice branch point mutation or a splice donor site mutation and leads to premature stop codons (S3 and S4 Figs).

Even though the encoded truncated proteins are detectable in heterologous *N. benthamiana* (Fig 2C), RNA-Seq analysis of virulent *Bgh* isolates on barley leaves suggests that these mutations result in significantly reduced transcript levels. The latter is possibly a consequence of nonsense-mediated mRNA decay (NMD) [41]. This observation, together with a high virulence frequency on Mla6 NILs in European *Bgh* populations [42], suggests that the loss of the AVR_{a6} effector gene does not have a detrimental impact on *Bgh* virulence. Future studies might clarify whether AVR_{a6} virulence function can be compensated by AVR_{a6} family members or more distantly related effectors.

A predicted common ribonuclease-like fold among *Blumeria* AVR_A, AVRPM3 and AVRPM2 effectors

AVR_{A6} was predicted to be structurally similar to CSEP0064 (Fig 3). Upon re-analysis of all previously reported *Bgh* AVR_A effectors using the version 5.0 of the IntFOLD structural prediction server, we report here evidence supporting a common structural fold amongst the so far isolated AVR_A effectors despite the lack of relatedness between their DNA and protein sequences (Fig 3). Moreover, AVR_A effectors appear to share this structural fold at least with *Bgt* AVRPM2 and $AVRPM3^{D3}$ effectors that are recognized by wheat NLRs PM2 and PM3, respectively (Fig 3; [22,35,36]). In addition, protein alignments and *in silico* tertiary structure modelling suggest that *Bgt* $AVRPM3^{A2/F2}$ and $AVRPM3^{B2/C2}$ also have a central α-helix that faces three to four β-sheets [22]. Even though AVR_A effectors seem to have a common predicted fold similar to RNases, the residues critical for catalytic activity are lacking in the predicted AVR_A structures and we did not detect ribonuclease activity when AVR_A effectors were co-incubated with RNA (Fig 4A).

Given that multi-allelic barley MLA, multi-allelic wheat PM3, and wheat PM2 NLRs are sequence-unrelated and are encoded on non-syntenic chromosomal locations, it is possible that these immune receptors arose by convergent evolution to detect distinct members of the structurally related superfamily of powdery mildew RALPH effectors.

We speculate on two evolutionary scenarios that might explain the diversity of extant RNase-like effectors in *Bgh* and *Bgt*. In a common descent scenario, all RALPH effectors have diversified from an "*ur*-RALPH", which was present in the last common ancestor prior to host specialization of grass powdery mildews [29]. For instance, striking sequence conservation of *AvrPm2* among *Blumeria ff spp secalis*, *tritici* and *hordei* [36] and the presence of orthologous candidate effector gene families among specialized forms of grass powdery mildews support a common descent model [43]. The relatively small number of RALPH effectors in dicot-infecting powdery mildew species such as *Erysiphe pisi* [44] and in the early-diverged *Parauncinula polyspora* [45] suggests that RALPHs could have evolved 80–90 million years ago [46]. However, the variable intron location in *Blumeria AVR* genes (S6 and S7 Figs) questions this hypothesis. In an alternative scenario, the predicted structural relatedness of known AVRPM and AVR_A effectors could be the product of convergent evolution from different fungal RNases in the order Erysiphales after the differentiation of *formae speciales*. In summary, our data is reminiscent of findings indicating the existence of sequence unrelated but structurally related MAX effectors (*Magnaporthe* Avrs and ToxB-like) that account for 10% of the *M. oryzae* effector repertoire in this Ascomycete pathogen [47]. Another example for sequence-diversified but structurally-related effectors are oomycete RXLR effectors, such as ATR1 and ATR13 in *Hyaloperonospora arabidopsidis* [48,49], and PexRD2 and AVR3a11 in *Phytophthora infestans* [50].

The LRRs of allelic MLA receptors determine recognition of matching AVR$_A$ effectors

Earlier work with hybrids built from MLA1 and MLA6 receptors demonstrated that the MLA LRR is a determinant of *Bgh* isolate-specific recognition [38]. In this previous study it could not be clarified whether the respective AVR$_A$ effectors are the only fungal components that determine isolate-specific recognition by the MLA LRR domains. We show here that the LRR of four MLA receptors (MLA1, MLA6, MLA10, and MLA22) is responsible for specific recognition of matching AVR$_A$ effectors. We found that for the recognition of AVR$_{A6,}$ the C-terminal six LRR repeats of MLA6 cannot be exchanged to the ones found in MLA1, while the 12 C-terminal LRR repeats of MLA1 cannot be exchanged to those of MLA6 for recognition of AVR$_{A1}$. Similarly, four C-terminal LRR repeats of the flax allelic L5 and L6 receptors are necessary for recognition of matching AvrL567 effectors [27]. Most sites of positive selection among MLA resistance specificities cluster on the predicted concave site of the C-terminal LRRs [19,20]. Thus, it is possible that these LRR residues are contact sites for specific recognition and association with structurally related AVR$_A$ effectors. We confirmed this assumption for the LRRs of MLA10 by observing an association of MLA22LRR10 with AVR$_{A10}$ when the proteins were co-expressed in plants or in yeast (Fig 6C).

Unexpectedly, whereas M11166, M16666, M61111, and M66111 chimeras clearly recognize the corresponding AVR$_A$ effectors in barley protoplasts (Fig 5A), the latter three hybrid receptors are non-functional in heterologous *N. benthamiana*. The resistance function of several barley *Mla* recognition specificities, including *Mla6*, is genetically dependent on *HvRar1*, *HvSgt1*, and *HvHsp90* [38,51,52], which form a chaperone/co-chaperone complex in which *Hv*HSP90 directly interacts with the LRR of MLA [52,53]. Thus, the hybrid MLA1/MLA6 receptors might be dependent on an additional barley protein for full resistance function. Interestingly, the function of M11166 is known to be fully independent of *HvSGT1* and *HvRAR1* in barley and we have shown here that this is the sole MLA6/MLA1 chimeric receptor functional in *N. benthamiana* [38,51].

Multiple polymorphic AVR$_{A10}$/AVR$_{A22}$ residues influence recognition by MLA10 and MLA22

AVR$_{a10}$ and *AVR$_{a22}$* effector alleles are maintained as a balanced polymorphism in a worldwide collection of *Bgh* isolates [11], which implies an important virulence function for the *AVR$_{a10}$*/*AVR$_{a22}$* gene, supported by its membership in the *Blumeria* core effectorome [40]. As the effector alleles with only 11 polymorphic amino acids likely adopt an identical protein structure, we aimed here to pinpoint polymorphic residues in AVR$_{A10}$/AVR$_{A22}$ recognized by MLA10 and MLA22, respectively. Some effector chimeras, including chimera11 or chimera13 containing only two polymorphic residues compared to the respective WT avirulence effectors, escaped recognition by MLA10 and MLA22, even though these are stable proteins in *N. benthamiana*. This is consistent with the observation that other naturally occurring virulent AVR$_A$ effector variants can escape recognition by only one or two amino acid substitutions in the respective AVR$_A$ polypeptides [11,28]. Similarly, one amino acid exchange in *Bgt* AVRPM3$^{A2/F2}$ leads to a loss of pathogen recognition [54]. We identified four residues in AVR$_{A10}$ that cannot be exchanged to the ones found in AVR$_{A22}$ without losing recognition by MLA10. Four different residues in AVR$_{A22}$ cannot be exchanged to the ones found in AVR$_{A10}$ without losing recognition by MLA22. Of note, chimera26 can be recognized by MLA10 and

MLA22 (Figs 8 and 9), further suggesting that differential regions in AVR_{A10} and AVR_{A22} are recognized by MLA10 and MLA22, respectively. Our findings are consistent with the identification of multiple residues, spread along the *Bgt* $AVRPM3^{B2/C2}$ effector polypeptide, that cannot be exchanged for specific detection by wheat PM3b or PM3c NLRs [22]. Multiple, additive contact points of the AvrL567-A and -D flax rust fungus alleles are recognized by the flax receptors L5 and L6, respectively [27]. In summary, our findings suggest that multiple residues on the AVR_A effector surface determine the specific recognition by MLA receptors, and this may influence the functional diversification process of these receptors.

Previous studies suggested that RALPH effectors are pseudoenzymes that cannot cleave RNA due to the absence of a catalytic amino acid triad present in the fungal F1 RNase that are needed for enzymatic RNA catalysis [30]. These catalytic residues are E58, R77, and H92 [55]. We found that only one residue involved in RNA catalysis (R81) is conserved in the deduced AVR_{A10}/AVR_{A22} RNase-like effectors. Notably, four amino acids in AVR_{A10} cannot be exchanged to the ones found in AVR_{A22} (D53, F77, H64, and W96), and these are located close to a predicted positively charged area on the effector's surface. In the F1 RNase, the corresponding area forms the catalytic cleft. Residues required for MLA22 recognition are found in a negatively charged surface patch away from the negatively charged area presumably recognized by MLA10 (Fig 11A and 11B). This data is underlined by the recognition of chimera26 through MLA10 and MLA22, as chimera26 carries both of the described recognition patches. Recently, a few RALPH effectors were found in *E. pisi*, which infects a dicotyledonous host, and structural predictions showed that residues for RNA catalysis are partially conserved and are located within a positively charged binding cleft [44]. This is in agreement with our findings for *Bgh* AVR_{A10} and AVR_{A22} but contrasts with the absence of any catalytic triad residue as well as a positively charged binding cleft in the structure of *Bgh* CSEP0064 [30]. If these residues, which are located in the predicted positively charged cleft, and are recognized by MLA10, are also involved in potential RNA binding of AVR_{A10} and AVR_{A22} remains to be determined.

Methods

Phylogenetic analysis of *Blumeria graminis* formae speciales candidate-secreted effector proteins

Secretomes for the *B. graminis* formae speciales *poae*, *lolium*, *avenae*, *tritici* 96224, *hordei* DH14, *secalis* S1459, *triticale* T1-20, and *dactylidis* were obtained as described in Frantzeskakis et al. 2019 [40]. Subsequently, protein sequences without the signal peptide were aligned using MAFFT v7.310 (command used: mafft—amino —6merpair—maxiterate 1000—thread 12; [56]). The resulting alignment was then passed to IQ-TREE v1.6.beta4 (command used: iqtree-1.6.beta4-Linux/bin/iqtree -m VT+R8 -s all_seqs.fa.aln -nt 12 -bb 1000; [57]), and the phylogenetic tree generated was visualized using ITOL (https://itol.embl.de/tree/13461102183294661576347461; [58]). If not already publicly available [40,43,59], proteomes used for secretome prediction were generated using the MAKER pipeline [60] as described previously [40].

Plant material

The barley cultivar Golden Promise was grown at 19˚C, 70% humidity and under a 16 h photoperiod. *N. benthamiana* plants were grown and maintained under standard greenhouse conditions.

Association analysis

RNA-seq read alignment, variant calling, and association analysis were performed as described in Saur *et al.*, 2019 [11].

Generation of expression vectors

Entry clones and destination constructs for the expression of *AVR_{a1}*, *AVR_{a1}-V1*, *AVR_{a10}*, *AVR_{a22}*, *AVR_{a10}-V/AVR_{a22}-V*, *Mla10*, *Mla22*, *Mla1*, *and Mla6* were previously published by Saur et al., 2019 [11]. *CSEP0058* (*BLGH_00697*) was cloned from the cDNA of *Bgh* isolate DH14 using the primers listed in S3 Table. *M16666*, *M61111*, *M11166*, and *M66111* DNA sequences with introns in the pUBI-NOS vector were previously published by Shen et al., 2003 [38], and for expression in *N. benthamiana* were amplified from the pUBI-NOS vector [38] and cloned into pENTR/D-TOPO without a stop codon (S3 Table). cDNAs of *AVR_{a6}*, *AVR_{A6}-V2*, *CSEP0333* (*BLGH00698*), and *BLGH_00700*, *chimeras 11*, *12*, *13*, *14*, *15*, *16*, and *23*, chimeric *Mla10Lrr22* and *Mla22Lrr10* were synthesized with or without a stop codon as pDONR221 (Km^R) entry clones by GeneArt (Thermo Fisher). *Chimeras 21*, *22*, *24*, *25*, *26*, *28*, *29*, and *30* were generated by site-directed mutagenesis PCR using primers listed in S3 Table. The integrity of all entry clones was confirmed by Sanger sequencing.

For transient expression assays in barley protoplasts, *N. benthamiana*, and yeast, the genes were recombined using LR-Clonase II (Thermo Fisher) into the pIPKb002 ($Spec^R$) [61], pGWB517 ($Spec^R$) [62], pXCGS-GW-mYFP ($Carb^R$) [63], the pLexA-GW ($Carb^R$) [64], or the pB42AD-GW ($Carb^R$) [64] gateway-compatible destination vectors. Additional constructs used in this study were described in Saur *et al*., 2019 [11].

Transient gene expression assays in barley protoplasts

The isolation and transfection of barley protoplasts was performed as described in Saur *et al*., 2019 [33]. In short, cDNAs of the *AVR_a*s were co-expressed with cDNAs of *Mla10*, *Mla22*, *Mla10Lrr22*, and *Mla22Lrr10* using the pIPKb002 vector with a strong ubiquitin promoter or with intron-containing DNA of chimeras *M16666*, *M11166*, *M61111*, or *M66111* in a pUBI-NOS-vector (described in Shen et al., 2003 [38]) in barley *cv*. Golden Promise protoplasts. Protoplast solution (300 μl of 3.5 x 10^5 cells/ml) was transfected with 4.5 μg of *LUC* reporter construct, 10 μg of *Mla* plasmid, and 6.5 μg of the respective *AVR_a* effector or an empty vector (*EV*). The protoplasts were incubated for 16 h at 21˚C in a plant growth chamber and then harvested by centrifugation at 1,000 x *g*. Subsequently, the supernatant was removed, and protoplasts were lysed by addition of 180 μl of cell culture lysis reagent (Promega, E1531). The LUC activity of samples was measured in a luminometer (Centro, LB960) using a 96-well plate in which 50 μl of protoplast lysate were mixed with 50 μl of the LUC substrate (Promega, E1501). The relative LUC units (RLU) were calculated by setting the absolute value of the EV sample to 1.

Transient gene expression assays in *Nicotiana benthamiana*

Expression constructs for AVR_A and MLA and respective chimeras were always freshly transformed into *Agrobacterium tumefaciens* strains GV3101::pm90 and GV3101::pm90RK and selected on LB media containing the respective antibiotic resistance. Single colonies were inoculated into liquid LB medium and grown overnight at 28˚C with agitation at 220 rpm to a maximal OD_{600} = 1.5. Agrobacteria were centrifuged at 2500 x *g* for 15 min and the pellet was resuspended in infiltration buffer (10 mM MES, pH 5.6, 10 mM $MgCl_2$, and 200 μM acetosyringone) to an OD_{600} of 1 to 1.2. The suspensions of Agrobacteria were incubated at 28˚C with shaking 150 rpm for at least 2 h. Leaves of four-week-old *N. benthamiana* plants were infiltrated with a 1:1 mix of bacteria carrying *AVR_a* constructs or *Mla* constructs. The cell death score was assessed at four days post infiltration. Leaf tissue was harvested two days post infiltration for western blot analysis and 40 hours for split-LUC assays.

Split-luciferase complementation assay

The assay was performed as described in Saur *et al*., 2019 [11].

Plant protein extraction and immunoprecipitation for detection of fusion proteins

N. benthamiana leaf material was frozen in liquid nitrogen and ground to a fine powder using a Retsch bead beater.

For the detection of AVR_A-nLUC and MLA-cLUC proteins, 50 mg of leaf tissue was resuspended in 150 μl of urea-SDS sample buffer (50 mM Tris-HCl pH 6.8, 2% SDS, 8 M urea, 2% β-mercaptoethanol, 5% glycerol, and 0.004% bromophenol blue) and vortexed at room temperature for 10 min before centrifugation at 16,000 × *g* for 10 min.

For the detection of AVR_A-mYFP and MLA-4xmyc proteins, 300 mg of ground leaf tissue were dissolved in 2 mL of ice cold extraction buffer (150 mM Tris-HCl, pH 7.5, 150 mM NaCl, 10 mM EDTA, 10% (v/v) glycerol, 10 mM DTT, 2% (v/v) plant protease inhibitor cocktail (Sigma), 1 mM NaF, 1 mM Na_3VO_4, 1 mM PMSF, and 0.5% (v/v) IGEPAL). Extracts were centrifuged twice for 16 min at 16,000 x *g* at 4˚C. For the detection of MLA-4xmyc proteins, the extracts were diluted 4:1 with 4 x SDS loading buffer for SDS-PAGE. Samples were heated for 5 min at 95˚C. For the detection of AVR_A-mYFP, the proteins were concentrated using GFP-trap-MA (Chromotek) beads. Beforehand, the beads were incubated in equilibration buffer (150 mM Tris-HCl, pH 7.5, 150 mM NaCl, 10 mM EDTA, pH 7.5, 10% Glycerol, 1.5% (w/v) BSA) for 1 hour at 4˚C with slow rotation. The protein extracts were incubated with the equilibrated beads for 4 h at 4˚C with slow rotation. Subsequently, the beads were washed five times with cold wash buffer at 4˚C. The conjugated proteins were stripped off the beads by boiling the samples in 30 μl 4 x Laemmli sample buffer at 95˚C for 10 min.

Samples were separated on 8% or 10% SDS-PAGE gels, blotted onto PVDF membranes and detected using anti-LUC (SIGMA L0159), anti-GFP (abcam ab6556) or anti-myc (abcam ab9106) antibodies followed by anti-rabbit IgG-HRP (Santa Cruz Biotechnology sc-2313). Proteins were detected with the SuperSignal West Femto chemiluminescent substrate (Thermo Fisher, catalog number 34095) using Gel Doc XR and a gel documentation system (Bio-Rad).

Protein expression and purification from *Escherichia coli*

AVR_{A6} (25–115) AVR_{A10} (21–119), and AVR_{A13} (21–122) were expressed in *E. coli* as fusion proteins with N-terminal GST tags. The expression plasmids pGEX6p-1 (GE Healthcare) were transformed into the *E. coli* strain BL21 (DE3) (Novagen) by heat shock and grown at 37˚C in Luria-Bertani broth to an OD_{600} of 0.6. Isopropyl-β-D-thiogalactoside (IPTG, Sigma) was added to induce protein expression at 18˚C for a further 12 h. The cells were harvested by centrifugation at 6,000 x *g* for 10 min at 4˚C and resuspended in resuspension buffer (25 mM TRIS pH 8, 150 mM NaCl). Cell suspensions were lysed by sonification. Cell debris was removed by centrifugation at 30,000*g* for 2 h. The soluble fractions were collected and allowed to flow through GST resin (GE Healthcare). After washing with two column volumes of the same buffer used for resuspension, another 2 ml of buffer and 10 μl of PreScission protease (GE Healthcare) were added to the column followed by overnight incubation to cleave off the AVR_A proteins from the GST resin. The cleaved AVR_A proteins were then eluted and further purified by size-exclusion chromatography using a Superdex 200 10/30 gel filtration column (GE Healthcare).

Protein expression and purification from insect cells

AVR_{A6} (25–115) AVR_{A10} (21–119), and AVR_{A13} (21–122) were expressed in insect cells as fusion proteins with N-terminal GST tags. The expression plasmids pFASTBAC1 (Invitrogen) were transformed into the *E. coli* strain DH10Bac (Invitrogen) by heat shock. Successful transformation was validated by blue-white selection and bacmids of positive colonies were subsequently isolated with a DNA Mini Kit (QIAGEN). Sf21 insect cells (Invitrogen) were transfected with sequence verified bacmids by CellfectinII (Thermo Fisher). After five days incubation at 28˚C, recombinant baculovirus P0 were harvested and used to amplify P1 virus for another three days. Insect cells were infected at concentration of 2.0×10^6–2.5×10^6 cells/ml with P1 virus for 60 h. Insect cells were harvested and re-suspended in resuspension buffer (25 mM TRIS pH 8, 150 mM NaCl,15mM imidazole) followed by sonification lysis. Cell debris were removed by centrifugation at 30,000*g* for 2 h. The soluble fractions were collected and allowed to flow through a GST affinity trap. After washing with two column volumes of the same buffer used for resuspension, another 2 ml of buffer and 10 μl of PreScission protease (GE Healthcare) were added to the column, followed by overnight incubation to cleave off the AVR_A proteins from the GST resin. The cleaved AVRA proteins were then eluted and further purified by size-exclusion chromatography using a Superdex 200 10/30 gel filtration column (GE Healthcare). The proteins were tested for RNase activity with the same method applied for *E. coli* purified proteins.

RNase activity assays

Leaf material from three-week-old barley *cv*. Golden Promise plants was harvested to extract total RNA using the RNeasy Plant Mini Kit (QIAGEN). The remaining genomic DNA was removed by treating RNA with TURBO DNase enzyme (Ambion). Purified AVR_A effectors from *E. coli* were incubated with denatured total barley RNA. Then, 30 μl reaction mixtures (1 μg RNA, 1 μM protein in 15 mM Tris-HCl (pH 8.0), 15 mM NaCl, 50 mM KCl, and 2.5 mM EDTA) were incubated at 25˚C for 90 min. RNase F1 (Sigma) was included as a positive control. For analysis by the Bioanalyzer 2100 (Agilent Technologies, USA) 10 μl of sample were used.

To test the consumption of native rabbit rRNA, purified AVR_A effectors were incubated with 20 μl of rRNA from rabbit reticulocyte lysate (Promega) following the method of Kao et al. 2001 [37]. 30 μl reaction mixtures (20 μl rabbit reticulocyte lysate, 1μM purified AVR_A effectors in 15 mM Tris-HCl pH 8.0, 15 mM NaCl, 50 mM KCl, 2.5 mM EDTA) were incubated at 25˚C. After 60 or 30 min, the reaction was terminated by adding 20 μl phenol/chloroform and was vortexed for 30 seconds. Samples were sedimented at 14,000 rpm for 15 min and 30 μl of the aqueous layer was removed and mixed with 6 μl electrophoresis loading buffer. For analysis by the Bioanalyzer 2100 (Agilent Technologies, USA) 10 μl of sample were used.

Yeast two-hybrid assays

Mla variants were cloned into the pLexA-GW vector [64] for expression with an N-terminal LexA activation domain under the control of a constitutive ADH1 promoter (BD-MLA). The AVR_a variants were cloned into pB42AD-GW [64] for expression with an N-terminal B42 activation domain followed by the HA tag under the control of an inducible GAL1 promoter ($AD\text{-}AVR_a$). Using the lithium acetate method [65], *Mla* bait constructs and AVR_a prey constructs were co-transformed into the yeast strain EGY4.8 p8op-lacZ and successful transformants were selected by colony growth on SD-UHW/Glu (4% (w/v) Glucose, 0.139% (w/v) yeast synthetic drop-out medium pH 5.8 without uracil, histidine, tryptophan, 0.67% (w/v) BD Difco yeast nitrogen base, and 2% (w/v) Bacto Agar). Yeast transformants were grown to

OD_{600} 1 in liquid SD-UHW/Glu before harvesting cells for serial dilution on SD-UHW/Gal/Raf media (SD-UHW without glucose but with 2% (w/v) Galactose 1% (w/v) Raffinose, with (-UHW) or without Leucine (-UHWL)) and incubated for 14 days at 30˚C.

Yeast protein extraction

For protein extraction, 10 ml of co-transformed yeast strains were grown to an OD_{600} of 1 in SD-UHW/Gal/Raf liquid medium at 30˚C with shaking at 200 rpm. The proteins were precipitated using the ammonium acetate method (modified from Karginov and Agaphonov et al., 2016 [66]). In short, cells were harvested by centrifugation at 700 x*g* for 5 min. The pellets were resuspended in 200 μl NH_4-acetate buffer (1 M $NH_4(CH_3COO)$, 150 mM NaCl, 30 mM Tris-HCl, pH 7.5, 10 mM PMSF, 5 mM EDTA, and one tablet of Protease Inhibitor Cocktail (Roche). The yeast suspension was transferred into BeadBug-prefilled tubes with 0.5-mm silica glass beads (Sigma) and ground in a Precellys homogenizer (two times at 6,200 rpm for 30 sec, break: 15 sec). Afterwards, the DNA was sheared using a Diogenode Bioruptur ultrasonic water bath (twice for 30 sec at high power, break: 90 sec). The suspension without the beads was transferred into a Protein LoBind tube (Eppendorf). The glass beads were washed three times with 250 μl NH_4-acetate buffer. The washes were combined with the suspension and incubated for 1.5 h on ice. Precipitated proteins were harvested by centrifugation (16,000 x *g* for 10 min). Precipitates were washed with 1 ml 1 M NaCl and the pellet was resuspended with 200 μl Urea-SDS sample buffer (50 mM Tris-HCl, pH 6.8, 2% SDS, 8 M Urea, 1% ß-mercaptoethanol, 2 mM EDTA, 5% glycerol, and 0.004% bromophenol blue) at room temperature. Resuspension in urea-SDS buffer and omission of the boiling step is essential for detection of LexA-MLA fusion proteins. For western blotting, 10–15 μl of the sample were loaded on 8% or 12% SDS page gels, blotted onto PVDF membranes and probed with either anti-HA (Merck, clone 3F10, RRID:AB_390914) or anti-LexA (Santa Cruz, Biotechnology, sc7544, RRID:AB_627883) primary antibodies, followed by incubation with secondary anti-rat (Santa Cruz Biotechnology, sc2065, RRID:AB_631756) or anti-mouse IgG-HRP antibodies (Santa Cruz Biotechnology, sc2005, RRID:AB_631736) for the detection of AVR_A or MLA proteins, respectively. HA and LexA fusion proteins were detected by HRP activity on SuperSignal West Femto Maximum Sensitivity Substrate (Thermo Fisher 34095) using a Gel Doc XR and gel documentation system (Bio-Rad).

Supporting information

S1 Fig. Transient co-expression of AVR_{a6} candidates with *Mla6* in cultivar (*cv.*) Golden Promise barley protoplasts. Transient co-expression of EV or cDNAs of *BLGH_00709* or *BLGH_00697* lacking their respective signal peptides together with *Mla6* and *pUBI*:*Luciferase* in *cv*. Golden Promise protoplasts. The LUC activity relative to the EV sample was measured as a proxy for cell death 16 hours post transfection. Bar diagrams represent mean relative LUC activity of eight transfections, which are represented by dots, while the standard deviation is indicated by error bars. Significant differences between samples were analyzed using a one-way ANOVA and siginificant difference is indicated by different letters. Calculated p-value: $p = 0.000331$
(TIF)

S2 Fig. Association of AVR_{a6} transcriptomic data with phenotypes of *Bgh* isolates on *Mla6* NILs. The table depicts infection phenotypes of 27 *Bgh* isolates on barley *Mla6* near-isogenic lines (NILs) [11,28] of the cultivar (*cv.*) Manchuria and *cv*. Pallas, a heatmap of the fragments per kilobase million (fpkm) expression data of AVR_{a6}, *BLGH_07092* and AVR_{a6} family members *BLGH_00698*, *BLGH_00697* and *BLGH_00700* and a list of the deduced AVR_{A6} proteins

expressed by each isolate.
(TIF)

S3 Fig. Schematic illustration of splice site mutations in *AVR$_{a6}$*, which presumably lead to virulence of *Bgh* isolates on *Mla6* NILs. (A) Schematic illustration depicting the three observed splice site mutations: Splice donor site, splice branch point, and splice acceptor site mutations. (B) Schematic illustration of the genomic, transcriptomic, and deduced protein sequences of the three *AVR$_{a6}$* effector variants: *AVR$_{a6}$*, *AVR$_{a6}$-V1*, and *AVR$_{a6}$-V2*. Depicted is the mutation in the consensus sequence of the branch point in *AVR$_{a6}$-V1* transcripts of *Bgh* isolates CC66 and CC148 and the splice donor site mutation in *AVR$_{a6}$-V2*, which can be found in transcripts and the genome of *Bgh* isolate K1. This splice site mutation likely lead to an intron retention, which is supported by RNA-seq reads. Intron retention introduces an early stop codon leading to anticipated truncation of the AVR$_{A6}$-V1 and AVR$_{A6}$-V2 proteins.
(TIF)

S4 Fig. Alignment of DNA, RNA, and protein sequences of AVR$_{A6}$, AVR$_{A6}$-V1 and AVR$_{A6}$-V2 variants including the signal peptide. (A) DNA sequence alignment of *AVR$_{a6}$*, *AVR$_{a6}$-V1*, and *AVR$_{a6}$-V2*. The sequence of *AVR$_{a6}$-V1* was deduced from RNA-seq reads. (B) RNA sequence alignment of *AVR$_{a6}$*, deduced *AVR$_{a6}$-V1*, and *AVR$_{a6}$-V2*. (C) Protein sequence of AVR$_{A6}$, deduced AVR$_{A6}$-V1, and AVR$_{A6}$-V2.
(TIF)

S5 Fig. Overlay of predicted AVR$_{A6}$ structure (red) with the X-ray crystallography structure of CSEP0064 (yellow) (PDB ID: 6fmb).
(TIF)

S6 Fig. Examination of the intron characteristic for RALPHs in *Bgt* and *Bgh* avirulence effectors. (A) Position of the intron, which was found to be characteristic for RALPH-like effectors in the gene models of *Bgt* and *Bgh AVR* effectors. Black boxes are the 5′ UTR and 3′ UTR, white boxes are the gene coding regions, dark grey boxes denote the signal peptides, and light grey boxes depict introns. The characteristic intron, which was found in RALPH effectors, is shown in yellow. (B) Protein sequence alignment of *Bgt* and *Bgh* avirulence effectors showing the amino acid similarity and identity using grey and black backgrounds, respectively. Red arrows depict the relative position of the intron. Two black bars at positions 37 and 133 of the alignment show two characteristic cysteines present in all effectors except for AVR$_{A13}$, which are predicted to form a disulfide bond.
(TIF)

S7 Fig. DNA sequence alignments of *Bgh* and *Bgt* AVR effectors. (A) DNA sequence alignment of *Bgt* and *Bgh* avirulence effectors including the signal peptide. Yellow background depicts the characteristic intron in RALPH effectors. B) Alignment of the intron sequence, which can be found in *Bgt* and *Bgh* RALPH avirulence effectors. Intron gDNA sequence alignment depicting identical nucleotides with a black background.
(TIF)

S8 Fig. Size exclusion chromatography and SDS-PAGE of purified AVR$_{A6}$, AVR$_{A10}$, and AVR$_{A13}$ effector proteins. (A) Size exclusion chromatogram (SEC) of AVR$_{A6}$, AVR$_{A10}$, and AVR$_{A13}$ showing absorbance at 280 nm (y-axis) against the retention volume (ml) (x-axis) and the respective fraction above (A34 and A36 for AVR$_{A6}$, A31 and A33 for AVR$_{A10}$; A32 and A34 for AVR$_{A13}$), which was used for further RNase activity assays. (B) Stain-free SDS-PAGE (Bio-rad) showing the fractions of purified AVR$_{A6}$, AVR$_{A10}$, and AVR$_{A13}$ proteins used for further RNase activity assays with a white arrow. AVR$_{A}$ protein fractions were separated on a

12% polyacrylamide gel and visualized by the ChemiDoc MP Imaging System (170–8280).
(TIF)

S9 Fig. Protein quality control of AVR_{A6}, AVR_{A10}, and AVR_{A13}. (A) Size exclusion chromatogram of AVR_{A6}, AVR_{A10}, and AVR_{A13} purified from insect cells. Fractions eluted at 18.5, 17, 17.5ml of AVR_{A6}, AVR_{A10}, and AVR_{A13} proteins were verified by SDS-PAGE (indicated by red, green and blue arrows) and used for further RNase activity assays. (B) After size exclusion, insect cell-purified AVR_{A6}, AVR_{A10}, and AVR_{A13} proteins or T1 RNase were incubated with denatured *Hv*RNA. All samples were separated on non-denaturing 2% agarose gels and analyzed on a Bioanalyzer to determine for RNA degradation.
(TIF)

S10 Fig. Amino acid sequence alignment of M61111, M66111, M16666, and M11166. Colored boxes depict different domains of the receptors: blue = CC-domain, green = NB-ARC domain, red = LRR as defined previously in [19]. Grey boxes depict individual LRRs.
(TIF)

S11 Fig. *N. benthamiana* corresponding to results of Fig 5. Pictures were taken under UV light (302 nm) at 5 days post transformation.
(TIF)

S12 Fig. Amino acid sequence alignment of MLA10, MLA22, MLA10LRR22, and MLA22LRR10 receptors. Colored boxes depict different domains of the receptors: blue = CC-domain, green = NB-ARC domain, red = LRR as defined previously in [19]. Grey boxes depict individual LRRs.
(TIF)

S13 Fig. *N. benthamiana* leaves corresponding to results shown in Fig 8. Pictures were taken at 5 days post transformation.
(TIF)

S14 Fig. HR indices of *N. benthamiana* leaf infiltrations. (A) HR index used for scoring cell death in *N. benthamiana*. 0 = no cell death, 1 = weak chlorosis of infiltrated spot, 2 = chlorosis, 3 = strong chlorosis with rare spots of collapsed, dead leaf material, 4 = strong cell death with collapsed leaf material. The color of the frames around cell death pictures indicates HR indices in stacked bar plots B-E. (B–E) Stacked bar plots showing the count of individual HR indices from independent leaf infiltrations. Significance of cell death scores was calculated by Fisher's exact test and an asterisk depicts $p < 0.05$: (B) MLA6, AVR_{A6}-1: $8.68xe^{-13}$; MLA1, AVR_{A1}: $2.6xe^{-11}$ (C) M11166, AVR_{A6}-1: $3.98xe^{-12}$; (D) MLA10, AVR_{A10}: $1.25xe^{-10}$; MLA22LRR10, AVR_{A10}: $3.07xe^{-07}$; MLA22, AVR_{A22}: $7.74xe^{-08}$; MLA10LRR22, AVR_{A22}: $5.8xe^{-07}$ (E) MLA10, AVR_{A10}: $3.07xe^{-29}$; MLA10, chimera26: $1.54xe^{-13}$; MLA10, chimera29: $3.73xe^{-12}$; MLA22, AVR_{A22}: $2.77xe^{-49}$; MLA22, chimera14: $6.68xe^{-28}$; MLA22, chimera22: $6.39xe^{-14}$; MLA22, chimera24: $1.5xe^{-11}$, MLA22; chimera26: $9.59xe^{-09}$.
(TIF)

S1 Table. Top-ranking AVR_{a6} candidates in the transcriptome-wide association study (TWAS) determined by gene-wise calling. * *The table columns show the new and former BLGH_ID, the description, the scaffold localization and the *p*-value of the top-ranking candidates for the gene-wise association of *Bgh* transcriptomes with infection phenotypes on *Mla6* near-isogenic lines (NILs). Color codes depict top-ranking AVR_{a6} candidates and are consistent with the color code used in Fig 1A: bright green: CSEP0254 paralogues, dark green:

BLGH_07092, dark red: BLGH_00697, bright red: BLGH_00700.
(TIF)

S2 Table. Top-ranking *AVR*$_{a6}$ candidates in the transcriptome-wide association study (TWAS) determined by variant-wise calling. * *The table columns depict the scaffold localization, the effect that the mutation has on the reference gene (non-synonymous mutation, gained stop codon), the codon change and the respective aa exchange, a gene description, the CSEP_ID and the *p*-value of the top-ranking candidates for the variant-wise association of *Bgh* transcriptomes with infection phenotypes on *Mla6* near-isogenic lines (NILs). Color codes designate top-ranking *AVR*$_{a6}$ candidates and are consistent with the color code used in Fig 1A: bright green: CSEP0254 paralogues, dark green: BLGH_07092 and bright red: BLGH_00700.
(TIF)

S3 Table. Primers used in this study.
(TIF)

Acknowledgments

We thank Sabine Haigis and Petra Köchner for excellent technical assistance and Yu Cao for the preparation of barley leaf RNA.

Author Contributions

Conceptualization: Saskia Bauer, Isabel M. L. Saur, Paul Schulze-Lefert.

Data curation: Saskia Bauer, Isabel M. L. Saur, Lamprinos Frantzeskakis, Barbara Kracher, Takaki Maekawa, Paul Schulze-Lefert.

Formal analysis: Saskia Bauer, Dongli Yu, Aaron W. Lawson, Isabel M. L. Saur, Lamprinos Frantzeskakis, Elke Logemann.

Funding acquisition: Isabel M. L. Saur, Paul Schulze-Lefert.

Investigation: Saskia Bauer, Dongli Yu, Aaron W. Lawson, Isabel M. L. Saur, Lamprinos Frantzeskakis, Elke Logemann, Takaki Maekawa, Paul Schulze-Lefert.

Methodology: Saskia Bauer, Dongli Yu, Elke Logemann.

Project administration: Paul Schulze-Lefert.

Resources: Isabel M. L. Saur, Takaki Maekawa, Paul Schulze-Lefert.

Software: Barbara Kracher.

Supervision: Isabel M. L. Saur, Jijie Chai, Paul Schulze-Lefert.

Validation: Isabel M. L. Saur.

Visualization: Saskia Bauer, Isabel M. L. Saur, Lamprinos Frantzeskakis, Barbara Kracher.

Writing – original draft: Saskia Bauer, Isabel M. L. Saur, Paul Schulze-Lefert.

Writing – review & editing: Saskia Bauer, Isabel M. L. Saur, Lamprinos Frantzeskakis, Barbara Kracher, Jijie Chai, Paul Schulze-Lefert.

References

1. Han G-Z. Origin and evolution of the plant immune system. New Phytol. 2019; 222: 70–83. https://doi.org/10.1111/nph.15596 PMID: 30575972

2. van der Burgh AM, Joosten MHAJ. Plant Immunity: Thinking Outside and Inside the Box. Trends Plant Sci. 2019; 24: 587–601. https://doi.org/10.1016/j.tplants.2019.04.009 PMID: 31171472
3. Periyannan S, Milne RJ, Figueroa M, Lagudah ES, Dodds PN. An overview of genetic rust resistance: From broad to specific mechanisms. PLoS Pathog. 2017; 13: e1006380–e1006380. https://doi.org/10.1371/journal.ppat.1006380 PMID: 28704545
4. Dyck PL, Kerber ER. Resistance of the Race-Specific Type. Cereal rusts. 1985; II.
5. Flor HH. Inheritance of pathogenicity in Melampsora lini. Phytopathology; 1942. pp. 653–669.
6. Jones JDG, Vance RE, Dangl JL. Intracellular innate immune surveillance devices in plants and animals. Science (80-). 2016; 354: aaf6395. https://doi.org/10.1126/science.aaf6395 PMID: 27934708
7. Jacob F, Vernaldi S, Maekawa T. Evolution and Conservation of Plant NLR Functions. Frontiers in Immunology. 2013. p. 297. https://doi.org/10.3389/fimmu.2013.00297 PMID: 24093022
8. Jubic LM, Saile S, Furzer OJ, El Kasmi F, Dangl JL. Help wanted: helper NLRs and plant immune responses. Curr Opin Plant Biol. 2019; 50: 82–94. https://doi.org/10.1016/j.pbi.2019.03.013 PMID: 31063902
9. Dodds PN, Lawrence GJ, Catanzariti A-M, Teh T, Wang C-IA, Ayliffe MA, et al. Direct protein interaction underlies gene-for-gene specificity and coevolution of the flax resistance genes and flax rust avirulence genes. Proc Natl Acad Sci. 2006; 103: 8888 LP– 8893. https://doi.org/10.1073/pnas.0602577103 PMID: 16731621
10. Krasileva K V, Dahlbeck D, Staskawicz BJ. Activation of an Arabidopsis Resistance Protein Is Specified by the in Planta Association of Its Leucine-Rich Repeat Domain with the Cognate Oomycete Effector. Plant Cell. 2010; 22: 2444 LP– 2458. https://doi.org/10.1105/tpc.110.075358 PMID: 20601497
11. Saur IML, Bauer S, Kracher B, Lu X, Franzeskakis L, Müller MC, et al. Multiple pairs of allelic MLA immune receptor-powdery mildew AVRA effectors argue for a direct recognition mechanism. Nürnberger T, Hardtke CS, Kroj T, editors. Elife. 2019; 8: e44471. https://doi.org/10.7554/eLife.44471 PMID: 30777147
12. Cesari S. Multiple strategies for pathogen perception by plant immune receptors. New Phytol. 2018; 219: 17–24. https://doi.org/10.1111/nph.14877 PMID: 29131341
13. Mackey D, Holt BF III, Wiig A, Dangl JL. RIN4 Interacts with Pseudomonas syringae Type III Effector Molecules and Is Required for RPM1-Mediated Resistance in Arabidopsis. Cell. 2002; 108: 743–754. https://doi.org/10.1016/s0092-8674(02)00661-x PMID: 11955429
14. Halterman D, Zhou F, Wei F, Wise RP, Schulze-Lefert P. The MLA6 coiled-coil, NBS-LRR protein confers AvrMla6-dependent resistance specificity to Blumeria graminis f. sp. hordei in barley and wheat. Plant J. 2001; 25: 335–348. https://doi.org/10.1046/j.1365-313x.2001.00982.x PMID: 11208025
15. Periyannan S, Moore J, Ayliffe M, Bansal U, Wang X, Huang L, et al. The Gene Sr33, an Ortholog of Barley Mla Genes, Encodes Resistance to Wheat Stem Rust Race Ug99. Science (80-). 2013; 341: 786 LP– 788. https://doi.org/10.1126/science.1239028 PMID: 23811228
16. Mago R, Zhang P, Vautrin S, Šimková H, Bansal U, Luo M-C, et al. The wheat Sr50 gene reveals rich diversity at a cereal disease resistance locus. Nat Plants. 2015; 1: 15186. https://doi.org/10.1038/nplants.2015.186 PMID: 27251721
17. Lücking R, Huhndorf S, Pfister DH, Plata ER, Lumbsch HT. Fungi evolved right on track. Mycologia. 2009; 101: 810–822. https://doi.org/10.3852/09-016 PMID: 19927746
18. Inukai T, Vales MI, Hori K, Sato K, Hayes PM. RMo1 Confers Blast Resistance in Barley and Is Located within the Complex of Resistance Genes Containing Mla, a Powdery Mildew Resistance Gene. Mol Plant-Microbe Interact. 2006; 19: 1034–1041. https://doi.org/10.1094/MPMI-19-1034 PMID: 16941907
19. Seeholzer S, Tsuchimatsu T, Jordan T, Bieri S, Pajonk S, Yang W, et al. Diversity at the Mla Powdery Mildew Resistance Locus from Cultivated Barley Reveals Sites of Positive Selection. Mol Plant-Microbe Interact. 2010; 23: 497–509. https://doi.org/10.1094/MPMI-23-4-0497 PMID: 20192836
20. Maekawa T, Kracher B, Saur IML, Yoshikawa-Maekawa M, Kellner R, Pankin A, et al. Subfamily-Specific Specialization of RGH1/MLA Immune Receptors in Wild Barley. Mol Plant-Microbe Interact. 2018; 32: 107–119. https://doi.org/10.1094/MPMI-07-18-0186-FI PMID: 30295580
21. Srichumpa P, Brunner S, Keller B, Yahiaoui N. Allelic Series of Four Powdery Mildew Resistance Genes at the Pm3 Locus in Hexaploid Bread Wheat. Plant Physiol. 2005; 139: 885 LP– 895. https://doi.org/10.1104/pp.105.062406 PMID: 16183849
22. Bourras S, Kunz L, Xue M, Praz CR, Müller MC, Kälin C, et al. The AvrPm3-Pm3 effector-NLR interactions control both race-specific resistance and host-specificity of cereal mildews on wheat. Nat Commun. 2019; 10: 2292. https://doi.org/10.1038/s41467-019-10274-1 PMID: 31123263
23. Bhullar NK, Street K, Mackay M, Yahiaoui N, Keller B. Unlocking wheat genetic resources for the molecular identification of previously undescribed functional alleles at the Pm3 resistance locus. Proc Natl Acad Sci. 2009; 106: 9519 LP– 9524. https://doi.org/10.1073/pnas.0904152106 PMID: 19470492

24. Yahiaoui N, Brunner S, Keller B. Rapid generation of new powdery mildew resistance genes after wheat domestication. Plant J. 2006; 47: 85–98. https://doi.org/10.1111/j.1365-313X.2006.02772.x PMID: 16740148

25. Yahiaoui N, Kaur N, Keller B. Independent evolution of functional Pm3 resistance genes in wild tetraploid wheat and domesticated bread wheat. Plant J. 2009; 57: 846–856. https://doi.org/10.1111/j.1365-313X.2008.03731.x PMID: 18980638

26. Krattinger SG, Keller B. Molecular genetics and evolution of disease resistance in cereals. New Phytol. 2016; 212: 320–332. https://doi.org/10.1111/nph.14097 PMID: 27427289

27. Ravensdale M, Bernoux M, Ve T, Kobe B, Thrall PH, Ellis JG, et al. Intramolecular Interaction Influences Binding of the Flax L5 and L6 Resistance Proteins to their AvrL567 Ligands. PLOS Pathog. 2012; 8: e1003004. Available: https://doi.org/10.1371/journal.ppat.1003004 PMID: 23209402

28. Lu X, Kracher B, Saur IML, Bauer S, Ellwood SR, Wise R, et al. Allelic barley MLA immune receptors recognize sequence-unrelated avirulence effectors of the powdery mildew pathogen. Proc Natl Acad Sci. 2016; 113: E6486–E6495. https://doi.org/10.1073/pnas.1612947113 PMID: 27702901

29. Spanu PD. Cereal immunity against powdery mildews targets RNase-Like Proteins associated with Haustoria (RALPH) effectors evolved from a common ancestral gene. New Phytol. 2017; 213: 969–971. https://doi.org/10.1111/nph.14386 PMID: 28079937

30. Pennington HG, Jones R, Kwon S, Bonciani G, Thieron H, Chandler T, et al. The fungal ribonuclease-like effector protein CSEP0064/BEC1054 represses plant immunity and interferes with degradation of host ribosomal RNA. PLOS Pathog. 2019; 15: e1007620. https://doi.org/10.1371/journal.ppat.1007620 PMID: 30856238

31. Pedersen C, van Themaat EVL, McGuffin LJ, Abbott JC, Burgis TA, Barton G, et al. Structure and evolution of barley powdery mildew effector candidates. BMC Genomics. 2012; 13: 694. https://doi.org/10.1186/1471-2164-13-694 PMID: 23231440

32. McGuffin LJ, Adiyaman R, Maghrabi AHA, Shuid AN, Brackenridge DA, Nealon JO, et al. IntFOLD: an integrated web resource for high performance protein structure and function prediction. Nucleic Acids Res. 2019; 47: W408–W413. https://doi.org/10.1093/nar/gkz322 PMID: 31045208

33. Saur IML, Bauer S, Lu X, Schulze-Lefert P. A cell death assay in barley and wheat protoplasts for identification and validation of matching pathogen AVR effector and plant NLR immune receptors. Plant Methods. 2019; 15: 118. https://doi.org/10.1186/s13007-019-0502-0 PMID: 31666804

34. Pliego C, Nowara D, Bonciani G, Gheorghe DM, Xu R, Surana P, et al. Host-Induced Gene Silencing in Barley Powdery Mildew Reveals a Class of Ribonuclease-Like Effectors. Mol Plant-Microbe Interact. 2013; 26: 633–642. https://doi.org/10.1094/MPMI-01-13-0005-R PMID: 23441578

35. Bourras S, McNally KE, Ben-David R, Parlange F, Roffler S, Praz CR, et al. Multiple Avirulence Loci and Allele-Specific Effector Recognition Control the *Pm3* Race-Specific Resistance of Wheat to Powdery Mildew. Plant Cell. 2015; 27: 2991 LP– 3012. https://doi.org/10.1105/tpc.15.00171 PMID: 26452600

36. Praz CR, Bourras S, Zeng F, Sánchez-Martín J, Menardo F, Xue M, et al. AvrPm2 encodes an RNase-like avirulence effector which is conserved in the two different specialized forms of wheat and rye powdery mildew fungus. New Phytol. 2017; 213: 1301–1314. https://doi.org/10.1111/nph.14372 PMID: 27935041

37. Kao R, Martínez-Ruiz A, del Pozo AM, Crameri R, Davies J. Mitogillin and Related Fungal Ribotoxins. In: Nicholson AWBT-M in E, editor. Ribonucleases—Part A. Academic Press; 2001. pp. 324–335. https://doi.org/10.1016/S0076-6879(01)41161-X

38. Shen Q-H, Zhou F, Bieri S, Haizel T, Shirasu K, Schulze-Lefert P. Recognition Specificity and RAR1/SGT1 Dependence in Barley Mla Disease Resistance Genes to the Powdery Mildew Fungus. Plant Cell. 2003; 15: 732 LP– 744. https://doi.org/10.1105/tpc.009258 PMID: 12615945

39. Wang C-IA, Gunčar G, Forwood JK, Teh T, Catanzariti A-M, Lawrence GJ, et al. Crystal Structures of Flax Rust Avirulence Proteins AvrL567-A and -D Reveal Details of the Structural Basis for Flax Disease Resistance Specificity. Plant Cell. 2007; 19: 2898 LP– 2912. https://doi.org/10.1105/tpc.107.053611 PMID: 17873095

40. Frantzeskakis L, Kusch S, Panstruga R. The need for speed: compartmentalized genome evolution in filamentous phytopathogens. Mol Plant Pathol. 2019; 20: 3–7. https://doi.org/10.1111/mpp.12738 PMID: 30557450

41. González CI, Bhattacharya A, Wang W, Peltz SW. Nonsense-mediated mRNA decay in Saccharomyces cerevisiae. Gene. 2001; 274: 15–25. https://doi.org/10.1016/s0378-1119(01)00552-2 PMID: 11674994

42. Dreiseitl A. Pathogenic divergence of Central European and Australian populations of Blumeria graminis f. sp. hordei. Ann Appl Biol. 2014; 165: 364–372. https://doi.org/10.1111/aab.12141

43. Menardo F, Praz CR, Wicker T, Keller B. Rapid turnover of effectors in grass powdery mildew (Blumeria graminis). BMC Evol Biol. 2017; 17: 223. https://doi.org/10.1186/s12862-017-1064-2 PMID: 29089018

44. Sharma G, Aminedi R, Saxena D, Gupta A, Banerjee P, Jain D, et al. Effector mining from the Erysiphe pisi haustorial transcriptome identifies novel candidates involved in pea powdery mildew pathogenesis. Mol Plant Pathol. 2019; 20: 1506–1522. https://doi.org/10.1111/mpp.12862 PMID: 31603276

45. Frantzeskakis L, Németh MZ, Barsoum M, Kusch S, Kiss L, Takamatsu S, et al. The Parauncinula polyspora Draft Genome Provides Insights into Patterns of Gene Erosion and Genome Expansion in Powdery Mildew Fungi. Turgeon BG, editor. MBio. 2019; 10: e01692–19. https://doi.org/10.1128/mBio.01692-19 PMID: 31551331

46. Takamatsu S, Niinomi S, Cabrera De ÁLvarez MG, Álvarez RE, Havrylenko M, Braun U. Caespitotheca gen. nov., an ancestral genus in the Erysiphales. Mycol Res. 2005; 109: 903–911. https://doi.org/10.1017/s0953756205003047 PMID: 16175792

47. de Guillen K, Ortiz-Vallejo D, Gracy J, Fournier E, Kroj T, Padilla A. Structure Analysis Uncovers a Highly Diverse but Structurally Conserved Effector Family in Phytopathogenic Fungi. PLOS Pathog. 2015; 11: e1005228. Available: https://doi.org/10.1371/journal.ppat.1005228 PMID: 26506000

48. Chou S, Krasileva K V, Holton JM, Steinbrenner AD, Alber T, Staskawicz BJ. Hyaloperonospora arabidopsidis ATR1 effector is a repeat protein with distributed recognition surfaces. Proc Natl Acad Sci. 2011; 108: 13323 LP– 13328. https://doi.org/10.1073/pnas.1109791108 PMID: 21788488

49. Leonelli L, Pelton J, Schoeffler A, Dahlbeck D, Berger J, Wemmer DE, et al. Structural Elucidation and Functional Characterization of the Hyaloperonospora arabidopsidis Effector Protein ATR13. PLOS Pathog. 2011; 7: e1002428. Available: https://doi.org/10.1371/journal.ppat.1002428 PMID: 22194684

50. Boutemy LS, King SRF, Win J, Hughes RK, Clarke TA, Blumenschein TMA, et al. Structures of Phytophthora RXLR effector proteins: A conserved but adaptable fold underpins functional diversity. J Biol Chem. 2011. https://doi.org/10.1074/jbc.M111.262303 PMID: 21813644

51. Halterman DA, Wise RP. A single-amino acid substitution in the sixth leucine-rich repeat of barley MLA6 and MLA13 alleviates dependence on RAR1 for disease resistance signaling. Plant J. 2004; 38: 215–226. https://doi.org/10.1111/j.1365-313X.2004.02032.x PMID: 15078326

52. Bieri S, Mauch S, Shen Q-H, Peart J, Devoto A, Casais C, et al. RAR1 Positively Controls Steady State Levels of Barley MLA Resistance Proteins and Enables Sufficient MLA6 Accumulation for Effective Resistance. Plant Cell. 2004; 16: 3480 LP– 3495. https://doi.org/10.1105/tpc.104.026682 PMID: 15548741

53. Azevedo C, Sadanandom A, Kitagawa K, Freialdenhoven A, Shirasu K, Schulze-Lefert P. The RAR1 Interactor SGT1, an Essential Component of R Gene-Triggered Disease Resistance. Science (80-). 2002; 295: 2073 LP– 2076. https://doi.org/10.1126/science.1067554 PMID: 11847307

54. McNally KE, Menardo F, Lüthi L, Praz CR, Müller MC, Kunz L, et al. Distinct domains of the AVRPM3A2/F2 avirulence protein from wheat powdery mildew are involved in immune receptor recognition and putative effector function. New Phytol. 2018; 218: 681–695. https://doi.org/10.1111/nph.15026 PMID: 29453934

55. Vassylyev DG, Katayanagi K, Ishikawa K, Tsujimoto-Hirano M, Danno M, Pähler A, et al. Crystal Structures of Ribonuclease F1 of Fusarium moniliforme in Its Free Form and in Complex with 2′GMP. J Mol Biol. 1993; 230: 979–996. https://doi.org/10.1006/jmbi.1993.1214 PMID: 8386773

56. Katoh K, Standley DM. MAFFT multiple sequence alignment software version 7: improvements in performance and usability. Mol Biol Evol. 2013/01/16. 2013; 30: 772–780. https://doi.org/10.1093/molbev/mst010 PMID: 23329690

57. Nguyen L-T, Schmidt HA, von Haeseler A, Minh BQ. IQ-TREE: A Fast and Effective Stochastic Algorithm for Estimating Maximum-Likelihood Phylogenies. Mol Biol Evol. 2014; 32: 268–274. https://doi.org/10.1093/molbev/msu300 PMID: 25371430

58. Letunic I, Bork P. Interactive tree of life (iTOL) v3: an online tool for the display and annotation of phylogenetic and other trees. Nucleic Acids Res. 2016; 44: W242–W245. https://doi.org/10.1093/nar/gkw290 PMID: 27095192

59. Müller MC, Praz CR, Sotiropoulos AG, Menardo F, Kunz L, Schudel S, et al. A chromosome-scale genome assembly reveals a highly dynamic effector repertoire of wheat powdery mildew. New Phytol. 2019; 221: 2176–2189. https://doi.org/10.1111/nph.15529 PMID: 30388298

60. Holt C, Yandell M. MAKER2: an annotation pipeline and genome-database management tool for second-generation genome projects. BMC Bioinformatics. 2011; 12: 491. https://doi.org/10.1186/1471-2105-12-491 PMID: 22192575

61. Himmelbach A, Zierold U, Hensel G, Riechen J, Douchkov D, Schweizer P, et al. A Set of Modular Binary Vectors for Transformation of Cereals. Plant Physiol. 2007; 145: 1192 LP– 1200. https://doi.org/10.1104/pp.107.111575 PMID: 17981986

62. NAKAGAWA T, SUZUKI T, MURATA S, NAKAMURA S, HINO T, MAEO K, et al. Improved Gateway Binary Vectors: High-Performance Vectors for Creation of Fusion Constructs in Transgenic Analysis of Plants. Biosci Biotechnol Biochem. 2007; 71: 2095–2100. https://doi.org/10.1271/bbb.70216 PMID: 17690442

63. García A V, Blanvillain-Baufumé S, Huibers RP, Wiermer M, Li G, Gobbato E, et al. Balanced Nuclear and Cytoplasmic Activities of EDS1 Are Required for a Complete Plant Innate Immune Response. PLOS Pathog. 2010; 6: e1000970. Available: https://doi.org/10.1371/journal.ppat.1000970 PMID: 20617163

64. Shen Q-H, Saijo Y, Mauch S, Biskup C, Bieri S, Keller B, et al. Nuclear Activity of MLA Immune Receptors Links Isolate-Specific and Basal Disease-Resistance Responses. Science (80-). 2007; 315: 1098 LP– 1103. https://doi.org/10.1126/science.1136372 PMID: 17185563

65. Daniel Gietz R, Woods RA. Transformation of yeast by lithium acetate/single-stranded carrier DNA/polyethylene glycol method. In: Guthrie C, Fink GRBT-M in E, editors. Guide to Yeast Genetics and Molecular and Cell Biology—Part B. Academic Press; 2002. pp. 87–96. https://doi.org/10.1016/S0076-6879(02)50957-5

66. Karginov A, Agaphonov M. A simple enrichment procedure improves detection of membrane proteins by immunoblotting. Biotechniques. 2016; 61: 260–261. https://doi.org/10.2144/000114474 PMID: 27839511

67. Jurrus E, Engel D, Star K, Monson K, Brandi J, Felberg LE, et al. Improvements to the APBS biomolecular solvation software suite. Protein Sci. 2017/10/24. 2018; 27: 112–128. https://doi.org/10.1002/pro.3280 PMID: 28836357

3. Supplementary Results

3.1 Mechanism for the NADase activity of plant TIR domain proteins

Given the significance of NOD-mediated tetramerization in TNL NADase activity, how can TIR domains themselves confer TNL-like NADase activity? To address this question, I co-crystalized RPP1^{TIR} with NAD$^+$ and solved the crystal structure of RPP1^{TIR} using molecular replacement. In the crystal structure, the RPP1^{TIR} domain forms a tetramer in which the NAD$^+$ hydrolyzed products ADPR and NAM bind to the catalytic centers formed by two head-to-tail asymmetric TIR dimers (Figure 4A). Structural comparison showed that the RPP1^{TIR} tetramer in the crystal is identical to that in the RPP1 resistosome, explaining why the TIR domain could perform the same enzymatic activity as full-length RPP1. This tetrameric RPP1^{TIR} also explained why the AE interfaces (interface involving helices αA and αE) were repeatedly observed in the crystal structures of TIR domain proteins, and mutations disrupting the AE interface impaired TIR-mediated cell death (Zhang et al., 2017; Williams et al., 2016).

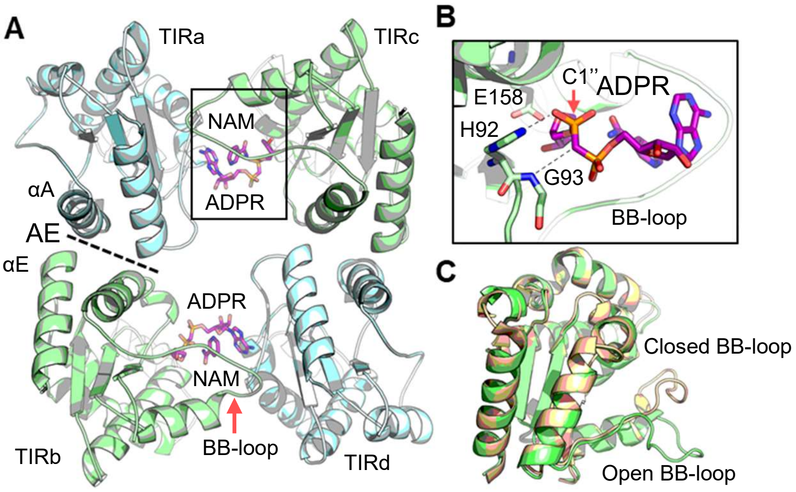

Figure 4 Mechanism for the NADase activity of RPP1^{TIR}
(A) Packing of four RPP1^{TIR} protomers in the crystal structure of RPP1^{TIR}. ADPR and nicotinamide (NAM) bind to the catalytic centers formed by head-to-tail asymmetric TIR dimers. BE interface refers to interface between the two head-to-tail TIR protomers (TIRa/TIRc). Some structural elements are labelled.
(B) Detailed interactions between the ribose sugar ring and one RPP1^{TIR}. The image represents a vertically rotated black frame in (A). Black dashed lines represent polar interactions. The C1'' atom is indicated by the red arrow.
(C) Structural comparison of RPP1^{TIR} (green) in (A) with free RPP1^{TIR} (PDB: 5TEB) (yellow). The BB-loop was labelled to highlight the difference in conformation.

The structure of product-bound RPP1^{TIR} provides insight into the catalytic mechanism of NAD$^+$ hydrolysis. The C1´´ position in the ribose sugar ring of ADPR faces the catalytic glutamic residue of RPP1^{TIR} (Figure 4B), suggesting that this residue is important for catalyzing NAM release from NAD$^+$ (Jia et al., 2022). Structural comparison reveals a striking difference between the previously reported free RPP1$^{\mathrm{TIR}}$ (PDB: 5TEB) and the product-bound RPP1$^{\mathrm{TIR}}$ (Figure 4C). In free RPP1$^{\mathrm{TIR}}$, the BB-loop adopts a closed conformation and RPP1$^{\mathrm{TIR}}$ forms a trimer (crystal packing) mediated by AE and DE interfaces (interface involving helices αD and αE) (Zhang et al., 2017). By contrast, in the product-bound structure (Figure 1A), the BB-loop adopts an open conformation, allowing a substrate such as NAD$^+$ to access the catalytic pocket. While RPP1$^{\mathrm{TIR}}$ was a monomer in solution, RPP1$^{\mathrm{TIR}}$ forms a tetramer when crystallized in the presence of NAD$^+$, which is almost identical to the tetrameric TIR domains observed in the RPP1 resistosome (Ma et al., 2020). This suggests that the tetramer in the RPP1$^{\mathrm{TIR}}$ crystal structure was likely induced by NAD$^+$.

3.2 The 2′,3′-cAMP/cGMP synthetase activity of plant TIR domain proteins

3.2.1 Substrate-induced L7$^{\mathrm{TIR}}$ filaments *in vitro*

The cryo-EM structure of the L7$^{\mathrm{TIR}}$ filaments suggests that its substrates, RNA or DNA, have a role in forming the filament structure. To test this hypothesis, we incubated L7$^{\mathrm{TIR}}$ monomer with *Arabidopsis* total RNA or genomic DNA (gDNA) and assayed the samples using negative staining EM. Compared to the L7$^{\mathrm{TIR}}$ monomer alone, incubation with RNA or DNA (Figure 5A-C) induced the formation of TIR filaments. The average lengths of L7$^{\mathrm{TIR}}$ filaments induced by RNA were shorter than those induced by DNA. This might result from more efficient TIR-mediated RNA hydrolysis, because our enzymatic activity assays showed that RNA is a more favorable substrate for TIR nuclease than DNA. Notably, L7$^{\mathrm{TIR}}$ can be clearly detected wrapping around DNA (Figure 5C).

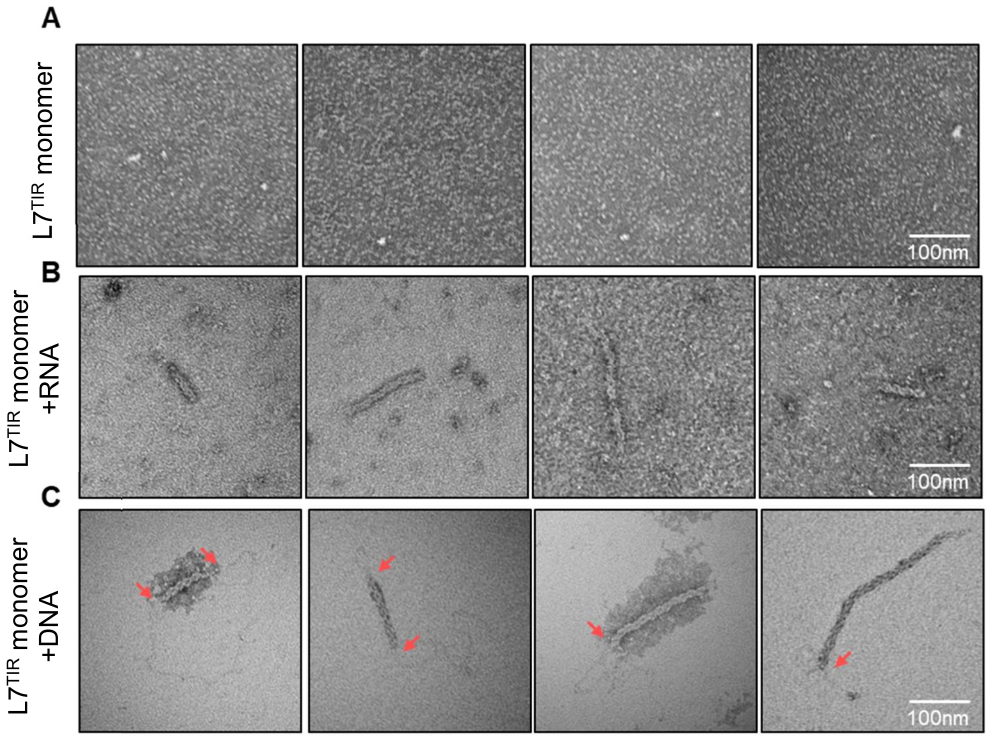

Figure 5. Reconstruction of L7^{TIR} filament *in vitro*

(A) Negative staining images of monomeric L7^{TIR}. Tag free L7^{TIR} protein eluted at 17 ml in Superose 6 SEC column was collected and incubated with water for 45 min before preparing the negative staining grid.

(B) Negative staining images of monomeric L7^{TIR} incubated with *Arabidopsis* total RNA. Protein in (A) was incubated with an excess of *Arabidopsis* total RNA for 45 min before preparation of negative staining sample.

(C) Negative staining images of monomeric L7^{TIR} incubated with *Arabidopsis* gDNA. Protein in (A) was incubated with excessive gDNA for 2 h. Red arrows point to the position where L7^{TIR} wraps around DNA.

3.2.2 Both DNA and RNA are substrates of TIR synthetases *in vitro*

Our enzymatic activity assays using *Arabidopsis* gDNA or total RNA suggested that TIR domain proteins harbor nuclease and synthetase activities. To dissect substrate selection of TIR synthetases, we used chemically synthesized polynucleotides including double-stranded DNA (dsDNA), single stranded RNA (ssRNA) and dsRNA with different sizes as substrates of L7^{TIR} to examine the 2′,3′-cAMP/cGMP synthetase activity of L7^{TIR}. The ssRNA was predicted to form secondary structures (http://rna.tbi.univie.ac.at/cgi-bin/RNAWebSuite/RNAfold.cgi).

After incubation with L7^{TIR}, all synthetic RNA produced 2′,3′-cNMPs, but only long-chain dsRNA poly (I:C) (1.5kb to 8kb) produced a comparable amount of 2′,3′-cCMP to *Arabidopsis* total RNA (Figure 6B, 6C and 6D), suggesting that RNA length is a determinant for L7^{TIR}-mediated 2′,3′-cNMP synthesis. 2′,3′-cAMP was also clearly detectable when dsDNA (PCR product) was used a substrate, but with a lower yield than dsRNA (Figure 6C). As a negative control, L7^{TIR} had no activity in producing 2′,3′-cAMP using ATP as substrate. This is likely because the phosphate group of ATP is at 5' position (Figure 6A). Taken together, these data suggest that TIR proteins are promiscuous in the substrates that they use for synthetase activity, as L7^{TIR} could catalyze the production of 2′,3′-cNMPs using different types of DNA and RNA as substrates. It is surprising that DNA can be a substrate of L7^{TIR} synthetase because DNA contains no 2′-hydroxyl group required for production of 2′,3′-cNMPs. Thus, it currently remains to be determined whether RNA or DNA or both are the genuine TIR substrates *in vivo*.

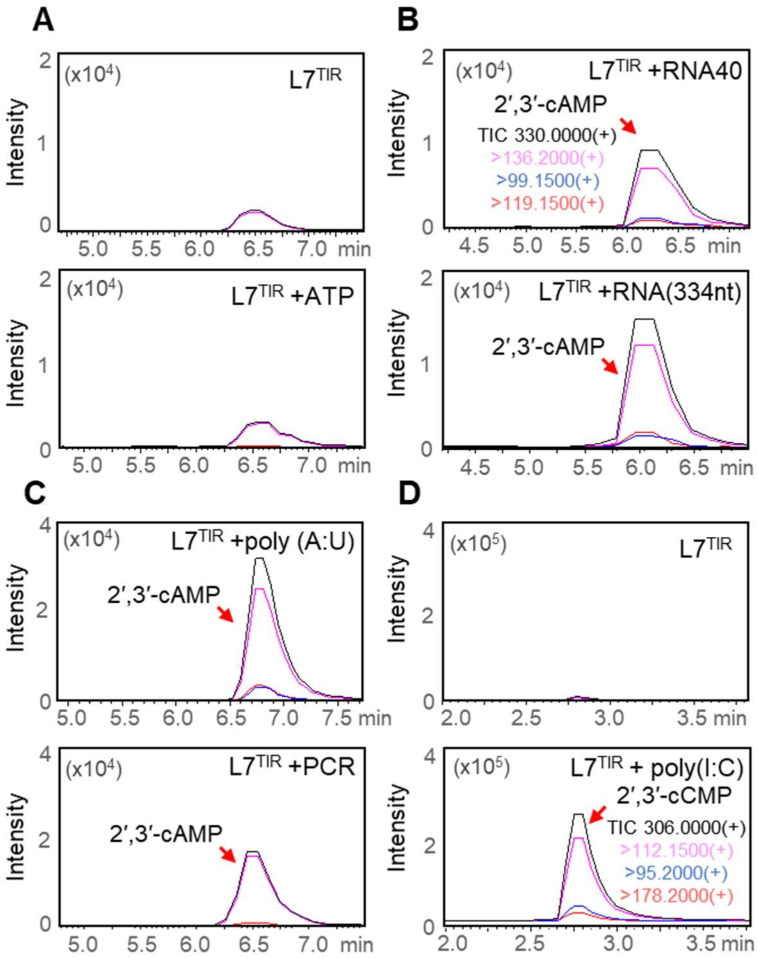

Figure 6. L7^{TIR} catalyses production of 2′,3′-cNMP using synthetic RNA/DNA as substrates

(A) L7^{TIR} displays no 2′,3′-cAMP synthetase activity when ATP was used as substrate. L7 ^{TIR} was incubated with water (top) and 100 µM ATP (bottom) at 25°C for 16 h. Reaction products were analyzed by LC-MS in multiple reaction monitoring (MRM) mode.

(B-D) L7^{TIR} displays 2′,3′-cNMP synthetase activity when synthetic RNA and DNA were used as substrates. L7^{TIR} (1 µM) was incubated with 100 ng RNA40 (20 nt ssRNA); RNA 334nt (mRNA transcribed from antisense mouse s-actin probe); 100 ng poly (A:U) (synthesized poly A:U); PCR product and 100 ng poly (I:C) (synthesized poly A:U), respectively. After 16 h reaction at 25°C, the products were analyzed by LC-MS. L7^{TIR} protein incubated with water was included as a negative control (D). RNA/DNA themselves do not produce 2′,3′-cNMP by themselves. MRM and retention time of 2′,3′-cAMP and 2′,3′-cCMP were confirmed using authentic standards. Black line indicates the total ion chromatogram (TIC), purple, blue and red lines indicate three different transitions. Data are depicted as a representative chromatogram of MRM analyses of more than two independent experiments.

3.2.3 Do full-length TNLs have 2′,3′-cNMP synthetase activity?

Given the 2′,3′-cNMP synthetase activity of TIR domain proteins, we then asked whether TNLs have a similar activity. To address this question, we examined the nuclease, 2′,3′-cAMP/cGMP synthetase and NADase activities of RPP1 alone and the RPP1-ATR1 complex purified from insect cells (Figure 7A) (Ma et al., 2020). The results from the assay indicated RPP1 alone showed stronger nuclease and 2′,3′-cAMP/cGMP synthetase activities. By contrast, a weaker NADase activity was found with the RPP1 protein (Figure 7B, 7C and 7D)

(Song et al., unpublished data). These results are consistent with the structural observation that TIR domains in the RPP1 resistosome do not form oligomers seen in the L7^{TIR} filament which are required for 2′,3′-cAMP/cGMP synthetase activity.

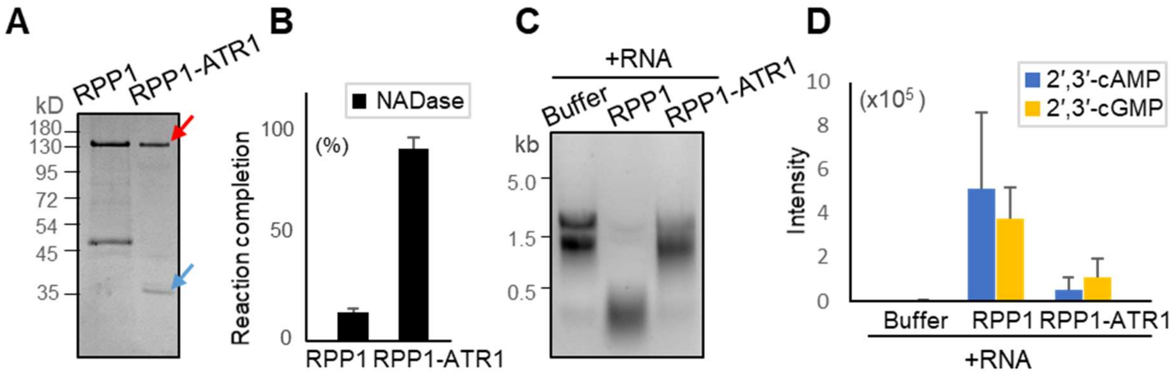

Figure 7. Resistosome formation of RPP1 compromises 2′,3′-cAMP/cGMP synthetase activity

(A) SDS-PAGE analysis of RPP1 alone and ATR1-RPP1 complex. Protein were purified using the same method as (Ma et al. 2020). RPP1 and ATR1 are highlighted by red and blue arrows, respectively.

(B) NADase activity assay of RPP1 alone and the ATR1-RPP1 complex. RPP1 and RPP1-ATR1 (0.5 µM) proteins were incubated with 100 µM NAD$^+$ in the presence of 1 mM $MgSO_4$ at 25°C for 16 h. Reaction mixtures were centrifuged and immediately applied for HPLC analysis. Reaction completion (%) of each sample was calculated as [1 – (concentration of unhydrolyzed NAD$^+$)/(concentration of NAD$^+$ before reaction)] × 100%. Data are depicted as average reaction completion of three independent experiments.

(C) RPP1 alone exhibits stronger RNase activity than RPP1-ATR1 complex *in vitro*. RPP1 and RPP1-ATR1 proteins (0.5 µM) were incubated with 100 ng *Arabidopsis* total RNA in the presence of 1 mM $MgSO_4$. After incubation at 25°C for 6 h, the reaction mixtures were analyzed by agarose gel electrophoresis.

(D) RPP1 alone exhibits stronger 2′,3′-cAMP/cGMP synthetase activity than RPP1-ATR1 *in vitro*. RPP1 and RPP1-ATR1 (0.5 µM) proteins were incubated with 100 ng *Arabidopsis* total RNA at 25°C for 16 h and the reaction products were analysed by LC-MS. Data are depicted as average peak intensities of two independent experiments.

The nuclease and 2′,3′-cAMP/cGMP synthetase activities of the RPP1-ATR complex, although much weaker than RPP1 alone, are not negligible. However, the TIR domains in the RPP1 resistosome are exclusive with the TIR oligomers in the L7^{TIR} filament. How can the RPP1-ATR1 complex still retain nuclease and 2′,3′-cAMP/cGMP synthetase activities? Based on the cryo-EM micrographs, RPP1-ATR1 could also exist as monomers and dimers besides forming tetramers (Ma, et al., unpublished data). It is therefore a plausible hypothesis that effector-primed non-tetrameric TNL could also form filament-like structures similar to those formed by L7^{TIR}. This is formally possible because of the largely solvent-exposed C-terminus of L7^{TIR} in the filament. Previous data showed that the DE interface mutant K200E of full-length L6 abolishes the cell death triggered by its corresponding effector AvrL567 (Zhang et al., 2017), suggesting that full-length TNLs may also require the DE interface and consequently the 2′,3′-cAMP/cGMP synthetase activity to be fully functional.

3.2.4 Wounding increase 2′,3′-cAMP/cGMP level in plants and promote TIR-mediated cell death

As discussed (section 2.2), transient co-expression of TIR proteins with 2′,3′-cAMP/cGMP PDEs impaired TIR-mediated cell death in *N. benthamiana*, supporting a critical role of these non-canonical cNMPs in TIR-mediated immune signaling. We then asked whether up-regulation of 2′,3′-cAMP/cGMP levels promotes the cell death activity of TIRs in plants. We first attempted to deliver 2′,3′-cAMP/cGMP into *Arabidopsis* protoplasts with PEG 4000 or incubate the protoplasts with Br-2′,3′-cAMP/cGMP. We unfortunately failed to observe cell death activity of these protoplasts (Figure 8A). Similarly, direct infiltration or petiole absorption (Dalakouras et al., 2018) of Br-2′,3′-cAMP also failed to cause macroscopic cell death in *N. benthamiana* leaves. These results can be explained by our model that both TIR NADase products and 2′,3′-cAMP/cGMP are necessary for TIR-mediated cell death. However, we cannot rule out the possibility that this could also be due to the poor ability of (Br-)2′,3′-cAMP/cGMP to permeate cell membranes or the requirement of other cNMPs.

To circumvent the difficulty in the uptake of 2′,3′-cAMP/cGMP by plants, we switched to inducing production of 2′,3′-cAMP/cGMP *in situ* by wounding. In agreement with previous data in *Arabidopsis* (Van Damme et al., 2014), we found that wounding of *N. benthamiana* leaves could increase 2′,3′-cAMP/cGMP levels 3-4-fold but caused no cell death (Figure 8B). This is consistent with our model that both 2′,3′-cAMP/cGMP and products of TIR NADase are required to trigger *EDS1*-dependent immune signaling. We then combined physical wounding and *Agrobacterium*-mediated expression of TIR proteins RBA1 or the TIR-only protein TX7 to test whether wounding affects TIR-mediated cell death. Further supporting our model, RBA1-mediated cell death developed earlier and concentrically with the wounded sites serving as centers (3 dpi), whereas the area of cell death was random in the untreated *Agrobacterium*-infiltrated region (Figure 8C). Visible cell death was also more pronounced at the *Agrobacterium* infiltration site of the untreated leaf than at the remaining areas of the leaf, which could be due to the mechanical wounding resulting from *Agrobacterium* infiltration. These data suggest that physical injury upregulates local 2′,3′-cAMP/cGMP accumulation and promotes TIR-mediated cell death.

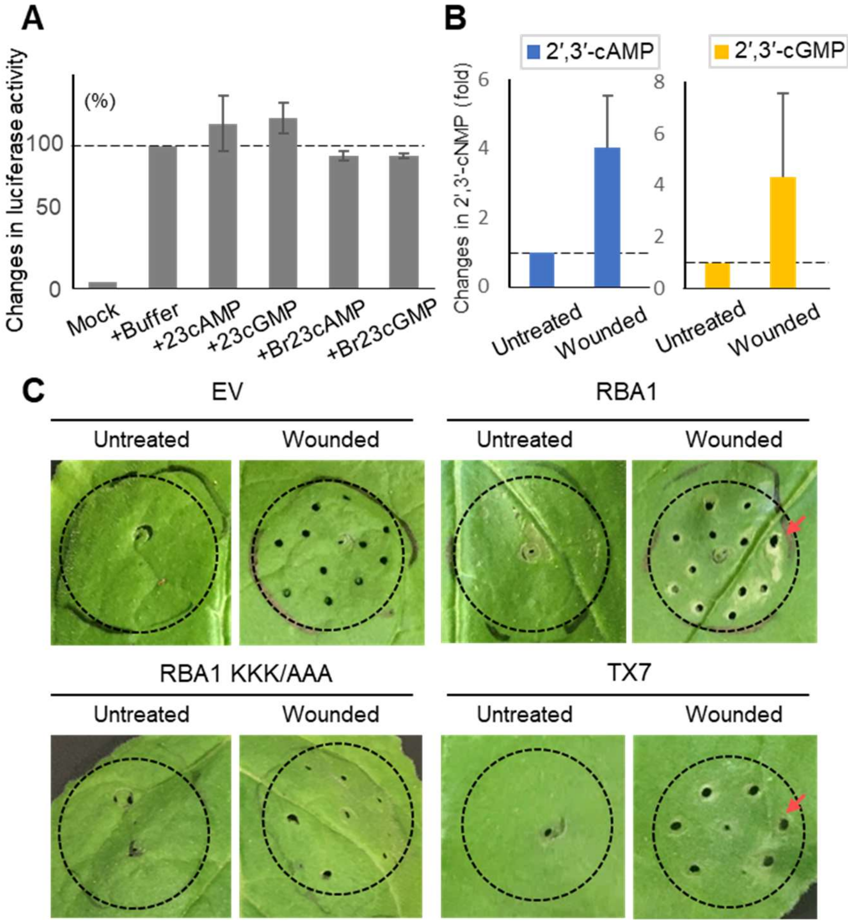

Figure 8. Trans-generation of 2′,3′-cAMP/cGMP by wounding promotes TIR-mediated cell death
(A) 2′,3′-cAMP/cGMP treatment cannot trigger cell death in Arabidopsis protoplasts. Isolation, transfection and luciferase activity measurements of *Arabidopsis* protoplasts were performed as described previously (Saur et al., 2019). Freshly isolated protoplasts were either transfected with 100 µM 2′,3′-cAMP or 2′,3′-cGMP together with the luciferase vector using PEG 4000 (+23cAMP and +23cGMP), or transfected with the luciferase vector and then incubated with 100 µM 8-Br-2′,3′-cAMP or 8-Br-2′,3′-cGMP (+Br23cAMP and +Br23cGMP). Luciferase activity was determined using a luminometer (Berthold Centro LB 960) at 16 h post transfection as a proxy for cell death. Luciferase activity of buffer treated protoplasts was normalized to 1.0. Luciferase activity of untransformed (Mock) protoplasts was included as a negative control. Data are depicted as the average activity changes of three independent experiments.
(B) Wounding induces 2′,3′-cAMP/cGMP accumulation in *N. benthamiana* leaves. The experiment was performed as previously described (Van Damme et al., 2014). In brief, plant leaves were physically damaged by a needle. After 45 min, wounded leaves and untreated leaves were harvested and flash-frozen. 2′,3′-cAMP levels in *N. benthamiana* leaf extracts were analyzed by LC-MS. Vertical axis: MS intensity (area) of 2′,3′-cAMP and 2′,3′-cGMP. For quantification, the internal standard 8-Br-2′,3′-cAMP was used. The levels of 2′,3′-cAMP/cGMP in untreated leaves were normalized to 1.0. Data are depicted as the average activity changes of three independent experiments.
(C) Right: Wounding promotes TIR-mediated cell death. RBA1- or TX7-mediated cell death initiates and propagates concentrically around wound sites (highlighted by red arrows). Left bottom: Wounding cannot complement cell death of RBA1 2′,3′-cAMP/cGMP deficient mutant. Left top: Physical injury alone is insufficient to trigger cell death in EV infiltrated area. Wounding was introduced at 24 hours post infiltration (hpi). Cell death was visually assessed and photographed at 2 dpi. The representative images from a single replicate of three independent experiments are shown.

Physical wounding did not cause a more pronounced cell death phenotype of *N. benthamiana* plants expressing RBA1 KKK/AAA, the 2′,3′-cAMP/cGMP synthetase activity deficient mutants (Figure 8C). This is not due to expression differences, because RBA1 KKK/AAA accumulated to a similar level to WT RBA1 in *N. benthamiana* (Yu et al., 2022). One possible explanation for this is that synchronized expression of 2′,3′-cAMP/cGMP and TIR NADase products is needed for their cooperative effect. This is relevant in our experimental setup because mechanical wounding causes a rapid (within 30-60 min) increase in the concentrations of 2′,3′-cAMP/cGMP in plants (Van Damme et al., 2014). Thus, a *trans*-combination of 2′,3′-cAMP/cGMP and the TIR NADase activities may not well mimic the spatiotemporal dynamics of a TIR bifunctional enzyme with these two activities. Nonetheless, the promotion of WT TIR-mediated cell death by wounding further supports the idea that 2′,3′-cAMP/cGMP play a key role in the cell death process. The failure to detect this phenotype on leaf zones transiently expressing RBA1 KKK/AAA rules out the possibility that the cell death phenotype facilitated by wounding is caused by other injury-induced responses, and further supports our current model that the simultaneous TIR 2′,3′-cAMP/cGMP synthetase and NADase activities are important for TIR-mediated cell death.

3.2.5 RNase T1 triggers *EDS1*-dependent and -independent cell death in plants

As introduced in (section 1.4.1), 2′,3′-cNMPs have long been known as intermediates of mRNA turnover by RNases. Indeed, I have observed 2′,3′-cAMP/cGMP synthetase activity of RNase T1 from *Aspergillus oryzae* when *Arabidopsis* total RNA was used as substrate (Yu et al., 2022). Transient expression of the RNase in *N. benthamiana* caused a strong cell death phenotype. This is unexpected because both NADase and 2′,3′-cAMP/cGMP activities are required for TIR-mediated cell death. A model to reconcile these data is that RNase T1-mediated cell death is dependent on its nuclease activity but not 2′,3′-cAMP/cGMP synthetase activity. However, this does not seem true, because the cell death phenotypes could be suppressed by 2′,3′-cAMP/cGMP PDE *At*NUDT7, *At*CPDase and *m*CNPase1 (Figure 9A). Another model is that RNase T1 first induces *EDS1*-independent cell death, which initially upregulates TIR genes and consequently induces *EDS1*-dependent cell death. To test this model, we expressed *RNase T1* in *N. benthamiana epss* line lacking EDS1 and its paralogues. As predicted, massive cell death was observed in the *N. benthamiana* mutant line. However, the phenotype was weaker than that in WT *N. benthamiana* expressing RBA1 (Figure 9B). These data suggest that both *EDS1*-dependent and *EDS1*-independent pathways are required for the cell death activity of *RNase T1*.

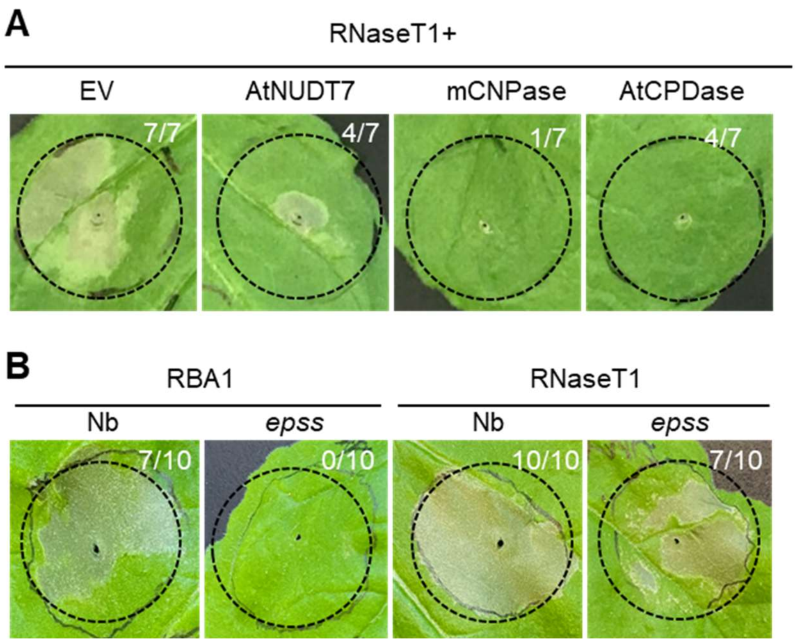

Figure 9. RNase T1-mediated cell death in *N. benthamiana* is partially dependent on EDS1
(A) Co-expression with 2′,3′-cAMP/cGMP phosphodiesterases suppresses RNaseT1-mediated cell death in *N. benthamiana.* Empty vector (EV) or indicated constructs were co-expressed with RNaseT1 in *N. benthamiana* plants. Cell death was visually assessed and photographed at 4 dpi. The representative images from a single replicate of two independent experiments are shown.
(B) Left: RBA1 mediated cell death is completely dependent on the EDS1 signaling pathway. Right: RNase T1 mediated cell death is partially dependent on the EDS1 signaling pathway. Cell death phenotype was visually assessed and photographed at 5 dpi. The numbers in parentheses indicate the numbers of leaves displaying cell death out of the total number of leaves infiltrated. Nb: *N. benthamiana*; *epss*: *eds1/pad4/sag101a/sag101b*. The representative images from a single replicate of two independent experiments are shown.

3.3 Interaction between FL NLRs and effectors

3.3.1 Direct interaction between MLAs and effectors was not detected *in vitro*

In the arms race between pathogens and plants, effectors evade NLR recognition by mutating key residues involved in interactions, which in turn drives the evolution of NLRs to diversify their recognition specificities. As a result, NLR gene clusters typically contain multiple paralogs. For example, the *MLA* genes encode an array of allelic CNLs, each recognizing a cognate AVR$_A$ effector from *Bgh* (Lu et al., 2016).

To test whether MLAs directly recognize their corresponding effectors, I first expressed MLAs in insect cells. After several unsuccessful attempts, including testing different insect cell lines, altering insect cell culturing conditions and testing different MLA constructs or site directed mutations, I synthesized cDNAs of MLAs with codons optimized for insect cells. Codon optimization has been shown to improve protein production for many proteins (Mauro and Chappell, 2018). Additionally, I also truncated the N-terminal amino acids which are known to be required for the cell death activity of ZAR1 (Wang et al., 2019) and other CNLs

(Adachi et al., 2019). With these changes, expression of several MLAs including MLA7, MLA10, MLA13 and MLA22 was significantly improved. However, codon optimization seems not to be universally effective, as expression of codon optimized MLA9 did not change (Figure 10A). The N-terminal SUMO tag of MLA10, MLA10 R158K and MLA10 R310K could be removed by PreScission protease (ppase), suggesting that expressed MLA10 protein had been correctly folded (Figure 10B). Similarly, AVR$_{A10}$ was well expressed in insect cells, making it possible to test the interaction with MLA10.

To test the interaction between MLAs and AVR$_{A}$ effectors, N-terminally 6×His-SUMO tagged MLA10 was co-expressed with C-terminally GST tagged AVR$_{A}$10 in insect cells. HSP90 and SGT1, which are known to stabilize NLR proteins in plants (Moran Luengo et al., 2019; Stuttmann et al., 2008), were also included in the co-expression. Although MLA10 and AvrA10 proteins were robustly expressed, I failed to detect a clear interaction between them. (Figure 10C). Similar results were also obtained with MLA13 and AVR$_{A}$13, and MLA13 and AVR$_{A}$13-v2, a virulent version of AVR$_{A}$13 which interacts with but cannot activate MLA13 (M. L. Saur et al., unpublished data) (Figure 10D).

I then tested MLA10 interaction with AVR$_{A}$10 using purified proteins. Purified GST-AVR$_{A}$10 was incubated individually with insect cell-purified His-tagged MLA10 and AVR$_{A}$10 proteins in the presence of dATP (0.1mM), and the mixtures were loaded onto GST beads. After extensive washing, proteins bound to the GST beads were detected. Consistent with the co-expression data, no clear interaction between the two proteins was detected (Figure 10E). It is noteworthy that flocculent debris were observed in the solution after incubation of MLA10 with AVR$_{A}$10 and both proteins were detected in the centrifuged pellet (Figure 10F). To eliminate the precipitation problem, I reduced the incubation time and then subjected the incubation mixture to SEC. The results showed that the MLA10 and AVR$_{A}$10 proteins were eluted in different fractions, indicating they did not form a stable complex (Figure 10G).

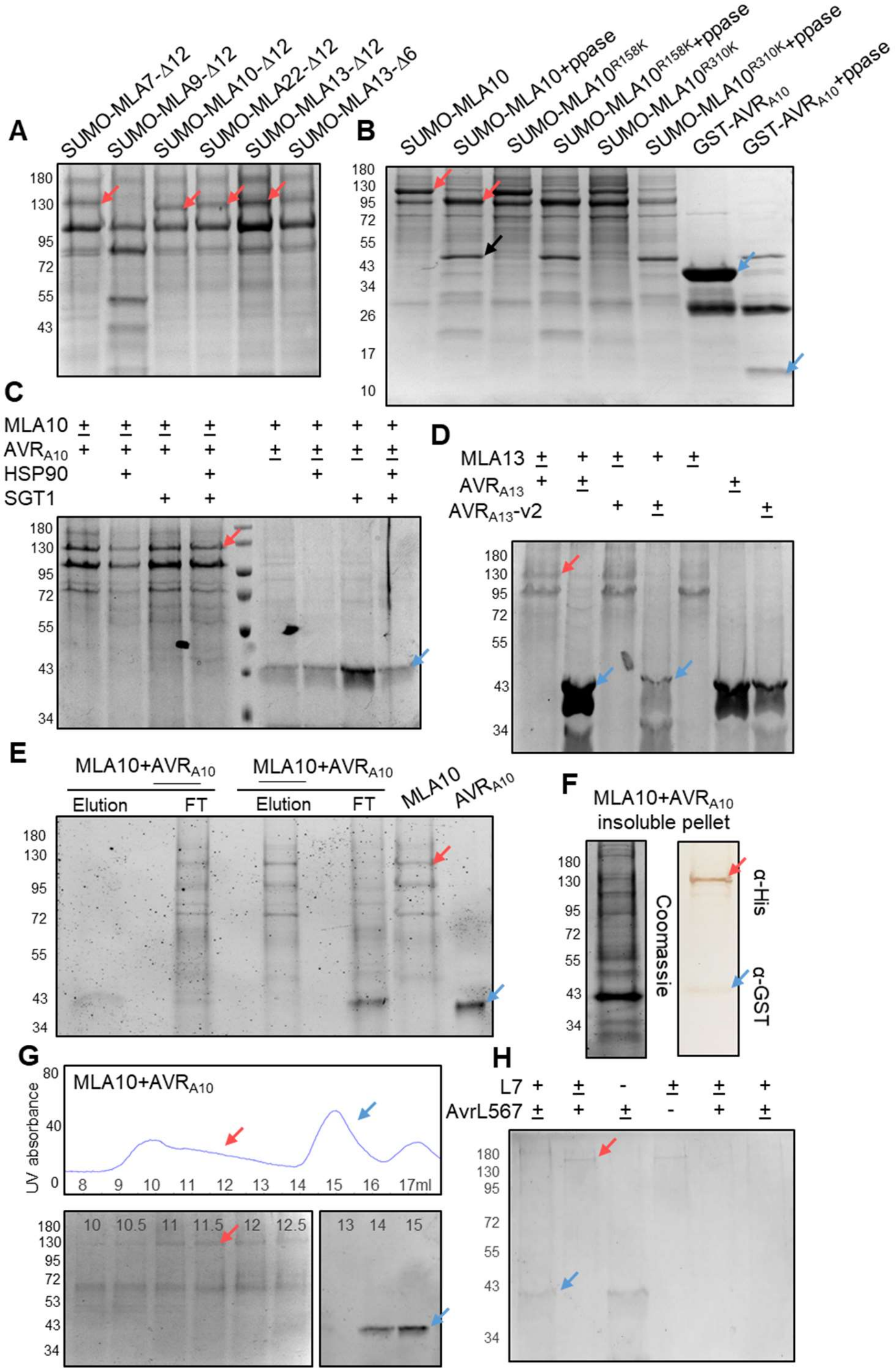

Figure 10. Direct interaction between MLA and AVR$_A$ effectors or L7 and AVRL567-A was not evident *in vitro*

(A) Expression of codon-optimized MLAs. Numbers at the left edge indicate the protein sizes of molecular weight markers (kD).

(B) Expression of codon-optimized MLA10. R158K and R310K mutations were made in the ATP binding pocket of MLA10 NBD, with the aim of attenuating ADP-dATP/ATP exchange and to avoid the autoactivation of MLA10 during expression.

(C) Interaction between MLA10 and AVR$_A$10 was not detected upon co-expression in insect cell. The plus symbols on top of the image indicate the proteins used for co-expression. The protein used for pull-down are underlined. MLA10 and AVR$_A$10 are highlighted by red and blue arrows, respectively.

(D) Interaction between MLA13 and AVR$_A$13 or AVR$_A$13 -v2 was not detected by co-expression in insect cells. Experiment was performed as described in (C).
(E) Interaction between MLA10 and AVR$_A$10 was not detected after incubation. Individually purified SUMO-His-MLA10 and AVR$_A$10-GST were first concentrated by protein concentrators (ThermoFisher) and loaded at the end of the SDS-page as protein inputs. These two proteins were mixed at 1:1 ratio in incubation buffer (100mM NaCl, 10mM Tris-HCl pH 8.0, 15mM imidazole, 0.1mM dATP) 4°C overnight. The incubated protein mixture was centrifuged at 12,000 *g* and loaded onto GST or His resin, respectively. The protein used for pull-down are underlined on top of the image. After loading, the FT was collected for protein tracking. Elution was performed after washing with two column-volumes of suspension buffer (100mM NaCl, 10mM Tris-HCl pH 8.0, 0.1mM dATP). MLA10 and AVR$_A$10 are highlighted by red and blue arrows, respectively.
(F) MLA10 and AVR$_A$10 were detected in the insoluble fraction after incubation. The centrifuged pellet from (C) was washed with suspension buffer twice and then subjected to SDS page. Both MLA10 and AVR$_A$10 were clearly detected in Western blot.
(G) MLA10 and AVR$_A$10 did not form a stable complex. The experiment was performed as described in (E) except that MLA10 and AVR$_A$10 were incubated for 1 h in the presence of 0.5 mM dATP.
(H) Interaction between L7 and AVRL-567A was not detected when co-expressed in insect cell. The experiment was performed as described in (C). L7 and AVRL-567A are highlighted by red and blue arrows, respectively.

I also tested the interaction between full length L7 and Avr567L-A. Their interaction was previously validated by yeast two-hybrid assays (Ravensdale et al., 2012). N-terminally 6×His-SUMO tagged L7 was co-expressed with C-terminally GST tagged Avr567L-A in insect cells. dATP (0.1 mM) was added to the purification buffer to prevent dissociation of the potential L7-Avr567L complex. Pull-down assay using GS4B beads detected no interaction between the two proteins (Figure 10H).

I have tried to reconstitute direct interactions of MLAs and L7 proteins with their cognate effectors, but without success. This may be due to several reasons: 1) Like other heterogeneously overexpressed proteins (Gasser et al., 2008), MLAs or L7 might not be fully folded when expressed in insect cells. 2) These NLRs require other host proteins for recognition of effector proteins. 3) The direct interactions between these NLRs and effectors may require specific subcellular locations, as both MLAs and L6 have the ability to shuffle between different cellular components (Shen et al., 2007; Takemoto et al., 2012).

3.3.2 Purification and analysis of the inactive CNL MLA27

To study the self-inhibition mechanism of MLAs, I purified MLA27 from insect cells (Figure 11A). The SEC result showed that the protein was eluted as monomers. This is further supported by negative staining EM analysis of the protein (Figure 11B). The MLA27 particles were uniformly distributed on cryo-EM grids, rendering it amenable to structural analysis (Figure 11B). After several iterations of two-dimensional (2D) classification, we were able to visualize the overall 2D shapes of the monomeric MLA27 particles, which are similar to the inactive ZAR1 particles (Wang et al., 2019b). Interestingly, the C-terminus of MLA27^{LRR} was in close contact with the MLA27^{NBD} in all the 2D classes (Figure 11C). By comparison, the LRR and NBD of ZAR1 were linked by RKS1 (Wang et al., 2019b). This suggests that the direct intramolecular interaction between LRR and NBD may lock MLA27 in a self-inhibited state. However, the 3D reconstruction of MLA27 was not successful probably due to the preferred orientation of MLA27, as most of the particles were 'C' shaped particles (Figure 11C, top). Grid tilting was tested to eliminate the problem, but the improvement was modest and did not significantly improve the 3D reconstruction of MLA27 (Figure 11C, bottom).

Taken together, based on the overall shape of MLA27 after cryo-EM 2D classification, we speculate that self-inhibition of MLA27 is likely mediated by the direct interaction between its LRR and NBD. Upon activation, this region may serve as an effector wedging point, causing steric clash and triggering conformational change in and activation of MLA27.

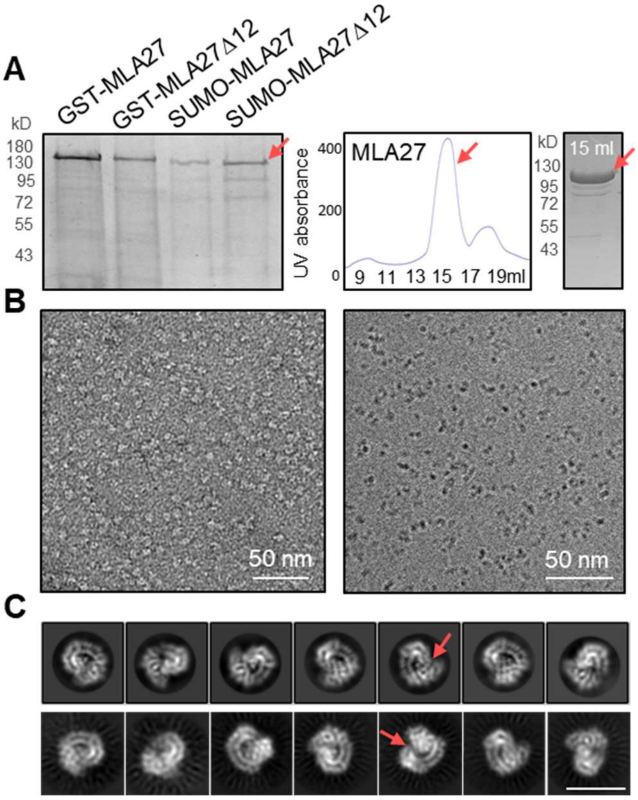

Figure 11. 2D averages of inactive MLA27
(A) Purification of MLA27. MLA27 proteins with different tags were purified from insect cells as described in Figure 8A. SUMO tags were removed from MLA27 by ppase digestion and the tag-free MLA27 proteins were subjected to superdex 200 column. Fraction eluted at 15 ml was visualized by SDS page. MLA27 is highlighted by the red arrows.
(B) Left: Representative negative staining micrograph of the monomeric MLA27. Right: Representative cryo-EM micrograph of MLA27.
(C) Representative 2D classes of inactive MLA27 with (bottom) or without (top) sample tilting. Red arrows indicate the potential contact site between MLA27^{NBD} and MLA27^{LRR}. White scale bar: 10 nm.

4. Discussion

4.1 Asymmetric dimers are critical for the NADase activity of TIR proteins

TNLs form tetrameric resistosomes upon recognition of their corresponding effectors as demonstrated by RPP1 and ROQ1 (Ma et al., 2020; Martin et al., 2020). In both resistosomes, opposite packing of two asymmetric head-to-tail TIR homodimers leads to the formation of two symmetric TIR homodimers. The asymmetric TIR homodimer forms an NAD^+ catalytic site mediated by the BB-loop, whereas the symmetric TIR homodimer mediated by the AE interface stabilizes this two-fold dimer of dimers. The asymmetric and symmetric dimers were also observed in the $RPP1^{TIR}$-ADPR tetramer (section 3.1). Remarkably, formation of similar asymmetric homodimers was recently shown to be required for the NADase activity of hSARM1 (Shi et al., 2022), suggesting a conserved mechanism for the activation of TIR NADase activity in plants and animals.

4.2 The DE interface and the enzymatic activities of TIRs

Typical bifunctional enzymes harbor two structural domains and catalyze two independent reactions at separate catalytic sites (Moore, 2004). However, this does not hold true for plant TIR proteins, as the conserved catalytic glutamate important for NADase activity is also required for 2′,3′-cAMP/cGMP synthesis (Yu et al., 2022). Our crystal structure of ADPR-bound $RPP1^{TIR}$ (section 3.1) and the cryo-EM structure of dsDNA-bound $L7^{TIR}$ revealed that these two enzymatic activities were catalyzed through two mutually exclusive TIR oligomeric forms.

The most striking difference between these two types of TIR oligomers lies in the DE interface (section 2.2). In the $RPP1^{TIR}$ tetramer, only part of the DE interface is involved in the formation of TIR asymmetric dimers. The interaction between DE interface with the open BB-loop forms the BE interface, which stabilizes the NAD^+ binding pocket (Hayden et al., 2021; Ma et al., 2020). By comparison, the intact DE interface is involved in the formation of $L7^{TIR}$ filament. Mutations in the DE interface of $L7^{TIR}$, such as $L7^{TIR}$ K200E, retained comparable NADase activity with WT $L7^{TIR}$, but the 2′,3′-cAMP/cGMP synthetase activity and the cell death activity was significantly compromised (Yu et al., 2022). DE interface mutants, such as $L6^{TIR}$ K200E, $L6^{TIR}$ P160Y, $RPV1^{TIR}$ P121Y and RBA1 K149E disrupted the TIR self-associations and auto-activities (Bernoux et al., 2011; Nishimura et al., 2017; Williams et al., 2016; Zhang et al., 2017). Taken together, these results show that the DE interface has an important role in the 2′,3′-cAMP/cGMP synthetase activity of TIR proteins by mediating filament formation.

4.3 Can TIR form filament *in vivo*?

Although evidence showing that TIR can form filaments *in vivo* is still missing, the formation of puncta by TIR proteins has been widely reported in plants. For example, *At*TX21 assembled into cytoplasmic aggregates when transiently overexpressed in tobacco (Nandety et al., 2013; Roth et al., 2017). RBA1 but not its AE and DE mutants, formed aggregate-like cyto-nucleoplasmic puncta (Nishimura et al., 2017). These data suggest that TIR proteins can form aggregates when overexpressed in plants. However, it remains unknown if these TIR aggregates were composed of DNA/RNA bound TIR filament or NADase-active TIR tetramer (section 3.1). In the future, testing whether the observed puncta formation can be disrupted by TIR DNA/RNA binding mutations will give more clues on whether TIR proteins can form filaments *in vivo*.

It is noteworthy that the $L7^{TIR}$-type tetramer mediated by AE and DE interfaces is sufficient for binding one turn of dsDNA, suggesting that filament formation is not indispensable for TIR nuclease and 2′,3′-cAMP/cGMP synthase activity. This could also explain why all the tested plant TIR proteins possess nuclease and 2′,3′-cAMP/cGMP synthase activities, while only some of them formed filaments *in vitro*. Therefore, formation of TIR filaments is not a requirement for their functions in vivo.

4.4 DNA/RNA sensors in animals

Recognition of cytosolic DNA/RNA plays a key role in the host immune system. In animals, the source of these cytosolic DNA/RNA molecules can be self-DNA fragments released from damaged organelles, or viral genomes emanating from invading viruses (Lee et al., 2019; Ryu, 2017). The self-DNA fragments, serving as intracellular DAMPs, are mainly perceived by innate immune DNA sensors, such as cGAS and absent in melanoma 2 (AIM2). cGAS utilizes two positively charged surfaces to interact with the backbone of dsDNA (Civril et al., 2013; Gao et al., 2013; Zhang et al., 2014). cGAS dimers assemble along the dsDNA axis, forming a ladder-like structure (Andreeva et al., 2017; Hooy and Sohn, 2018). DNA binding activates cGAS enzyme activity by opening its catalytic site (Goubau et al., 2013). Once activated, cGAS converts GTP and ATP into 2′,3′-cGAMP, which activates the downstream STING immune signaling pathway as a second messenger (Amadio et al., 2021; Motwani et al., 2019).

AIM2 is a cytoplasmic sensor for double-stranded DNA (dsDNA) and is composed of a C-terminal HIN domain ($AIM2^{HIN}$) and an N-terminal PYD ($AIM2^{PYD}$). Structural studies demonstrated that $AIM2^{HIN}$ directly contacts dsDNA to form a filamentous structure coating the dsDNA molecule (Jin et al., 2012; Morrone et al., 2015). As a consequence, $AIM2^{PYD}$ are brought into close proximity, seeding the filament formation of ASC through the PYD-PYD interaction to activate downstream inflammatory pathways (Hauenstein et al., 2015; Morrone et al., 2015). Interferon gamma-inducible protein 16 (IFI16) is another DNA sensor carrying two tandem HIN domains (Unterholzner et al., 2010). Nuclear-cytoplasmic shuttling activity enables IFI16 to perceive dsDNA at both subcellular locations, which leads to different activities (Kerur et al., 2011; Li et al., 2021; Li et al., 2012; Veeranki and Choubey, 2012).

Intracellular viral RNA is mainly sensed by retinoic-acid-inducible gene-I (RIG-I). RIG-I also interacts with dsRNA and forms a filament-like structure (Myong et al., 2009; Peisley et al., 2013). Filament assembly of RIG-I proteins clusters their N-terminal CARDs and consequently up-regulates interferons by recruiting the signaling adaptor, mitochondrial antiviral signaling protein (MAVS) (Hou et al., 2011). While RIG-I is a viral RNA-specific sensor (Hornung et al., 2006; Pichlmair et al., 2006), mis-recognition of self RNA can also happen and lead to constitutive RIG-I activation (Stok et al., 2020), suggesting that the distinction between self and non-self RNA is not clear cut.

4.5 Can plant TIR proteins act as DNA/RNA sensors?

Can intracellular DNA/RNA also be perceived in plants, and if so, what kind of immune responses do plants mount upon perception? Our data raise the possibility that TIR proteins may sense DNA/RNA in plants. In contrast to animal DNA/RNA sensors that use DNA/RNA as platforms to activate their immune activities, plant TIRs hydrolyze accessible DNA/RNA to catalyze 2′,3′-cAMP/cGMP production that amplifies plant immune responses.

In this scenario, the misplaced host DNA may be bound and hydrolyzed by cytosolic TIR proteins to initiate host immune responses. In addition, the origin of RNA/DNA is not important for TIR 2′,3′-cNMP synthetase activity, as $L7^{TIR}$ can also use synthetic RNA/DNA as substrates (section 3.2.2). Therefore, it is also a plausible hypothesis that plant TIR proteins can hydrolyze exogenous RNA/DNA such as cytosolic viral genomes, and produce 2′,3′-cNMP to confer anti-viral immunity.

4.6 Biological implications of TNL alternative splicing

Notably, several TNLs, including RPS4, L6, N and M, are able to produce alternatively spliced transcripts encoding TX and TN proteins in response to pathogen infection, and in some cases these alternatively spliced TIR domain proteins contribute to the full function of TNLs (Jordan et al., 2002).

Alternative *RPS4* transcripts terminated by premature stop codons lead to three truncated open reading frames (ORFs), all of which carry TIR domains but lack most of the LRR domain (Zhang and Gassmann, 2003, 2007). Pathogen infection transiently upregulates alternative transcripts of truncated RPS4, indicating a dynamic regulation of the truncated TNLs (Zhang and Gassmann, 2003, 2007). Transgenic expression of alternative spliced RPS4 ORF was not sufficient to confer resistance against DC3000 AvrRps4 in RLD *Arabidopsis* (a naturally AvrRps4-susceptible accession). Furthermore, removal of the introns, which abolishes the production of alternative spliced RPS4 truncations, leads to pathogen susceptibility (Zhang and Gassmann, 2007). Similarly, transgenic expression of the intronless TNL *N* is also insufficient to achieve full resistance to tobacco mosaic virus (Baker, 2000). These results collectively suggest that the coordinated expression of alternative and regular transcripts of truncated-TNLs and FL-TNLs, is required for the full immune functions of TIR proteins. However, it is noteworthy that alternative splicing does not occur in all TNLs (Jordan et al., 2002), and it is not always required for the immune response as transgenic expression of intronless L6 showed resistance comparable to WT gene (Ayliffe et al., 1999).

As demonstrated for RPP1, TNLs are NADase holoenzymes but lack 2′,3′-cNMP synthetase activity once they form resistosomes, whereas TIR domain proteins have both 2′,3′-cNMP synthetase and NADase activities. We also have evidence that 2′,3′-cAMP/cGMP have a critical role in promoting TIR signaling. Thus, a plausible biological implication of the alternative TNL splicing is that TIR domain-containing proteins produced by alternatively spliced transcripts function as 2′,3′-cNMP synthetases, which produce the non-canonical cNMPs to promote TNL-mediated plant immune responses.

4.7 Nuclease activity is not sufficient for TIR-mediated cell death

In animals, DNA damage induced by spontaneous base hydrolysis and natural stress can trigger apoptotic responses (Cregan et al., 2004; Roos and Kaina, 2006). In contrast, co-expressing RBA1 or RNase T1 with 2′,3′-cNMP PDEs significantly delayed cell death development. This suggests that DNA damage mediated by TIR nuclease activities is not sufficient for the cell death activity of TIRs *in planta*.

In plants, *EDS1*-dependent DNA damage occurred during NLR activation and was regarded as an intrinsic component of plant immunity (Cesari, 2018; Rodriguez et al., 2018). Plant DNA damage caused by SA pretreatment is able to boost immune responses (Yan et al., 2013), suggesting that DNA damage may be an active defense strategy for plants to defend themselves from pathogen invasion. It might be that the fragmented DNAs are either perceived by intracellular DNA/RNA receptors or released to warn bystander cells against the potential threat; both of these mechanisms may activate immune signaling pathways but not directly lead to plant cell death.

4.8 How do 2′,3′-cAMP/cGMP promote immune responses in plants

CNGCs belong to the superfamily of voltage-gated ion channels activated by 3′,5′-cNMP (Jarratt-Barnham et al., 2021; Zelman et al., 2012). However, partial activation of CNGCs by non-canonical cNMPs has also been reported in animals (VanSchouwen and Melacini, 2017). In *Arabidopsis*, CNGCs are involved in plant development, abiotic stress and both PTI and ETI responses via increasing cytosolic Ca^{2+} levels (Tian et al., 2019; Wang et al., 2019a; Yu et al., 2019). Our data do not support a role of 3′,5′-cNMP in TIR-mediated signaling, as co-expression with 3′,5′-cNMP-specific PDE had no effect on RBA1 cell death activity in *N. benthamiana*. *CNGC2* or *CNGC4* null mutants display ‘defense, no death’ (*dnd*) phenotype in ETI (Jurkowski GI, 2004; Yu IC, 1998), whereas Ca^{2+} generated by a CNGC2/4 heteromeric channel promotes PTI responses (Tian et al., 2019). Over-accumulation of CNGC19 and CNGC20 in *bak1/serk4* mutant plants was associated with increased Ca^{2+} influx and cell death, which required ADR1s, RNLs downstream of TIRs (Wu et al., 2020; Yu et al., 2019), suggesting that TIR signaling may converge with the activity of these two CNGC channels. Consistently, a gain-of-function mutation in the CNGC20 channel facilitates both PTI and ETI responses in an *EDS1*-dependent manner (Zhao et al., 2021). Since 2′,3′-cNMPs also have a critical role in promoting TIR signaling (section 3.2.4), it is therefore reasonable to hypothesize that CNGCs may be targets of cytosolic 2′,3′-cNMPs *in planta*.

In animals, 2′,3′-cNMPs have been detected in the extracellular space (Verrier et al., 2012). However, the cellular localization of 2′,3′-cNMPs remains unknown in plants. If plant 2′,3′-cNMPs also function extracellularly, they might act as DAMPs to activate plant PTI. PTI signaling was recently shown to upregulate TIR levels (Pruitt et al., 2021; Tian et al., 2021), which in turn promote expression of 2′,3′-cNMPs. This is consistent with our model wherein 2′,3′-cNMPs function in a self-amplification manner to promote TIR signaling. In the future, it will be of interest to investigate whether 2′,3′-cNMPs have a role in the PTI potentiation of ETI.

4.9 RNase T1 generates immune signals that do not converge on EDS1 signaling pathway

As described in (section 3.2.5), RNase T1 was able to trigger *EDS1*-independent cell death. The RNase T1-mediated cell death was attenuated by co-expression with 2′,3′-cAMP/cGMP PDEs, suggesting that depletion of cytosolic RNA is not responsible for *EDS1*-independent cell death in plants. What other activities of RNase T1 may contribute to *EDS1*-independent cell death?

Unlike plant TIRs, RNase T1 could also catalyze the production of 2′,3′-cGMP using 3′-GMP as substrate (Loverix et al., 1998). By comparison, no 2′,3′-cAMP was produced by $L7^{TIR}$ when using 2′-AMP or 3′-AMP as substrates (Yu et al., unpublished data). Although the potential immunomodulatory function and cellular concentration of 3′-GMP have not been reported, one hypothesis is that RNase T1- mediated 3′-GMP over-consumption leads to *EDS1*-independent cell death *in planta*.

As introduced in (section 1.4.1), RNase T1 could also catalyze the production of 2′,3′-cyclophosphate-terminated RNA oligonucleotides (Shigematsu et al., 2018). RNase T2 has been reported to produce 2′,3′-cyclophosphate-terminated RNA oligonucleotides and activate the TLR8 signaling pathway in animals (Greulich et al., 2019; Ostendorf et al., 2020). Similarly, plant *RNase T2* is also associated with pathogen defense responses, as transgenic tomato lines with suppressed RNase T2 expression revealed a higher susceptibility to pathogen infection (Singh et al., 2020). Therefore, another hypothesis is that the 2′,3′-cyclophosphate-terminated RNA oligonucleotides may be associated with *EDS1*-independent cell death in plants, though the underlying mechanism remains unclear.

4.10 Negative regulation of plant immunity by 2′,3′-cAMP/cGMP PDE

As immune positive regulators, it is reasonable to assume that levels of 2′,3′-cAMP/cGMP are kept under tight control and subject to negative regulation. Metabolism of 2′,3′-cNMPs to 2′-NMPs, 3′-NMPs has been demonstrated in animals (Trapp et al., 1988) and plants (Genschik et al., 1997; Tyc et al., 1987), suggesting that these non-canonical cNMPs are turned over in different species.

Our data showed that *At*NUDT7 specifically metabolizes 2′,3′-cNMPs but not 3′,5′-cNMPs *in vitro* and negatively regulates *RBA1*-mediated cell death in *N. benthamiana. Atnudt7* mutant plants accumulated higher levels of 2′,3′-cAMP/cGMP compared with WT and *Atnudt7 eds1* double mutant plants (Yu et al., 2022), reinforcing our conclusion that 2′,3′-cAMP/cGMP is required for *EDS1*-dependent immune responses. Since *At*NUDT7 is responsive to numerous abiotic and biotic stresses (Marco R. Straus, 2010), the 2′,3′-cAMP/cGMP PDE activity of *At*NUDT7 activity implicates a broad role for *At*NUDT7 and possibly 2′,3′-cAMP/cGMP in the regulation of different plant stress responses.

2′,3′-cAMP/cGMP may also serve as targets for the invading pathogens to subvert plant resistance. The Nudix effector XopQ specifically hydrolyze 2´,3´-cAMP/cGMP, explaining the XopQ-mediated inhibition of *EDS1*-depednent cell death in *Nicotiana* species (Adlung and Bonas, 2017). XopQ can be directly recognized by the TNL ROQ1 and induce *EDS1*-dependent ETI responses. In the ROQ1 resistosome, ROQ1 binds to the active site of XopQ (Martin et al.,

2020) and probably blocks its Nudix hydrolase activity. Thus, recognition of XopQ not only initiates ETI signaling, but also negates the 2´,3´-cAMP/cGMP PDE activity of XopQ. Whether different XopQ expression levels have contrasting impacts on TIR-mediated immune responses remains an open question. Taken together, the tight control and negative regulation of 2′,3′-cAMP/cGMP levels from both host and pathogen sides further highlight the critical role of these non-canonical cNMPs in plant immune response.

4.11 Why do RALPH effectors adopt RNase-like fold?

During infection, fungi secrete a broad variety of RNases into the host (Lacadena et al., 2007). In contrast to the ribotoxins, other fungus-secreted RNases do not have toxicity, for example, the *B. graminis* RALPH effectors (Pedersen et al., 2012). In contrast to the ribotoxins, the non-cytotoxic RNases lack an extended positively charged loop, which is presumed to be important for interaction with host rRNA (Lacadena et al., 2007). Moreover, the RNase catalytic triad is missing in the non-cytotoxic secreted RNases as demonstrated by the RALPH effector, CSEP0064/BEC1054 (Pennington et al., 2019). Our result showed that AVR_A effectors do not exert RNase activities *in vitro*.

Why then, do these RALPH effectors all adopt RNase-like folds? Given that host cell death is lethal for obligate biotrophic pathogens, the virulence activity of the abundantly delivered RALPH effectors may be related to the maintenance of host cell viability. CSEP0064/BEC1054 binds rRNA and prevent its degradation by host ribosome-inhibiting proteins (RIPs) (Pennington et al., 2019), suggesting that RALPH effectors may protect host RNA integrity.

It is also possible that the RNase activity is irrelevant to the genuine virulence function of RALPH effectors. Due to their massive secretion during infection, RALPH effectors adopted a stable and easy-to-express scaffold. RNase-like folding fits this requirement; for instance, RNase T1 was still stable near pH 5.0, and could be folded into a native conformation under 1.0 M NaCl (Pace and Grimsley, 1988; Pace et al., 1988). The RNase activity that may be harmful for the plants, was lost during evolution. Indeed, instead of being an RNase, the virulence function of *B. graminis* RALPH effector CSEP0027 is carried out by targeting barley catalase *Hv*CAT1, and likely by altering host ROS homeostasis (Yuan et al., 2021a).

5. Supplementary Methods

In this section I only list the additional methods which have not been integrated into the published studies.

5.1 Purification and crystallization of RPP1^{TIR}

RPP1^{TIR} (residues 60–254) and RPP1^{TIR} (residues 84–254) were cloned into pFastBac1 (Invitrogen) with an N-terminal GST tag. The constructs were used for generating recombinant baculovirus in sf21 insect cells (Invitrogen). RPP1^{TIR} was expressed in sf21 insect cells with recombinant baculovirus infection at 28 °C for 60 h. The infected cells were harvested and lysed by sonification in buffer containing 25 mM Tris-HCl pH 8.0, 150 mM NaCl. The cell lysates were centrifuged at 30,000 *g* for 1.5 h. The supernatants containing soluble proteins were collected and allowed to flow through GST4B resin (approximately 200 µl per column, GE Healthcare). After washing with three column volumes of sonification buffer, the fusion proteins were incubated with PreScission protease at 4 °C overnight to remove the N-terminal GST tag. The digested RPP1^{TIR} proteins flowed through the columns in buffer containing 25 mM Tris-HCl pH 8.0, and 150 mM NaCl.

Pure RPP1^{TIR} proteins were concentrated to 8mg/ml after SEC. RPP1^{TIR} (residues 60–254) and RPP1^{TIR} (residues 84–254) were individually incubated with 4 mM NAD^{+} (ten times the molar concentration of the protein). After two hours, the RPP1^{TIR}-NAD^{+} was centrifuged at 12,000 *g* for 10 min and immediately applied for crystal screening. Protein crystals were generated by mixing the protein with an equal amount of well solution (1.0 µL) by the hanging-drop vapor-diffusion method. After several rounds of crystallization condition optimizations, the best RPP1^{TIR} (residues 84–254) crystals were obtained under the condition of 20 % w/v polyethylene glycol 3000 (PEG3000), 100 mM HEPES pH 7.5, 200 mM sodium acetate. The crystals were flash frozen in liquid nitrogen using 12.5 % w/v glycerol as the cryoprotection buffer and sent for synchrotron analysis.

5.2 Reconstruction of L7^{TIR} filament *in vitro*

L7^{TIR} was subjected to Superose 6 10/300 gel filtration column (GE Healthcare). Fractions eluted at 17 ml (approximately L7^{TIR} monomer size) was collected and incubated with water, *Arabidopsis* total RNA and gDNA respectively. After 45 min (for RNA incubated L7^{TIR}) and 2 h (for water and DNA incubated L7^{TIR}), 3 µl of each sample (0.1mg/ml) was applied to formvar carbon grids glow-discharged for 45 s at high level in Harrick Plasma after 2 min evacuation. The sample stayed on grid for 1 min at room temperature and dried by touching the edge of a filter paper. 3 µl 2% uranyl acetate was then applied to the grid for 45 s. The excess stain was removed. Grids were dried at room temperature for 2 min. Samples were imaged using Hitachi H-7650 120 kV transmission electron microscope (TEM) and images were recorded with an AMT XR-41 camera.

5.3 Production and detection of 2′,3′-cNMP *in vitro*

The purified L7^{TIR} protein (1 µM) was incubated with 100 µM ATP, 100 ng RNA40 (20 nt ssRNA, Miltenyi Biotec); RNA 334nt (mRNA transcribed from antisense mouse s-actin probe offered in MAXIscript kit); 100 ng poly (A:U) (synthesized poly A:U, InvivoGen); PCR product and 100 ng poly (I:C) (synthesized poly A:U, InvivoGen), respectively. After incubation at 25°C for 16 h, the samples were centrifuged at 12,000 g for 10 min, and the supernatant was applied to LC-MS/MS for metabolite identification and quantification. RPP1 and RPP1-ATR1 proteins (0.5 µM) were incubated with 100 ng *Arabidopsis* total RNA in the presence of 1 mM $MgSO_4$. RPP1 and RPP1-ATR1 (0.5 µM) proteins were incubated with *Arabidopsis* total RNA at 25°C for 16 h and the reaction products were analysed by LC-MS.

Chromatography was performed on a Nexera XR 40 series HPLC (Shimadzu) using a Synergi 4µM Fusion-RP 80 Å 150x2mm column (Phenomenex). The column temperature was maintained at 40°C and the sample tray at 4°C. Samples (10µl) were injected at a flow rate of 0.2 ml/min using 10 mM ammonium formate at pH 4.2 and methanol as mobile phases A and B, respectively. Metabolites were eluted using the profile 0-8 min, 8-90% B; 8-10 min, 90% B; 10-10.1 min 90-8% B; 10.1-20 min, 8% B. The LCMS-8060 triple quadrupole mass spectrometer with electro spray ionization (Shimadzu) was operated in positive mode. Scheduled multiple reaction monitoring (MRM) was used to monitor analyte parent ion to product ion formation. MRM conditions were optimized using authentic standard chemicals including: 2′,3′-cAMP ($[M+H]^+$ 330.00>136.20, 330.00>99.15, 330.00>119.15), 2′,3′-cGMP ($[M+H]^+$ 346.00>152.15, 346.00 >135.20, 346.00>110.15), 2′,3′-cCMP ($[M+H]^+$ 306.00>112.15, 306.00>95.20, 306.00>178.20). Both Q1 and Q3 quadrupoles were maintained in unit resolution. LabSolutions LCMS v5.97 software was used for data acquisition and LabSolutions Postrun for processing (both Shimadzu). Metabolites were quantified by scheduled MRM peak integration using external calibration curves of standard chemicals.

5.4 Protoplast isolation and 2′,3′-cAMP/cGMP treatment

Protoplasts were isolated from 3-week-old *A. thaliana* leaves and transfected as previously described (Saur et al., 2019b). Isolated protoplasts were transfected at OD_{600} 0.4 with 5 µg LUC reporter vector (pZmUBQ:LUC) (Muller et al., 2005). One group of protoplasts was co-transfected with 2′,3′-cAMP (100 µM) or with 2′,3′-cGMP (100 µM) in the presence of 40% PEG4000. 2′,3′-cAMP/cGMP was removed together with transfection buffer after 15 min. Another group of protoplasts were incubated with Br-2′,3′-cAMP (100 µM) or Br-2′,3′-cGMP (100 µM) after LUC reporter vector transfection in regeneration buffer. All protoplasts were incubated at 20°C for 16 h. Luminescence was measured using a luminometer (Centro, LB960). Changes in luciferase activity were calculated by dividing the absolute luminescence value of (Br-)2′,3′-cNMP treated samples by the buffer treated samples. The LUC value from buffer-treated protoplast was set as 1.0.

5.5 Purification of FL NLR and effectors

Codon optimized MLA7 (13–959), MLA9 (13–951), MLA10 (1–951), MLA10 (13–951), MLA13(7–959), MLA13 (13–959), MLA22 (13–959), MLA27 (1–957), MLA27 (13–957) and L7 (26–1294) were cloned into the pFastBac1 (Invitrogen) with an N-terminal 6×His-SUMO tag. MLA27 (1–957), MLA27 (13–957) were cloned into pFastBac1 with an N-terminal GST tag. The constructs were used for generating recombinant baculovirus in sf21 insect cells (Invitrogen). 6×His-SUMO-tagged MLAs and L7 were expressed in sf21 insect cells with recombinant baculovirus infection at 28 °C for 60 h. The infected cells were harvested and lysed by sonification in buffer containing 25 mM Tris-HCl pH 8.0, 150 mM NaCl and 15 mM imidazole. The cell lysates were centrifuged at 30,000 *g* for 1.5 h. The supernatants containing soluble proteins were collected and allowed to flow through Ni-NTA resin (approximately 200 µl per column, GE Healthcare). After washing with three column volumes of sonification buffer, proteins were eluted by His elution buffer containing 25 mM Tris-HCl pH 8.0, and 150 mM NaCl and 200 mM imidazole. GST-tagged MLA27 proteins were purified as described for RPP1$^{\mathrm{TIR}}$, but were eluted with GST elution buffer containing 25 mM Tris-HCl pH 8.0, and 150 mM NaCl and 50 mM reduced glutathione (GSH).

AVR$_{\mathrm{A10}}$ (21–119), AVR$_{\mathrm{A13}}$(21–122), AVR$_{\mathrm{A13}}$-V2(21–119) AVRL-567A (24–151) were cloned into the pFastBac1 with a C-terminal GST tag. Proteins were purified as described for GST tagged MLA27. For co-expression, the baculovirus of NLR and effector were mixed at the ratio of 2:1 and used to co-infect insect cells. Proteins were expressed in sf21 insect cells at 28 °C for 48 h.

Acknowledgements

First and foremost, I am extremely grateful to my family for their *pro bono* help and encouragement all along my way. Likewise, I greatly thank my supervisors, Prof. Dr. Jijie Chai and Prof. Dr. Paul Schulze-Lefert, for their continuous support, invaluable advice and patience during my PhD study, which are no less than my family. As Chinese idiom says, "A day as a teacher, a lifetime as a father". The memorable time working and getting along with you will always stay with me.

I would like to thank all the lab members from AG. Chai, AG. PSL, all lab members in Tsinghua University and our collaborators in Singapore. I would not have been able to complete my PhD without the help from any of them. For the TIR studies, I need to give special thanks to Asst Prof. Dr. Bin Wu, Wen Song, Yu Cao and Jan Jirschitzka. There were many ‘eureka moments’ when discussing and working with them. Thanks also to Li Liu, Eddie Yong Jun Tan, Elke Logemann, Marlin Eh and Aaron W. Lawson. For the MLA and AVR$_{A}$ study, I am very grateful to Jizong Wang, Xiaoxiao Zhang, Saskia Bauer, Isabel M. L. Saur and Yuang Wu for sharing experience, providing materials and offering helps.

Last but not least, great thanks to my TAC member Elmar Behrmann, to MPIPZ PhD coordinator Stephan Wagner, to MPIPZ scientific editing coordinator Neysan Donnelly and to all the faculties in Max Planck Institute and University of Cologne.

Curriculum Vitae

Dongli Yu

Carl-von-Linne weg 10 50829 Köln | +49 017635594332 | dyu@mpipz.mpg.de

Education

- Max Planck Institute for Plant Breeding Research Sep 2017- present
  PhD in Biochemistry and Biology
- Wageningen University Nov 2016- Jun 2017
  Master Internship of Plant Pathology
- Nanjing Agricultural University Sep 2014- Jun 2017
  Master of Agronomy in Plant Pathology GPA: 86.34/100
- Nanjing Agricultural University Sep 2010- Jun 2014
  Bachelor of Agronomy in Plant Protection GPA: 86.71/100

Publications

- **D Yu**[#], W Song[#], E Tan[#], L Liu, Y Cao, J Jirschitzka, E Li, E Logemann, C Xu, S Huang, A Jia, X Chang, Z Han, B Wu, P Schulze-Lefert, J Chai. TIR domains of plant immune receptors are 2′,3′-cAMP/cGMP synthetases mediating cell death. *Cell*. 2022
- S Huang[#], A Jia[#], W Song[#], G Hessler[#], Y Meng[#], Y Sun, L Xu, H Laessle, J Jirschitzka, S Ma, Y, Xiao, **D Yu**, J Hou, R Liu, H Sun, X Liu, Z Han, J Chang, J Parker, J Chai. Identification and receptor mechanism of TIR-catalyzed small molecules in plant immunity. *Science*. 2022
- A Jia[#], S Huang[#], W Song[#], J Wang[#], Y Meng[#], Y Sun[#], L Xu, H Laessle, J Jirschitzka, J Hou, T Zhang, W Yu, G Hessler, E Li, S Ma, **D Yu**, J Gebauer, U Baumann, X Liu, Z Han, J Chang, JE. Parker, J Chai. TIR-catalyzed ADP-ribosylation reactions produce signaling molecules for plant immunity. *Science*. 2022
- A Forderer[#], **D Yu**[#], E Li[#], J Chai. Resistosomes at the interface of pathogens and plants. *Curr. Opin. Plant Biol.* 2022
- C Sheng, **D Yu**, X Li, H Yu, Y Zhang, M Saqib Bilal, H Ma, X Zhang, A Baig, P Nie, H Zhao. OsAPX1 positively contributes to rice blast resistance. *Front. Plant Sci*. 2022
- S Bauer, **D Yu**, L Frantzeskakis, B Kracher, E Logemann, I Saur, J Chai, T Maekawa, P Schulze-Lefert. Leucine-rich repeats in allelic barley MLA immune receptors recognize a predicted common RNase-like fold in sequence-unrelated powdery mildew avirulence effectors through multiple contact residues. *PLoS Pathog*. 2020.
- W Song[#], A Forderer[#], **D Yu**[#], J Chai. Structural biology of plant defence. *New Phytol.* 2020
- S Ma[#], D Lapin[#], L Liu[#], X Zhang[#], W Song[#], Y Sun, E Logemann, **D Yu**, J Wang, J Jirschitzka, Z Han, J Parker, P Schulze-Lefert, J Chai. Direct pathogen-induced assembly of an NLR immune receptor complex to form a holoenzyme. *Science.* 2020.

Conference attendance

- Molecular Plant-Microbe Interaction (IS-MPMI). Moderator. Jun 2021
- International Union of Crystallography (ICUr). Attendee. Aug 2021
- EMBO workshop cell death in immunity and inflammation. Attendee. Aug 2019

Teaching experience

- University of Cologne, biochemistry practical course teaching assistant Dec 2021

References

Abel, S., Krauss, G.-J., and Glund, K. (1989). Ribonuclease in tomato vacuoles: high-performance liquid chromatographic analysis of ribonucleolytic activities and base specificity. Biochimica et Biophysica Acta (BBA)-Protein Structure and Molecular Enzymology *998*, 145-150.

Adachi, H., Contreras, M.P., Harant, A., Wu, C.H., Derevnina, L., Sakai, T., Duggan, C., Moratto, E., Bozkurt, T.O., Maqbool, A.*, et al.* (2019). An N-terminal motif in NLR immune receptors is functionally conserved across distantly related plant species. Elife *8*.

Adlung, N., and Bonas, U. (2017). Dissecting virulence function from recognition: cell death suppression in Nicotiana benthamiana by XopQ/HopQ1-family effectors relies on EDS1-dependent immunity. The Plant journal : for cell and molecular biology *91*, 430-442.

Afzal, A.J., da Cunha, L., and Mackey, D. (2011). Separable fragments and membrane tethering of Arabidopsis RIN4 regulate its suppression of PAMP-triggered immunity. Plant Cell *23*, 3798-3811.

Alexander, F., Dongli, Y., Ertong, L., and Jijie, C. (2022a). Resistosomes at the interface of pathogens and plants. Curr Opin Plant Biol *21;67:102212*.

Alexander, F., Ertong, L., Aaron, L., Ya-nan Deng, Yue Sun, Elke Logemann, Xiaoxiao Zhang, Jie Wen, Zhifu Han, Junbiao Chang*, et al.* (2022b). A wheat resistosome defines common principles of immune receptor channels. bioRxiv.

Amadio, R., Piperno, G.M., and Benvenuti, F. (2021). Self-DNA Sensing by cGAS-STING and TLR9 in Autoimmunity: Is the Cytoskeleton in Control? Front Immunol *12*, 657344.

Andreeva, L., Hiller, B., Kostrewa, D., Lassig, C., de Oliveira Mann, C.C., Jan Drexler, D., Maiser, A., Gaidt, M., Leonhardt, H., Hornung, V.*, et al.* (2017). cGAS senses long and HMGB/TFAM-bound U-turn DNA by forming protein-DNA ladders. Nature *549*, 394-398.

Axtell, M.J., and Staskawicz, B.J. (2003). Initiation of RPS2-specified disease resistance in Arabidopsis is coupled to the AvrRpt2-directed elimination of RIN4. Cell *112*, 369-377.

Ayliffe, M.A., Frost, D.V., Finnegan, E.J., Lawrence, G.J., Anderson, P.A., and Ellis, J.G. (1999). Analysis of alternative transcripts of the flax L6 rust resistance gene. Plant J *17*, 287-292.

Azarashvili, T., Krestinina, O., Galvita, A., Grachev, D., Baburina, Y., Stricker, R., Evtodienko, Y., and Reiser, G. (2009). Ca2+-dependent permeability transition regulation in rat brain mitochondria by 2',3'-cyclic nucleotides and 2',3'-cyclic nucleotide 3'-phosphodiesterase. Am J Physiol Cell Physiol *296*, C1428-1439.

Azita, L., Erez Yirmiya, Gil Amitai, Allen Lu, Jeremy Garb, Benjamin R. Morehouse, Samuel J. Hobbs, Philip J. Kranzusch, and Sorek, R. (2022). Viruses inhibit TIR gcADPR signaling to overcome bacterial defense. bioRxiv.

Baker, S.P.D.-K.B.J. (2000). Alternatively spliced N resistance gene transcripts: Their possible role in tobacco mosaic virus resistance. PNAS *vol. 97*.

Barbero, F., Guglielmotto, M., Capuzzo, A., and Maffei, M.E. (2016). Extracellular Self-DNA (esDNA), but Not Heterologous Plant or Insect DNA (etDNA), Induces Plasma Membrane Depolarization and Calcium Signaling in Lima Bean (Phaseolus lunatus) and Maize (Zea mays). Int J Mol Sci *17*.

Bartsch, M., Gobbato, E., Bednarek, P., Debey, S., Schultze, J.L., Bautor, J., and Parker, J.E. (2006). Salicylic acid-independent ENHANCED DISEASE SUSCEPTIBILITY1 signaling in Arabidopsis immunity and cell death is regulated by the monooxygenase FMO1 and the Nudix hydrolase NUDT7. The Plant cell *18*, 1038-1051.

Bauer, S., Yu, D., Lawson, A.W., Saur, I.M.L., Frantzeskakis, L., Kracher, B., Logemann, E., Chai, J., Maekawa, T., and Schulze-Lefert, P. (2021). The leucine-rich repeats in allelic barley MLA immune receptors define specificity towards sequence-unrelated powdery mildew avirulence effectors with a predicted common RNase-like fold. PLoS Pathog *17*, e1009223.

Bernoux, M., Ve, T., Williams, S., Warren, C., Hatters, D., Valkov, E., Zhang, X., Ellis, J.G., Kobe, B., and Dodds, P.N. (2011). Structural and functional analysis of a plant resistance protein TIR domain reveals interfaces for self-association, signaling, and autoregulation. Cell Host Microbe *9*, 200-211.

Bi, G., Su, M., Li, N., Liang, Y., Dang, S., Xu, J., Hu, M., Wang, J., Zou, M., Deng, Y*., et al.* (2021). The ZAR1 resistosome is a calcium-permeable channel triggering plant immune signaling. Cell *184*, 3528-3541 e3512.

Bonardi, V., Tang, S., Stallmann, A., Roberts, M., Cherkis, K., and Dangl, J.L. (2011). Expanded functions for a family of plant intracellular immune receptors beyond specific recognition of pathogen effectors. Proc Natl Acad Sci U S A *108*, 16463-16468.

Botos, I., Segal, D.M., and Davies, D.R. (2011). The structural biology of Toll-like receptors. Structure *19*, 447-459.

Cannesan, M.A., Gangneux, C., Lanoue, A., Giron, D., Laval, K., Hawes, M., Driouich, A., and Vicre-Gibouin, M. (2011). Association between border cell responses and localized root infection by pathogenic Aphanomyces euteiches. Ann Bot *108*, 459-469.

Cao, Y., Liang, Y., Tanaka, K., Nguyen, C.T., Jedrzejczak, R.P., Joachimiak, A., and Stacey, G. (2014). The kinase LYK5 is a major chitin receptor in Arabidopsis and forms a chitin-induced complex with related kinase CERK1. Elife *3*.

Cesari, S. (2018). Multiple strategies for pathogen perception by plant immune receptors. New Phytol *219*, 17-24.

Cheng, W., Munkvold, K.R., Gao, H., Mathieu, J., Schwizer, S., Wang, S., Yan, Y.B., Wang, J., Martin, G.B., and Chai, J. (2011). Structural analysis of Pseudomonas syringae AvrPtoB bound to host BAK1 reveals two similar kinase-interacting domains in a type III Effector. Cell Host Microbe *10*, 616-626.

Chivasa, S., Murphy, A.M., Hamilton, J.M., Lindsey, K., Carr, J.P., and Slabas, A.R. (2009a). Extracellular ATP is a regulator of pathogen defence in plants. Plant J *60*, 436-448.

Chivasa, S., Tome, D.F., Murphy, A.M., Hamilton, J.M., Lindsey, K., and Carr, J.P. (2009b). Extracellular ATP: a modulator of cell death and pathogen defense in plants. Plant Signal Behav *4*, 1078-1080.

Chodasiewicz, M., Kerber, O., Gorka, M., Moreno, J.C., Maruri-Lopez, I., Minen, R.I., Sampathkumar, A., Nelson, A.D.L., and Skirycz, A. (2022). 2',3'-cAMP treatment mimics the stress molecular response in Arabidopsis thaliana. Plant Physiol *188*, 1966-1978.

Choi, J., Tanaka, K., Cao, Y., Qi, Y., Qiu, J., Liang, Y., Lee, S.Y., and Stacey, G. (2014). Identification of a plant receptor for extracellular ATP. Science *343*, 290-294.

Civril, F., Deimling, T., de Oliveira Mann, C.C., Ablasser, A., Moldt, M., Witte, G., Hornung, V., and Hopfner, K.P. (2013). Structural mechanism of cytosolic DNA sensing by cGAS. Nature *498*, 332-337.

Coaker, G., Falick, A., and Staskawicz, B. (2005). Activation of a phytopathogenic bacterial effector protein by a eukaryotic cyclophilin. Science *308*, 548-550.

Collier, S.M., Hamel, L.P., and Moffett, P. (2011). Cell death mediated by the N-terminal domains of a unique and highly conserved class of NB-LRR protein. Mol Plant Microbe Interact *24*, 918-931.

Couto, D., and Zipfel, C. (2016). Regulation of pattern recognition receptor signalling in plants. Nat Rev Immunol *16*, 537-552.

Cregan, S.P., Dawson, V.L., and Slack, R.S. (2004). Role of AIF in caspase-dependent and caspase-independent cell death. Oncogene *23*, 2785-2796.

Dalakouras, A., Jarausch, W., Buchholz, G., Bassler, A., Braun, M., Manthey, T., Krczal, G., and Wassenegger, M. (2018). Delivery of Hairpin RNAs and Small RNAs Into Woody and Herbaceous Plants by Trunk Injection and Petiole Absorption. Front Plant Sci *9*, 1253.

Dangl, J.L., and Jones, J.D.G. (2019). A pentangular plant inflammasome. Science *364*, 31-32.

Daskalov, A., Habenstein, B., Sabate, R., Berbon, M., Martinez, D., Chaignepain, S., Coulary-Salin, B., Hofmann, K., Loquet, A., and Saupe, S.J. (2016). Identification of a novel cell death-inducing domain reveals that fungal amyloid-controlled programmed cell death is related to necroptosis. Proc Natl Acad Sci U S A *113*, 2720-2725.

de Jonge, R., van Esse, H.P., Kombrink, A., Shinya, T., Desaki, Y., Bours, R., van der Krol, S., Shibuya, N., Joosten, M.H., and Thomma, B.P. (2010). Conserved fungal LysM effector Ecp6 prevents chitin-triggered immunity in plants. Science *329*, 953-955.

Denning, N.L., Aziz, M., Gurien, S.D., and Wang, P. (2019). DAMPs and NETs in Sepsis. Front Immunol *10*, 2536.

Deshpande, R.A., and Shankar, V. (2002). Ribonucleases from T2 family. Crit Rev Microbiol *28*, 79-122.

Dolina, J.S., Lee, J., Griswold, R.Q., Labarta-Bajo, L., Kannan, S., Greenbaum, J.A., Bahia El Idrissi, N., Pont, M.J., Croft, M., and Schoenberger, S.P. (2020). TLR9 Sensing of Self-DNA Controls Cell-Mediated Immunity to Listeria Infection via Rapid Conversion of Conventional CD4(+) T Cells to Treg. Cell Rep *31*, 107249.

Doron, S., Melamed, S., Ofir, G., Leavitt, A., Lopatina, A., Keren, M., Amitai, G., and Sorek, R. (2018). Systematic discovery of antiphage defense systems in the microbial pangenome. Science *359*.

Dou, D., Kale, S.D., Wang, X., Jiang, R.H., Bruce, N.A., Arredondo, F.D., Zhang, X., and Tyler, B.M. (2008). RXLR-mediated entry of Phytophthora sojae effector Avr1b into soybean cells does not require pathogen-encoded machinery. Plant Cell *20*, 1930-1947.

Dou, D., and Zhou, J.M. (2012). Phytopathogen effectors subverting host immunity: different foes, similar battleground. Cell Host Microbe *12*, 484-495.

Duran-Flores, D., and Heil, M. (2014). Damaged-self recognition in common bean (Phaseolus vulgaris) shows taxonomic specificity and triggers signaling via reactive oxygen species (ROS). Front Plant Sci *5*, 585.

Duran-Flores, D., and Heil, M. (2018). Extracellular self-DNA as a damage-associated molecular pattern (DAMP) that triggers self-specific immunity induction in plants. Brain Behav Immun *72*, 78-88.

Duxbury, Z., Wang, S., MacKenzie, C.I., Tenthorey, J.L., Zhang, X., Huh, S.U., Hu, L., Hill, L., Ngou, P.M., Ding, P.*, et al.* (2020). Induced proximity of a TIR signaling domain on a plant-mammalian NLR chimera activates defense in plants. Proc Natl Acad Sci U S A *117*, 18832-18839.

Essuman, K., Summers, D.W., Sasaki, Y., Mao, X., Yim, A.K.Y., DiAntonio, A., and Milbrandt, J. (2018). TIR Domain Proteins Are an Ancient Family of NAD(+)-Consuming Enzymes. Curr Biol *28*, 421-430 e424.

Feng, F., Yang, F., Rong, W., Wu, X., Zhang, J., Chen, S., He, C., and Zhou, J.M. (2012). A Xanthomonas uridine 5'-monophosphate transferase inhibits plant immune kinases. Nature *485*, 114-118.

Figley, M.D., Gu, W., Nanson, J.D., Shi, Y., Sasaki, Y., Cunnea, K., Malde, A.K., Jia, X., Luo, Z., Saikot, F.K.*, et al.* (2021). SARM1 is a metabolic sensor activated by an increased NMN/NAD(+) ratio to trigger axon degeneration. Neuron *109*, 1118-1136 e1111.

Fitzgerald, K.A., and Kagan, J.C. (2020). Toll-like Receptors and the Control of Immunity. Cell *180*, 1044-1066.

Fitzgerald, K.A., Palsson-McDermott, E.M., Bowie, A.G., Jefferies, C.A., Mansell, A.S., Brady, G., Brint, E., Dunne, A., Gray, P., Harte, M.T.*, et al.* (2001). Mal (MyD88-adapter-like) is required for Toll-like receptor-4 signal transduction. Nature *413*, 78-83.

Flor, H.H. (1942). The inheritance of pathogenicity in a cross between physiologic races 22 and 24 of Melampsora lini. . Phytopathology Research *32:5.*

Fontaine, B.M., Martin, K.S., Garcia-Rodriguez, J.M., Jung, C., Briggs, L., Southwell, J.E., Jia, X., and Weinert, E.E. (2018). RNase I regulates Escherichia coli 2',3'-cyclic nucleotide monophosphate levels and biofilm formation. Biochem J *475*, 1491-1506.

Friesen, T.L., Faris, J.D., Solomon, P.S., and Oliver, R.P. (2008). Host-specific toxins: effectors of necrotrophic pathogenicity. Cell Microbiol *10*, 1421-1428.

Gallucci, S., and Maffei, M.E. (2017). DNA Sensing across the Tree of Life. Trends Immunol *38*, 719-732.

Gao, D., Wu, J., Wu, Y.T., Du, F., Aroh, C., Yan, N., Sun, L., and Chen, Z.J. (2013). Cyclic GMP-AMP synthase is an innate immune sensor of HIV and other retroviruses. Science *341*, 903-906.

Gasser, B., Saloheimo, M., Rinas, U., Dragosits, M., Rodriguez-Carmona, E., Baumann, K., Giuliani, M., Parrilli, E., Branduardi, P., Lang, C*., et al.* (2008). Protein folding and conformational stress in microbial cells producing recombinant proteins: a host comparative overview. Microb Cell Fact *7*, 11.

Gawehns, F., Houterman, P.M., Ichou, F.A., Michielse, C.B., Hijdra, M., Cornelissen, B.J., Rep, M., and Takken, F.L. (2014). The Fusarium oxysporum effector Six6 contributes to virulence and suppresses I-2-mediated cell death. Mol Plant Microbe Interact *27*, 336-348.

Ge, X., Li, G.J., Wang, S.B., Zhu, H., Zhu, T., Wang, X., and Xia, Y. (2007). AtNUDT7, a negative regulator of basal immunity in Arabidopsis, modulates two distinct defense response pathways and is involved in maintaining redox homeostasis. Plant Physiol *145*, 204-215.

Ge, X., and Xia, Y. (2008). The role of AtNUDT7, a Nudix hydrolase, in the plant defense response. Plant Signal Behav *3*, 119-120.

Geisler, S., Huang, S.X., Strickland, A., Doan, R.A., Summers, D.W., Mao, X., Park, J., DiAntonio, A., and Milbrandt, J. (2019). Gene therapy targeting SARM1 blocks pathological axon degeneration in mice. J Exp Med *216*, 294-303.

Genschik, P., Hall, J., and Filipowicz, W. (1997). Cloning and characterization of the Arabidopsis cyclic phosphodiesterase which hydrolyzes ADP-ribose 1'',2''-cyclic phosphate and nucleoside 2',3'-cyclic phosphates. The Journal of biological chemistry *272*, 13211-13219.

Gilley, J., and Coleman, M.P. (2010). Endogenous Nmnat2 is an essential survival factor for maintenance of healthy axons. PLoS Biol *8*, e1000300.

Gluck, A., and Wool, I.G. (1996). Determination of the 28 S ribosomal RNA identity element (G4319) for alpha-sarcin and the relationship of recognition to the selection of the catalytic site. J Mol Biol *256*, 838-848.

Gohre, V., Spallek, T., Haweker, H., Mersmann, S., Mentzel, T., Boller, T., de Torres, M., Mansfield, J.W., and Robatzek, S. (2008). Plant pattern-recognition receptor FLS2 is directed for degradation by the bacterial ubiquitin ligase AvrPtoB. Curr Biol *18*, 1824-1832.

Goubau, D., Deddouche, S., and Reis e Sousa, C. (2013). Cytosolic sensing of viruses. Immunity *38*, 855-869.

Greulich, W., Wagner, M., Gaidt, M.M., Stafford, C., Cheng, Y., Linder, A., Carell, T., and Hornung, V. (2019). TLR8 Is a Sensor of RNase T2 Degradation Products. Cell *179*, 1264-1275 e1213.

Grund, E., Tremousaygue, D., and Deslandes, L. (2019). Plant NLRs with Integrated Domains: Unity Makes Strength. Plant Physiol *179*, 1227-1235.

Gust, A.A., and Felix, G. (2014). Receptor like proteins associate with SOBIR1-type of adaptors to form bimolecular receptor kinases. Curr Opin Plant Biol *21*, 104-111.

Han, Z., Sun, Y., and Chai, J. (2014). Structural insight into the activation of plant receptor kinases. Current Opinion in Plant Biology *20: 55– 63*.

Hander, T., Fernandez-Fernandez, A.D., Kumpf, R.P., Willems, P., Schatowitz, H., Rombaut, D., Staes, A., Nolf, J., Pottie, R., Yao, P*., et al.* (2019). Damage on plants activates Ca(2+)-dependent metacaspases for release of immunomodulatory peptides. Science *363*.

Hauenstein, A.V., Zhang, L., and Wu, H. (2015). The hierarchical structural architecture of inflammasomes, supramolecular inflammatory machines. Curr Opin Struct Biol *31*, 75-83.

Hayden, B., Xiahao, H., Maxwell X. Rank, Natsumi, M., and Bostjan, K. (2021). Self-association configures the NAD+-binding site of plant NLR TIR domains. BioRxiv.

Hooy, R.M., and Sohn, J. (2018). The allosteric activation of cGAS underpins its dynamic signaling landscape. Elife *7*.

Hornung, V., Ellegast, J., Kim, S., Brzozka, K., Jung, A., Kato, H., Poeck, H., Akira, S., Conzelmann, K.K., Schlee, M.*, et al.* (2006). 5'-Triphosphate RNA is the ligand for RIG-I. Science *314*, 994-997.

Horsefield, S., Burdett, H., Zhang, X., Manik, M.K., Shi, Y., Chen, J., Qi, T., Gilley, J., Lai, J.S., Rank, M.X.*, et al.* (2019). NAD(+) cleavage activity by animal and plant TIR domains in cell death pathways. Science *365*, 793-799.

Hou, F., Sun, L., Zheng, H., Skaug, B., Jiang, Q.X., and Chen, Z.J. (2011). MAVS forms functional prion-like aggregates to activate and propagate antiviral innate immune response. Cell *146*, 448-461.

Hou, S., Liu, Z., Shen, H., and Wu, D. (2019). Damage-Associated Molecular Pattern-Triggered Immunity in Plants. Front Plant Sci *10*, 646.

Hu, Z., Yan, C., Liu, P., Huang, Z., Ma, R., Zhang, C., Wang, R., Zhang, Y., Martinon, F., Miao, D.*, et al.* (2013). Crystal structure of NLRC4 reveals its autoinhibition mechanism. Science *341*, 172-175.

Huang, S., Jia, A., Song, W., Hessler, G., Yonggang, M., Yue Sun, Lina Xu, Henriette Laessle, Jan Jirschitzka, Shoucai Ma*, et al.* (2022). Identification and receptor mechanism of TIR-catalyzed small molecules in plant immunity. Science.

Hurlburt, N.K., Chen, L.H., Stergiopoulos, I., and Fisher, A.J. (2018). Structure of the Cladosporium fulvum Avr4 effector in complex with (GlcNAc)6 reveals the ligand-binding mechanism and uncouples its intrinsic function from recognition by the Cf-4 resistance protein. PLoS Pathog *14*, e1007263.

Iba, T., Murai, M., Nagaoka, I., and Tabe, Y. (2014). Neutrophil extracellular traps, damage-associated molecular patterns, and cell death during sepsis. Acute Med Surg *1*, 2-9.

Jackson, E.K. (2017). Discovery and Roles of 2',3'-cAMP in Biological Systems. Handb Exp Pharmacol *238*, 229-252.

Jackson, E.K., Ren, J., and Mi, Z. (2009). Extracellular 2',3'-cAMP is a source of adenosine. J Biol Chem *284*, 33097-33106.

Jacob, P., Kim, N.H., Wu, F., El-Kasmi, F., Chi, Y., Walton, W.G., Furzer, O.J., Lietzan, A.D., Sunil, S., Kempthorn, K.*, et al.* (2021). Plant "helper" immune receptors are Ca(2+)-permeable nonselective cation channels. Science *373*, 420-425.

Jambunathan, N., and Mahalingam, R. (2006). Analysis of Arabidopsis growth factor gene 1 (GFG1) encoding a nudix hydrolase during oxidative signaling. Planta *224*, 1-11.

Janjusevic, R., Abramovitch, R.B., Martin, G.B., and Stebbins, C.E. (2006). A bacterial inhibitor of host programmed cell death defenses is an E3 ubiquitin ligase. Science *311*, 222-226.

Jarratt-Barnham, E., Wang, L., Ning, Y., and Davies, J.M. (2021). The Complex Story of Plant Cyclic Nucleotide-Gated Channels. Int J Mol Sci *22*.

Jia, A., Huang, S., Song, W., Wang, J., Yonggang, M., Yue Sun, Lina Xu, Henriette Laessle, Jan Jirschitzka, J.H., Tiantian Zhang, Wenquan Yu, Giuliana Hessler, Ertong Li, Shoucai Ma, Dongli Yu, Jan Gebauer, Ulrich Baumann, Xiaohui Liu, Zhifu Han, , Junbiao Chang*, et al.* (2022). TIR-catalyzed ADP-ribosylation reactions produce signaling molecules for plant immunity. Science.

Jin, T., Perry, A., Jiang, J., Smith, P., Curry, J.A., Unterholzner, L., Jiang, Z., Horvath, G., Rathinam, V.A., Johnstone, R.W.*, et al.* (2012). Structures of the HIN domain:DNA complexes reveal ligand binding and activation mechanisms of the AIM2 inflammasome and IFI16 receptor. Immunity *36*, 561-571.

Jones, J.D., and Dangl, J.L. (2006). The plant immune system. Nature *444*, 323-329.

Jordan, T., Schornack, S., and Lahaye, T. (2002). Alternative splicing of transcripts encoding Toll-like plant resistance proteins - what's the functional relevance to innate immunity? Trends Plant Sci *7*, 392-398.

Jurkowski GI, S.R., Jr., Yu IC, Ham JH, Sharma SB, Klessig DF, Fengler KA, Bent AF (2004). Arabidopsis DND2, a second cyclic nucleotide-gated ion channel gene for which mutation causes the "defense, no death" phenotype. . Molecular plant-microbe interactions *17(5):511-520.*

Ka, D., Oh, H., Park, E., Kim, J.H., and Bae, E. (2020). Structural and functional evidence of bacterial antiphage protection by Thoeris defense system via NAD(+) degradation. Nat Commun *11*, 2816.

Kaku, H., Nishizawa, Y., Ishii-Minami, N., Akimoto-Tomiyama, C., Dohmae, N., Takio, K., Minami, E., and Shibuya, N. (2006). Plant cells recognize chitin fragments for defense signaling through a plasma membrane receptor. Proc Natl Acad Sci U S A *103*, 11086-11091.

Karasov, T.L., Kniskern, J.M., Gao, L., DeYoung, B.J., Ding, J., Dubiella, U., Lastra, R.O., Nallu, S., Roux, F., Innes, R.W., *et al.* (2014). The long-term maintenance of a resistance polymorphism through diffuse interactions. Nature *512*, 436-440.

Kelley, B.S., Lee, S.J., Damasceno, C.M., Chakravarthy, S., Kim, B.D., Martin, G.B., and Rose, J.K. (2010). A secreted effector protein (SNE1) from Phytophthora infestans is a broadly acting suppressor of programmed cell death. Plant J *62*, 357-366.

Kerur, N., Veettil, M.V., Sharma-Walia, N., Bottero, V., Sadagopan, S., Otageri, P., and Chandran, B. (2011). IFI16 acts as a nuclear pathogen sensor to induce the inflammasome in response to Kaposi Sarcoma-associated herpesvirus infection. Cell Host Microbe *9*, 363-375.

Kessler, S.C., Zhang, X., McDonald, M.C., Gilchrist, C.L.M., Lin, Z., Rightmyer, A., Solomon, P.S., Turgeon, B.G., and Chooi, Y.H. (2020). Victorin, the host-selective cyclic peptide toxin from the oat pathogen Cochliobolus victoriae, is ribosomally encoded. Proc Natl Acad Sci U S A *117*, 24243-24250.

Kettles, G.J., Bayon, C., Sparks, C.A., Canning, G., Kanyuka, K., and Rudd, J.J. (2018). Characterization of an antimicrobial and phytotoxic ribonuclease secreted by the fungal wheat pathogen Zymoseptoria tritici. New Phytol *217*, 320-331.

Khakh, B.S. (2009). ATP-gated P2X receptors on excitatory nerve terminals onto interneurons initiate a form of asynchronous glutamate release. Neuropharmacology *56*, 216-222.

Kong, G., Zhao, Y., Jing, M., Huang, J., Yang, J., Xia, Y., Kong, L., Ye, W., Xiong, Q., Qiao, Y., *et al.* (2015). The Activation of Phytophthora Effector Avr3b by Plant Cyclophilin is Required for the Nudix Hydrolase Activity of Avr3b. PLoS Pathog *11*, e1005139.

Kosmacz, M., Gorka, M., Schmidt, S., Luzarowski, M., Moreno, J.C., Szlachetko, J., Leniak, E., Sokolowska, E.M., Sofroni, K., Schnittger, A., *et al.* (2019). Protein and metabolite composition of Arabidopsis stress granules. New Phytol *222*, 1420-1433.

Kosmacz, M., Luzarowski, M., Kerber, O., Leniak, E., Gutierrez-Beltran, E., Moreno, J.C., Gorka, M., Szlachetko, J., Veyel, D., Graf, A., *et al.* (2018). Interaction of 2',3'-cAMP with Rbp47b Plays a Role in Stress Granule Formation. Plant Physiol *177*, 411-421.

Kourelis, J., and van der Hoorn, R.A.L. (2018). Defended to the Nines: 25 Years of Resistance Gene Cloning Identifies Nine Mechanisms for R Protein Function. Plant Cell *30*, 285-299.

Krestinina, O., Azarashvili, T., Baburina, Y., Galvita, A., Grachev, D., Stricker, R., and Reiser, G. (2015). In aging, the vulnerability of rat brain mitochondria is enhanced due to reduced level of 2',3'-cyclic nucleotide-3'-phosphodiesterase (CNP) and subsequently increased permeability transition in brain mitochondria in old animals. Neurochem Int *80*, 41-50.

Kuthanova, A., Opatrny, Z., and Fischer, L. (2008). Is internucleosomal DNA fragmentation an indicator of programmed death in plant cells? J Exp Bot *59*, 2233-2240.

Lacadena, J., Alvarez-Garcia, E., Carreras-Sangra, N., Herrero-Galan, E., Alegre-Cebollada, J., Garcia-Ortega, L., Onaderra, M., Gavilanes, J.G., and Martinez del Pozo, A. (2007). Fungal ribotoxins: molecular dissection of a family of natural killers. FEMS Microbiol Rev *31*, 212-237.

Laflamme, B., Dillon, M.M., Martel, A., Almeida, R.N.D., Desveaux, D., and Guttman, D.S. (2020). The pan-genome effector-triggered immunity landscape of a host-pathogen interaction. Science *367*, 763-768.

Laluk, K., and Mengiste, T. (2010). Necrotroph attacks on plants: wanton destruction or covert extortion? Arabidopsis Book *8*, e0136.

Lapin, D., Kovacova, V., Sun, X., Dongus, J.A., Bhandari, D., von Born, P., Bautor, J., Guarneri, N., Rzemieniewski, J., Stuttmann, J.*, et al.* (2019). A Coevolved EDS1-SAG101-NRG1 Module Mediates Cell Death Signaling by TIR-Domain Immune Receptors. Plant Cell *31*, 2430-2455.

Lee, D., Bourdais, G., Yu, G., Robatzek, S., and Coaker, G. (2015). Phosphorylation of the Plant Immune Regulator RPM1-INTERACTING PROTEIN4 Enhances Plant Plasma Membrane H(+)-ATPase Activity and Inhibits Flagellin-Triggered Immune Responses in Arabidopsis. Plant Cell *27*, 2042-2056.

Lee, H.C., Chathuranga, K., and Lee, J.S. (2019). Intracellular sensing of viral genomes and viral evasion. Exp Mol Med *51*, 1-13.

Lewis, J.D., Lee, A.H., Hassan, J.A., Wan, J., Hurley, B., Jhingree, J.R., Wang, P.W., Lo, T., Youn, J.Y., Guttman, D.S.*, et al.* (2013). The Arabidopsis ZED1 pseudokinase is required for ZAR1-mediated immunity induced by the Pseudomonas syringae type III effector HopZ1a. Proc Natl Acad Sci U S A *110*, 18722-18727.

Li, D., Xie, L., Qiao, Z., Zhu, J., Yao, H., Qin, Y., Yan, Y., Chen, Z., and Ma, F. (2021). IFI16 Isoforms with Cytoplasmic and Nuclear Locations Play Differential Roles in Recognizing Invaded DNA Viruses. J Immunol *207*, 2699-2709.

Li, T., Diner, B.A., Chen, J., and Cristea, I.M. (2012). Acetylation modulates cellular distribution and DNA sensing ability of interferon-inducible protein IFI16. Proc Natl Acad Sci U S A *109*, 10558-10563.

Li, Y., Pazyra-Murphy, M.F., Avizonis, D., de Sa Tavares Russo, M., Tang, S., Chen, C.Y., Hsueh, Y.P., Bergholz, J.S., Jiang, T., Zhao, J.J.*, et al.* (2022). Sarm1 activation produces cADPR to increase intra-axonal Ca++ and promote axon degeneration in PIPN. J Cell Biol *221*.

Liang, W., van Wersch, S., Tong, M., and Li, X. (2018). TIR-NB-LRR immune receptor SOC3 pairs with truncated TIR-NB protein CHS1 or TN2 to monitor the homeostasis of E3 ligase SAUL1. New Phytol.

Liebrand, T.W., van den Burg, H.A., and Joosten, M.H. (2014). Two for all: receptor-associated kinases SOBIR1 and BAK1. Trends Plant Sci *19*, 123-132.

Liu, J., Elmore, J.M., Lin, Z.J., and Coaker, G. (2011). A receptor-like cytoplasmic kinase phosphorylates the host target RIN4, leading to the activation of a plant innate immune receptor. Cell Host Microbe *9*, 137-146.

Liu, S., Wang, J., Han, Z., Gong, X., Zhang, H., and Chai, J. (2016). Molecular Mechanism for Fungal Cell Wall Recognition by Rice Chitin Receptor OsCEBiP. Structure *24*, 1192-1200.

Liu, T., Liu, Z., Song, C., Hu, Y., Han, Z., She, J., Fan, F., Wang, J., Jin, C., Chang, J.*, et al.* (2012). Chitin-induced dimerization activates a plant immune receptor. Science *336*, 1160-1164.

Lorang, J., Kidarsa, T., Bradford, C.S., Gilbert, B., Curtis, M., Tzeng, S.C., Maier, C.S., and Wolpert, T.J. (2012). Tricking the guard: exploiting plant defense for disease susceptibility. Science *338*, 659-662.

Loverix, S., Laus, G., Martins, J.C., Wyns, L., and Steyaert, J. (1998). Reconsidering the energetics of ribonuclease catalysed RNA hydrolysis. Eur J Biochem *257*, 286-290.

Lu, X., Kracher, B., Saur, I.M., Bauer, S., Ellwood, S.R., Wise, R., Yaeno, T., Maekawa, T., and Schulze-Lefert, P. (2016). Allelic barley MLA immune receptors recognize sequence-unrelated avirulence effectors of the powdery mildew pathogen. Proc Natl Acad Sci U S A *113*, E6486-E6495.

Lu, Y., and Tsuda, K. (2021). Intimate Association of PRR- and NLR-Mediated Signaling in Plant Immunity. Mol Plant Microbe Interact *34*, 3-14.

Luteijn, R.D., Zaver, S.A., Gowen, B.G., Wyman, S.K., Garelis, N.E., Onia, L., McWhirter, S.M., Katibah, G.E., Corn, J.E., Woodward, J.J.*, et al.* (2019). SLC19A1 transports immunoreactive cyclic dinucleotides. Nature *573*, 434-438.

Ma, S., Lapin, D., Liu, L., Sun, Y., Song, W., Zhang, X., Logemann, E., Yu, D., Wang, J., Jirschitzka, J.*, et al.* (2020). Direct pathogen-induced assembly of an NLR immune receptor complex to form a holoenzyme. Science *370*.

Mackey, D., Holt, B.F., 3rd, Wiig, A., and Dangl, J.L. (2002). RIN4 interacts with Pseudomonas syringae type III effector molecules and is required for RPM1-mediated resistance in Arabidopsis. Cell *108*, 743-754.

Mahdi, L.K., Huang, M., Zhang, X., Nakano, R.T., Kopp, L.B., Saur, I.M.L., Jacob, F., Kovacova, V., Lapin, D., Parker, J.E.*, et al.* (2020). Discovery of a Family of Mixed Lineage Kinase Domain-like Proteins in Plants and Their Role in Innate Immune Signaling. Cell Host Microbe *28*, 813-824 e816.

Marco R. Straus, S.R., Emiel Ver Loren van Themaat, Michael Bartsch and Jane E. Parker (2010). Salicylic acid antagonism of EDS1-driven cell deathis important for immune and oxidative stress responsesin Arabidopsis. The plant jounal *62, 628–640.*

Martel, A., Laflamme, B., Seto, D., Bastedo, D.P., Dillon, M.M., Almeida, R.N.D., Guttman, D.S., and Desveaux, D. (2020). Immunodiversity of the Arabidopsis ZAR1 NLR Is Conveyed by Receptor-Like Cytoplasmic Kinase Sensors. Front Plant Sci *11*, 1290.

Martin, R., Qi, T., Zhang, H., Liu, F., King, M., Toth, C., Nogales, E., and Staskawicz, B.J. (2020). Structure of the activated ROQ1 resistosome directly recognizing the pathogen effector XopQ. Science *370*.

Mauro, V.P., and Chappell, S.A. (2018). Considerations in the Use of Codon Optimization for Recombinant Protein Expression. Methods Mol Biol *1850*, 275-288.

Mazzoleni, S., Bonanomi, G., Incerti, G., Chiusano, M.L., Termolino, P., Mingo, A., Senatore, M., Giannino, F., Carteni, F., Rietkerk, M.*, et al.* (2015). Inhibitory and toxic effects of extracellular self-DNA in litter: a mechanism for negative plant-soil feedbacks? New Phytol *205*, 1195-1210.

Meador, J., 3rd, Cannon, B., Cannistraro, V.J., and Kennell, D. (1990). Purification and characterization of Escherichia coli RNase I. Comparisons with RNase M. Eur J Biochem *187*, 549-553.

Medina-Castellanos, E., Esquivel-Naranjo, E.U., Heil, M., and Herrera-Estrella, A. (2014). Extracellular ATP activates MAPK and ROS signaling during injury response in the fungus Trichoderma atroviride. Front Plant Sci *5*, 659.

Meyers, B.C., Morgante, M., and Michelmore, R.W. (2002). TIR-X and TIR-NBS proteins: two new families related to disease resistance TIR-NBS-LRR proteins encoded in Arabidopsis and other plant genomes. Plant J *32*, 77-92.

Miya, A., Albert, P., Shinya, T., Desaki, Y., Ichimura, K., Shirasu, K., Narusaka, Y., Kawakami, N., Kaku, H., and Shibuya, N. (2007). CERK1, a LysM receptor kinase, is essential for chitin elicitor signaling in Arabidopsis. Proc Natl Acad Sci U S A *104*, 19613-19618.

Moore, B. (2004). Bifunctional and moonlighting enzymes: lighting the way to regulatory control. Trends Plant Sci *9*, 221-228.

Moran Luengo, T., Mayer, M.P., and Rudiger, S.G.D. (2019). The Hsp70-Hsp90 Chaperone Cascade in Protein Folding. Trends Cell Biol *29*, 164-177.

Morrone, S.R., Matyszewski, M., Yu, X., Delannoy, M., Egelman, E.H., and Sohn, J. (2015). Assembly-driven activation of the AIM2 foreign-dsDNA sensor provides a polymerization template for downstream ASC. Nat Commun *6*, 7827.

Motwani, M., Pesiridis, S., and Fitzgerald, K.A. (2019). DNA sensing by the cGAS-STING pathway in health and disease. Nat Rev Genet *20*, 657-674.

Muller, J., Piffanelli, P., Devoto, A., Miklis, M., Elliott, C., Ortmann, B., Schulze-Lefert, P., and Panstruga, R. (2005). Conserved ERAD-like quality control of a plant polytopic membrane protein. Plant Cell *17*, 149-163.

Myong, S., Cui, S., Cornish, P.V., Kirchhofer, A., Gack, M.U., Jung, J.U., Hopfner, K.P., and Ha, T. (2009). Cytosolic viral sensor RIG-I is a 5'-triphosphate-dependent translocase on double-stranded RNA. Science *323*, 1070-1074.

Nandety, R.S., Caplan, J.L., Cavanaugh, K., Perroud, B., Wroblewski, T., Michelmore, R.W., and Meyers, B.C. (2013). The role of TIR-NBS and TIR-X proteins in plant basal defense responses. Plant Physiol *162*, 1459-1472.

Naveed, Z.A., Wei, X., Chen, J., Mubeen, H., and Ali, G.S. (2020). The PTI to ETI Continuum in Phytophthora-Plant Interactions. Front Plant Sci *11*, 593905.

Ngou, B.P.M., Ahn, H.K., Ding, P., and Jones, J.D.G. (2021). Mutual potentiation of plant immunity by cell-surface and intracellular receptors. Nature *592*, 110-115.

Ngou, B.P.M., Ahn, H.K., Ding, P., Redkar, A., Brown, H., Ma, Y., Youles, M., Tomlinson, L., and Jones, J.D.G. (2020). Estradiol-inducible AvrRps4 expression reveals distinct properties of TIR-NLR-mediated effector-triggered immunity. J Exp Bot *71*, 2186-2197.

Nishimura, M.T., Anderson, R.G., Cherkis, K.A., Law, T.F., Liu, Q.L., Machius, M., Nimchuk, Z.L., Yang, L., Chung, E.H., El Kasmi, F*., et al.* (2017). TIR-only protein RBA1 recognizes a pathogen effector to regulate cell death in Arabidopsis. Proc Natl Acad Sci U S A *114*, E2053-E2062.

Nonaka, G., Ishikawa, T., Liu, T.T., Nakajima, H., and Kitamoto, K. (2000). Genetic analysis of growth inhibition of yeast cells caused by expression of Aspergillus oryzae RNase T1. Biosci Biotechnol Biochem *64*, 2152-2158.

Ofir, G., Herbst, E., Baroz, M., Cohen, D., Millman, A., Doron, S., Tal, N., Malheiro, D.B.A., Malitsky, S., Amitai, G*., et al.* (2021). Antiviral activity of bacterial TIR domains via immune signalling molecules. Nature *600*, 116-120.

Oh, M.H., Wu, X., Clouse, S.D., and Huber, S.C. (2011). Functional importance of BAK1 tyrosine phosphorylation in vivo. Plant Signal Behav *6*, 400-405.

Oliver, J., Erin L. Baggs, Charles Uhlmann, Federica Locci, Henriette L. Läßle, Katharina Melkonian, Kiara Käufer, Joram A. Dongus, Hirofumi Nakagami, Ksenia V. Krasileva*, et al.* (2021). Differential EDS1 requirement for cell death activities of plant TIR-domain proteins. BioRxiv.

Olombrada, M., Lazaro-Gorines, R., Lopez-Rodriguez, J.C., Martinez-Del-Pozo, A., Onaderra, M., Maestro-Lopez, M., Lacadena, J., Gavilanes, J.G., and Garcia-Ortega, L. (2017). Fungal Ribotoxins: A Review of Potential Biotechnological Applications. Toxins (Basel) *9*.

Ostendorf, T., Zillinger, T., Andryka, K., Schlee-Guimaraes, T.M., Schmitz, S., Marx, S., Bayrak, K., Linke, R., Salgert, S., Wegner, J*., et al.* (2020). Immune Sensing of Synthetic, Bacterial, and Protozoan RNA by Toll-like Receptor 8 Requires Coordinated Processing by RNase T2 and RNase 2. Immunity *52*, 591-605 e596.

Pace, C.N., and Grimsley, G.R. (1988). Ribonuclease T1 is stabilized by cation and anion binding. Biochemistry *27*, 3242-3246.

Pace, C.N., Grimsley, G.R., Thomson, J.A., and Barnett, B.J. (1988). Conformational stability and activity of ribonuclease T1 with zero, one, and two intact disulfide bonds. J Biol Chem *263*, 11820-11825.

Pedersen, C., Ver Loren van Themaat, E., McGuffin, L.J., Abbott, J.C., Burgis, T.A., Barton, G., Bindschedler, L.V., Lu, X., Maekawa, T., Wessling, R.*, et al.* (2012). Structure and evolution of barley powdery mildew effector candidates. BMC Genomics *13*, 694.

Peisley, A., Wu, B., Yao, H., Walz, T., and Hur, S. (2013). RIG-I forms signaling-competent filaments in an ATP-dependent, ubiquitin-independent manner. Mol Cell *51*, 573-583.

Pennington, H.G., Jones, R., Kwon, S., Bonciani, G., Thieron, H., Chandler, T., Luong, P., Morgan, S.N., Przydacz, M., Bozkurt, T.*, et al.* (2019). The fungal ribonuclease-like effector protein CSEP0064/BEC1054 represses plant immunity and interferes with degradation of host ribosomal RNA. PLoS Pathog *15*, e1007620.

Pham, A.Q., Cho, S.H., Nguyen, C.T., and Stacey, G. (2020). Arabidopsis Lectin Receptor Kinase P2K2 Is a Second Plant Receptor for Extracellular ATP and Contributes to Innate Immunity. Plant Physiol *183*, 1364-1375.

Pichlmair, A., Schulz, O., Tan, C.P., Naslund, T.I., Liljestrom, P., Weber, F., and Reis e Sousa, C. (2006). RIG-I-mediated antiviral responses to single-stranded RNA bearing 5'-phosphates. Science *314*, 997-1001.

Pruitt, R.N., Gust, A.A., and Nurnberger, T. (2021). Plant immunity unified. Nat Plants *7*, 382-383.

Pusztahelyi, T. (2018). Chitin and chitin-related compounds in plant-fungal interactions. Mycology *9*, 189-201.

Ranf, S., Gisch, N., Schaffer, M., Illig, T., Westphal, L., Knirel, Y.A., Sanchez-Carballo, P.M., Zahringer, U., Huckelhoven, R., Lee, J.*, et al.* (2015). A lectin S-domain receptor kinase mediates lipopolysaccharide sensing in Arabidopsis thaliana. Nat Immunol *16*, 426-433.

Ravensdale, M., Bernoux, M., Ve, T., Kobe, B., Thrall, P.H., Ellis, J.G., and Dodds, P.N. (2012). Intramolecular interaction influences binding of the Flax L5 and L6 resistance proteins to their AvrL567 ligands. PLoS Pathog *8*, e1003004.

Ravensdale, M., Nemri, A., Thrall, P.H., Ellis, J.G., and Dodds, P.N. (2011). Co-evolutionary interactions between host resistance and pathogen effector genes in flax rust disease. Mol Plant Pathol *12*, 93-102.

Reichler, S.A., Torres, J., Rivera, A.L., Cintolesi, V.A., Clark, G., and Roux, S.J. (2009). Intersection of two signalling pathways: extracellular nucleotides regulate pollen germination and pollen tube growth via nitric oxide. J Exp Bot *60*, 2129-2138.

Ren, J., Mi, Z., Stewart, N.A., and Jackson, E.K. (2009). Identification and quantification of 2',3'-cAMP release by the kidney. J Pharmacol Exp Ther *328*, 855-865.

Riedl, S.J., Li, W., Chao, Y., Schwarzenbacher, R., and Shi, Y. (2005). Structure of the apoptotic protease-activating factor 1 bound to ADP. Nature *434*, 926-933.

Rodriguez, E., Chevalier, J., El Ghoul, H., Voldum-Clausen, K., Mundy, J., and Petersen, M. (2018). DNA damage as a consequence of NLR activation. PLoS Genet *14*, e1007235.

Roos, W.P., and Kaina, B. (2006). DNA damage-induced cell death by apoptosis. Trends Mol Med *12*, 440-450.

Rubartelli, A., and Lotze, M.T. (2007). Inside, outside, upside down: damage-associated molecular-pattern molecules (DAMPs) and redox. Trends Immunol *28*, 429-436.

Rufian, J.S., Rueda-Blanco, J., Lopez-Marquez, D., Macho, A.P., Beuzon, C.R., and Ruiz-Albert, J. (2021). The bacterial effector HopZ1a acetylates MKK7 to suppress plant immunity. New Phytol *231*, 1138-1156.

Ryerson, D.E., and Heath, M.C. (1996). Cleavage of Nuclear DNA into Oligonucleosomal Fragments during Cell Death Induced by Fungal Infection or by Abiotic Treatments. Plant Cell *8*, 393-402.

Ryu, W.-S. (2017). Virus Life Cycle. Molecular Virology of Human Pathogenic Viruses *2017 : 31–45*.

Sanchez-Vallet, A., Saleem-Batcha, R., Kombrink, A., Hansen, G., Valkenburg, D.J., Thomma, B.P., and Mesters, J.R. (2013). Fungal effector Ecp6 outcompetes host immune receptor for chitin binding through intrachain LysM dimerization. Elife *2*, e00790.

Sarris, P.F., Duxbury, Z., Huh, S.U., Ma, Y., Segonzac, C., Sklenar, J., Derbyshire, P., Cevik, V., Rallapalli, G., Saucet, S.B.*, et al.* (2015). A Plant Immune Receptor Detects Pathogen Effectors that Target WRKY Transcription Factors. Cell *161*, 1089-1100.

Saur, I.M., Bauer, S., Kracher, B., Lu, X., Franzeskakis, L., Muller, M.C., Sabelleck, B., Kummel, F., Panstruga, R., Maekawa, T.*, et al.* (2019a). Multiple pairs of allelic MLA immune receptor-powdery mildew AVRA effectors argue for a direct recognition mechanism. Elife *8*.

Saur, I.M.L., Bauer, S., Lu, X., and Schulze-Lefert, P. (2019b). A cell death assay in barley and wheat protoplasts for identification and validation of matching pathogen AVR effector and plant NLR immune receptors. Plant Methods *15*, 118.

Seeholzer, S., Tsuchimatsu, T., Jordan, T., Bieri, S., Pajonk, S., Yang, W., Jahoor, A., Shimizu, K.K., Keller, B., and Schulze-Lefert, P. (2010). Diversity at the Mla powdery mildew resistance locus from cultivated barley reveals sites of positive selection. Mol Plant Microbe Interact *23*, 497-509.

Shan, L., He, P., Li, J., Heese, A., Peck, S.C., Nurnberger, T., Martin, G.B., and Sheen, J. (2008). Bacterial effectors target the common signaling partner BAK1 to disrupt multiple MAMP receptor-signaling complexes and impede plant immunity. Cell Host Microbe *4*, 17-27.

Shen, C., Vohra, M., Zhang, P., Mao, X., Figley, M.D., Zhu, J., Sasaki, Y., Wu, H., DiAntonio, A., and Milbrandt, J. (2021). Multiple domain interfaces mediate SARM1 autoinhibition. Proc Natl Acad Sci U S A *118*.

Shen, Q.H., Saijo, Y., Mauch, S., Biskup, C., Bieri, S., Keller, B., Seki, H., Ulker, B., Somssich, I.E., and Schulze-Lefert, P. (2007). Nuclear activity of MLA immune receptors links isolate-specific and basal disease-resistance responses. Science *315*, 1098-1103.

Shen, Q.H., Zhou, F., Bieri, S., Haizel, T., Shirasu, K., and Schulze-Lefert, P. (2003). Recognition specificity and RAR1/SGT1 dependence in barley Mla disease resistance genes to the powdery mildew fungus. Plant Cell *15*, 732-744.

Shi, Y., Kerry, P.S., Nanson, J.D., Bosanac, T., Sasaki, Y., Krauss, R., Saikot, F.K., Adams, S.E., Mosaiab, T., Masic, V.*, et al.* (2022). Structural basis of SARM1 activation, substrate recognition, and inhibition by small molecules. Mol Cell *82*, 1643-1659 e1610.

Shigematsu, M., Kawamura, T., and Kirino, Y. (2018). Generation of 2',3'-Cyclic Phosphate-Containing RNAs as a Hidden Layer of the Transcriptome. Front Genet *9*, 562.

Shimizu, T., Nakano, T., Takamizawa, D., Desaki, Y., Ishii-Minami, N., Nishizawa, Y., Minami, E., Okada, K., Yamane, H., Kaku, H.*, et al.* (2010). Two LysM receptor molecules, CEBiP and OsCERK1, cooperatively regulate chitin elicitor signaling in rice. Plant J *64*, 204-214.

Singh, N.K., Paz, E., Kutsher, Y., Reuveni, M., and Lers, A. (2020). Tomato T2 ribonuclease LE is involved in the response to pathogens. Mol Plant Pathol *21*, 895-906.

Stok, J.E., Vega Quiroz, M.E., and van der Veen, A.G. (2020). Self RNA Sensing by RIG-I-like Receptors in Viral Infection and Sterile Inflammation. J Immunol *205*, 883-891.

Stuttmann, J., Parker, J.E., and Noel, L.D. (2008). Staying in the fold: The SGT1/chaperone machinery in maintenance and evolution of leucine-rich repeat proteins. Plant Signal Behav *3*, 283-285.

Sun, X., Lapin, D., Feehan, J.M., Stolze, S.C., Kramer, K., Dongus, J.A., Rzemieniewski, J., Blanvillain-Baufume, S., Harzen, A., Bautor, J.*, et al.* (2021). Pathogen effector recognition-dependent association of NRG1 with EDS1 and SAG101 in TNL receptor immunity. Nat Commun *12*, 3335.

Sun, Y., Li, L., Macho, A.P., Han, Z., Hu, Z., Zipfel, C., Zhou, J.M., and Chai, J. (2013). Structural basis for flg22-induced activation of the Arabidopsis FLS2-BAK1 immune complex. Science *342*, 624-628.

Sun, Y., Li, P., Shen, D., Wei, Q., He, J., and Lu, Y. (2019). The Ralstonia solanacearum effector RipN suppresses plant PAMP-triggered immunity, localizes to the endoplasmic reticulum and nucleus, and alters the NADH/NAD(+) ratio in Arabidopsis. Mol Plant Pathol *20*, 533-546.

Takemoto, D., Rafiqi, M., Hurley, U., Lawrence, G.J., Bernoux, M., Hardham, A.R., Ellis, J.G., Dodds, P.N., and Jones, D.A. (2012). N-terminal motifs in some plant disease resistance proteins function in membrane attachment and contribute to disease resistance. Mol Plant Microbe Interact *25*, 379-392.

Tanaka, K., Gilroy, S., Jones, A.M., and Stacey, G. (2010). Extracellular ATP signaling in plants. Trends Cell Biol *20*, 601-608.

Tang, J., Han, Z., Sun, Y., Zhang, H., Gong, X., and Chai, J. (2015). Structural basis for recognition of an endogenous peptide by the plant receptor kinase PEPR1. Cell Res *25*, 110-120.

Thomma, B.P., Nurnberger, T., and Joosten, M.H. (2011). Of PAMPs and effectors: the blurred PTI-ETI dichotomy. Plant Cell *23*, 4-15.

Tian, H., Wu, Z., Chen, S., Ao, K., Huang, W., Yaghmaiean, H., Sun, T., Xu, F., Zhang, Y., Wang, S.*, et al.* (2021). Activation of TIR signalling boosts pattern-triggered immunity. Nature *598*, 500-503.

Tian, W., Hou, C., Ren, Z., Wang, C., Zhao, F., Dahlbeck, D., Hu, S., Zhang, L., Niu, Q., Li, L.*, et al.* (2019). A calmodulin-gated calcium channel links pathogen patterns to plant immunity. Nature *572*, 131-135.

Trapp, B.D., Bernier, L., Andrews, S.B., and Colman, D.R. (1988). Cellular and subcellular distribution of 2',3'-cyclic nucleotide 3'-phosphodiesterase and its mRNA in the rat central nervous system. Journal of neurochemistry *51*, 859-868.

Tyc, K., Kellenberger, C., and Filipowicz, W. (1987). Purification and characterization of wheat germ 2',3'-cyclic nucleotide 3'-phosphodiesterase. The Journal of biological chemistry *262*, 12994-13000.

Unterholzner, L., Keating, S.E., Baran, M., Horan, K.A., Jensen, S.B., Sharma, S., Sirois, C.M., Jin, T., Latz, E., Xiao, T.S.*, et al.* (2010). IFI16 is an innate immune sensor for intracellular DNA. Nat Immunol *11*, 997-1004.

Van Damme, T., Blancquaert, D., Couturon, P., Van Der Straeten, D., Sandra, P., and Lynen, F. (2014). Wounding stress causes rapid increase in concentration of the naturally occurring 2',3'-isomers of cyclic guanosine- and cyclic adenosine monophosphate (cGMP and cAMP) in plant tissues. Phytochemistry *103*, 59-66.

van der Hoorn, R.A., and Kamoun, S. (2008). From Guard to Decoy: a new model for perception of plant pathogen effectors. Plant Cell *20*, 2009-2017.

van Wersch, S., Tian, L., Hoy, R., and Li, X. (2020). Plant NLRs: The Whistleblowers of Plant Immunity. Plant Commun *1*, 100016.

VanSchouwen, B., and Melacini, G. (2017). Regulation of HCN Ion Channels by Non-canonical Cyclic Nucleotides. Handb Exp Pharmacol *238*, 123-133.

Ve, T., Vajjhala, P.R., Hedger, A., Croll, T., DiMaio, F., Horsefield, S., Yu, X., Lavrencic, P., Hassan, Z., Morgan, G.P.*, et al.* (2017). Structural basis of TIR-domain-assembly formation in MAL- and MyD88-dependent TLR4 signaling. Nat Struct Mol Biol *24*, 743-751.

Veeranki, S., and Choubey, D. (2012). Interferon-inducible p200-family protein IFI16, an innate immune sensor for cytosolic and nuclear double-stranded DNA: regulation of subcellular localization. Mol Immunol *49*, 567-571.
Veronese, P., Nakagami, H., Bluhm, B., Abuqamar, S., Chen, X., Salmeron, J., Dietrich, R.A., Hirt, H., and Mengiste, T. (2006). The membrane-anchored BOTRYTIS-INDUCED KINASE1 plays distinct roles in Arabidopsis resistance to necrotrophic and biotrophic pathogens. Plant Cell *18*, 257-273.
Verrier, J.D., Jackson, T.C., Bansal, R., Kochanek, P.M., Puccio, A.M., Okonkwo, D.O., and Jackson, E.K. (2012). The brain in vivo expresses the 2',3'-cAMP-adenosine pathway. J Neurochem *122*, 115-125.
Vorobjeva, N.V., and Chernyak, B.V. (2020). NETosis: Molecular Mechanisms, Role in Physiology and Pathology. Biochemistry (Mosc) *85*, 1178-1190.
Waller, T.J., and Collins, C.A. (2021). An NAD+/NMN balancing act by SARM1 and NMNAT2 controls axonal degeneration. Neuron *109*, 1067-1069.
Wan, L., Essuman, K., Anderson, R.G., Sasaki, Y., Monteiro, F., Chung, E.H., Osborne Nishimura, E., DiAntonio, A., Milbrandt, J., Dangl, J.L.*, et al.* (2019a). TIR domains of plant immune receptors are NAD(+)-cleaving enzymes that promote cell death. Science *365*, 799-803.
Wan, W.L., Frohlich, K., Pruitt, R.N., Nurnberger, T., and Zhang, L. (2019b). Plant cell surface immune receptor complex signaling. Curr Opin Plant Biol *50*, 18-28.
Wang, C., Zhou, M., Zhang, X., Yao, J., Zhang, Y., and Mou, Z. (2017). A lectin receptor kinase as a potential sensor for extracellular nicotinamide adenine dinucleotide in Arabidopsis thaliana. Elife *6*.
Wang, G., Roux, B., Feng, F., Guy, E., Li, L., Li, N., Zhang, X., Lautier, M., Jardinaud, M.F., Chabannes, M.*, et al.* (2015). The Decoy Substrate of a Pathogen Effector and a Pseudokinase Specify Pathogen-Induced Modified-Self Recognition and Immunity in Plants. Cell Host Microbe *18*, 285-295.
Wang, J., Liu, X., Zhang, A., Ren, Y., Wu, F., Wang, G., Xu, Y., Lei, C., Zhu, S., Pan, T.*, et al.* (2019a). A cyclic nucleotide-gated channel mediates cytoplasmic calcium elevation and disease resistance in rice. Cell Res *29*, 820-831.
Wang, J., Wang, J., Hu, M., Wu, S., Qi, J., Wang, G., Han, Z., Qi, Y., Gao, N., Wang, H.W.*, et al.* (2019b). Ligand-triggered allosteric ADP release primes a plant NLR complex. Science *364*.
Wang, Y., Li, J., Hou, S., Wang, X., Li, Y., Ren, D., Chen, S., Tang, X., and Zhou, J.M. (2010). A Pseudomonas syringae ADP-ribosyltransferase inhibits Arabidopsis mitogen-activated protein kinase kinases. Plant Cell *22*, 2033-2044.
Wen, F., Curlango-Rivera, G., Huskey, D.A., Xiong, Z., and Hawes, M.C. (2017). Visualization of extracellular DNA released during border cell separation from the root cap. Am J Bot *104*, 970-978.
Wen, F., White, G.J., VanEtten, H.D., Xiong, Z., and Hawes, M.C. (2009). Extracellular DNA is required for root tip resistance to fungal infection. Plant Physiol *151*, 820-829.
Williams, S.J., Yin, L., Foley, G., Casey, L.W., Outram, M.A., Ericsson, D.J., Lu, J., Boden, M., Dry, I.B., and Kobe, B. (2016). Structure and Function of the TIR Domain from the Grape NLR Protein RPV1. Front Plant Sci *7*, 1850.
Willmann, R., Lajunen, H.M., Erbs, G., Newman, M.A., Kolb, D., Tsuda, K., Katagiri, F., Fliegmann, J., Bono, J.J., Cullimore, J.V.*, et al.* (2011). Arabidopsis lysin-motif proteins LYM1 LYM3 CERK1 mediate bacterial peptidoglycan sensing and immunity to bacterial infection. Proc Natl Acad Sci U S A *108*, 19824-19829.
Wu, Y., Gao, Y., Zhan, Y., Kui, H., Liu, H., Yan, L., Kemmerling, B., Zhou, J.M., He, K., and Li, J. (2020). Loss of the common immune coreceptor BAK1 leads to NLR-dependent cell death. Proc Natl Acad Sci U S A *117*, 27044-27053.

Wu, Z., Tian, L., Liu, X., Zhang, Y., and Li, X. (2021). TIR signal promotes interactions between lipase-like proteins and ADR1-L1 receptor and ADR1-L1 oligomerization. Plant Physiol *187*, 681-686.

Xiao, S., Ellwood, S., Calis, O., Patrick, E., Li, T., Coleman, M., and Turner, J.G. (2001). Broad-spectrum mildew resistance in Arabidopsis thaliana mediated by RPW8. Science *291*, 118-120.

Xu, L., Wang, J., Xiao, Y., Han, Z., and Chai, J. (2022). Structural insight into chitin perception by chitin elicitor receptor kinase 1 of Oryza sativa. J Integr Plant Biol.

Xue, L., Cong, J., Hongbo, Y., Wanting, H., Fang, L., Renchun, F., Jiankun, X., and Qian-Hua, S. (2021). The barley powdery mildew effectors CSEP0139 and CSEP0182 suppress cell death and promote B. graminis fungal virulence in plants. Phytopathology Research.

Yamaguchi, Y., Huffaker, A., Bryan, A.C., Tax, F.E., and Ryan, C.A. (2010). PEPR2 is a second receptor for the Pep1 and Pep2 peptides and contributes to defense responses in Arabidopsis. Plant Cell *22*, 508-522.

Yamaguchi, Y., Pearce, G., and Ryan, C.A. (2006). The cell surface leucine-rich repeat receptor for AtPep1, an endogenous peptide elicitor in Arabidopsis, is functional in transgenic tobacco cells. Proc Natl Acad Sci U S A *103*, 10104-10109.

Yan, S., Wang, W., Marques, J., Mohan, R., Saleh, A., Durrant, W.E., Song, J., and Dong, X. (2013). Salicylic acid activates DNA damage responses to potentiate plant immunity. Mol Cell *52*, 602-610.

Yu, D., Song, W., Tan, E.Y.J., Liu, L., Cao, Y., Jirschitzka, J., Li, E., Logemann, E., Xu, C., Huang, S.*, et al.* (2022). TIR domains of plant immune receptors are 2',3'-cAMP/cGMP synthetases mediating cell death. Cell.

Yu IC, P.J., Bent AF (1998). Gene-for-gene disease resistance without the hypersensitive response in Arabidopsis dnd1 mutant. . Proceedings of the National Academy of Sciences of the United States of America *95(13):7819-7824.*

Yu, X., Xu, G., Li, B., de Souza Vespoli, L., Liu, H., Moeder, W., Chen, S., de Oliveira, M.V.V., Ariadina de Souza, S., Shao, W.*, et al.* (2019). The Receptor Kinases BAK1/SERK4 Regulate Ca(2+) Channel-Mediated Cellular Homeostasis for Cell Death Containment. Curr Biol *29*, 3778-3790 e3778.

Yuan, H., Jin, C., Pei, H., Zhao, L., Li, X., Li, J., Huang, W., Fan, R., Liu, W., and Shen, Q.H. (2021a). The Powdery Mildew Effector CSEP0027 Interacts With Barley Catalase to Regulate Host Immunity. Front Plant Sci *12*, 733237.

Yuan, M., Jiang, Z., Bi, G., Nomura, K., Liu, M., Wang, Y., Cai, B., Zhou, J.M., He, S.Y., and Xin, X.F. (2021b). Pattern-recognition receptors are required for NLR-mediated plant immunity. Nature *592*, 105-109.

Yuan, M., Ngou, B.P.M., Ding, P., and Xin, X.F. (2021c). PTI-ETI crosstalk: an integrative view of plant immunity. Curr Opin Plant Biol *62*, 102030.

Zelman, A.K., Dawe, A., Gehring, C., and Berkowitz, G.A. (2012). Evolutionary and structural perspectives of plant cyclic nucleotide-gated cation channels. Front Plant Sci *3*, 95.

Zeng, L., Velasquez, A.C., Munkvold, K.R., Zhang, J., and Martin, G.B. (2012). A tomato LysM receptor-like kinase promotes immunity and its kinase activity is inhibited by AvrPtoB. Plant J *69*, 92-103.

Zhang, J., Li, W., Xiang, T., Liu, Z., Laluk, K., Ding, X., Zou, Y., Gao, M., Zhang, X., Chen, S.*, et al.* (2010). Receptor-like cytoplasmic kinases integrate signaling from multiple plant immune receptors and are targeted by a Pseudomonas syringae effector. Cell Host Microbe *7*, 290-301.

Zhang, J., Shao, F., Li, Y., Cui, H., Chen, L., Li, H., Zou, Y., Long, C., Lan, L., Chai, J.*, et al.* (2007). A Pseudomonas syringae effector inactivates MAPKs to suppress PAMP-induced immunity in plants. Cell Host Microbe *1*, 175-185.

Zhang, J., and Zhou, J.M. (2010). Plant immunity triggered by microbial molecular signatures. Mol Plant *3*, 783-793.
Zhang, X., Bernoux, M., Bentham, A.R., Newman, T.E., Ve, T., Casey, L.W., Raaymakers, T.M., Hu, J., Croll, T.I., Schreiber, K.J.*, et al.* (2017). Multiple functional self-association interfaces in plant TIR domains. Proc Natl Acad Sci U S A *114*, E2046-E2052.
Zhang, X., and Mou, Z. (2009). Extracellular pyridine nucleotides induce PR gene expression and disease resistance in Arabidopsis. Plant J *57*, 302-312.
Zhang, X., and Mou, Z. (2012). Expression of the human NAD(P)-metabolizing ectoenzyme CD38 compromises systemic acquired resistance in Arabidopsis. Mol Plant Microbe Interact *25*, 1209-1218.
Zhang, X., Wu, J., Du, F., Xu, H., Sun, L., Chen, Z., Brautigam, C.A., Zhang, X., and Chen, Z.J. (2014). The cytosolic DNA sensor cGAS forms an oligomeric complex with DNA and undergoes switch-like conformational changes in the activation loop. Cell Rep *6*, 421-430.
Zhang, X.C., and Gassmann, W. (2003). RPS4-mediated disease resistance requires the combined presence of RPS4 transcripts with full-length and truncated open reading frames. Plant Cell *15*, 2333-2342.
Zhang, X.C., and Gassmann, W. (2007). Alternative splicing and mRNA levels of the disease resistance gene RPS4 are induced during defense responses. Plant Physiol *145*, 1577-1587.
Zhao, C., Tang, Y., Wang, J., Zeng, Y., Sun, H., Zheng, Z., Su, R., Schneeberger, K., Parker, J.E., and Cui, H. (2021). A mis-regulated cyclic nucleotide-gated channel mediates cytosolic calcium elevation and activates immunity in Arabidopsis. New Phytol *230*, 1078-1094.
Zhao, M., Wang, J., Ji, S., Chen, Z., Xu, J., Tang, C., Chen, S., Kang, Z., and Wang, X. (2018). Candidate Effector Pst_8713 Impairs the Plant Immunity and Contributes to Virulence of Puccinia striiformis f. sp. tritici. Front Plant Sci *9*, 1294.
Zhou, C., Chen, X., Planells-Cases, R., Chu, J., Wang, L., Cao, L., Li, Z., Lopez-Cayuqueo, K.I., Xie, Y., Ye, S.*, et al.* (2020). Transfer of cGAMP into Bystander Cells via LRRC8 Volume-Regulated Anion Channels Augments STING-Mediated Interferon Responses and Anti-viral Immunity. Immunity *52*, 767-781 e766.
Zhou, J., Wu, S., Chen, X., Liu, C., Sheen, J., Shan, L., and He, P. (2014). The Pseudomonas syringae effector HopF2 suppresses Arabidopsis immunity by targeting BAK1. Plant J *77*, 235-245.
Zhou, J.M., and Chai, J. (2008). Plant pathogenic bacterial type III effectors subdue host responses. Curr Opin Microbiol *11*, 179-185.
Zhou, J.M., and Zhang, Y. (2020). Plant Immunity: Danger Perception and Signaling. Cell *181*, 978-989.
Zipfel, C., Kunze, G., Chinchilla, D., Caniard, A., Jones, J.D., Boller, T., and Felix, G. (2006). Perception of the bacterial PAMP EF-Tu by the receptor EFR restricts Agrobacterium-mediated transformation. Cell *125*, 749-760.
Zipfel, C., Robatzek, S., Navarro, L., Oakeley, E.J., Jones, J.D., Felix, G., and Boller, T. (2004). Bacterial disease resistance in Arabidopsis through flagellin perception. Nature *428*, 764-767.